Study of the neutrino mass hierarchy with the atmospheric neutrino data observed in Super-Kamiokande

By
Lee Ka Pik
October 2012

Abstract

This thesis presents the full three flavor neutrino oscillation analysis carried out with Super-Kamiokande atmospheric neutrino data in order to obtain information on the mass hierarchy for the first time. The entire set of oscillation parameters, which include two mass differences Δm^2_{12} and Δm^2_{32}, three mixing angles θ_{12}, θ_{23}, θ_{13}, and the CP phase parameter δ_{CP}, and the mass hierarchies are considered. This is the first study to probe the mass hierarchy with neutrino and anti-neutrino enriched event samples from the Super-Kamiokande atmospheric neutrino data.

Super-Kamiokande is a 50 kton water Cherenkov detector which started taking data since 1996. All the observed data of atmospheric neutrino through running periods SK-I, SK-II, SK-III and SK-IV collected from 1996 to 2012 are used in this analysis.

Data selection is summarized in this thesis. The separation of neutrino and anti-neutrino enriched samples with likelihood method is also presented.

Sensitivity study shows that the newly developed neutrino and anti-neutrino enriched samples help to improve the sensitivity on mass hierarchy and other oscillation parameters. The analysis are carried out for both cases of free θ_{13} and fixed θ_{13}. In case of fixed θ_{13}, inverted hierarchy is slightly favoured with significance $\Delta\chi^2 (= \chi^2_{min}(NH) - \chi^2_{min}(IH))$ of 1.2, which is still low to draw a conclusion for the mass hierarchy. It is expected that the mass hierarchy can be constrained with atmospheric neutrinos with longer exposure time or larger detector size in future experiments.

Study of the neutrino mass hierarchy with the atmospheric neutrino data observed in Super-Kamiokande

by

Lee Ka Pik

October 2012

Acknowledgements

I would like thank my supervisor Prof. Kajita for giving me the chance to study atmospheric neutrino. Under his continuous guidance, I have learnt a lot of things. I am very grateful that I am given a chance to join this experiment.

I would like to thank Prof. Masato Shiozawa for his excellent guidance and patience. He gave me a lot of valuable suggestions throughout the whole process of oscillation analysis.

I would also like to express my gratitude to Prof. Y. Suzuki, for his valuable advice on the analysis.

I would also like to thank Prof. Y. Hayato and Dr. K. Okumura, for their continuous support and encouragement.

I would like to thank members of the atmospheric neutrino analysis group especially Prof. S. Moriyama, Dr. M. Miura, Dr. Y. Obayashi, Dr. J. Kameda, Dr. S. Nakayama, Dr. H. Kaji, Prof. Y. Itow, Prof. E. Kearns, Prof. C. Walter, Dr. S. Mine, Dr. J.L. Raaf, Dr. R. Wendell, T. Wongirad.

I would also like to thank other ICRR staff members, Prof. M. Nakahata and Dr. Y. Koshio.

I would like to thank my friends who support and encourage me all the time. Dr. C. Ishihara, Dr. T. Iida, Dr. M. Ikeda, Dr. T. Tanaka, Dr. K. Ueshima, T. F. McLachlan, K. Ueno, T. Yokozawa, K. Iyogi, M. Dziomba, P. de Perio, K. Choi and T. Irvine.

This analysis is based on the hard work by all members of Super-Kamiokande. I would like to express my gratitude to all members supporting this experiment.

I would like to specially thank K. Watanabe for her continuous support throughout my stay in Japan.

Lastly, I would like to express my deep gratitude to my family who support me all the time.

Contents

Acknowledgements **i**

Table of Contents **ii**

List of Figures **v**

List of Tables **xvi**

1 Introduction **1**
- 1.1 Neutrino Oscillation . . . 1
- 1.2 Neutrino Oscillation Experiments . . . 3
  - 1.2.1 Solar and Reactor Neutrino Observations . . . 3
  - 1.2.2 Atmospheric Neutrino and Accelerator Neutrino . . . 4
  - 1.2.3 Mixing Angle θ_{13} Measurement by Accelerator and Reactor Neutrinos . . . 5
  - 1.2.4 Summary for Neutrino Oscillation Parameters and Remaining Issues . . . 7
- 1.3 Sub-Dominant Effects of Atmospheric Neutrino Oscillation . . . 8

2 The Super-Kamiokande Detector **13**
- 2.1 Cherenkov Radiation . . . 14
- 2.2 Detector . . . 16
  - 2.2.1 Water Tank . . . 16
  - 2.2.2 Photomultiplier Tube for the Inner Detector . . . 17
  - 2.2.3 Photomultiplier Tube for the Outer Detector . . . 18
  - 2.2.4 Outer Detector (OD) Segmentation . . . 19
- 2.3 Water Purification System . . . 20
- 2.4 Air Purification System . . . 20
- 2.5 Electronics and Data Acquisition System for SK-I to SK-III Periods . . . 21
  - 2.5.1 Inner Detector Electronics and Data Acquisition System . . . 21
  - 2.5.2 Outer Detector Electronics and Data Acquisition System . . . 22
  - 2.5.3 Trigger . . . 23
- 2.6 Electronics and Data Acquisition System for SK-IV Period . . . 24
  - 2.6.1 Trigger . . . 26
  - 2.6.2 Improvement by the Electronics and Data Acquisition System in SK-IV Period . . . 27

3 Simulation of Atmospheric Neutrino 29
3.1 Atmospheric Neutrino Flux . . . 29
3.2 Neutrino Interaction . . . 35
  3.2.1 Charged Current Quasi-Elastic Scattering . . . 35
  3.2.2 Neutral Current Quasi-Elastic Scattering . . . 36
  3.2.3 Single Meson Production . . . 37
  3.2.4 Deep Inelastic Scattering . . . 42
  3.2.5 Coherent Pion Production . . . 42
  3.2.6 Nuclear Effects . . . 43
3.3 Detector Simulation . . . 45
  3.3.1 Particle Tracking . . . 45
  3.3.2 Cherenkov Photon Tracking in Water . . . 45
  3.3.3 Response of PMT . . . 46

4 Calibration 47
4.1 Detector Calibration . . . 47
  4.1.1 Absolute Gain Calibration . . . 47
  4.1.2 Relative Gain Calibration . . . 48
  4.1.3 Relative Timing Calibration . . . 49
  4.1.4 Water Scattering Measurement with a Laser . . . 50
  4.1.5 Water Transparency Measurement with Cosmic Ray Muons . . . 51
4.2 Energy Calibration . . . 57
  4.2.1 High Energy Stopping Muons . . . 57
  4.2.2 Low Energy Stopping Muons . . . 57
  4.2.3 Neutrino Induced π^0 Events . . . 61
  4.2.4 Decay Electrons . . . 63
  4.2.5 Summary of the Energy Scale Calibration . . . 65
  4.2.6 Time Variation of Energy Scale . . . 65
  4.2.7 Detector Uniformity of Energy Scale . . . 68

5 Data Selection 70
5.1 Reduction for Fully Contained Events . . . 71
  5.1.1 First Reduction . . . 72
  5.1.2 Second Reduction . . . 72
  5.1.3 Third Reduction . . . 75
  5.1.4 Fourth Reduction . . . 83
  5.1.5 Fifth Reduction . . . 83
  5.1.6 FC Reduction Summary . . . 87
5.2 Reduction for Partially Contained Events . . . 89
  5.2.1 First Reduction . . . 89
  5.2.2 Second Reduction . . . 93
  5.2.3 Third Reduction . . . 95
  5.2.4 Fourth Reduction . . . 96
  5.2.5 Fifth Reduction . . . 98
  5.2.6 PC Reduction Summary . . . 103
  5.2.7 PC OD Stop/Through Separation . . . 104

5.3 Reduction for Upward-going Muon Events 107
5.3.1 Charge cut 107
5.3.2 Zenith Angle Cut 107
5.3.3 Scanning 107
5.3.4 UPMU Reduction Summary 108
5.3.5 Background Estimation for Upward-going Muon 110
5.3.6 Upward Through-going Showering Muon 113
5.4 Event Reconstruction 115
5.4.1 Vertex Fitting 116
5.4.2 Ring Counting 117
5.4.3 Particle Identification 120
5.4.4 Precise Vertex Fitting 125
5.4.5 Momentum Reconstruction 129
5.4.6 Decay Electron Search 129
5.4.7 π^0 Reconstruction 130

6 Neutrino Oscillation Analysis 131
6.1 Overview 131
6.2 Data Set 131
6.2.1 Selection for Sub-GeV sample 131
6.2.2 Selection for Multi-GeV Multi-Ring E-like Sample 135
6.2.3 Separation of CCν_e and CC$\overline{\nu}_e$ events in Multi-GeV E-like samples 138
6.2.4 Data Set For the Oscillation Analysis 144
6.3 Oscillation Effect 149
6.4 Analysis Method 153
6.4.1 Definition of χ^2 153
6.5 Systematic Uncertainties 154
6.5.1 Systematic Errors in Neutrino flux 163
6.5.2 Systematic Errors in Neutrino Interactions 168
6.5.3 Systematic Errors in Event Selection and Reconstruction 173
6.6 Sensitivity Study 176
6.7 Results 178
6.8 Discussion 188
6.8.1 Event Samples Contributing to the Sensitivity to Mass Hierarchy 188
6.8.2 Effect of Systematic Errors 189
6.8.3 Consistency with Other Experiments 193

7 Conclusion 195

Bibliography 197

List of Figures

1.1 Proton and helium spectra from primary cosmic rays. [22] 4

1.2 90% C.L. allowed regions of oscillation parameters for $\nu_\mu \leftrightarrow \nu_\tau$ oscillation. Horizontal axis is $\sin^2 2\theta_{23}$ and the vertical axis is Δm^2_{32}.The results are taken from SK zenith angle analysis (solid line)[36], L/E results (dashed line)[31], MINOS experiment(dotted line)[34] and K2K(dotted and dashed line)[32]. 6

1.3 Three-neutrino mass-squared spectrum, for the two mass hierarchies. 8

1.4 Left: ν_μ to ν_e (or ν_e to ν_μ) transition probability in the Earth; Right: ν_μ to ν_e (or ν_e to ν_μ) transition probability in vacuum. $\cos\Theta_\nu$ = -1 corresponds to upward direction and $\cos\Theta_\nu = 0$ corresponds to horizontal direction. (Δm^2_{23}, $\sin^2\theta_{23}$, $\sin^2\theta_{13}$) = (2.1×10^{-3} eV^2, 0.5, 0.04) is assumed in the plots [43]. 9

1.5 Left: ν_e transition probability P_{ex} as a function of energy E_ν and zenith angle, assuming oscillation parameters (Δm^2_{12}, Δm^2_{23}, $\sin^2\theta_{12}$, $\sin^2\theta_{23}$) = (7.7×10^{-5} eV^2, 2.1×10^{-3} eV^2, 0.3, 0.5); Right: Electron flux ratio Φ^{osc}_e/Φ^0_e. There is an excess (a deficit) for $\sin^2\theta_{23}$ in the first (second) octant as shown in the top (bottom) figure. As for $\sin^2\theta_{23} = 0.5$, both small excess and deficit are seen as shown in the middle figure. [43]. 11

1.6 Left: Probability of $\nu_\mu \to \nu_e$ oscillation as a function of zenith angle and neutrino energy, in case of (Δm^2_{12}, Δm^2_{23}, $\sin^2\theta_{12}$, $\sin^2\theta_{23}$, $\sin^2\theta_{13}$, δ_{CP}) = (7.7×10^{-5}, 2.1×10^{-3}, 0.3, 0.5, 0.04, 0°). Right: ν_e flux ratio Φ_{osc}/Φ_0 assuming the same oscillation parameters as the left figure. Figures taken from [43]. 12

2.1 Super-Kamiokande detector and its location in Mountain Ikenoyama. 14

2.2 Visual display of a typical neutrino event in the Super-Kamiokande detector. The size of the small circles indicates the amount of Cherenkov photons detected in each PMT. The Cherenkov ring pattern is clearly visible. (Event taken from SK-IV period.) 15

2.3 Supporting frame of PMTs. 16

2.4 Schematic view of the 20-inch PMT used in Super-Kamiokande. 17

2.5 Quantum efficiency distribution of the 20-inch PMT used in the ID against wavelength and the relative Cherenkov spectrum through pure water. [135] 19

2.6 Single photoelectron distribution of the 20-inch PMT. 20

2.7 PMT case used to cover 20-inch PMT in the inner detector since SK-II period. . 21

2.8 A schematic view of the OD region. [43] 21

2.9 Left: SK-II OD event display of a partially contained event, without OD segmentation; Right: SK-III OD event displa of a partially contained event, with OD segmentation. [43] 22

2.10 Block diagram of analog input part of the ATM module. 23
2.11 Schematic view of the ID data acquisition system for SK-I to SK-III periods. 24
2.12 Schematic view of the OD data acquisition system for SK-I to SK-III periods. 25
2.13 Overview of the ID trigger scheme for SK-I to SK-III periods. 26
2.14 Block diagram of the QTC and its surroundings (Data acquisition system for SK-IV period). [53] 27
2.15 Block diagram of one QTC channel. Each channel has three gain ranges: small, medium and large. (Data acquisition system for SK-IV period)[53] 28
2.16 Timing chart for QTC operation. (Data acquisition system for SK-IV period) [53] 28

3.1 Primary cosmic ray proton flux used in Honda flux calculation (line) and the observed results (points) [55]. Observation data points are taken from Webber [60] (crosses), LEAP [61] (upward triangles), MASS1 [62] (open circles), CAPRICE [63] (vertical diamonds), IMAX [64] (downward triangles), BESS98 [65] (circles), AMS [66] (squares), Ryan [67] (horizontal diamonds), JACEE [68] (downward open triangles), Ivanenko [69] (upward open triangles), Kawamura [70] (open squares) and Runjob [71] (open diamonds). 30
3.2 Comparison of the secondary cosmic ray muon flux observed at Tsukuba (left), Mt. Norikura (middle) with the BESS detector [79] and at ballon altitudes at Fort Summer [80]. Plots taken from [149]. 31
3.3 Schematic view of effective areas of primary cosmic rays interacting with air molecules for 1-dimentional calculation and 3-dimentional calculation. Solid arrows represent primary cosmic rays and dotted arrows represent neutrinos. The 3-dimentional calculation gives larger area for near-horizontal directions (from the view of the SK detector), which induces an enhancement of neutrino flux. [43] 32
3.4 Comparison of 3-dimensional and 1-dimensional calculations of neutrino fluxes at Super-K. Squares represent ν_μ, asterisks represents $\bar{\nu_\mu}$, vertical diamonds represent ν_e, horizontal diamonds represend $\bar{\nu_e}$ for 3-dimensional calculation. Solid lines represent ν fluxes and dotted lines represent $\bar{\nu}$ fluxes for 1-dimensional calculation. [56] 32
3.5 Zenith angle dependence of atmospheric neutrino flux for different energy regions. The higher lines represent ν_μ and $\overline{\nu}_\mu$ and the lower lines represent ν_e and $\overline{\nu}_e$. [149] 33
3.6 Comparison of atmospheric neutrino fluxes averaged over all directions (left) and flavor ratio (right). Red solid line represents Honda 11 flux. Dashed line represents the Bartol flux, dotted line represents the FLUKA flux, and blue dashed line represents Honda 06 flux. [149] 33
3.7 Flavor ratio $(\nu_\mu + \bar{\nu_\mu})/(\nu_e + \bar{\nu_e})$ as a function of neutrino energy and zenith angle. Calculation is based on Honda flux. [43] 34
3.8 Charged current quasi-elastic interaction cross section of (a) ν_μ and (b) $\bar{\nu_\mu}$, with experimental data from ANL [93], Gargamelle [94] [95], BNL [96], Serpukhov [97] and SKAT [98]. Solid line indicates scattering off a free proton, the dashed line indicates scattering off bound nucleons in ^{16}O. 37
3.9 Cross section for ν_μ charged current single pion productions. Solid lines are NEUT calculations, points are experimental data. [136] 39
3.10 Cross section for $\bar{\nu_\mu}$ charged current single pion productions. Solid lines are NEUT calculations, points are experimental data. [136] 40

3.11 Cross section for neutral current single pion productions. Lines are NEUT calculations, with solid lines for ν_μ and dashed line for $\bar{\nu_\mu}$. Points are experimental data taken from [104] (dot) and [105] (square). [136] 41
3.12 Cross section for DIS charged current ν_μ (upper lines and points) and $\bar{\nu_\mu}$ (lower lines and points) interactions. GRV98 is used with Bodek-Yang correction in NEUT, as shown by the dashed lines. The points represent experimental data. [136] 43
3.13 Cross section of $\pi^+ -^{12} C$ scattering as a function of π^+ momentum. Solid lines are NEUT calculation before tuning, dashed lines are NEUT calculation after tuning. Points with error bars are experimental data. [119] 44

4.1 The charge distribution of a typical PMT. 47
4.2 Schematic view of the relative gain measurement system. 48
4.3 Schematic view of the timing measurement system using a laser. 49
4.4 TQ-map, a measured two-dimensional plot of timing against charge distribution. Horizontal axis represents charge of each hit and vertical axis represents hit timing. 50
4.5 Positions of the eight laser light injects in the SK tank. "Top old" refers to the original SK-I light injector which is still being used at the moment. 51
4.6 Typical laser light injector event. 52
4.7 PMT hit time distribution in different detector regions for data and Monte Carlo (after tuning by scattering and absorption parameters). 53
4.8 Water coefficients for December 2009. The top plot shows absorption, the middle plot shows symmetric scattering and the bottom plot shows asymmetric scattering. From these data, the average and error on the mean are calculated. The averages for 337 nm, 375 nm, 405 nm and 445 nm are shown by the numbers on the plots respectively. 53
4.9 A example of fitting. Fitted water coefficient functions for Apr 2009. The solid lines show the fitting in SK4 and the dashed lines show the SK3 functions. Points are coefficient averages and error bars are the error on the mean. 54
4.10 Schematic view of the attenuation length measurement with vertically penetrating cosmic ray muons. Arrows from the muon track (solid line) show the trajectories of Cherenkov photons. l_i is the flight length of the Cherenkov photons detected by the i-th PMT. 55
4.11 Effective observed charge for through-going muons as a function of photon pathlengths (l), where Q is the detected charge and $f(\theta)$ is the PMT acceptance. . . 55
4.12 Time variation of water attenuation lengths for SK-I, SK-II, SK-III and SK-IV. . 56
4.13 Upper left panel shows the reconstructed momentum distribution $P_{p.e.}$ for data (circles with error bars) and MC (solid line). Upper right panel shows the reconstructed opening angle distribution, also for data and MC. Lower two panels show the correlation between reconstructed Cherenkov opening anlge θ_C and the reconstructed momentum $P_{p.e.}$ for data (left) and MC (right). All distributions are made from SK-II. 58
4.14 Left panels show the averaged ratio of momentum derived from charge to that derived from the opening angle ($P_{p.e.}$ / P_θ) as a function of reconstructed momentum $P(\theta)$ for data (solid line) and MC (dashed line). Right panels show the ratio of MC events to data in the corresponding left panel. 60

4.15 Invariant mass distribution of neutrino induced π^0 events of observed data (dot) and MC (boxes). MC are normalized to the livetime of the observed data. 62
4.16 Momentum distribution of decay electrons of data (dot) and MC (solid line) for each SK period. MC events are normalized by number of observed data. 64
4.17 Summary of absolute energy scale calibration for each SK period. Horizontal axis shows the momentum range and vertical axis shows the deviation of data from MC predictions. 66
4.18 Time variation of the reconstructed momentum of decay electrons (left) and the averaged momentum/range of stopping muons (right) as a function of elapsed days from 1 April 1996 for each SK period. Dotted (dashed) lines show ±1% (±2%) from mean value in each SK period. 67
4.19 Uniformity of the detector gain as a function of zenith angle for each SK period. From top to bottom: SK-I, SK-II, SK-III and SK-IV. Y-axis is the ratio of MC to data of the averaged momentum of decay-electrons. 69

5.1 Schematic view of observed atmospheric neutrino in SK. 70
5.2 Expected neutrino spectra of different event categories. 71
5.3 FC 2nd reduction criterion (1). NHITA$_{800}$ distributions for SK-IV. (a) shows the observed data after the FC 1st reduction. (b) shows FC Monte Carlo events after FC 1st reduction. (c) shows the final samples for both data and Monte Carlo events, where the number of Monte Carlo events is normalized to that of the data. The arrow at NHITA$_{800}$ = 30 is the cut in the FC 2nd reduction for SK-IV. In Figure (c), there are some events remaining at region NHITA$_{800}$ > 30, they are events with either PE$_{total}$ > 100,000 p.e.s or OD trigger off or both. 73
5.4 FC 2nd reduction criterion (2). PE$_{max}$/PE$_{300}$ distributions for SK-IV. (a) shows the data after the FC 1st reduction. (b) shows FC Monte Carlo events after the FC 1st reduction. (c) shows the final samples for the data and Monte Carlo events, where the number of Monte Carlo events is normalized to that of the data. Selection criteria is shown by arrows in the plots. 74
5.5 FC 3rd reduction criterion (1) for through-going muons cut. Scatter plot of the number of hit OD PMTs within 8 m of the entering point NHITA$_{in}$ (x-axis) and the exiting point NHITA$_{out}$ (y-axis) for SK-IV. (a) shows the data after the FC 2nd reduction. (b) shows FC Monte Carlo events after the FC 2nd reduction. (c) shows the final samples for data (bottom left) and Monte Carlo (bottom right) events. Selection criteria are indicted by solid lines. 76
5.6 FC 3rd reduction criterion for stopping muon cut. Number of hit OD PMTs near the entrance points of muons (NHITA$_{in}$) for SK-IV. (a) shows the data after the FC 2nd reduction. (b) shows FC Monte Carlo events after the FC 2nd reduction. (c) shows final samples for both data and Monte Carlo. The selection criteria are shown by arrows. 78
5.7 Positions of the twelve cable holes. The 4 red circles indicate cable holes installed with veto counters. 79
5.8 Schematic view of a cable hole muon and a veto counter. 79
5.9 FC 3rd reduction criterion for flasher event cut. The timing distributions of (i) a typical flasher event and (ii) a typical FC neutrino event. The arrows show the time window for counting NMIN$_{100}$. 80

5.10 FC 3rd reduction criterion for flasher event cut. NMIN_{100} distributions for SK-IV. (a) shows the data after the FC 2nd reduction. (b) shows FC Monte Carlo events after the FC 2nd reduction. (c) shows the final samples for data and the Monte Carlo events, in which the number of Monte Carlo events is normalized to that of the data. Selection criteria are shown by arrows. 82

5.11 FC 5th reduction invisible muon cut. NHITAC_{early} distribution satisfying the criteria $\mathrm{PE}_{tot} < 1000$ p.e.s and $\mathrm{DIST}_{clust} > 500$ cm for SK-IV. (a) shows the data after FC 4th reduction. (b) shows the FC Monte Carlo events after FC 4th reduction. (c) shows the final samples for data and Monte Carlo events whose number is normalized to that of the data. The Selection criteria is shown by the arrows. 84

5.12 FC 5th reduction coincidence muon cut. PE_{late} distributions for SK-IV. (a) shows the data after the FC 4th reduction. (b) shows the Monte Carlo events after the FC 4th reduction. (c) shows the final sample for both data and the Monte Carlo events whose number of events is normalized to that of the data. The selection criteria is shown by the arrows. In (c), there are some events with PElate > 20, as they are events with $\mathrm{PE}_{500} > 300$ p.e.s and hence are not removed by criteria (1). 86

5.13 NHITAC distributions for FC and PC final examples for SK-I (top left), SK-II (top right), SK-III (bottom left) and SK-IV (bottom right). Points show the observed data and error bars, solid lines show the Monte Carlo events assuming no oscillation (dashed lines) and $\nu_\nu \leftrightarrow \nu_\tau$ 2-flavor oscillation with ($\sin^2 2\theta$, Δm^2) = (1.00, 2.5×10^{-3} eV^2) (solid lines). 88

5.14 PC 1st reduction criterion (2). Top left and right plots are the scatter plots of NHITA_{top} (x-axis) and NHITA_{bottom} (y-axis). Top left figure shows the raw data, and top right figure shows the PC Monte Carlo events with vertex in the fiducial volume. Bottom left and right plots show 1-dimentional plot of NHITA_{top} and NHITA_{bottom} distributions respectively for the final sample for both data (black dots) and Monte Carlo (red lines). All plots are for SK-IV. 90

5.15 PC 1st reduction criterion (3). The upper plots are the scatter plots of NHITA_{endcap} and NHITA_{barrel}. The upper left plot shows the raw data and the upper right plot shows the PC Monte Carlo events with vertex in the fiducial volume. Bottom left and right plots show 1-dimentional plot of NHITA_{endcap} and NHITA_{barrel} for final samples for both data and Monte Carlo respectively. All the plots are for SK-IV. 91

5.16 PC 1st reduction criterion (4). Top plots are the scatter plots of number of good OD hits and ODR_{mean}. Top left plot shows the raw data and top right plot shows the PC Monte Carlo events with vertex in the fiducial volume. The bottom plot shows the 1-dimentional plots of ODR_{mean} of both data (black dots) and Monte Carlo (red line). All the plots are for SK-IV. 92

5.17 Schematic view of the algorithm to find hit clusters in PC 2nd reduction. Charged observed in each patch are represented by circles, whose sizes are proportional to the number of p.e.s. Arrows represent the vector charge gradient, pointing to the highest charge among the neighbouring patches. 93

5.18 PC 2nd reduction criterion (2) for SK-III. Distributions of number of OD hit PMTs in the 2nd OD hit cluster. (a) shows the data after PC 1st reduction. (b) shows PC Monte Carlo after PC 1st reduction. (c) shows the final sample for both data and Monte Carlo. The selection criteria is shown by arrows. 94
5.19 PC 2nd reduction criterion (3) for SK-III. Scatter plots of NHITA_{endcap} and NHITA_{side}. (a) shows the data after PC 1st reduction, (b) shows PC Monte Carlo after the 1st reduction. (c) and (d) shows the final samples for data and Monte Carlo respectively. The cut criteria are shown by solid lines. 95
5.20 PC 4th reduction for SK-IV, criteria (1) to (4) for the final samples. Distributions for criteria (1) to (4) for data (black dots) and Monte Carlo (red lines) for the final sample. 97
5.21 PC 5th reduction Corner clipping muon cut B for SK-IV. The plot shows the distribution of the distance from the vertex reconstructed by Point-fit to the nearest fringe of ID, for the final sample for both data (black dots) and Monte Carlo (red line) events. 101
5.22 PC 5th reduction Through-going muon cut D for SK-IV. Upper left plot shows the data after PC 4th reduction while the upper right plot shows the PC Monte Carlo. The bottom left and right plots show the final samples for data and Monte Carlo respectively. 102
5.23 Number of background events outside fiducial volume as a function of distance between reconstructed vertex and the ID wall for SK-III. The solid line shows the fitted exponential curve. 105
5.24 Distribution of PE_{anti} / PE_{exp} for PC stop / through separation for SK-I (top left), SK-II (top right), SK-III (bottom left) and SK-IV (bottom right). The points represent the data with error bar. The shaded regions represent MC of true stopping and true through-going events without oscillation and normalized to data livetime. The selection criteria is shown by the arrow. 106
5.25 Distribution of NHITEX for UPMU stop/through separation for SK-I (top left), SK-II (top right), SK-III (bottom left) and SK-IV (bottom right). Points shows the observed data, dashed line show MC assuming no oscillation and solid line shows MC with $\nu_\mu \leftrightarrow \nu_\tau$ 2-flavor oscillation with ($\sin^2 2\theta$, Δm^2) = (1.00, 2.5 × 10^{-3} eV^2). Selection criteria are shown by arrows. 109
5.26 Scatter plots of zenith versus azimuth directions for stopping muons (left) and through-going muons (right) for SK-IV. 110
5.27 Azimuthal angle distributions for stopping muon (left) and through-going muons (right) for SK-IV. Region (1) has thicker-mountain, while region (2) has thinner-mounter. White histograms show the events of downward-going muons, while the black histograms show the upward-going muons. 111
5.28 Zenith angle distributions for stopping muon (left) and through-going muon (right) for SK-IV in both regions (1) and (2). Solid curves are fitted functions to estimate the background contamination. Zenith angle bins are divided equally to 18 bins between -0.1 < $\cos\theta$ < 0.08. 112
5.29 Energy spectrum of primary neutrino for upward stopping (dotted line), non-showering (dashed line) and showering (solid line) muon events. 113

5.30 Distributions for UPMU showering separation for SK-IV. Scatter plot of $\Delta(Q)$ against χ^2 of UPMU through-going events are shown for data (top left) and MC (top right) (normalized to data lifetime). $\Delta(Q)$ distribution is shown in the bottom panel for data (points) and MC (red solid line). The cut is shown by red dashed line. 114
5.31 Distance between the reconstructed vertex and the true vertex for FC MC Multi-GeV multi-ring μ-like sample for SK-IV. Colored region shows 68% of all events. 116
5.32 The basic idea to find ring candidates. By drawing rings around the hit PMTs with Cherenkov opening angle of 42° from the vertex, center of the actual Cherenkov ring can be identified. 117
5.33 Ring counting likelihood distribution for SK-I, SK-II, SKIII and SK-IV sub-GeV samples. Dots are data and solid lines are MC events. 118
5.34 Ring counting likelihood distribution for SK-I, SK-II, SKIII and SK-IV multi-GeV samples. Dots are data and solid lines are MC events. 119
5.35 Event display of single-ring electron (left) and single-ring muon (right) neutrino MC event. 120
5.36 PID likelihood distribution for FC sub-GeV 1-ring samples for SK-I, SK-II, SK-III and SK-IV. Points represent the data, red lines represent Monte Carlo, the shaded green regions represent the MC CCQE ν_μ events. 121
5.37 PID likelihood distribution for FC multi-GeV 1-ring samples for SK-I, SK-II, SK-III and SK-IV. Points represent the data, red lines represent Monte Carlo, the shaded green regions represent the MC CCQE ν_μ events. 122
5.38 PID likelihood distribution for FC sub-GeV multi-ring samples for SK-I, SK-II, SK-III and SK-IV. Points represent the data, red lines represent Monte Carlo, the shaded green regions represent the MC CCQE ν_μ events. 123
5.39 PID likelihood distribution for FC multi-GeV multi-ring samples for SK-I, SK-II, SK-III and SK-IV. Points represent the data, red lines represent Monte Carlo, the shaded green regions represent the MC CCQE ν_μ events. 124
5.40 Distance between the true vertex and the reconstructed vertex of FC MC sample for SK-IV. Left: Sub-GeV 1-ring elike. Right: Sub-GeV 1-ring μ-like. 125
5.41 Distance between the true vertex and the reconstructed vertex of FC MC sample for SK-IV. Left: Multi-GeV 1-ring elike. Right: Multi-GeV 1-ring μ-like. 125
5.42 Distance between the true vertex and the reconstructed vertex of PC MC sample for SK-IV. 126
5.43 Angular difference between true direction and reconstructed direction of FC MC samples for SK-IV. Left: Sub-GeV 1-ring e-like. Right: Sub-GeV 1-ring μ-like. . 126
5.44 Angular difference between true direction and reconstructed direction of FC MC samples for SK-IV. Left: Mult-GeV 1-ring e-like. Right: Multi-GeV 1-ring μ-like. 127

6.1 Distribution of invariant mass from the π^0 fitter for CCQE (black solid line) and NC (red dashed line) in SK-IV FC sub-GeV single-ring e-like MC events, in five energy regions (from left to right): (1) $P_e <$ 250 MeV/c, (2) 250 MeV/c $\leq P_e$ $<$ 400 MeV/c, (3) 400 MeV/c $\leq P_e <$ 630 MeV/c, (4) 630 MeV/c $\leq$ P $<$ 1000 MeV/c, (5) 1000 MeV/c $< P_e$. The arrows show the events which are taken to be π^0-like. 132

6.2 Distributions used in the π^0 selection for CCQE (black solid line) and NC (red dashed line) in SK-IV FC sub-GeV single-ring e-like MC events, in four energy regions (from top to bottom): (1) 250 MeV/c $\leq P_e <$ 400 MeV/c, (2) 400 MeV/c $\leq P_e <$ 630 MeV/c, (3) 630 MeV/c $\leq$ P $<$ 1000 MeV/c, (4) 1000 MeV/c $< P_e$. In order to select π^0-like and e-like events more efficiently, an additional likelihood selection is applied for events with momentum above 250 MeV/c. The distributions of the three likelihood variables used are shown: energy fraction carried by the second fitted ring (left column), the π^0 mass (middle column) and Δ-likelihood (right column). All distributions are normalized to the histogram area. 134
6.3 Distributions of the variables used in the multi-GeV multi-ring e-like (MME) likelihood for SK-IV. From left to write: PID of the most energetic ring, number of decay electrons, momentum fraction of the most energetic ring, distance between the vertex and the decay electron. From bottom to top, each plot represents an energy bins: (1) 1.33 - 2.5 GeV, (2) 2.5 - 5.0 GeV, (3) 5.0 - 10.0 GeV, (4) 10 - 20 GeV, (5) $>$ 20 GeV. Energy bins correspond to the energy of the most energetic ring. Black solid line represents CCν_e+$\overline{\nu}_e$ and red dashed line represents CC$\nu_\mu + \overline{\nu}_\mu$ and NC. All distributions are normalized to the histogram area. . . 137
6.4 Distribution of number of decay electrons in both data and MC for SK-IV multi-GeV single-ring e-like sample. From bottom to top regions: CCν_e (red), CC$\overline{\nu}_e$ (green), CC$\nu_\mu + \overline{\nu}_\mu$ (blue) and NC (yellow). Data is represented by black dots. MC is normalized to data livetime 1097 days. Two-flavor oscillations ($\sin^2 2\theta$, Δ_m) = (1.0, 2.5$\times10^{-3}$ eV^2) is assumed. Events on left hand side of the arrow is taken as $\overline{\nu}_e$-like sample and those on the right hand side of the arrow is taken as ν_e-like sample. 139
6.5 Diagram showing the interaction of ν_e with the nuclei in water, and the Feynman y = (E'-E)/E where E is the initial energy of the incoming ν_e and E' is the energy of the outgoing electron. 140
6.6 Distributions of the variables used in the MME ν_e and $\overline{\nu}_e$ separation likelihood for SK-IV. From left to right: number of decay electrons, number of rings, momentum fraction of the most energetic ring. From bottom to top, there are five energy bins: (1) 1.33 - 2.5 GeV, (2) 2.5 - 5.0 GeV, (3) 5.0 - 10.0 GeV, (4) 10 - 20 GeV, (5) $>$ 20 GeV. Energy bins correspond to the energy of the most energetic ring. Black solid line represents CCν_e and red dashed line represents CC$\overline{\nu}_e$. All distributions are normalized to the historgram area. Area of the histograms are normalized to their corresponding areas. 142
6.7 Distribution of the ν_e and $\overline{\nu}_e$ separation likelihood for SK-IV 500 years MC. Solid line represents CC ν_e, dashed line represents CC$\overline{\nu}_e$ and dotted line represents NC events. The arrow shows the cut which is made at 0. For events having $L_{\nu_e/\overline{\nu}_e}$ $>$ 0, they are taken as ν_e-like events, and for events having $L_{\nu_e/\overline{\nu}_e} <$ 0, they are taken as $\overline{\nu}_e$-like events. 143
6.8 Summary of selection steps for the Multi-GeV e-like samples. 144
6.9 Flux ratio of electron neutrino for oscillations with parameters (Δm^2_{12}, Δm^2_{32}, $\sin^2\theta_{12}$, $\sin^2\theta_{23}$, $\sin^2\theta_{13}$, δ_{CP}) = (7.6 $\times$ 10^{-5}, 2.4 $\times$ 10^{-3}, 0.31, 0.5, 0.025, 220°). The flux ratio is the comparison between flux with and without oscillation. . . . 149

6.10 Zenith angle distribution for multi-GeV single-ring + multi-ring ν_e-like (top) and multi-GeV single-ring + multi-ring $\overline{\nu}_e$-like (bottom) samples in SK-IV. The y-axis shows the number of events with oscillations divided by the number of events without oscillations. Oscillation paramters are (Δm^2_{12}, Δm^2_{32}, $\sin^2\theta_{12}$, $\sin^2\theta_{13}$, δ_{CP}) = (7.6×10^{-5} eV^2, 2.4×10^{-3} eV^2, 0.31, 0.025, 40°). Oscillations at different values of $\sin^2\theta_{23} = 0.4$ (green), 0.5 (red), 0.6 (blue) for normal hierarchy (dashed line) and inverted hierarchy (solid line) are shown. 151

6.11 Zenith angle distributions of the ratio of number of events with oscillation to that without oscillation, assuming oscillation parameters (Δm^2_{12}, Δm^2_{32}, $\sin^2\theta_{12}$, $\sin^2\theta_{23}, sin^2\theta_{13}$) = ($7.7 \times 10^{-5}$, 2.66×10^{-3}, 0.30, 0.425, 0.025) in normal hierarchy case for SK-IV. Cases with $\delta_{CP} = 80°$ (blue dotted line), 220° (red solid line) and 300° (green dashed line) are shown. The error bars represent the size of the error with SK-I + SK-II + SK-III + SK-IV data livetime. 152

6.12 Definition of the binning used in the neutrino oscillation analysis. FC: 370 bins, PC: 60 bins, UPMU: 50 bins. White boxes indicate that momentum bin is divided into 10 zenith angle bins between -1 < $\cos\theta$ < 1 for FC and PC, -1 < $\cos\theta$ < 0 for UPMU. Shaded boxes indicate the momentum bin is not further divided into zenith angle bins. FC single-ring e-like 1-decay, π^0-like, μ-like 2-decay samples and 2-ring π^0 sample are not divided into zenith angle bins. 155

6.13 Contribution of each error source for atmospheric neutrino flux [78] is shown in the upper plot. Absolute normalization uncertainty due to only δ_π (atmospheric muon data (pion producion)) and δ_σ (hadronic interaction mode) as a function of neutrino energy is shown in the lower plot. 163

6.14 Flavor ratio $(\nu_\mu + \overline{\nu}_\mu)/(\nu_e + \overline{\nu}_e)$ of the atmospheric neutrino flux. Vertical axis stands for the double ratio, FLUKA flux/Honda flux is represented by solid lien, Bartol flux/Honda flux is represented by dashed line. The kink at 8 GeV in FLUKA flux due to technical treatment is corrected in the application. 164

6.15 Anti-neutrino / neutrino double ratio for $\overline{\nu}_e/\nu_e$ (left) and $\overline{\nu}_\mu/\nu_\mu$ (right). Solid (dashed) line indicates the double ratio with FLUKA (Bartol) flux. 165

6.16 Neutrino flight length as a function of zenith angle. Solid curve represents the flight length used in our analysis and dashed curve represents that for the compressed density structure of atmosphere by 10%. 167

6.17 Ratio of calculated neutrino flux in which the fluxes and Bartol (solid line) and FLUKA (dashed line) are normalized by Honda flux. 168

6.18 Top left: ratio of CCQE cross section, Nieves model normalized by the Smith and Monitz model, for $\nu_e + \overline{\nu}_e$ (solid line) and $\nu_\mu + \overline{\nu}_\mu$ (dashed line). Top right: $(\nu_\mu + \overline{\nu}_\mu)/(\nu_e + \overline{\nu}_e)$ ratio. Bottom: $(\overline{\nu}/\nu)$ ratio. 169

6.19 Predicted cross section (left) and the $\overline{\nu}/\nu$ ratio (right) of the Hernandez model normalized by that of the Rein and Sehgal model for $\nu_\mu p \to \mu^- p\pi^+$ (solid line), $\nu_\mu n \to \mu^- p\pi^0$ (dashed line) and $\nu_\mu n \to \mu^- p\pi^+$ (dotted line). 170

6.20 π^+ scattering on carbon target in: quasi-elastic channel (top left), absorption channel (top right), total reaction channel (bottom left) and single charge exchange channel (bottom right). 172

6.21 Pion multiplicity plotted as a function of W^2 for NEUT simulation (left) and for the data from the CHORUS experiment (right). 174

6.22 The plots show χ^2 distributions for $\sin^2\theta_{23}$ (top left), Δm^2_{23} (top right) and δ_{CP} (bottom) for the sensitivity study carried out with data livetime assuming normal hierarchy and oscillation parameters of ($\sin^2\theta_{12}$, Δm^2_{12}, $\sin^2\theta_{23}$, Δm^2_{32}, $\sin^2\theta_{13}$, δ_{CP}) = (0.304, 7.66×10^{-5}, 0.5, 2.66×10^{-3}, 0.025, 300°). Black line represents the distribution for normal hierarchy, and red line represents the distribution for inverted hierarchy. 177

6.23 SK-I + SK-II + SK-III + SK-IV zenith angle distributions for FC events for data (line with error bar) and MC assuming no oscillation (grey dashed line), best fit results at normal hierarchy (red solid line) and best fit results at inverted hierarchy (blue dashed line). From top to the bottom: Sub-GeV 1-ring e-like 0-decay, Sub-GeV μ-like 0-decay, Sub-GeV μ-like 1-decay 180

6.24 SK-I + SK-II + SK-III + SK-IV zenith angle distributions for FC events for data (line with error bar) and MC assuming no oscillation (grey dashed line), best fit results at normal hierarchy (red solid line) and best fit results at inverted hierarchy (blue dashed line). From top to the bottom: Multi-GeV 1-ring ν_e-like, Multi-GeV 1-ring $\overline{\nu}_e$-like, Multi-GeV 1-ring μ-like. 181

6.25 SK-I + SK-II + SK-III + SK-IV zenith angle distributions for FC events for data (line with error bar) and MC assuming no oscillation (grey dashed line), best fit results at normal hierarchy (red solid line) and best fit results at inverted hierarchy (blue dashed line). From top to the bottom: Multi-GeV multi-ring ν_e-like, Multi-GeV multi-ring $\overline{\nu}_e$-like, Multi-GeV multi-ring μ-like. 182

6.26 SK-I + SK-II + SK-III + SK-IV zenith angle distributions for FC events for data (line with error bar) and MC assuming no oscillation (grey dashed line), best fit results at normal hierarchy (red solid line) and best fit results at inverted hierarchy (blue dashed line). From top to the bottom: PC stop, PC through . . 183

6.27 SK-I + SK-II + SK-III + SK-IV zenith angle distributions for FC events for data (line with error bar) and MC assuming no oscillation (grey dashed line), best fit results at normal hierarchy (red solid line) and best fit results at inverted hierarchy (blue dashed line). From top to the bottom: UPMU stopping, UPMU non-showering, UPMU showering. 184

6.28 $\Delta\chi^2 = \chi^2 - \chi^2_{min}$ distributions of $\Delta\chi^2$ as a function of Δm^2_{32}, $\sin^2\theta_{23}$, δ_{CP} and $\sin^2\theta_{13}$ (in case of free θ_{13}) for normal hierarchy case. Black line represents fixed $\sin^2\theta_{13} = 0.025$ and blue line represents free θ_{13}. 185

6.29 $\Delta\chi^2 = \chi^2 - \chi^2_{min}$ distributions as a function of Δm^2_{32}, $\sin^2\theta_{23}$, δ_{CP} and $\sin^2\theta_{13}$ (in case of free θ_{13}) for inverted hierarchy case. Black line represents fixed $\sin^2\theta_{13}$ = 0.025 and blue line represents free θ_{13}. 186

6.30 Contours of Δm^2_{32} and $\sin^2 2\theta_{23}$ (left) and Δm^2_{32} and $\sin^2\theta_{23}$ (right) for the normal mass hierarchy, at fixed θ_{13}. The three lines indicate allowed regions at 68% C.L. 90% C.L. and 99% C.L. respectively, defined as $\Delta\chi^2$ = 2.3, 4.6 and 9.2 respectively. The star shows the best fit point. 187

6.31 Contours of Δm^2_{32} and $\sin^2 2\theta_{23}$ (left) and Δm^2_{32} and $\sin^2\theta_{23}$ (right) for the inverted mass hierarchy, at fixed θ_{13}. The three lines indicate allowed regions at 68% C.L. 90% C.L. and 99% C.L. respectively, defined as $\Delta\chi^2$ = 2.3, 4.6 and 9.2 respectively. The star shows the best fit point. 187

6.32 The numbers on the x-axis indicate the event sample types (18 types in total, with SK-I + SK-II + SK-III + SK-IV data). The upper panel shows the $\Delta\chi^2$ between normal hierarchy and inverted hierarchy contributed by each event sample of the data at the best fit oscillation parameters. The lower panel shows the $\Delta\chi^2$ between normal hierarchy and inverted hierarchy expected to be contributed by each event sample for MC, assuming the "true" oscillation parameters the same as the best fit parameters. 188
6.33 Distribution of $\Delta\chi^2$ as a function of δ_{CP} for normal hierarchy (black line) and inverted hierarchy (red line). 189
6.34 Contours of Δm^2_{32} and $\sin^2 2\theta_{23}$ allowed regions for normal hierarchy (left) and inverted hierarchy (right) for free θ_{13}. New results from this study is represented by blue solid line, and the best fit point is represented by the triangle. 194
6.35 Contours of Δm^2_{32} and $\sin^2 2\theta_{23}$ allowed regions for normal hierarchy (left) and inverted hierarchy (right) for fixed θ_{13}. New results from this study is represented by blue solid line, and the best fit point is represented by the triangle. 194

7.1 Expected sensitivity of mass hierarchy by Hyper Kamiokande (whose fiducial volume is 25 times of Super Kamiokande) as a function of years of exposure. . . 196

List of Tables

1.1 Summary of global best fit of neutrino oscillation parameters, taken from [39] . . 7

2.1 Specification of the 20-inch PMT used in Super-Kamiokande. 18

2.2 Trigger conditions for each SK period. *All inner PMTs are protected with acrylic covers. 25

3.1 List of processes considered in the simulator. 45

5.1 Selection efficiencies and number of events for FC sample are summarized for each SK period. Selection efficiencies are for events whose real vertex is in the fiducial volume for reduction steps 1 to 5, while the selection efficiency for 5th (FV) is for events whose fitted vertex is in the fiducial volume, and number of OD hits $<$ 16 (10 for SK-I) and visible energy $>$ 30 MeV. Number of events for MC are normalized without oscillation to real data livetime, 1489.2, 798.6, 518.1 and 1097.0 days for SK-I, SK-II, SK-III and SK-IV respectively. 87

5.2 Estimated contamination by each background source. Sub-GeV means events with $E_{vis} < 1.3$ GeV and Multi-GeV means events with $E_{vis} > 1.3$ GeV. 88

5.3 Selection efficiencies and number of events for PC sample are summarized for each SK period. Selection efficiencies are for events whose real vertex is in the fiducial volume (after 5th (FV) step, fitted vertex instead of real vertex is considered) and number of OD hits $>$ 15 (9 for SK-I) and total observed charge $>$ 3000 p.e.s. Number of events for MC are normalized to real data livetime, 1489.2, 798.6, 518.1 and 1097.0 days for SK-I, SK-II, SK-III and SK-IV respectively, 2-flavor oscillation with $(\sin^2 2\theta, \Delta m^2) = (1.00, 2.5 \times 10^{-3}\ \text{eV}^2)$ is assumed. 104

5.4 Estimated contamination by cosmic ray muons for PC. 104

5.5 Number of events of UPMU summarized for each SK period. Number of MC (without oscillation) events and event rate are calculated by normalization of data livetime, 1645.9, 827.7, 635.6, 1096.7 days for SK-I, SK-II, SK-III and SK-IV respectively. 108

5.6 Uncertainties of background events which is the contamination by horizontal muons to the UPMU sample in the zenith angle $-0.1 < \cos\theta < 0$. 111

5.7 Vertex resolutions for each SK period. 127

5.8 angular resolutions for each SK period. 128

6.1 Number of FC sub-GeV events and their compositions of neutrino interaction modes for SK-IV MC scaled to the SK-IV livetime 1097 days with 2-flavor oscillation with ($\sin^2 2\theta$, Δ_m) = (1.0, 2.5×10^{-3} eV^2). The upper (lower) table shows e-like (μ-like) samples. The right column shows the composition before separation into sub-samples. After the separation, the CCQE purity has increased. 133

6.2 Composition of interaction modes in case of with and without MME likelihood for SK-IV MC scaled to 1097 days. Two-flavor oscillations ($\sin^2 2\theta$, Δ_m) = (1.0, 2.5×10^{-3} eV^2) is assumed. 135

6.3 Composition of interaction modes in case of with and without MME likelihood for SK-III MC scaled to 518.1 days. Two-flavor oscillations ($\sin^2 2\theta$, Δ_m) = (1.0, 2.5×10^{-3} eV^2) is assumed. 136

6.4 Composition of interaction modes for multi-GeV single-ring e-like samples for SK-III and SK-IV respectively. Purity of CC$\nu_e + \overline{\nu}_e$ is higher for SK-IV due to the improvement in electronics in the SK-IV period. 138

6.5 Interaction mode composition of multi-GeV single-ring ν_e-like and $\overline{\nu}_e$-like samples for SK-IV. MC is normalized to data livetime 1097 days. Two-flavor oscillations ($\sin^2 2\theta$, Δ_m) = (1.0, 2.5×10^{-3} eV^2) is assumed. The separation increases the composition of CCν_e in ν_e-like sample by 5.2% and that of CC$\overline{\nu}_e$ in $\overline{\nu}_e$-like sample by 6.1%. 139

6.6 Interaction mode composition of multi-GeV multi-ring ν_e-like and $\overline{\nu}_e$-like samples for SK-IV. MC is normalized to data livetime 1097 days. Two-flavor oscillations ($\sin^2 2\theta$, Δ_m) = (1.0, 2.5×10^{-3} eV^2) is assumed. The separation increases the composition of CCν_e in ν_e-like sample by 3.3% and that of CC$\overline{\nu}_e$ in $\overline{\nu}_e$-like sample by 1.5%. 141

6.7 Summary of number of events for both data and MC in each SK run period. Number of MC events is normalized by data livetime, assuming 2-flavor mixing at (Δm^2_{23}, $\sin^2\theta_{23}$) = (2.1 × 10^{-3}, 0.5). 148

6.8 Systematic errors related to neutrino flux calculation. They (except for solar activities) are common in all SK periods. The second column shows the best fit value of the systematic error parameter ϵ_i and the third column shows the estimated 1σ error size. 156

6.9 Systematic errors related to neutrino interactions. They are common between all SK periods. The second column shows the best fit value of the systematic error parameter ϵ_i and the third column shows the estimated 1σ error size. 157

6.10 Systematic errors related to event reduction for each SK period. "Fit" column shows the best fit value of the systematic error parameter ϵ_i and "σ" column shows the estimated 1σ error size. 158

6.11 Systematic errors related to event reconstruction and selection for SK-I. The second column shows the best fit value of the systematic error parameter ϵ_i and the third column shows the estimated 1σ error size. 159

6.12 Systematic errors related to event reconstruction and selection for SK-II. The second column shows the best fit value of the systematic error parameter ϵ_i and the third column shows the estimated 1σ error size. 160

6.13 Systematic errors related to event reconstruction and selection for SK-III. The second column shows the best fit value of the systematic error parameter ϵ_i and the third column shows the estimated 1σ error size. 161

6.14 Systematic errors related to event reconstruction and selection for SK-IV. The second column shows the best fit value of the systematic error parameter ϵ_i and the third column shows the estimated 1σ error size. 162
6.15 Estimated uncertainties of up/down ratio (1σ values) for different event samples. They are common for SK-I, SK-II, SK-III and SK-IV periods. 166
6.16 Estimated uncertainties of horizontal/vertical ratio (1σ values) for different event samples. They are common for SK-I, SK-II, SK-III and SK-IV periods. 166
6.17 1σ values for systematic uncertainties of single-ring π^0-like events selection for SK-I, SK-II, SK-III and SK-IV. 175
6.18 $\Delta\chi^2$ ($= | \chi^2_{min(NH)} - \chi^2_{min(IH)} |$) estimated with and without multi-GeV 1-ring and multi-ring e-like samples separated into ν_e and $\overline{\nu}_e$-like samples. 176
6.19 Results of the allowed region of each neutrino oscillation parameter at 68% and 90% C.L. for normal hierarchy at fixed θ_{13}, where 68% C.L. is defined as $\chi^2 - \chi^2_{min} = 1.0$ and 90% C.L. is defined as $\chi^2 - \chi^2_{min} = 2.7$. 178
6.20 Results of the allowed region of each neutrino oscillation parameter at 68% and 90% C.L. for inverted hierarchy at fixed θ_{13}, where 68% C.L. is defined as $\chi^2 - \chi^2_{min} = 1.0$ and 90% C.L. is defined as $\chi^2 - \chi^2_{min} = 2.7$. 179
6.21 Results of the allowed region of each neutrino oscillation parameter at 68% C.L. and 90% C.L. for normal hierarchy at fixed θ_{13}, where 68% C.L. is defined as $\chi^2 - \chi^2_{min} = 1.0$ and 90% C.L. is defined as $\chi^2 - \chi^2_{min} = 2.7$. 179
6.22 Results of the allowed region of each neutrino oscillation parameter at 68% C.L. and 90% C.L. for inverted hierarchy at fixed θ_{13}, where 68% C.L. is defined as $\chi^2 - \chi^2_{min} = 1.0$ and 90% C.L. is defined as $\chi^2 - \chi^2_{min} = 2.7$. 179
6.23 Best fit values at assumed normal and inverted hierarchies in the original sensitivity study carried out in Section 6.6. 190
6.24 Best fit values and $\Delta\chi^2$ for normal and inverted hierarchies for data fitted with ν flux related systematic errors halved. 190
6.25 Best fit values and $\Delta\chi^2$ for normal and inverted hierarchies for data fitted with ν flux related systematic errors increased by 50%. 191
6.26 Best fit values and $\Delta\chi^2$ for normal and inverted hierarchies for data fitted with ν interactions related systematic errors halved. 191
6.27 Best fit values and $\Delta\chi^2$ for normal and inverted hierarchies for data fitted with ν interactions related systematic errors increased by 50%. 192
6.28 Best fit values and $\Delta\chi^2$ for normal and inverted hierarchies for data fitted with event reconstruction related systematic errors halved. 192
6.29 Best fit values and $\Delta\chi^2$ for normal and inverted hierarchies for data fitted with event reconstruction related systematic errors increased by 50%. 193

Chapter 1

Introduction

Currently the universe is in matter dominated state, while comparable amounts of matter and anti-matter were created in the Big-Bang. CP violation is believed to contribute to asymmetry between matter and anti-matter, so that matter remains during the expansion and cooling process of the universe [1]. CP invariance is observed to be violated in weak interactions of quark sector [2], while CP violation in lepton sector is not observed yet. Neutrino oscillation provides a way to observe the CP violation in lepton sector. Moreover, observations showed that neutrino mixing angles are very different from those of quarks, which suggests that the mass ordering might not be as expected by the knowledge from the quark sector.

1.1 Neutrino Oscillation

Neutrinos are leptons which lack electric charge and are extremely difficult to detect as they pass through ordinary matter almost without disturbance. There are three flavours of neutrinos, electron neutrino (ν_e), muon neutrino (ν_μ) and tau neutrino (ν_τ). They are assumed to be massless by the Standard Model. However, neutrino oscillations have been observed in solar [3], atmospheric [4], accelerator[5] and reactor [6] [7] experiments, which implies neutrino flavor eigenstates are actually made up of superposition of neutrino mass eigenstates [8], suggesting physics beyond the Standard Model.

Neutrino oscillation was proposed by Maki, Nakagawa, Sakata [9] and Pontecorvo [10]. The flavor eigenstates can be written as superposition of mass eigenstates:

$$\mid \nu_\alpha \rangle = \sum_{i=1}^{3} U_{\alpha i} \mid \nu_i \rangle \tag{1.1}$$

where $\mid \nu_\alpha \rangle$ is the flavor eigenstate ν_e, ν_μ or ν_τ, $\mid \nu_i \rangle$ is the mass eigenstates ν_1, ν_2 and ν_3. U is the Maki-Nakagawa-Sakata-Pontecorvo (MNSP) matrix which is a 3×3 matrix describing the transformation between different neutrino flavor eigenstates:

$$U = \begin{pmatrix} 1 & 0 & 0 \\ 0 & \cos\theta_{23} & \sin\theta_{23} \\ 0 & -\sin\theta_{23} & \cos\theta_{23} \end{pmatrix} \times \begin{pmatrix} \cos\theta_{13} & 0 & \sin\theta_{13} \\ 0 & e^{-i\delta} & 0 \\ -\sin\theta_{13} & 0 & \cos\theta_{13} \end{pmatrix}$$

$$\times \begin{pmatrix} \cos\theta_{12} & \sin\theta_{12} & 0 \\ -\sin\theta_{12} & \cos\theta_{12} & 0 \\ 0 & 0 & 1 \end{pmatrix} \times \begin{pmatrix} e^{i\rho} & 0 & 0 \\ 0 & e^{i\sigma} & 0 \\ 0 & 0 & 1 \end{pmatrix} \quad (1.2)$$

The time evolution of the four eigenstates is:

$$\begin{aligned} \mid \nu_\alpha(t)\rangle &= \sum_i U_{\alpha i} \exp(-iE_i t) \mid \nu_i(t=0)\rangle && (1.3) \\ &= \sum_i \sum_{\alpha'} U_{\alpha i} U^*_{\alpha' i} \exp(-iE_i t) \mid \nu'_\alpha(t=0)\rangle && (1.4) \end{aligned}$$

where E_i is the eigenvalue of the mass eigenstate $\mid \nu_i\rangle$. The probability for flavor eigenstate ν_α at t=0 to change to state ν_β at time t is:

$$\begin{aligned} P(\nu_\alpha \to \nu_\beta) &= \mid \langle \nu_\beta(t) \mid \nu_\alpha(0)\rangle \mid^2 && (1.5) \\ &= \mid \sum_i U_{\beta i} U^*_{\alpha i} \exp(-iE_i t) \mid^2 && (1.6) \\ &= \sum_i \mid U_{\alpha i} U_{\beta i} \mid^2 + \sum_{i \neq j} U_{\alpha i} U^*_{\beta i} U^*_{\alpha j} U_{\beta j} \exp(-i(E_i - E_j)t) && (1.7) \end{aligned}$$

The above equations show that the flavor transition phenomenon, neutrino oscillation, occurs due to the mixing of the mass eigenstate of the non-zero-mass neutrinos.

The mixing matrix U can be simplified into the two-flavor mixing case:

$$U = \begin{pmatrix} \cos\theta & \sin\theta \\ -\sin\theta & \cos\theta \end{pmatrix} \quad (1.8)$$

Transition probability shown in equation (1.7) can be simplified into:

$$P(\nu_\alpha \to \nu_\beta) = \sin^2 2\theta \sin^2(\frac{(E_i - E_j)t}{2}). \quad (1.9)$$

If neutrinos have non-zero mass, the following approximation is taken:

$$\begin{aligned} E_i - E_j &= \sqrt{(m_i^2 + p_i^2)} - \sqrt{(m_j^2 + p_j^2)} && (1.10) \\ &= p_i(1 + \frac{m_i^2}{p_i^2})^{\frac{1}{2}} - p_j(1 + \frac{m_i^2}{p_j^2})^{\frac{1}{2}} && (1.11) \\ &\approx (p + \frac{m_i^2}{2p}) - (p + \frac{m_j^2}{2p}) && (1.12) \\ &\approx \frac{\Delta m_{ij}^2}{2E}. && (1.13) \end{aligned}$$

where $\Delta m_{ij}^2 \equiv m_i^2 - m_j^2$ is the mass-squared difference of the neutrino mass eigenstates.

Substituting equation (1.13) into equation (1.9), with neutrino flight length L_ν and neutrino energy E_ν, the survival probability of ν_α in two-flavor mixing case is:

$$\begin{aligned} P(\nu_\alpha \to \nu_\beta) &= 1 - \sin^2 2\theta \sin^2(\frac{\Delta m_{ij}^2 L_\nu}{4E_\nu}) && (1.14) \\ &= 1 - \sin^2 2\theta \sin^2(\frac{1.27\Delta m_{ij}^2(eV^2) L_\nu(km)}{E_\nu(GeV)}) && (1.15) \end{aligned}$$

As shown above, the oscillation probability depends on the mixing angle θ, the mass square difference Δm_{ij}^2, neutrino flight length L_ν and neutrino energy E_ν. The oscillation amplitude is at maximum when $\frac{L_\nu(km)}{E_\nu(GeV)} \sim \frac{\pi}{2.54\times\Delta m_{ij}^2(eV^2)}$. Therefore, neutrino oscillation experiments can probe the neutrino squared mass difference.

1.2 Neutrino Oscillation Experiments

There are many experiments which have observed neutrino oscillation and measured the neutrino oscillation parameters which includes the mixing angle and the squared mass difference. Some of these experiments are introduced in this section.

1.2.1 Solar and Reactor Neutrino Observations

Electron neutrinos are produced by nuclear reactions $4p \rightarrow^4 He + 2e^+ + 2\nu_e + \gamma$ in the Sun. Homestake experiment is the oldest experiment that measured solar neutrinos [3]. Electron neutrinos were measured by the reaction $\nu_e +^{37} Cl \rightarrow e^- +^{37} Ar$ inside the detector which contained 520 tons of chlorine, then the produced radioactive Ar atoms which have a half life of 35 days were extracted and counted by measuring its radioactivity. The number of Ar detected is the number of neutrino interactions in the detector. The count rate was 2.56 SNU (Solar Neutrino Unit, 1 SNU = 10^{-36} captures/atom/s), while the Standard Solar Model predicted a rate of 7.6 SNU [16]. Later experiments SAGE [11] and GALLEX [12] measured electron neutrinos by the interaction $\nu_e +^{71} Ga \rightarrow e^- +^{71} Ge$ and the produced Ge atoms which is also a radioactive isotope (half life 11.43 days) were counted, deficit was also observed. The Kamiokande experiment[13] which was a water Cherenkov detector, which detected neutrinos with different method (detections of Cherenkov rings emitted by leptons produced by neutrinos in water), also observed the deficit. This discrepancy in measured and predicted neutrino flux is referred to as the "solar neutrino problem".

The Sudbury Neutrino Observatory (SNO) [14] which is a D_2O Cherenkov detector measures ν_e and total fluxes ($\nu_e + \nu_\mu + \nu_\tau$) of neutrinos coming from the Sun through the charged current (CC) reactions $\nu_e + d \rightarrow p + p + e^-$, neutral current (NC) reactions $\nu_x + d \rightarrow p + n + \nu_x$ and elastic scattering (ES) reactions $\nu_x + e^- \rightarrow \nu_x + e^-$. The total number of neutrinos detected agrees with the predicted number from the Standard Solar Model, with about one third of the total number electron neutrinos. On the other hand, Super-Kamiokande (SK) experiment which is a H_2O Cherenkov detector also made the observation through elastic scattering reactions [15] [17]. As SK alone cannot indicate non-electron flavor components of neutrinos, only when SK and SNO results are combined, there was an indication for non-electron flavor neutrinos, so combination of the results of SNO and SK showed the MSW solution explains the observed flux [18].

The KamLAND experiment confirmed the above results of SNO and SK [19]. KamLAND is a liquid scintillator type detector, which detects the $\bar{\nu_e}$ from the nuclear power reactor units with the reaction of inverse β-decay $\bar{\nu_e} + p \rightarrow e^+ + n$. The prompt signal from e^+ together with the delayed coincidence of the gamma from the neutron capture significantly reduces the background. The nuclear power reactor units are on average 180 km away from the detector. The energy of the $\bar{\nu_e}$ from nuclear power reactor is about 3 MeV, from equation (1.15), the experiment is sensitive to Δm_{12}^2 down to 10^{-6} eV order.

The combined oscillation results of solar neutrino experiments (SNO, SK and Borexino[20]) and KamLAND gives[21]:

$$7.4 \times 10^{-5} < \Delta m_{12}^2 < 7.8 \times 10^{-5} eV^2, \tag{1.16}$$

$$0.30 < \sin^2 \theta_{12} < 0.32 \tag{1.17}$$

1.2.2 Atmospheric Neutrino and Accelerator Neutrino

Primary cosmic rays consists of mostly protons and Helium nuclei. The energy spectrum of primary cosmic rays measured by different experiments is shown in Figure 1.1. When primary cosmic rays enters the Earth's atmosphere, hadronic interactions between the protons and the Helium nuclei produce secondary cosmic rays which includes pions and kaons:

$$p + N \rightarrow \pi^+ + \pi^- + ... \tag{1.18}$$

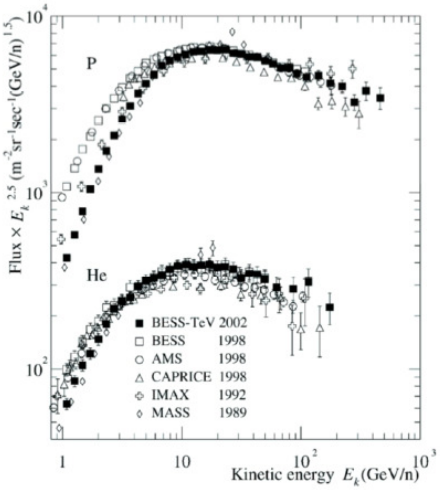

Figure 1.1: Proton and helium spectra from primary cosmic rays. [22]

These pions and kaons further decay into muons, electrons and atmospheric neutrons as shown below:

$$\pi^+ \rightarrow \mu^+ + \nu_\mu \tag{1.19}$$

$$\hookrightarrow e^+ + \nu_e + \bar{\nu_\mu}, \tag{1.20}$$

$$\pi^- \rightarrow \mu^- + \bar{\nu_\mu} \tag{1.21}$$

$$\hookrightarrow e^- + \bar{\nu_e} + \nu_\mu \tag{1.22}$$

Atmospheric neutrinos are the ν_e, $\bar{\nu_e}$, ν_μ and $\bar{\nu_\mu}$ in the above reactions. Energy spectrum of atmospheric neutrinos peaks at around 40 MeV and extends up to above TeV while neutrino flight length ranges from ∼10 to ∼ 10^4 km, which correspond to the production height from about 15 km to the diameter of the Earth (∼13000 km, neutrinos produced at the other side of the Earth). Atmospheric neutrino experiments have enough statistics for neutrino energies above several hundred MeV, hence observation of atmospheric neutrinos gives sensitivity of Δm^2 of $10^{-1} \sim 10^{-4} eV^2$ (equation (1.15)).

The predicted total flux of atmospheric neutrinos has about 10% uncertainty in the GeV region, which is mainly due to uncertainty of hadronic interaction cross sections. On the other hand, uncertainty of the flavor ratio $(\nu_\mu + \bar{\nu_\mu})/(\nu_e + \bar{\nu_e})$ is only about 2% for neutrino energy below 10 GeV [23]. The flavor ratio has been measured by several experiments (Kamiokande [24] [25], IMB-3 [26] [27], Soudan2 [28]) and reported in terms of a double ratio $R \equiv (N_\mu/N_e)_{Data}/(N_\mu/N_e)_{MC}$, where N_μ (N_e) is the number of muon (electron) events produced by charged current interactions. The measured flavor ratio was roughly one half of what expected, which was suggested to be due to neutrino oscillation.

Super-Kamiokande (SK) reported in 1998 that the zenith angle distributions of ν_μ events have a deficit in the upward direction which gave evidence for neutrino oscillation [4]. Moreover, MACRO [29] and SK [30] studied upward-going muons produced by energetic ν_μ in the rock surrounding the detector through charged current interactions. The observed zenith angle distributions did not agree with the no-oscillation analysis, instead they were consistent with the $\nu_\mu \leftrightarrow \nu_\tau$ oscillation hypothesis. Later SK reported observation of a dip in the L/E distribution which was predicted from the flavor transition probability of neutrino oscillation [31]. Atmospheric neutrino oscillation was then later confirmed by long-baseline experiments using ν_μ beam produced by accelerators such as K2K [32] and MINOS [33] which measure ν_μ disappearance in flight.

The two-flavor neutrino oscillation parameters from MINOS [34] are constrained to be:

$$2.24 \times 10^{-3} < \Delta m^2_{32} < 2.44 \times 10^{-3} eV^2, \tag{1.23}$$

$$\sin^2(2\theta_{23}) > 0.90 \tag{1.24}$$

at 90% C.L.

The two-flavor neutrino oscillation parameters from the Super-Kamiokande [35] are constrained to be:

$$1.5 \times 10^{-3} < \Delta m^2_{32} < 3.4 \times 10^{-3} eV^2, \tag{1.25}$$

$$\sin^2(2\theta_{23}) > 0.92 \tag{1.26}$$

at 90% C.L.

1.2.3 Mixing Angle θ_{13} Measurement by Accelerator and Reactor Neutrinos

The third mixing angle θ_{13} was investigated by the CHOOZ experiment[37] which detected reactor $\bar{\nu_e}$ by the inverse β-decay reaction $\bar{\nu_e} + p \rightarrow e^+ + n$. The nuclear reactor was 1km away from the Gadolinium-loaded liquid scintillator detector. The distortion of the energy spectrum of $\bar{\nu_e}$ was investigated. $\bar{\nu_e}$ survival probability is expressed as:

$$P(\bar{\nu_e} \rightarrow \bar{\nu_e}) = 1 - \sin^2 2\theta_{13} \sin^2(\frac{1.27 \Delta m^2_{13} L}{E_\nu}) \tag{1.27}$$

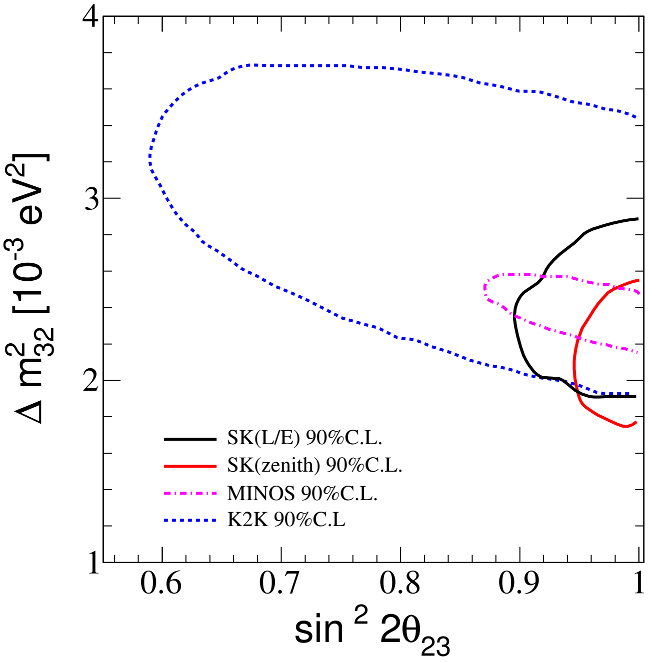

Figure 1.2: 90% C.L. allowed regions of oscillation parameters for $\nu_\mu \leftrightarrow \nu_\tau$ oscillation. Horizontal axis is $\sin^2 2\theta_{23}$ and the vertical axis is Δm^2_{32}.The results are taken from SK zenith angle analysis (solid line)[36], L/E results (dashed line)[31], MINOS experiment(dotted line)[34] and K2K(dotted and dashed line)[32].

The upper limit given by the CHOOZ experiment is[37]:

$$\sin^2 2\theta_{13} < 0.15 \tag{1.28}$$

at 90% C.L. The CHOOZ experiment ended without giving any evidence of non-zero θ_{13}.

Later the T2K experiment searches for ν_e appearance by using a conventional neutrino beam produced at J-PARC and directed 2.5° off-axis to SK at a distance of 295 km. T2K experiment gives indication for non-zero θ_{13} [38]:

$$0.03(0.04) < \sin^2 2\theta_{13} < 0.28(0.34) \tag{1.29}$$

at 90% C.L. (assuming $\sin^2 2\theta_{23} = 1.0$, $\mid \Delta m^2_{23} \mid = 2.4 \times 10^{-3}$ eV^2, $\delta_{CP} = 0$) for normal (inverted) mass hierarchy.

Recently the Daya Bay Reactor Neutrino Experiment and the Reactor Experiment for Neutrino Oscillation (RENO) experiment both measured non-zero θ_{13}.

Daya Bay Reactor Neutrino Experiment detects $\bar{\nu_e}$ from the reactors of the Daya Bay Nuclear Power Plant and Ling Ao Nuclear Power Plants in China with inverse β-decay reaction $\bar{\nu_e} + p \rightarrow e^+ + n$ in Gadolinium-loaded liquid scintillator [6].

The results from Daya Bay experiment is [6]

$$\sin^2 2\theta_{13} = 0.092 \pm 0.016(stat) \pm 0.005(syst). \tag{1.30}$$

RENO experiment also observes $\bar{\nu}_e$ from the reactors at the Yonggwang Nuclear Power Plant in Korea through the inverse β-decay reactions in hydrocarbon liquid scintillators detectors [7].

Results from RENO is [7]

$$\sin^2 2\theta_{13} = 0.113 \pm 0.013(stat) \pm 0.019(syst). \tag{1.31}$$

As reactor neutrino experiments constrained θ_{13}, their combined results are used in this study. By considering the weighed mean $\bar{x}$,

$$\bar{x} = \frac{\sum_{i=1}^{n} \frac{x_i}{\sigma_i^2}}{\sum_{i=1}^{n} \frac{1}{\sigma_i^2}} \tag{1.32}$$

and the invariance of the weighed mean $\sigma_{\bar{x}}^2$:

$$\sigma_{\bar{x}}^2 = \frac{1}{\sum_{i=1}^{n} \frac{1}{\sigma_i^2}} \tag{1.33}$$

the combined result of Daya Bay experiment and RENO experiment is

$$\sin^2 2\theta_{13} = 0.099 \pm 0.014. \tag{1.34}$$

Atmospheric neutrino data has also been used to constrain θ_{13} in the three-flavor mixing framework with [44] and without [43] one mass scale dominance approximation , the detailed analysis will be discussed in section 1.3.

1.2.4 Summary for Neutrino Oscillation Parameters and Remaining Issues

The global best fit results of neutrino oscillation parameters are summarized in Table 1.1.

Parameter	Best fit ± 1σ C.L.
Δm_{12}^2	$7.58\ ^{+0.22}_{-0.26} \times 10^{-5}$ eV^2
$\sin^2\theta_{12}$	$0.306\ ^{+0.018}_{-0.015}$
$\sin^2 2\theta_{13}$	0.099 ± 0.014
$\sin^2\theta_{23}$	$0.42\ ^{+0.08}_{-0.03}$
$\lvert\Delta m_{13}^2\ \rvert$	$2.35\ ^{0.12}_{009} \times 10^{-3}$ eV^2

Table 1.1: Summary of global best fit of neutrino oscillation parameters, taken from [39]

Neutrino oscillation is well understood and the non-zero mass of neutrinos is confirmed, at the same time there are several remaining questions about the neutrino oscillation.

Neutrino oscillation experiments are measuring the mass differences (Δm_{12}^2 and Δm_{23}^2) instead of the absolute mass, therefore the mass ordering is not yet known. Figure 1.2.4 shows

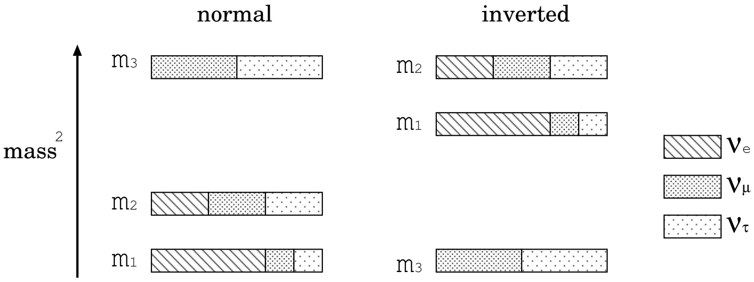

Figure 1.3: Three-neutrino mass-squared spectrum, for the two mass hierarchies.

the conceptual diagram for the two cases of mass ordering. With $m_3 \gg m_2 > m_1$, it is defined as normal hierarchy, while with $m_3 \ll m_1 < m_2$, it is defined as inverted hierarchy. One of the remaining questions is whether the mass ordering is normal hierarchy or inverted hierarchy.

Another remaining question is the value of the CP-violation phase δ_{CP}. As T2K and reactor experiments gives evidence that θ_{13} is non-zero, as the CP-violation phase δ_{CP} appears as a combination with θ_{13} as shown in equation (1.1), it becomes possible to probe the value of δ_{CP} and also to address the issue of CP-violation in the lepton sector.

As atmospheric neutrino experiments cover a wide range of L/E_ν, it is possible to measure the effect of three-flavor oscillation including θ_{13}, 1-2 parameters and δ_{CP}

1.3 Sub-Dominant Effects of Atmospheric Neutrino Oscillation

Atmospheric neutrino data are well fitted to $\nu_\mu \to \nu_\tau$ 2-flavor oscillation. In 3-flavor oscillation, ν_e oscillation is also considered. ν_e oscillation is due to the sub-dominant oscillation due to θ_{13} mixing and/or Δm^2_{12} induced oscillation. Matter effect [40] plays an important role in these oscillation schemes.

Oscillation of atmospheric ν_e in vacuum are expressed as (with Δm^{12} set to zero):

$$\begin{aligned} P(\nu_e \to \nu_e) &= 1 - \sin^2 2\theta_{13} \sin^2(\frac{1.27\Delta m^2_{23} L}{E}) && (1.35) \\ P(\nu_\mu \to \nu_e) &= P(\nu_e \to \nu_\mu) && (1.36) \\ &= \sin^2\theta_{23} \sin^2 2\theta_{13} \sin^2(\frac{1.27\Delta m^2_{23} L}{E}) && (1.37) \end{aligned}$$

For the oscillation probability of the neutrinos traversing the Earth, the Earth's matter potential due to the forward scattering amplitude of charged current ν_e and $\bar{\nu_e}$ interactions with electrons has to be taken into account. The Earth contains a large number of electrons, ν_e interacts with these electrons via W bosons while ν_μ and ν_τ do not.

When considering the matter effect in the $\nu_\mu \to \nu_e$ oscillation ($\Delta m^{12} \sim 0$) as shown in equation (1.37), θ_{13} and Δm^2_{23} are replaced by the corresponding mixing parameters in matter ($\theta_{13,M}$ and $\Delta m^2_{23,M}$ respectively). For constant matter density [41],

$$P(\nu_\mu \to \nu_e) = P(\nu_e \to \nu_\mu) = \sin^2\theta_{23}\sin^2 2\theta_{13,M}\sin^2(\frac{1.27\Delta m^2_{23,M}L_\nu}{E_\nu}) \tag{1.38}$$

where

$$\begin{aligned} \Delta m^2_{23,M} &= \Delta m^2_{23}\sqrt{(\cos 2\theta_{13} - A_{CC}/\Delta m^2_{23})^2 + \sin^2\theta_{13}} && (1.39)\\ \sin^2\theta_{13,M} &= \frac{\sin^2 2\theta_{13}}{(\cos 2\theta_{13} - A_{CC}/\Delta m^2_{23})^2 + \sin^2 2\theta_{13}} && (1.40)\\ A_{CC} &= 2\sqrt{2}G_F N_e E_\nu && (1.41) \end{aligned}$$

When $\mid A_{CC}/\Delta m^2_{23} \mid = \cos 2\theta_{13}$, Mikheyev-Smirnov-Wolfenstein (MSW) [40] resonant enhancement occurs to either neutrinos or anti-neutrinos, depending on the mass hierarchy (normal hierarchy or inverted hierarchy, respectively). Left hand side of figure 1.4 shows the oscillation probability of $\nu_\mu \to \nu_e$ when neutrinos traveling through the Earth as a function of neutrino energy and zenith angle with a more realistic matter density, while the right figure shows the oscillation probability in vacuum for comparison. The resonance enhancement is seen in 2-10 GeV region in the upward direction with Chooz limit assumed. The enhancement occurs for neutrinos (antineutrinos) in normal (inverted) hierarchy case.

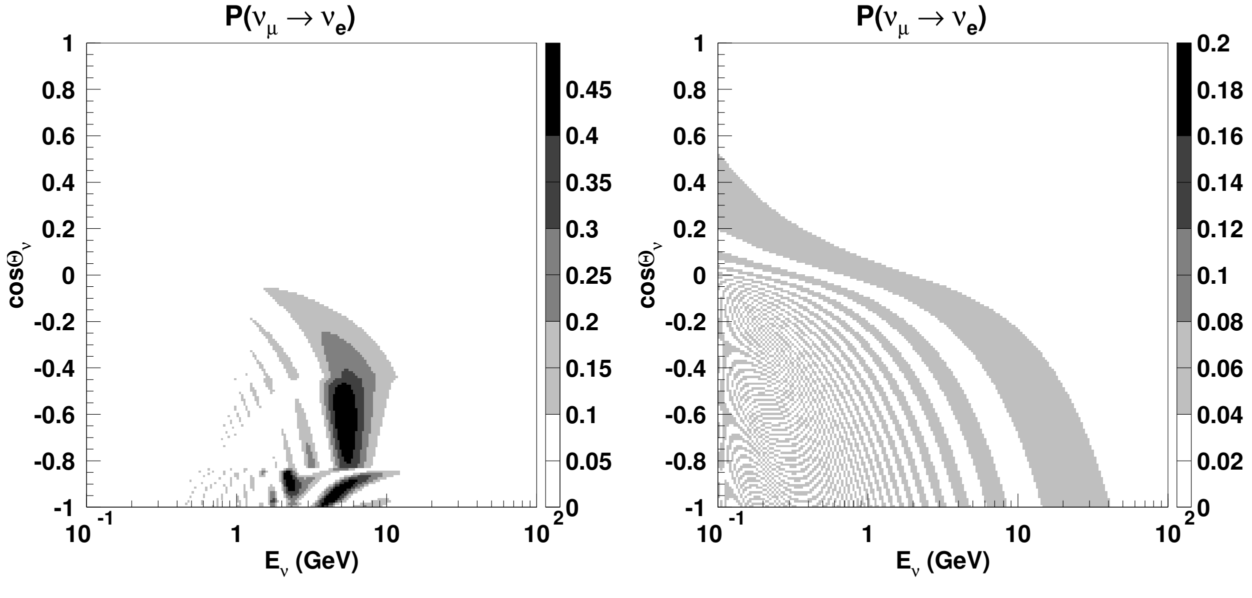

Figure 1.4: Left: ν_μ to ν_e (or ν_e to ν_μ) transition probability in the Earth; Right: ν_μ to ν_e (or ν_e to ν_μ) transition probability in vacuum. $\cos\Theta_\nu$ = -1 corresponds to upward direction and $\cos\Theta_\nu$ = 0 corresponds to horizontal direction. (Δm^2_{23}, $\sin^2\theta_{23}$, $\sin^2\theta_{13}$) = (2.1×10^{-3} eV^2, 0.5, 0.04) is assumed in the plots [43].

When oscillation driven by LMA-MSW effect obtained from solar neutrino parameters (Δm^2_{12}, θ_{12}) is considered, oscillation effect can be seen in low energy region even if $\theta_{13} = 0$. Assuming $\theta_{13} \sim 0$, ν_e oscillation probability in constant matter density can be written as [42]:

$$
\begin{aligned}
P(\nu_e \leftrightarrow \nu_e) &= 1 - P_{ex} && (1.42)\\
P(\nu_e \leftrightarrow \nu_\mu) &= \cos^2\theta_{23} P_{ex} && (1.43)\\
P(\nu_\mu \leftrightarrow \nu_\mu) &= 1 - \cos^4\theta_{23} P_{ex} - \sin^2 2\theta_{23}(1 - \sqrt{1 - P_{ex}}\cos\phi) && (1.44)
\end{aligned}
$$

where

$$
\begin{aligned}
\phi &\sim (\Delta m^2_{31} + \sin^2\theta_{12}\Delta m^2 21)\frac{L}{2E_\nu} && (1.45)\\
P_{ex}(\nu_e \rightarrow \nu_x) &= \sin^2 2\theta 12, M \sin^2(\frac{\Delta m^2_{21} L_\nu}{4E_\nu}\frac{\sin^2 2\theta_{12}}{\sin^2 2\theta_{12,M}}) && (1.46)\\
\cos 2\theta_{12,M} &= \frac{\cos 2\theta_{12}}{\sqrt{(\cos 2\theta_{12} - A_{CC}/\Delta m^2_{12})^2 + \sin^2 2\theta_{12}}} && (1.47)
\end{aligned}
$$

Figure 1.5 shows P_{ex} as a function of neutrino energy and zenith angle with a more realistic matter density. The oscillated atmospheric ν_e flux is written as:

$$
\begin{aligned}
\Phi_e^{osc} &= \Phi_e^0 \cdot P(\nu_e \rightarrow \nu_e) + \Phi_\mu^0 \cdot P(\nu_\mu \rightarrow \nu_e) && (1.48)\\
&= \Phi_e^0(1 + P_{ex}(r\cos^2\theta_{23} - 1)) && (1.49)\\
\frac{\Phi_e^{osc}}{\Phi_e^0} &= P_{ex}(r\cos^2\theta_{23} - 1) && (1.50)
\end{aligned}
$$

where r = N_μ/N_e. r in equation (1.50) is about 2 in low energy region, in case $\sin^2\theta_{23} \neq 0.5$, ν_e oscillation effect can be seen in either flux excess or deficit as shown in the right side of Figure 1.5. If $\cos^2\theta_{23}$ is greater than 0.5 ($\theta_{23}< 45°$), an enhancement of flux is expected, if $\cos^2\theta_{23}$ is less than 0.5 ($\theta_{23}> 45°$), a deficit of flux is expected. Figure 1.5 shows the flux ratio for $\sin^2\theta_{23} = 0.4$, 0.5 and 0.6.

Two sub-dominant oscillation schemes are described above with the approximation of $\Delta m^2_{12} \sim 0$ or $\theta_{13} \sim 0$ respectively. In order to describe the oscillation effect due to the interference between (Δm^2_{13}, θ_{13}) and (Δm^2_{12}, θ_{12}), full oscillation parameters have to be taken into account without taking approximation in θ_{13} and Δm^2_{12}. Full oscillation parameters include all relevant oscillation parameters including the CP violation phase δ_{CP}. When considering all oscillation parameters, $\nu_\mu \leftrightarrow \nu_e$ transition probability in constant matter density is [45]:

$$
\begin{aligned}
P(\nu_\mu \leftrightarrow \nu_e) = &\cos^2\widetilde{\theta}_{13}\cos^2\theta_{23} P_{e2}\\
&+\sin^2\widetilde{\theta}_{13}\cos^2\widetilde{\theta}_{13}\sin^2\theta_{23}(2 - P_{e2})\\
&-2\sin^2\widetilde{\theta}_{13}\cos^2\widetilde{\theta}_{13}\sin\theta_{23}\cos\theta_{23}(\cos\delta R_2 - \sin\delta I_2) && (1.51)
\end{aligned}
$$

where

$$
\begin{aligned}
P_{e2} &= \sin^2 2\theta_{12,M}\sin^2\frac{\phi_m}{2} && (1.52)\\
R_2 &= -\sin 2\theta_{12,M}\cos 2\theta_{12,M}\sin^2\frac{\phi_m}{2} && (1.53)\\
I_2 &= -\frac{1}{2}\sin 2\theta_{12,M}\sin\phi_m && (1.54)
\end{aligned}
$$

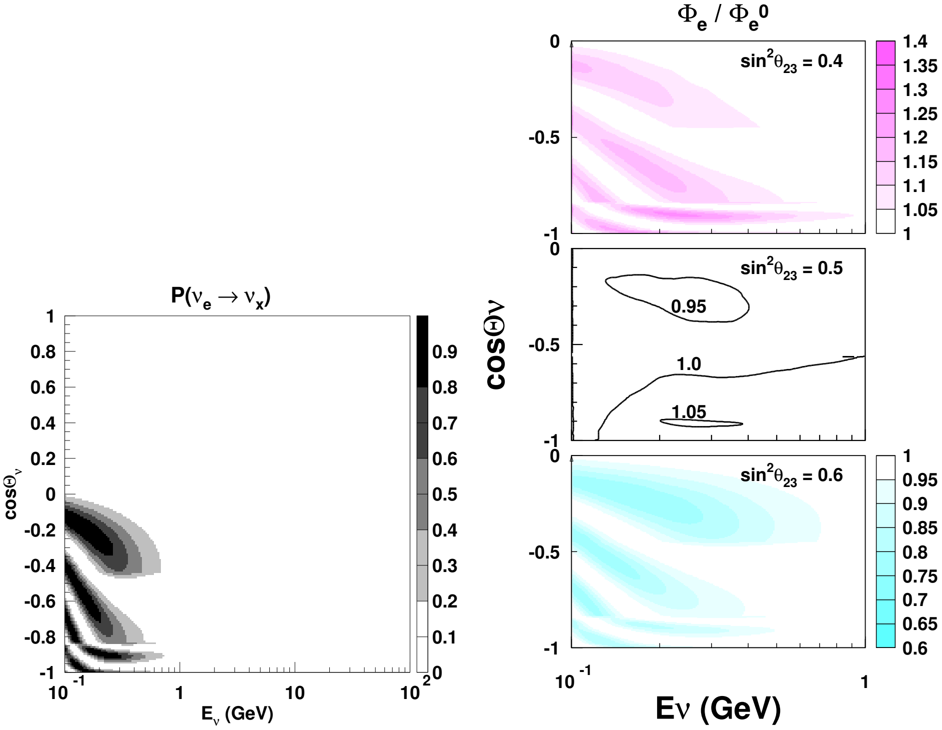

Figure 1.5: Left: ν_e transition probability P_{ex} as a function of energy E_ν and zenith angle, assuming oscillation parameters (Δm^2_{12}, Δm^2_{23}, $\sin^2\theta_{12}$, $\sin^2\theta_{23}$) = (7.7×10^{-5} eV^2, 2.1×10^{-3} eV^2, 0.3, 0.5); Right: Electron flux ratio Φ_e^{osc}/Φ_e^0. There is an excess (a deficit) for $\sin^2\theta_{23}$ in the first (second) octant as shown in the top (bottom) figure. As for $\sin^2\theta_{23} = 0.5$, both small excess and deficit are seen as shown in the middle figure. [43].

ϕ_m is the phase oscillation in matter and $\widetilde{\theta}_{13}$ is the mixing angle in matter, with $\widetilde{\theta}_{13} \approx \theta_{13,M}$.

When full oscillation scheme is considered, ν_e oscillation occurs with CP violation phase. Figure 1.6 shows P($\nu_\mu \to \nu_e$) as a function of zenith angle and neutrino energy with realistic matter density. Electron neutrino oscillation appears in both sub-GeV and multi-GeV region as shown in the figure. Sub-GeV (multi-GeV) is defined to be less (greater) than 1.33 GeV in visible energy in a water Cherenkov detector. The ratio between the expected electron events (N_e) and the non-oscillation electron events (N_e^0) is:

$$\frac{N_e}{N_e^0} = (P_{ee}-1) + rP_{e\mu} \tag{1.55}$$

$$\simeq \Delta_1(\theta_{13}) + \Delta_2(\theta_{12}, \Delta m^2_{12}) + \Delta_3(\theta_{13}, \theta_{12}, \Delta m^2_{12}, \delta_{CP}) \tag{1.56}$$

where r = N_μ/N_e, and r $\sim$ 2 to 3.5 in a few MeV to 10 GeV. The term $\Delta_1(\theta_{13})$ arises for $\theta_{13} > 0$ and is independent of Δm^2_{12}. $\Delta_2(\theta_{12}, \Delta m^2_{12})$ arises for $\Delta m^2_{12} > 0$ and is independent of θ_{13}. The last term $\Delta_3(\theta_{13}, \theta_{12}, \Delta m^2_{12}, \delta_{CP})$ depends on both Δm^2_{12} and θ_{13} and it is the only term which depends on CP phase values. These three terms affect different energy regions. $\Delta_1(\theta_{13})$ induces electron excess in the multi-GeV region, $\Delta_2(\theta_{12}, \Delta m^2_{12})$ induces excess or deficit

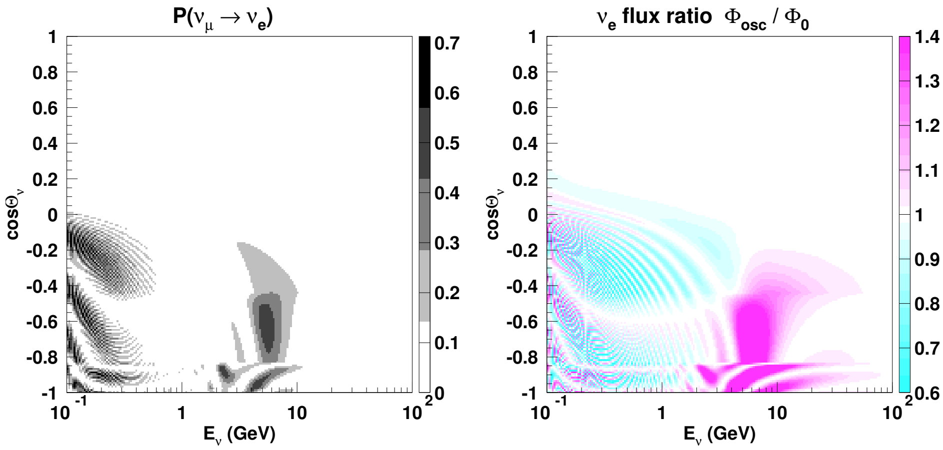

Figure 1.6: Left: Probability of $\nu_\mu \rightarrow \nu_e$ oscillation as a function of zenith angle and neutrino energy, in case of (Δm^2_{12}, Δm^2_{23}, $\sin^2\theta_{12}$, $\sin^2\theta_{23}$, $\sin^2\theta_{13}$, δ_{CP}) = (7.7×10^{-5}, 2.1×10^{-3}, 0.3, 0.5, 0.04, 0°). Right: ν_e flux ratio Φ_{osc}/Φ_0 assuming the same oscillation parameters as the left figure. Figures taken from [43].

in the sub-GeV region depending on the octant of $\sin^2\theta_{23}$, $\Delta_3(\theta_{13}, \theta_{12}, \Delta m^2_{12}, \delta_{CP})$ has effect in both sub-GeV and multi-GeV regions due to the interference between (Δm^2_{32}, θ_{13}) and (Δm^2_{12}, θ_{12}) induced oscillations. By looking at the interference of the sub-dominant effects of the atmospheric neutrino, the CP phase can also be studied.

This study aims to probe the mass hierarchy and to obtain the oscillation parameter values (Δm^2_{12}, Δm^2_{23}, θ_{23}, θ_{13}, CP phase (δ_{CP})) by studying the full neutrino oscillation. This is the first analysis in Super-Kamiokande experiment to probe the mass hierarchy by separating the event samples into neutrinos and anti-neutrinos. Outline of this thesis is:

Chapter 2 describes the Super-Kamiokande detector.

Chapter 3 describes the simulation for atmospheric neutrinos observed in Super-Kamiokande.

Chapter 4 describes the detector calibration.

Chapter 5 describes the data of atmospheric neutrinos.

Chapter 6 describes the analysis and the results.

Chapter 2

The Super-Kamiokande Detector

Super-Kamiokande is a cylindrical 50 kTon water Cherenkov detector located at Kamioka Observatory of Institute for Cosmic Ray Research in Gifu Prefecture, Japan. Figure 2.1 shows the schematic view of the detector and its location in Mountain Ikenoyama. Geographic coordinates of the site is 36°25'N and 137°18'E, the altitude above sea level is 370 m. The detector is located in a zinc mine under the top of Mountain Ikenoyama which has a mean rock overburden of $\sim$ 1000 m ($\sim$ 2700 m water equivalent). The rock overburden shields the detector against cosmic ray muon background, hence the cosmic ray muon flux at the Super-Kamiokande site is reduced by 5 orders of magnitude when compared with the flux on the Earth surface. The detector is mainly composed of the water tank and the photomultiplier tubes (PMTs) which detect Cherenkov radiation due to charged particles in the water.

The main purpose of the Super-Kamiokande experiment are to search for nucleon decays and the studies of various types of neutrinos which include atmospheric neutrinos, solar neutrinos, neutrinos from supernova and neutrinos from other astrophysical sources. The Super-Kamiokande detector is also used as a target for artificial neutrino beam in long-baseline neutrino oscillation experiment.

The Super-Kamiokande experiment started taking data in April, 1996 and continued the observation for five years within the SK-I running period till the detector maintenance in July, 2001. During water refilling after the maintenance, an accident occurred in November 2001 in which more than half of the PMTs were destroyed. After the accident, the Super-Kamiokande detector was rebuilt with half of the original PMT density in the inner detector and resumed observation from October, 2002, which is referred to as SK-II running period. SK-II continued measurement for three years until October 2005, in which reconstruction work was carried out to resume the PMT density. Super-Kamiokande restarted observation in June, 2006 with the same PMT density as SK-I period, this period is referred to as SK-III period. As new electronics module for the detector was developed, the new electronics was installed in September 2008, starting the SK-IV running period.

In this thesis, the data observed in all SK periods: SK-I (1996-2001), SK-II (2002-2005), SK-III (2006-2008) and SK-IV (from 2008 up to 2012 Feb) running periods are used.

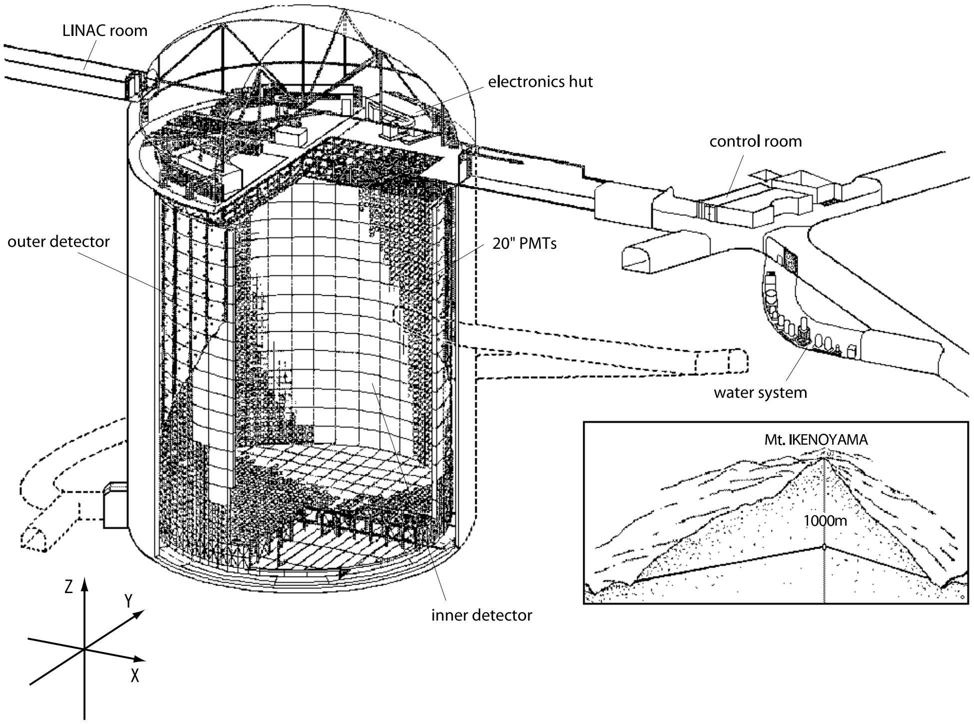

Figure 2.1: Super-Kamiokande detector and its location in Mountain Ikenoyama.

2.1 Cherenkov Radiation

The Super-Kamiokande detector observes relativistic charged particles in water by detecting the emitted Cherenkov light. Cherenkov light is emitted when the velocity of a charged particle exceeds speed of light in the medium:

$$v \geq \frac{c}{n} \tag{2.1}$$

where v is the velocity of the charged particle, c is the speed of light in vacuum and n is the refractive index of the medium[46]. Momentum threshold of Cherenkov radiation is determined by the refractive index of the medium and the particle mass. As the refraction index of water is about 1.34, the momentum thresholds of Cherenkov radiation for electrons, muons, charged pions and protons are 0.57, 118, 156 and 1051 MeV/c respectively.

Cherenkov light is emitted in a cone shape with a characteristic half opening angle θ_C along the direction of travel of the particle. The half opening angle (Cherenkov angle) is determined by:

$$\cos\theta_C = \frac{1}{n\beta} \tag{2.2}$$

where $\beta = v/c$. For particle with $\beta \sim 1$ in water, the Cherenkov angle is about 42°.

The number of photons emitted by Cherenkov radiation is written as a function of wavelength λ:

$$\frac{d^2N}{dxd\lambda} = \frac{2\pi\alpha}{^2}(1 - \frac{1}{n^2\beta^2}) \tag{2.3}$$

where x is the path length of the charged particle and α is the fine structure constant. About 340 photons/cm are emitted between the wavelength range of 300 nm to 600 nm, which is the sensitive wavelength region of the PMTs used in the Super-Kamiokande detector.

The Cherenkov light emitted by charged particles are projected as ring images on the wall inside the detector. Super-Kamiokande detects the Cherenkov photons by PMTs arranged on the wall and the Cherenkov ring patterns can be recognized. Figure 2.2 shows the visual display of a typical neutrino event observed in the Super-Kamiokande detector.

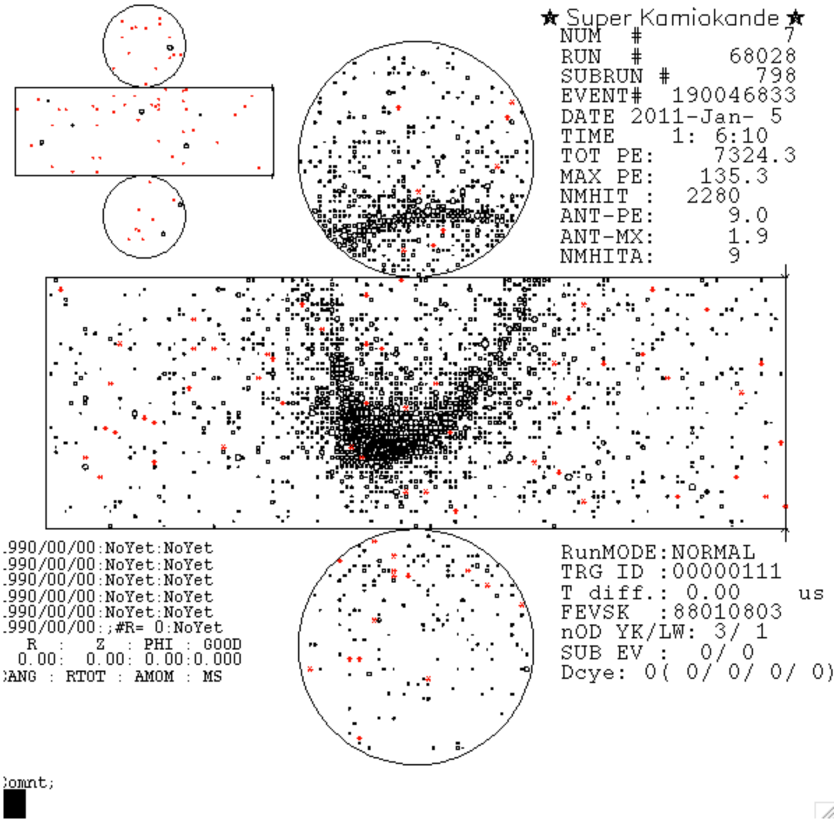

```
★ Super Kamiokande ★
NUM   #          7
RUN   #      68028
SUBRUN #       798
EVENT#  190046833
DATE 2011-Jan- 5
TIME     1: 6:10
TOT PE:     7324.3
MAX PE:    135.3
NMHIT :   2280
ANT-PE:      9.0
ANT-MX:      1.9
NMHITA:      9
```

```
.990/00/00:NoYet:NoYet
.990/00/00:NoYet:NoYet
.990/00/00:NoYet:NoYet
.990/00/00:NoYet:NoYet
.990/00/00:NoYet:NoYet
.990/00/00:;#R= 0:NoYet
   R  :   Z  : PHI : GOOD
  0.00:  0.00: 0.00:0.000
ANG : RTOT : AMOM : MS
```

```
RunMODE:NORMAL
TRG ID :00000111
T diff.: 0.00     us
FEVSK  :88010803
nOD YK/LW: 3/ 1
SUB EV :  0/ 0
Dcye: 0( 0/ 0/ 0/ 0)
```

```
omnt;
```

Figure 2.2: Visual display of a typical neutrino event in the Super-Kamiokande detector. The size of the small circles indicates the amount of Cherenkov photons detected in each PMT. The Cherenkov ring pattern is clearly visible. (Event taken from SK-IV period.)

2.2 Detector

2.2.1 Water Tank

The water tank of Super-Kamiokande is in cylindrical shape with 41.4 m height and 39.3 m diameter. 50 kTon highly pure water is filled in this water tank. The water tank is optically separated into two concentrical cylindrical regions by a PMT support structure and two opaque sheets. The two regions are referred to as the inner detector and outer detector respectively (Figure 2.3).

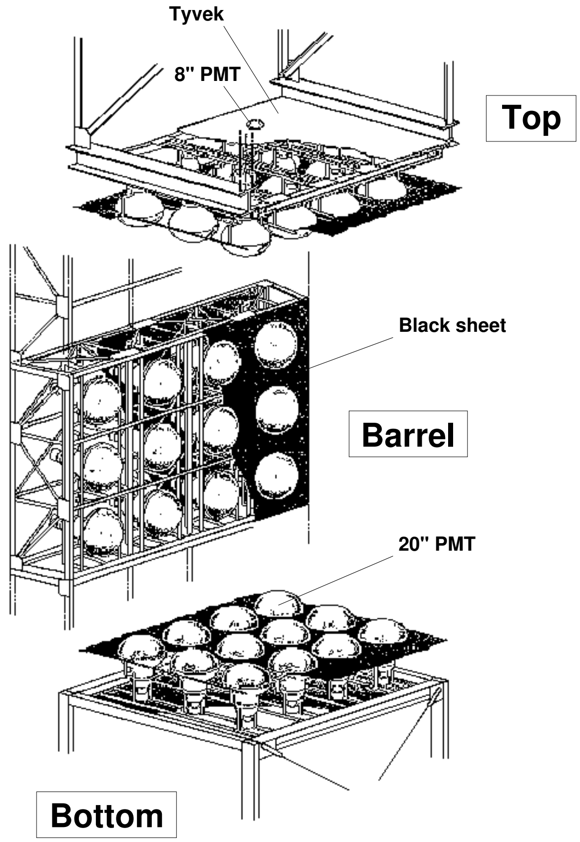

Figure 2.3: Supporting frame of PMTs.

The inner detector (ID) contains 32 kTon water with dimension of 36.2 m height and 33.8 m diameter. 11,146 inward facing 20-inch PMTs are installed to the supporting frame uniformly at 70 cm intervals in SK-I period. The effective photocathode coverage of the ID was about 40%, and the rest of the surface is covered with black polyethylene terephthalate sheet (called "black sheet"). In SK-II period, 5,182 20-inch PMTs (about half of the original PMT density) were installed to the supporting frame and the photocathode coverage was about 20%. From SK-III period and onwards, the photocathode coverage is resumed to about 40% with 11,129 PMTs.

The outer detector (OD) surrounds the ID with thickness of 2.05 m on the top and bottom, and 2.2 m along the barrel wall. The OD is monitored by 1,885 outward facing 8-inch PMTs installed to outer side of the supporting frame. A 60 cm × 60 cm wavelength shifting plate is attached to each OD PMT. The wall is covered with reflective material called ”tyvek sheet” to improve light collection efficiency. The OD is used as a veto counter for cosmic ray muons and to tag outgoing charged particles. The ∼2 m thick water layer serves as a shield to attenuate gamma ray and neutrons from surrounding rocks. The inner and outer volumes are separated by a 55 cm thick dead region in which no PMT is installed. Stainless steel frame, signal cables and high voltage cables of all the PMTs are contained in this dead region.

2.2.2 Photomultiplier Tube for the Inner Detector

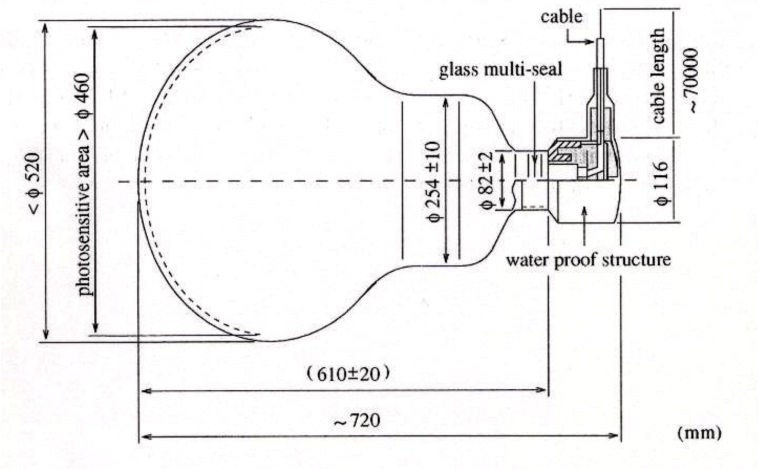

Figure 2.4: Schematic view of the 20-inch PMT used in Super-Kamiokande.

PMTs used in the ID (Hamamatsu R3600) have photocathode with a diameter of 50 cm (20 inch). This 20 inch PMT was developed by Hamamatsu Photonics K.K. in cooperation with Kamiokande collaborators [47]. Later, the dynode structure and the bleeder circuit were modified to improve timing response and photo collection efficiency for Super-Kamiokande [48]. Figure {pmt shows a schematic view of the PMT. The PMT specification is listed in table 2.1.

The photocathode of the PMT is coated with bi-alkali (Sb-K-Cs) which has high spectral sensitivity to Cherenkov light and low thermionic emission. Quantum efficiency (22%) peaks at the wavelength 360-400 nm region, which also corresponds to the peak of the relative Cherenkov spectrum through pure water as shown in figure 2.5. The dynode structure and the bleeder circuit are optimized to achieve high collection efficiency, fast timing response and good energy resolution. Average collection efficiency at the first dynode is 70% which is uniform within 7% everywhere on the photocathode. Gain of the ID PMT is 10^7 at a high voltage of 1500 V to 2000 V. FIgure 2.6 shows the charge distribution for single photoelectron signal, a clear 1

Shape	Hemispherical
Photocathode area	50 cm diamater
Window material	Bialkali (Sb-K-Cs)
Quantum efficiency	22% at = 390 nm
Dynodes	11 stage Venetian blind type
Gain	10^7 at $\sim$ 2000 V
Dark current	200 nA at 10^7 gain
Dark pulse rate	3 kHz at 10^7 gain
Cathode non-uniformity	<10%
Anode non-uniformity	<40%
Transit time	90 nsec at 10^7 gain
Transit time spread	2.2 nsec (1 σ) for 1 p.e. equivalent signals
Weight	13 kg
Pressure tolerance	6 kg/cm^2 water proof

Table 2.1: Specification of the 20-inch PMT used in Super-Kamiokande.

photoelectron (p.e.) peak can be seen. The transit time spread of the single photoelectron signal is about 2.2 nsec. The average dark noise rate at 0.25 photoelectrons (p.e.s) threshold used in SK-I was about 3 kHz.

Magnetic field over 100 mG affects photoelectron trajectories inside the PMT and makes the timing resolution worse. Geomagnetic field at the detector site is about 450 mG. In order to compensate the geomagnetic field, 26 sets of horizontal and vertical Hermholtz coils are arranged around the tank, such that the magnetic field inside the detector is reduced to about 50 mG.

On November 12th, 2001, while the SK tank was being refilled upon the completion of the maintenance work, one ID PMT at the bottom of the tank imploded, triggering a cascade implosions of PMTs. About 60% ID and OD PMTs were destroyed in this accident. After this accident, all the inner PMTs are instrumented with acrylic covers from SK-II period onwards to avoid this kind of chain reaction of implosions. A clear 12 mm thick UV-transparent acrylic dome is put over the photocathode area of each PMT and the side of the PMT is protected with Fiber-Reinforced Plastic (FPR) shield with holes letting water flow in and out of the case freely, as shown in figure 2.7. Transparency of the acrylic cover for photons with normal incidence in water is more than 96% above wavelength 350 nm.

2.2.3 Photomultiplier Tube for the Outer Detector

As for the OD, 1,885 8-inch PMTs are installed. The photocathode of the OD PMT is fitted with 60 cm × 60 cm × 1.3 cm wavelength shifter plate, which increases light collection efficiency by 60%. Even though the timing resolution at single photoelectron slightly degrades from 13 nsec to 15 nsec because of the plate, since the OD is used as a veto counter rather than particle tracker, poor timing resolution has little consequence while higher light collection efficiency is of more importance.

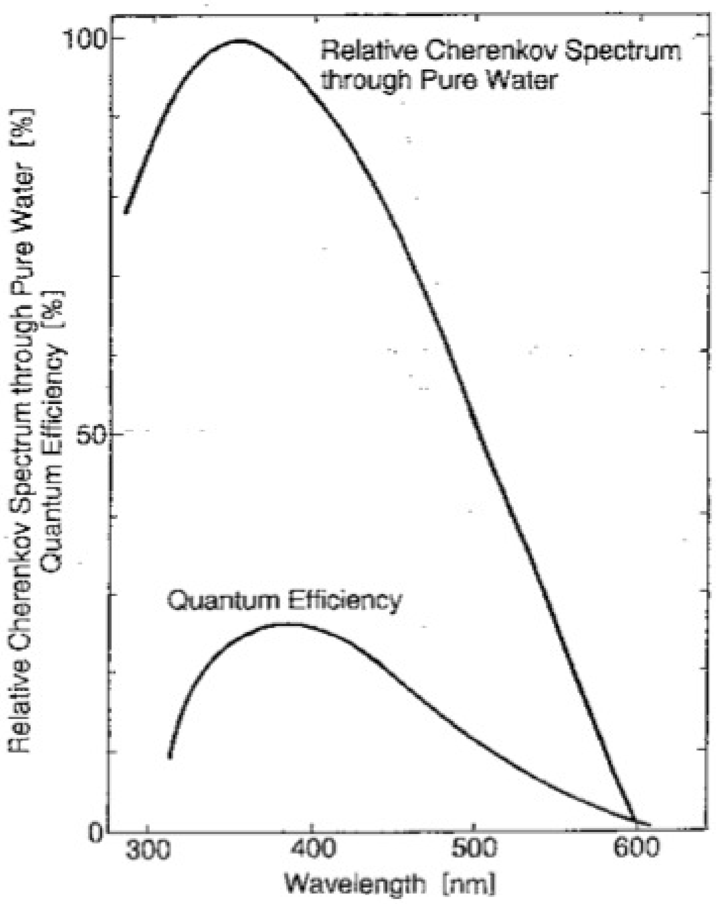

Figure 2.5: Quantum efficiency distribution of the 20-inch PMT used in the ID against wavelength and the relative Cherenkov spectrum through pure water. [135]

2.2.4 Outer Detector (OD) Segmentation

Tyvek sheet was installed to separate top and wall regions, and bottom and wall barrel regions of the OD before the start of the SK-III period. Figure 2.8 shows a schematic view of the OD segmentation.

OD aims to distinguish particles (mostly muons) produced in the ID from cosmic ray muons. Particles (mostly muons) produced inside the ID would leave only one signal in the OD when going out of the detector, while cosmic ray muons would leave one signal in the OD when getting into the detector and then leave another signal in the OD while going out of the detector, leaving two signals in total in the OD. The installation of the OD segmentation aims to separate the signal in the ID and the OD more efficiently.

Figure 2.9 shows the OD event display of a simulated partially contained (PC) event which is a particle produced inside the ID and then goes out around the bottom edge of the tank. The left figure shows the SK-II detector configuration (without the tyvek sheet for the OD segmentation)

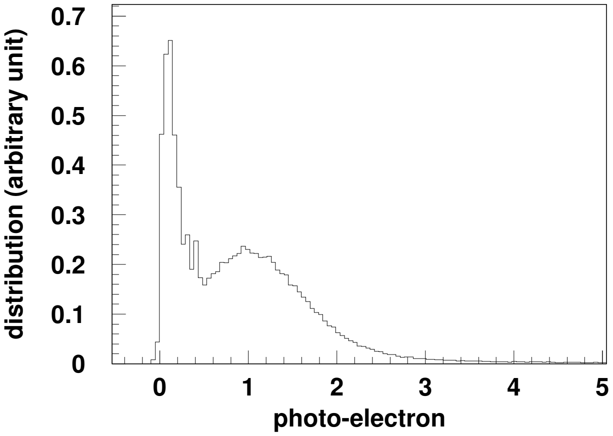

Figure 2.6: Single photoelectron distribution of the 20-inch PMT.

and the right figure shows the SK-III detector configuration (with the tyvek sheet for the OD segmentation between top, bottom and barrel region of the OD installed). Because of the tyvek sheet, the OD signal in SK-III can be clearly seen at the bottom corner of the detector. The tyvek sheet improves the efficiency of the event selection process for partially contained (PC) events.

2.3 Water Purification System

Water used in the tank of the Super-Kamiokande experiment is produced from abundant spring water in the mine. The water in the tank is continuously circulated through the water purification system at a flow rate of 35 ton/hour in order to keep high attenuation length. Another important role of the water purification system is to remove radioactive materials in the water, especially radon (Rn), which is a background source for the solar neutrino observation in the MeV energy region.

2.4 Air Purification System

Clean air with low radon level is essential inside the detector and in the experimental area. To keep low radon level, radon-free air is produced by the purification system in the mine and is continuously pumped into the space above the water surface inside the tank at a positive pressure to prevent radon in the SK dorm air from entering the tank and dissolving into the purified water [49]. Radon concentration in the radon-free air is less than 3 mBq/m^3. The air purification system is composed of compressors, a buffer tank, driers and filters. The air flow rate is about 18 m^3/hour.

Figure 2.7: PMT case used to cover 20-inch PMT in the inner detector since SK-II period.

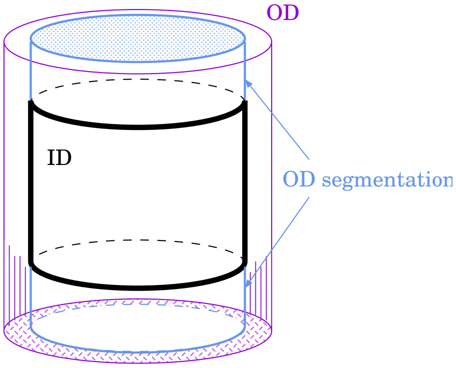

Figure 2.8: A schematic view of the OD region. [43]

2.5 Electronics and Data Acquisition System for SK-I to SK-III Periods

Electronics and data acquisition system for SK-I to SK-III periods is described in this section, as new electronics was installed in September 2008 which corresponds to the SK-IV period, the new electronics will be described in the next section.

2.5.1 Inner Detector Electronics and Data Acquisition System

During SK-I to SK-III periods, ID PMT signals were processed by custom built electronics modules called ATM (Analog-Timing-Module) of the TKO standard (TRISTAN KEK Online) [50] [51]. The ATM module records the integrated charge and the arrival timing information of all PMT signal.

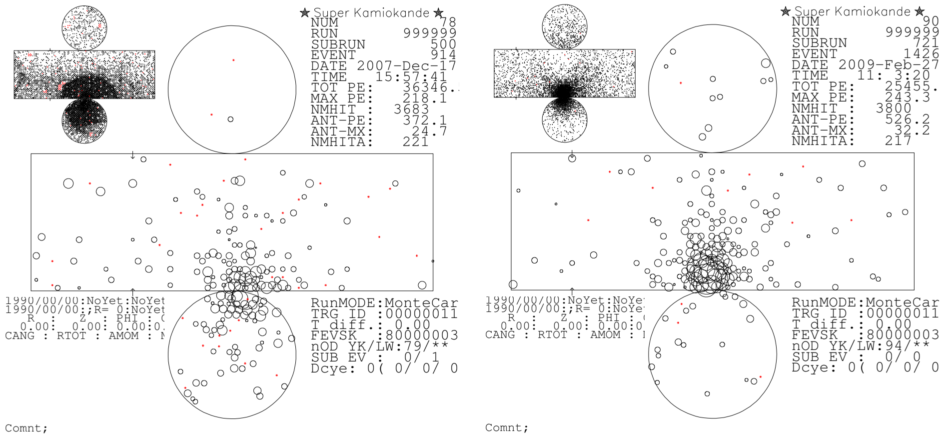

Figure 2.9: Left: SK-II OD event display of a partially contained event, without OD segmentation; Right: SK-III OD event displa of a partially contained event, with OD segmentation. [43]

Figure 2.10 shows the block diagram of the analog input part of the ATM module. Each input channel of ATM from the PMT has two switching pairs of Charge to Analog Converter (QAC) and Time to Analog Converter (TAC) to minimize electronics dead time during the data taking for two successive events (such as muon followed by its decay electrons). All PMT signal sent to ATM are amplified 100 times, then they are divided into four signals. One of the four signals is sent to the discriminator, and when the pulse height of the PMT signal exceeds the threshold (which is set to 0.23 p.e.s), a 400 ns gate signal for QAC and a start signal for TAC are generated. At the same time, a rectangular signal called HITSUM (200 ns width and 15 mV pulse height) is sent to the global trigger module. Other two out of the four signals are fed to QAC. When a global trigger is issued, a stop signal is sent to TAC, then the information in QAC and TAC are digitized by ADC. The digitized charge and timing information are stored in internal FIFO memory in ATM. In case no global trigger is issued within 1.3 s, all information in QAC and TAC would be cleared. ATM has 450 pC dynamic range with a resolution of 0.2 pC, and 1.3 s dynamic range with a resolution of 0.4 ns. The remaining one signal out of the four signals becomes an output signal of ATM called PMTSUM. Figure 2.11 shows a schematic view of the ID data acquisition system. Signals from 12 PMTs are fed into 1 ATM board. There are in total 946 ATM boards installed in 48 TKO crates. The digitized data in the ATM FIFO memory are then sent to VME memory modules called SMP (Super Memory Partner) for every 16 events. 48 SMP are installed in 8 VME crates, with 1 SMP module handles the data of 20 ATMs. The data in SMP memories are read out by 8 slave computers and then sent to the online host computer.

2.5.2 Outer Detector Electronics and Data Acquisition System

For the OD data acquisition system, the schematic view is shown in figure 2.12 [52]. The paddle cards distribute high voltage from the main frame to the OD PMTs. A coaxial cable is used to supply the high voltage to the OD PMT and send signal from the OD PMT, then these

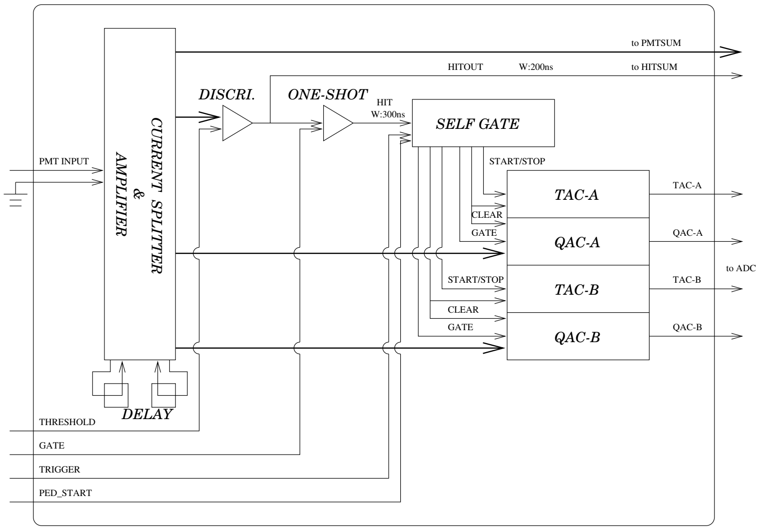

Figure 2.10: Block diagram of analog input part of the ATM module.

cards pick off the PMT signals through a high voltage capacitor. Signals from the OD PMTs are then sent to Charge to Time Converter (QTC), which converts the PMT signal to a rectangular pulse whose width is proportional to the input charge. At the same time, a rectangular HITSUM signal is generated by the QTC and sent to a global trigger module. The threshold of the QTC is set to 0.25 p.e.. When a global trigger is received, the leading edge and the width of the rectangular pulse are converted to timing and charge information respectively by LeCroy 1877 multi-hit TDC module. The dynamic range is set to 16 s which starts from 10 s before the global trigger timing.

2.5.3 Trigger

The ID trigger schematic diagram is shown in figure 2.13. When an ID PMT signal exceeds the threshold, an ATM generates a rectangular HITSUM signal with 15 mV pulse height and 200 ns pulse width. These signals are analog-summed over all PMTs to generate an ID-HITSUM signal. The pulse height of the ID-HITSUM signal is proportional to the number of hit PMTs within 200 ns time window. There are three types of trigger signals derived from the ID-HITSUM signal. In SK-I , the high energy (HE) trigger is generated when the pulse height of ID-HITSUM signal exceeds a threshold of -340 mV, which corresponds to 31 hits within a 200 ns time window. The threshold for low energy (LE) trigger is -320 mV, which corresponds to 29 hits. This is equivalent to a signal expected from a 5.7 MeV electron assuming 50 % trigger efficiency. Trigger rates for HE and LE triggers are $\sim$5 Hz and $\sim$11 Hz respectively. Super low energy (SLE) trigger was implemented in May 1997 to lower the solar neutrino analysis threshold. The threshold level for the SLE trigger was lowered gradually with increasing trigger CPU power. The threshold was set to -186 mV, which corresponds to 4.6 MeV electron, in July 2000. Its trigger rate is $\sim$1 kHz. In SK-II and SK-III, the same trigger scheme were used, with the trigger conditions listed in table 2.2.

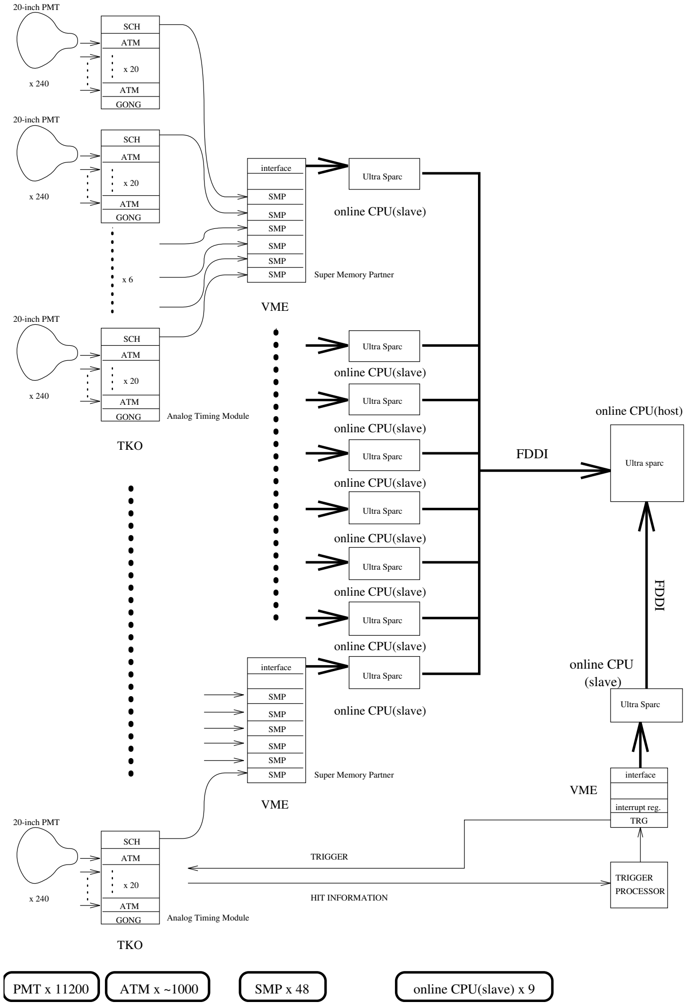

Figure 2.11: Schematic view of the ID data acquisition system for SK-I to SK-III periods.

OD trigger is generated by similar procedure. When an OD PMT signal exceeds a threshold, a QTC module generates a rectangular pulse wit 20 mV height and 200 ns in width. The signals are also analog-summed to generate an OD-HITSUM signal. Threshold of the OD trigger is 19 hits within 200 ns time window.

Four types of trigger signals (HE, LE, SLE, OD) are fed to a hardware trigger module TRG which generates a global trigger signal when any of the four trigger signals is issued.

2.6 Electronics and Data Acquisition System for SK-IV Period

In order to achieve zero dead time, SK detector's front end electronics were replaced in September 2008. The new electronics [53] are described in this section.

In SK-IV, the former electronics ATM was replaced by new electronics QBEE (QTC-Based Electronics with Ethernet). It has an integrated 3-channel device for PMT signal readout.

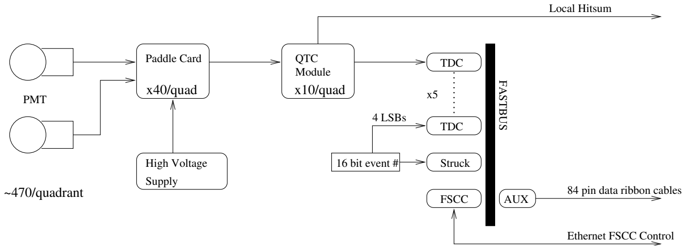

Figure 2.12: Schematic view of the OD data acquisition system for SK-I to SK-III periods.

	SK-I	SK-II	SK-III
Period	Apr 1996 - Jul 2001	Oct 2002 - Oct 2005	Jun 2006 - Sep 2008
number of ID PMTs	11,146	5,182*	11,129*
Photocathode coverage	40%	20 %	40 %
HE trigger threshold	-340 mV	-180 mV	-320 mV
LE trigger threshold	-320 mV	-152 mV	-302 mV
SLE trigger threshold	-186 mV	-110 mV	-186 mV
Other features			Tyvek sheet installed for OD segmentation

Table 2.2: Trigger conditions for each SK period. *All inner PMTs are protected with acrylic covers.

This application-specific integrated circuit (ASIC) called the high-speed charge-to-time converter (QTC) IWATSU CLC101 was designed in CMOS 0.35 μm technology. It has built-in discriminators to trigger its integrated circuits by itself and encodes the amount of input charge to timing signal, where the leading edge represents the timing and the width represents the integrated charge of the input signal.

Figure 2.14 shows the block diagram of the QTC and its surroundings. The QTC has three input channels per chip and each channel has three gain ranges (small, medium and large). The overall charge dynamic range of the QTC is 0.2 - 2500 pC if the gain ratio of the three ranges is set to 1: $\frac{1}{7}$: $\frac{1}{49}$. Figure 2.15 shows the block diagram of one QTC channel. Input signals from PMTs are amplified by a low-noise-amplifier (LNA), delayed by a low-pass filter (LPF), processed by a voltage-to-current (V/I) converter, and integrated by a capacitor. The sum of the input-signal waveform to the capacitors can be monitored through an output signal designated PMTSUM.

The QTC is charge sensitive. Charge integration starts when the amplified input signal crosses the discriminator threshold. The leading edge of the output signal represents the timing when the charge integration starts. A trigger flag signal (HIT) is generated at the same time. After a charging period is determined by the timer block, the integrated signal starts to be discharged by a constant current source. The discharging time is thus proportional to the

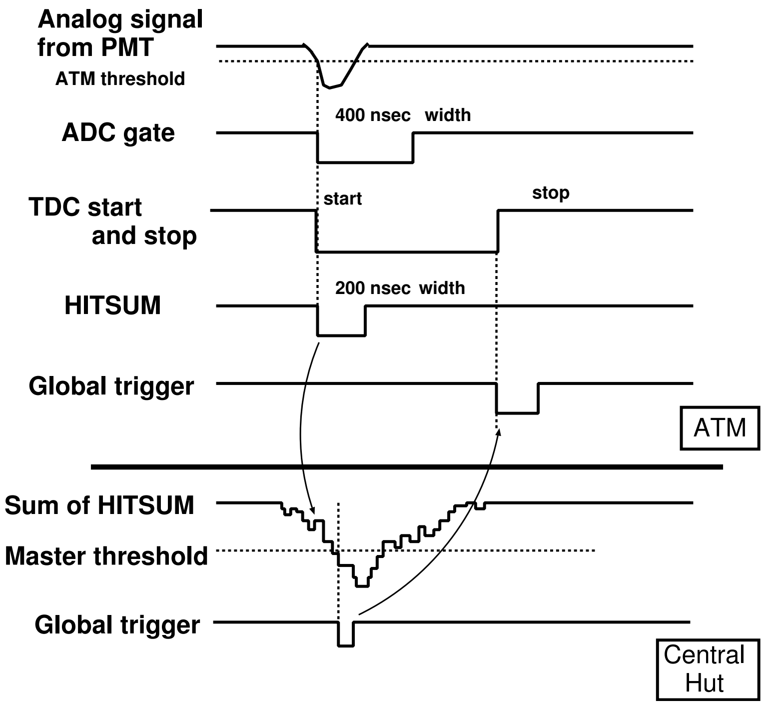

Figure 2.13: Overview of the ID trigger scheme for SK-I to SK-III periods.

integrated charge, which in turn is reflected in the width of the output signal. Hence the QTC output signal contains both timing and charge information.

In figure 2.15, the timer block contains three timers: a charging timer, a discharging timer and a VETO timer. The timers generate timing gates by ramps with constant discharge current and comparators. The time length for these gates are controlled by digital-to-analog converters (DACs) for discharge current and comparator threshold levels.

2.6.1 Trigger

Figure 2.16 shows the timing chart for QTC operation. The charging timer, which is triggered by the discriminator output signal, operates for $\sim$ 400 ns. During the charge gate, the switch between the V/I converter and charging capacitor closes and input charge accumulates in the capacitor. Then after the charge gate, the discharging timer operates for $\sim$ 350 ns. During the discharge gate, the switch between the discharging current source and capacitor closes, the arriving input signals are ignored. The trailing edge of the QTC output signal represents the time when the integrated signal voltage decreases to the comparator threshold level. Hence, the QTC output signal becomes wider when the input signal gets larger. At the end of the discharge gate, reset and VETO signals are issued, all QTC circuits except VETO timer are reinitialized. Input signals within $\sim$ 150 ns after the discharge gate are ignored. the processing time for one input signal is $\sim$ 900 ns in total.

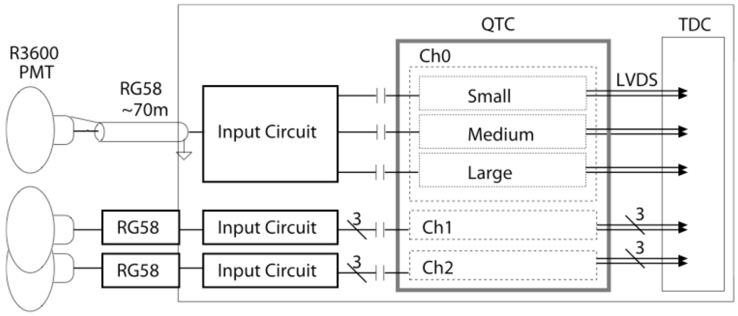

Figure 2.14: Block diagram of the QTC and its surroundings (Data acquisition system for SK-IV period). [53]

2.6.2 Improvement by the Electronics and Data Acquisition System in SK-IV Period

The triggering system during SK-I, SK-II and SK-III period had hardware trigger (by HITSUM), while the new data acquisition (DAQ) readout system used in SK-IV use software trigger instead. The new system records all hits and apply software triggers,and it is collecting data at 60 kHz frequency and 17 μs TDC window. There is no dead time for the SK-IV DAQ system, so that all data are taken. The saturation points of the electronic modules also increases from the original $\sim$250 photoelectrons during the SK-I to SK-III periods to $\sim$1200 photoelectrons in the new system. Due to these improvement, the decay-electron tagging efficiency becomes higher and dynamic range also became wider in the SK-IV period.

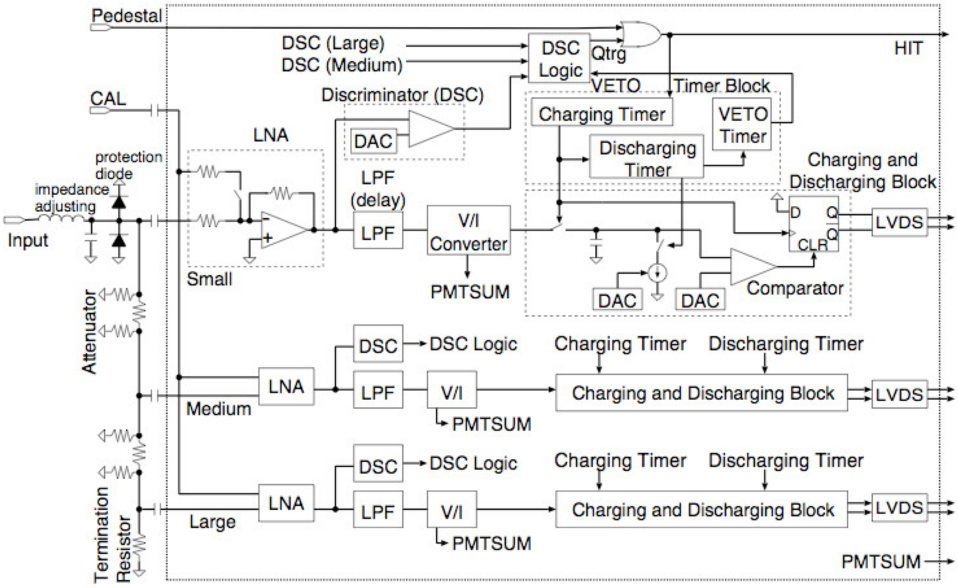

Figure 2.15: Block diagram of one QTC channel. Each channel has three gain ranges: small, medium and large. (Data acquisition system for SK-IV period)[53]

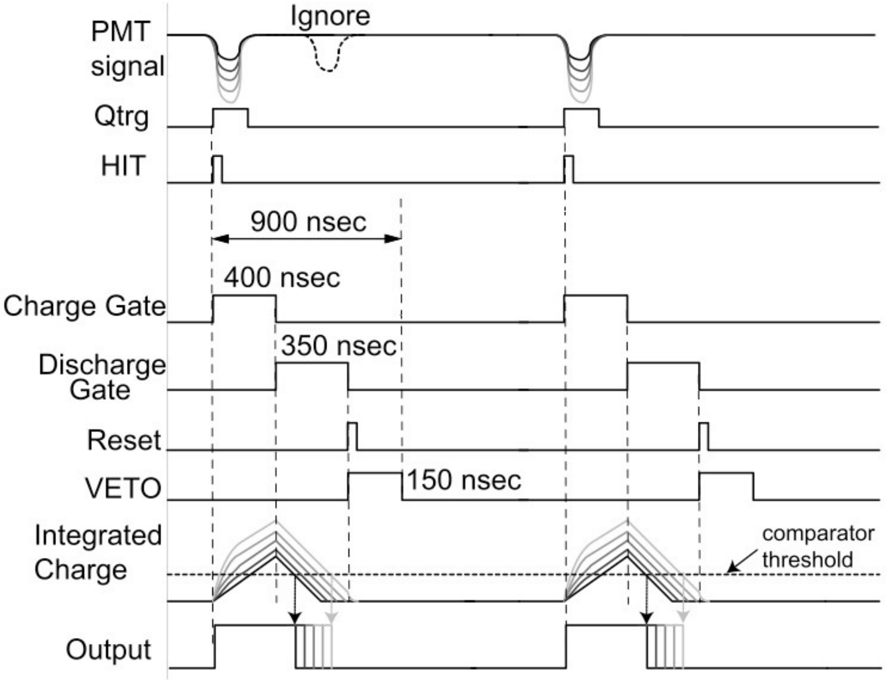

Figure 2.16: Timing chart for QTC operation. (Data acquisition system for SK-IV period) [53]

Chapter 3

Simulation of Atmospheric Neutrino

Atmospheric neutrino events in Super-Kamiokande are simulated by Monte-Carlo method. The Monte Carlo simulation is composed of three parts: atmospheric neutrino flux, neutrino interactions and particle tracking in the detector. By considering neutrino flux and cross-sections, expected events observed in the detector are calculated during a certain period. The produced particles have information such as vertex, direction, momentum and so on. With these information, the detector simulation simulates the particle, Cherenkov photon emission, photon propagation and response of the detector hardware. The simulated events are reconstructed in the same way as the real observed data. They are called Monte Carlo (MC) events in this thesis.

This chapter describes the neutrino flux model, NEUT library which is the simulator of neutrino interaction kinematics and detector simulation.

3.1 Atmospheric Neutrino Flux

There are several atmospheric neutrino flux models calculated by M. Honda et al. [23] [54] [55] [149](Honda flux), G. Battistoni et al. [57] (Fluka flux) and G. Barr at al. [58] (Bartol flux). Honda flux is adopted as the default model in this analysis, with the difference between Honda flux and the two other flux models are considered as the systematic uncertainties. As the Honda flux only covers the energy range up to 10 TeV, the Volkava flux [59] is adopted to simulate events having energy above 10 TeV.

The atmospheric neutrino flux is a convolution of the primary spectrum at the top of the atmosphere with the yield of neutrinos per primary particle. In order to reach the atmosphere and interact, the primary cosmic rays must first pass through the geomagnetic field. Hence, the calculation of the flux of neutrinos includes flux of primary cosmic rays, filtering effect of the geomagnetic field and the yield of neutrinos per primary particle [56].

The primary cosmic ray flux model, which is the input of the neutrino flux calculation, is determined by experimental measurements. Figure 3.1 shows the model used in the Honda flux calcution (solid line) and the comparison with different models [55]. The primary cosmic ray spectrum has been precisely measured by BESS and AMS experiments up to 100 GeV [65] [66]. The cosmic ray flux changes according to the turbulence of solar activities, which is lower when solar activities are high (solar maximum) than when the solar activities are low (solar minimum). The difference of cosmic ray flux between solar minimum and solar maximum is more than a factor of two for 1 GeV cosmic rays, while the difference is about 10 % for 10 GeV cosmic rays.

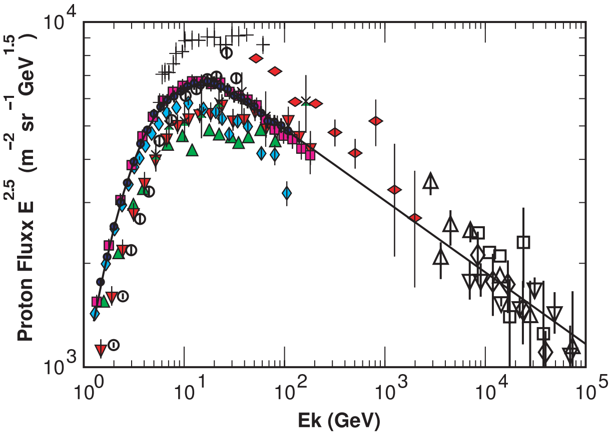

Figure 3.1: Primary cosmic ray proton flux used in Honda flux calculation (line) and the observed results (points) [55]. Observation data points are taken from Webber [60] (crosses), LEAP [61] (upward triangles), MASS1 [62] (open circles), CAPRICE [63] (vertical diamonds), IMAX [64] (downward triangles), BESS98 [65] (circles), AMS [66] (squares), Ryan [67] (horizontal diamonds), JACEE [68] (downward open triangles), Ivanenko [69] (upward open triangles), Kawamura [70] (open squares) and Runjob [71] (open diamonds).

In Honda flux, the US Standard Atmosphere model [72] is used for the density structure of the atmosphere which gives zenith angle dependence of atmospheric neutrinos. Geomagnetic field effects are calculated based on the IGRF2005 model [73].

Primary cosmic ray protons and nuclei interact with air molecules in the Earth's atmosphere. Secondary particles (mostly pions and kaons) are produced through these hadronic interactions. In the hadronic interactions between the cosmic rays and air molecules, two theoretical models are used in the calculation: JAM [150] interaction model for primary cosmic ray energies less than 32 GeV, and DPMJET-III [75] for energies greater than 32 GeV. Pions and kaons generated from the hadronic interactions further decay into muons and neutrinos.

In order to make sure that the simulation of the hadronic interactions is correct and to fine tune the hadronic interactions in the simulation, the flux of the resulting cosmic ray muons from the simulation is compared with external experiment data. The flux of the cosmic ray muons have been measured by several experiments such as BESS [76] and L3+C [77]. DPMJET-III used in the Honda flux is modified based on the measurements by BESS and L3+C. JAM used in the Honda flux for the lower energy hadronic interactions is also modified based on the experimental studies at Tsukuba [79], Mt. Norikura [81] and at ballon altitudes at Fort Summer [80]. Figure 3.2 shows the comparison of the observed muon flux at different altitudes and the calculation with JAM and DPMJET-III.

In the calculation of neutrino flux, interactions and propagation of particles are treated in a 3-dimentional way, considering the curvature of charged particles in geomagnetic field. In the 3-dimentional calculation, there is an enhancement of neutrino flux in the near-horizontal direction when compared with the 1-dimentional calculation. This can be explained by the difference in effective area as shown in Figure 3.3. This effect is significant for low energy neutrinos (less than 1 GeV), for which transverse momentum of the secondary particles in

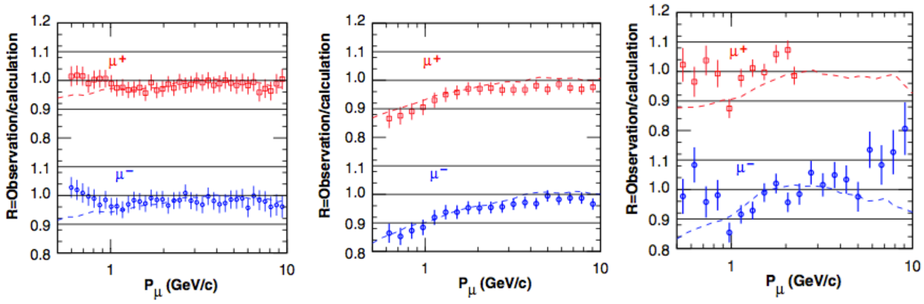

Figure 3.2: Comparison of the secondary cosmic ray muon flux observed at Tsukuba (left), Mt. Norikura (middle) with the BESS detector [79] and at ballon altitudes at Fort Summer [80]. Plots taken from [149].

hadronic interactions and bending of muons in the geomagnetic field are significant. Figure 3.4 shows the zenith angle distribution of neutrino flux at four different energy ranges. The near-horizontal flux enhancement in the lower energy regions (less than 1 GeV) is due to the 3-dimensional effect, while the enhancement in the higher energy regions (above1 GeV) is mostly due to muons reaching the ground before they decay near vertical.

Figure 3.5 shows the calculated zenith angle distributions of neutrino flux for three different neutrino energies (0.32 GeV, 1.0 GeV and 3.2 GeV).

The calculated energy spectrum and flux ratio between $\nu_e + \bar{\nu_e}$ and $\nu_\mu + \bar{\nu_\mu}$ of atmospheric neutrinos at the SK site is shown in Figure 3.6 for Honda flux, Fluka flux and Bartol flux, the flux of $\nu_e + \bar{\nu_e}$ and $\nu_\mu + \bar{\nu_\mu}$ is averaged over all of the direction. The flavor ratio is about 2 for neutrino energies below a few GeV and it becomes larger than 2 as the neutrino energies increase, as more cosmic ray muons reach the ground before decaying.

The flavor ratio also depends on the zenith angle and the energy of the incoming neutrinos as shown in Figure 3.7.

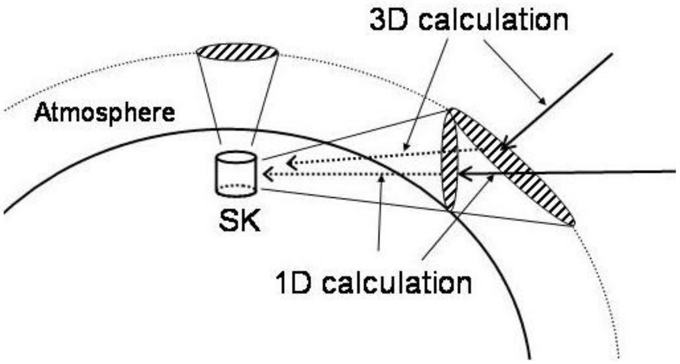

Figure 3.3: Schematic view of effective areas of primary cosmic rays interacting with air molecules for 1-dimentional calculation and 3-dimentional calculation. Solid arrows represent primary cosmic rays and dotted arrows represent neutrinos. The 3-dimentional calculation gives larger area for near-horizontal directions (from the view of the SK detector), which induces an enhancement of neutrino flux. [43]

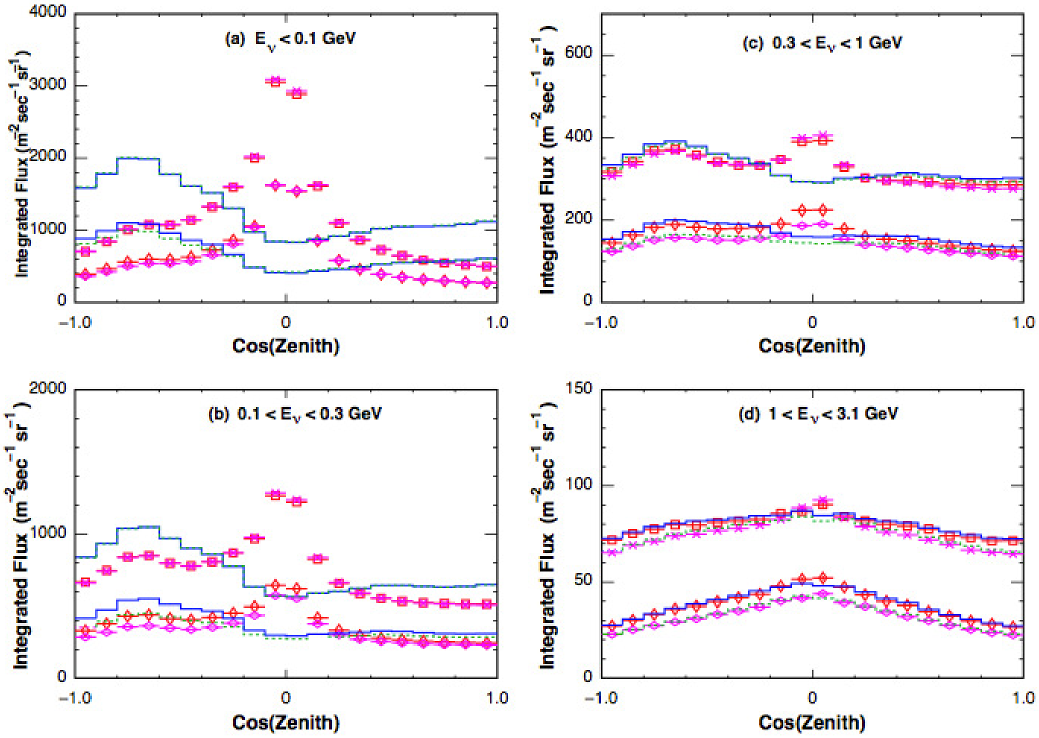

Figure 3.4: Comparison of 3-dimensional and 1-dimensional calculations of neutrino fluxes at Super-K. Squares represent ν_μ, asterisks represents $\bar{\nu_\mu}$, vertical diamonds represent ν_e, horizontal diamonds represend $\bar{\nu}_e$ for 3-dimensional calculation. Solid lines represent ν fluxes and dotted lines represent $\bar{\nu}$ fluxes for 1-dimensional calculation. [56]

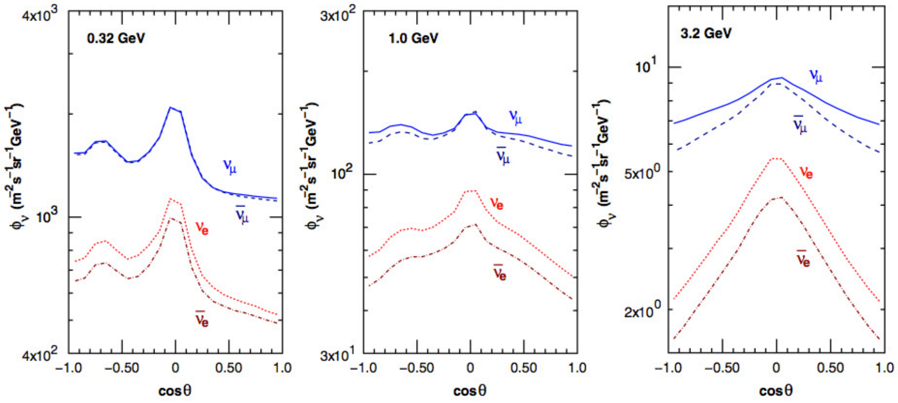

Figure 3.5: Zenith angle dependence of atmospheric neutrino flux for different energy regions. The higher lines represent ν_μ and $\overline{\nu}_\mu$ and the lower lines represent ν_e and $\overline{\nu}_e$. [149]

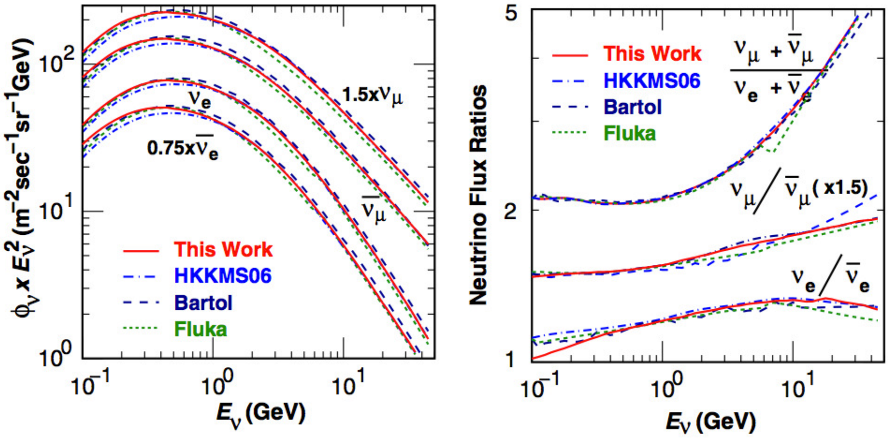

Figure 3.6: Comparison of atmospheric neutrino fluxes averaged over all directions (left) and flavor ratio (right). Red solid line represents Honda 11 flux. Dashed line represents the Bartol flux, dotted line represents the FLUKA flux, and blue dashed line represents Honda 06 flux. [149]

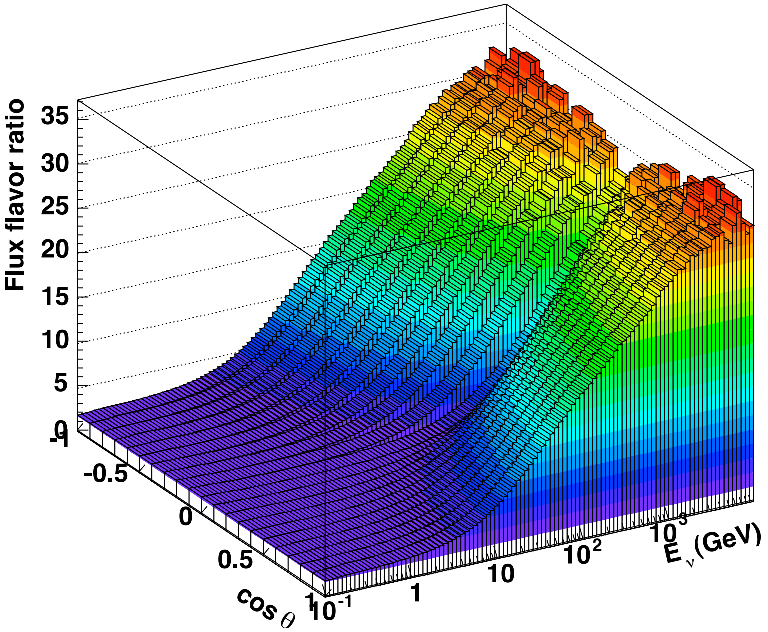

Figure 3.7: Flavor ratio $(\nu_\mu + \bar{\nu_\mu})/(\nu_e + \bar{\nu_e})$ as a function of neutrino energy and zenith angle. Calculation is based on Honda flux. [43]

3.2 Neutrino Interaction

Atmospheric neutrinos interact with nucleons and electrons in water and the rock surrounding the SK detector. In this atmospheric neutrino analysis, the Monte Carlo (MC) simulation has the neutrino events generated through the simulation of the neutrino interaction with water nuclei and the rock. Generation volumes include the rock surrounding the SK detector (assumed to spread spherically up to 4 km from the detector), the OD region and the region inside ID.

A simulation program library NEUT [84] [85] is used for the simulation of neutrino interactions. In the NEUT simulator, the following interactions are considered:

CC/NC (quasi-)elastic scattering $\nu + N \to l + N'$

CC/NC single meson production $\nu + N \to l + N' + meson$

CC/NC deep inelastic interaction $\nu + N \to l + N' + hadrons$

CC/NC coherent pion production $\nu +^{16} O \to l +^{16} O + \pi$

where N and N' are nucleons (proton or neutron) and l is a lepton. These interactions are explained in the following sections.

3.2.1 Charged Current Quasi-Elastic Scattering

The charged quasi-elastic scattering for free protons (hydrogen atoms) is treated in this simulator as described by Llewellyn-Smith [86]. For free nucleon, the differential cross section is:

$$\frac{d\sigma^{\bar{\nu}}}{dq^2} = \frac{M^2 G_F^2 cos^2\theta_C}{8\pi E_\nu^2}[A(q^2) + B(q^2)\frac{s-u}{M^2} + C(q^2)\frac{(s-u)^2}{M^4}] \tag{3.1}$$

where E_ν is the neutrino energy, $M = 0.938$ MeV is the nucleon mass, G_F is the Fermi coupling constant, θ_C is the Cabibo angle, $q = p_\nu - p_l$ is the four-momentum transfer, s and u are Mandelstam variables [86]. The factors A, B and C are given as:

$$\begin{aligned}
A(q^2) &= \frac{m^2-q^2}{4M^2}[(4-\frac{q^2}{M^2})|F_A|^2 - (4+\frac{q^2}{M^2})|F_V^1|^2 \\
&\quad -\frac{q^2}{M^2}|\xi F_V^2|^2(1+\frac{q^2}{4M^2}) - \frac{4q^2 F_V^1 \xi F_V^2}{M^2} \\
&\quad -\frac{m}{M}((F_V^1+\xi F_V^2)^2 + |F_A|^2)] &(3.2)\\
B(q^2) &= \frac{q^2}{M^2}(F_A(F_V^1+\xi F_V^2)) &(3.3)\\
C(q^2) &= \frac{1}{4}(|F_A|^2 + |F_V^1|^2 - \frac{q^2}{4M^2}|\xi F_V^2|^2) &(3.4)
\end{aligned}$$

where m is the outgoing lepton mass, ξ is defined as anomalous magnetic moment $\mu_p - \mu_n = 3.71$. Vector form factors $F_V^1(q^2)$ and $F_V^2(q^2)$ and axial vector form factor $F_A(q^2)$ are determined experimentally and given by:

$$
\begin{aligned}
F_V^1(q^2) &= (1-\frac{q^2}{4M^2})^{-1}[G_E(q^2)-\frac{q^2}{4M^2}G_M(q^2)] && (3.5)\\
\xi F_V^2(q^2) &= (1-\frac{q^2}{4M^2})^{-1}[G_E(q^2)-G_M(q^2)] && (3.6)\\
F_A(q^2) &= -1.232(1-\frac{q^2}{M_A^2})^{-2} && (3.7)\\
G_E &= (1+\xi)^{-1}G_M(q^2)=(1-\frac{q^2}{M_V^2})^{-2} && (3.8)
\end{aligned}
$$

where G_E and G_M are the electric and magnetic form vector respectively, $M_V = 0.84GeV$ and $M_A = 1.21GeV$ are the vector and axial vector masses respectively with both values taking into account the experimental results from K2K and MiniBooNE [88] [89] [90].

The same M_A value (1.21 GeV) is also assumed for single meson productions. M_A value affects the cross section as it is a function of Q^2. For larger M_A, interactions with high Q^2 and therefore larger scattering angles are enhanced. Uncertainty of the M_A value in this analysis is estimated to be 10% by the total uncertainty adopted to the K2K and MiniBooNE results.

For scattering off bound nucleons in ^{16}O, nuclear effects such as Fermi motion of the nucleons and Pauli exclusion principle are taken into account as described by the Smith and Moniz model [87]. As nucleus are fermions, the outgoing momentum of the nucleons in the interactions has to be larger than the Fermi surface momentum to allow quasi-elastic scattering to occur. The Fermi surface momentum is assumed to be 225 MeV/c in this simulator.

Other theoretical models such as Nieves *et al.* [91] and Nakamura *et al.* [92] have been developed to account for nuclear effects in neutrino interactions at intermediate energy ranges besides the Smith and Moniz model. In this analysis, these models are used in the systematic uncertainty estimation for neutrino interactions and nuclear effects.

Figure 3.8 shows the cross section of quasi-elastic scattering for the calculation from NEUT and comparison with experimental data.

3.2.2 Neutral Current Quasi-Elastic Scattering

As for the differential cross section of neutral current quasi-elastic scattering, it is of the same form as equation 3.1, with $\cos\theta_C$ replaced by unity, and nucleon form factors replaced by corresponding neutral current (NC) nucleon form factors [99]:

$$
\begin{aligned}
\tilde{F}_V^{1,N} &= \pm\frac{1}{2}F_V^1-(2sin^2\theta_W)F_N^1,\\
\tilde{F}_V^{2,N} &= \pm\frac{1}{2}F_V^2-(2sin^2\theta_W)F_N^2 && (3.9)
\end{aligned}
$$

where

$$
F_V^1=\frac{\tilde{G}_E^V-\frac{q^2}{4M^2}\tilde{G}_M^V}{1-\frac{q^2}{4M^2}}, F_V^2=\frac{\tilde{G}_M^V-\tilde{G}_E^V}{1-\frac{q^2}{4M^2}}
$$

$$
F_N^1=\frac{\tilde{G}_E^N-\frac{q^2}{4M^2}\tilde{G}_M^N}{1-\frac{q^2}{4M^2}}, F_N^2=\frac{\tilde{G}_M^N-\tilde{G}_E^N}{1-\frac{q^2}{4M^2}}
$$

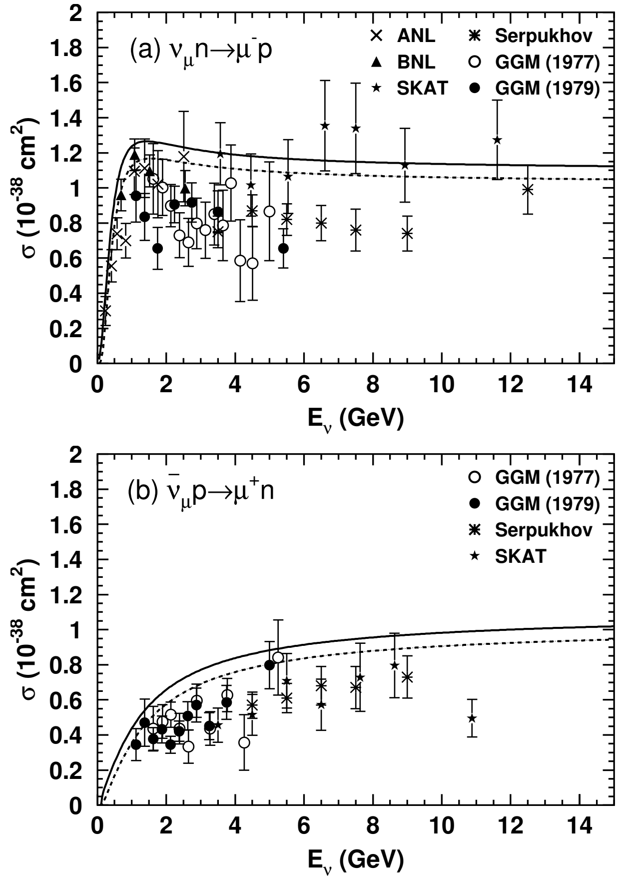

Figure 3.8: Charged current quasi-elastic interaction cross section of (a) ν_μ and (b) $\bar{\nu_\mu}$, with experimental data from ANL [93], Gargamelle [94] [95], BNL [96], Serpukhov [97] and SKAT [98]. Solid line indicates scattering off a free proton, the dashed line indicates scattering off bound nucleons in ^{16}O.

$$\tilde{F}_A = \frac{1}{2}(F_A^s \pm F_A) = \frac{1}{2}(\Delta s \pm g_A)(1 - \frac{q^2}{M_A^2})^{-2} \tag{3.10}$$

$$\tilde{F}_p = \frac{2M^2\tilde{F}_A}{m_\pi^2 - q^2} \tag{3.11}$$

where N = p, n and the upper (lower) sign is for proton (neutron). In NEUT, the weak mixing angle is set to $sin^2\theta_W = 0.23117$, and the strange quark contribution Δs is set to 0.

3.2.3 Single Meson Production

Single meson production via baryon resonances is the dominant hadron production process in the region where the invariant mass of the hadronic system is less than about 2.0 GeV/c^2. Our simulation for the process is based on Rein and Sehgal's model [100] . It is used to simulate the resonance production of single π, η and K. It assumes one meson is generated by the decay of intermediate resonances:

$$\nu + N \rightarrow l + N^* \tag{3.12}$$

$$N^* \rightarrow N' + meson \tag{3.13}$$

Equations (3.12) is resonance production while (3.13) is resonance decay, in which N and N' are nucleons and N^* is a baryon resonance. Invariant mass W of the intermediate baryon resonances is restricted to be less than 2 GeV/c^2. For W greater than 2 GeV/c^2, the interactions are simulated as a part of deep inelastic scattering which will be described in next section.

Rein's method [101] is used to determine the angular distribution of the pion in the final state for the P$_{33}$(1232) resonance. As for other resonances, the angular distribution of the generated pion is set to be isotropic in the resonance rest frame. The angular distribution of π^+ was measured for $\nu_\mu p \rightarrow \mu^- p \pi^+$ [102]. The results agree well with the prediction by NEUT.

Pauli exclusion principle in the baryon resonance decay is considered by requiring the nucleon momentum to be greater than the Fermi surface momentum.

It is known that a baryon resonance in a nucleus can be absorbed without producing a meson [103]. NEUT considers such phenomenon and 20% of the resonance events do not have mesons generated and only leptons and nucleons are produced.

Figure 3.9, 3.10 and 3.11 show the cross section of single meson production for charged current ν_μ, charged current $\bar{\nu_\mu}$ and neutral current respectively, from both NEUT calculation and experimental data.

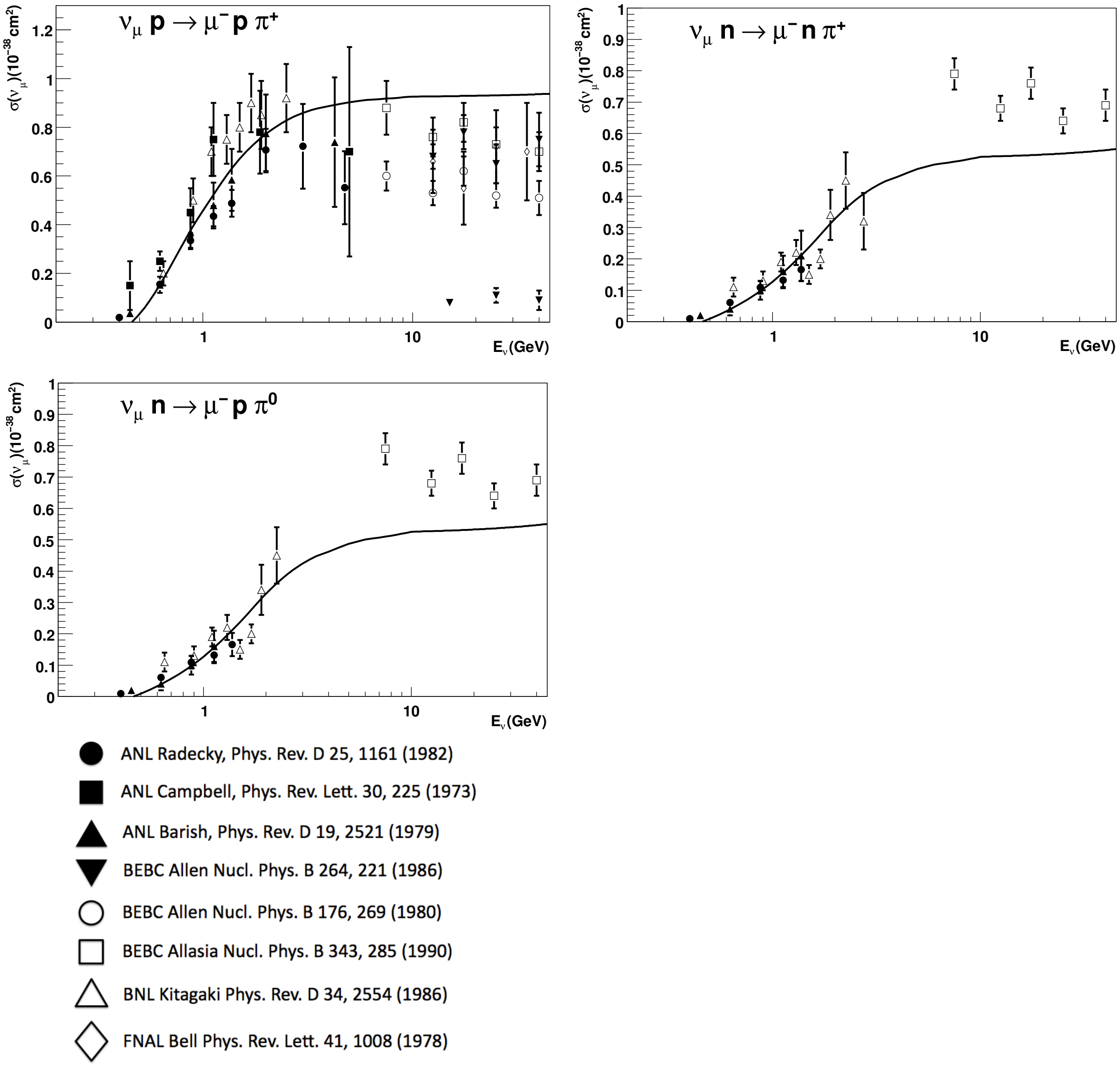

Figure 3.9: Cross section for ν_μ charged current single pion productions. Solid lines are NEUT calculations, points are experimental data. [136]

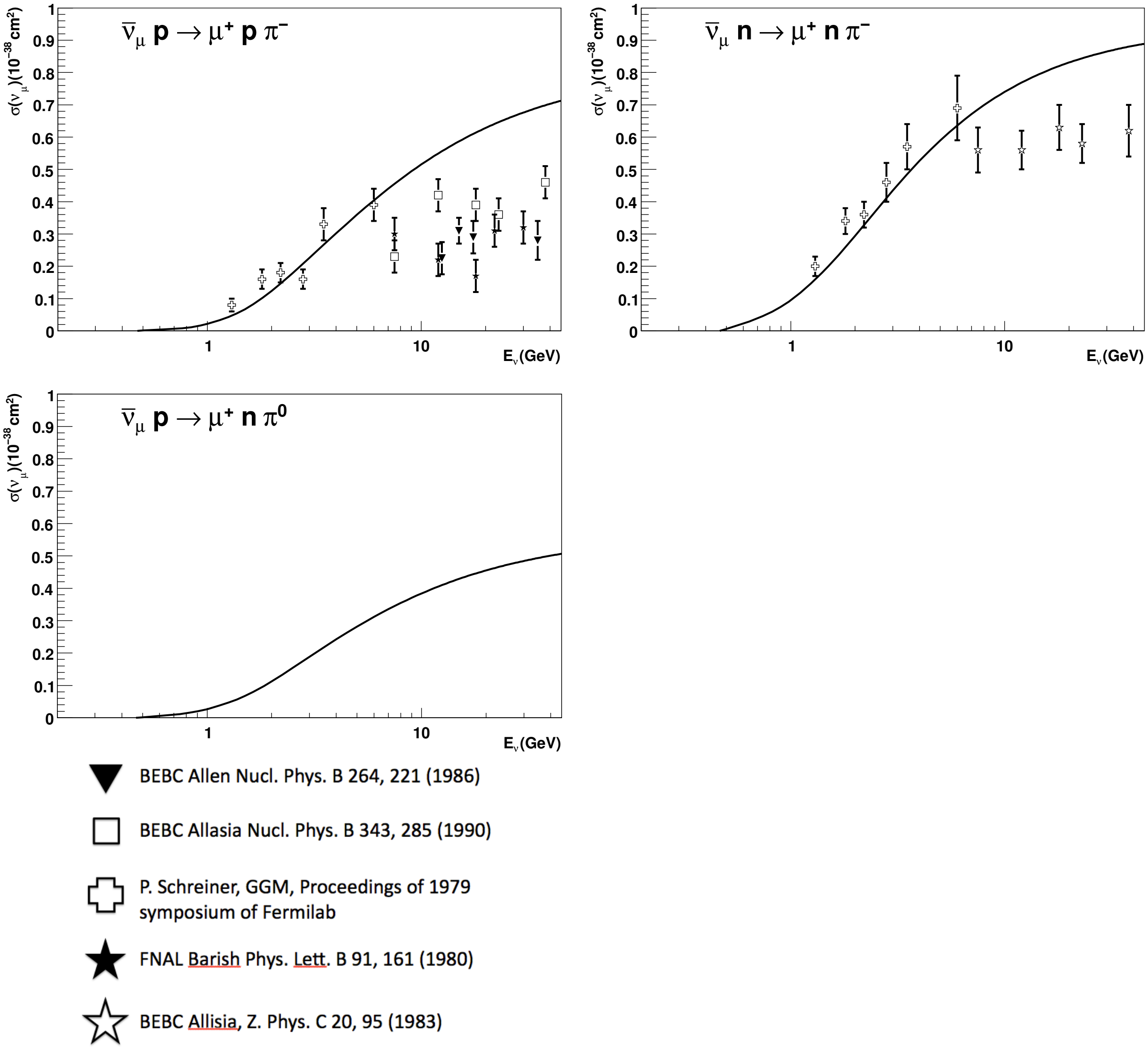

Figure 3.10: Cross section for $\bar{\nu_\mu}$ charged current single pion productions. Solid lines are NEUT calculations, points are experimental data. [136]

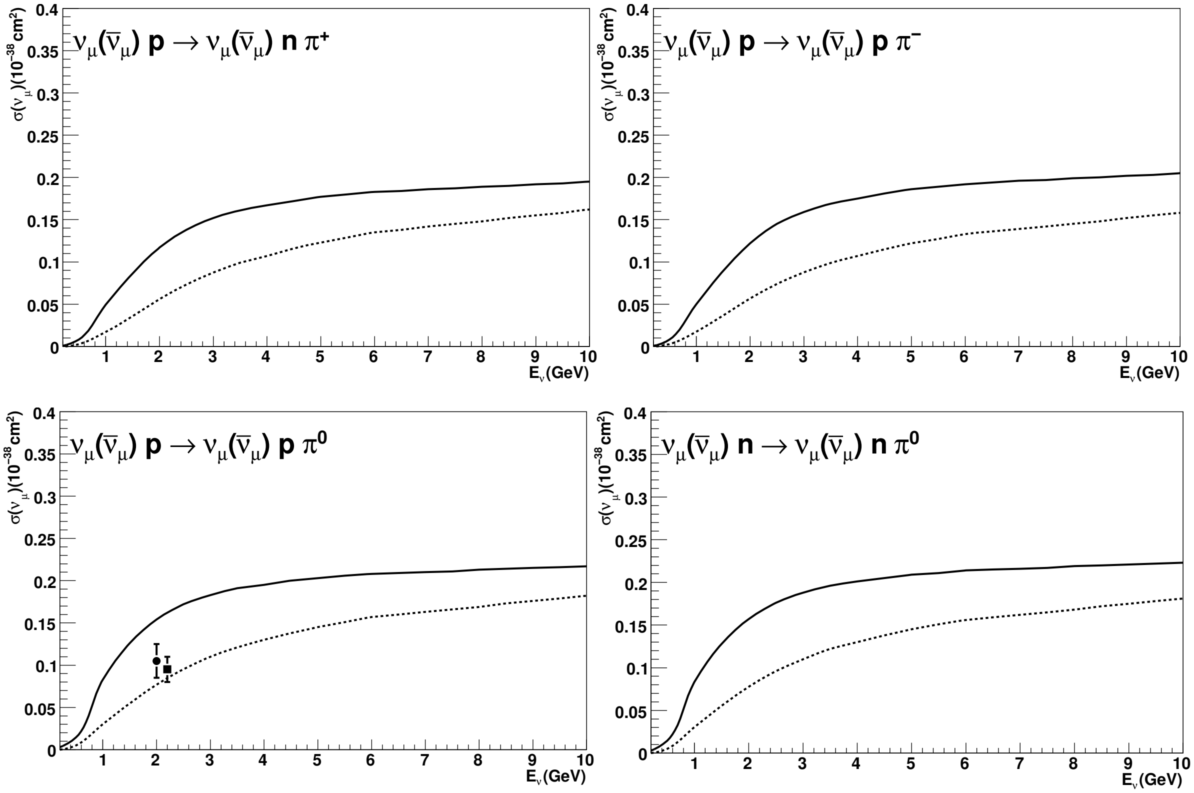

Figure 3.11: Cross section for neutral current single pion productions. Lines are NEUT calculations, with solid lines for ν_μ and dashed line for $\bar{\nu_\mu}$. Points are experimental data taken from [104] (dot) and [105] (square). [136]

3.2.4 Deep Inelastic Scattering

The cross section of charged current deep inelastic scattering in the range of the invariant mass W > 1.3 GeV/c^2 is [106]:

$$\begin{aligned}
\frac{d^2\sigma^{\nu,\bar{\nu}}}{dxdy} &= \frac{G_F^2 M_N E_\nu}{\pi}((1-y+\frac{y^2}{2}+C_1)F_2(x,q^2) \pm y(1-\frac{y}{2}+C_2)xF_3(x,q^2)) \\
C_1 &= \frac{yM_l^2}{4M_N E_\nu x} - \frac{xyM_N}{2E_\nu} - \frac{m_l^2}{4E_\nu^2} - \frac{m_l^2}{2M_N E_\nu x} \\
C_2 &= -\frac{m_l^2}{4M_N E_\nu x}
\end{aligned} \tag{3.14}$$

where $x = -q^2/(2M(E_\nu - E_l))$ and $y = (E_\nu - E_l)/E_\nu$ are Bjorken scaling parameters, M_N is nucleon mass, m_l is outgoing lepton mass, E_ν and E_l are the energy of incoming neutrino and outgoing lepton in the laboratory frame respectively. The nucleon structure functions F_2 and xF_3 are taken from the Parton distribution function (PDF) of GRV98 [107]. The correction given by A. Bodek and U.K. Yang are adopted to use the PDF in lower Q^2 region [108].

In NEUT, the cross section of deep inelastic scattering induced by neutral current interactions are assumed to have relations estimated from experimental results [109] [110].

As the range 1.3<W<2.0 GeV/c^2 overlaps with that in single pion production, $n_\pi \geq 2$ is required in this W region. Therefore, the kinematics of the hadronic system are simulated by two different methods for these two invariant mass ranges:

In the region of 1.3<W<2.0 GeV/c^2, only pions are considered as outgoing mesons. The average pion multiplicity is estimated from the results of Fermilab 15-foot hydrogen bubble chamber experiment [111]:

$$\langle n_\pi \rangle = 0.09 + 1.83 \ln W^2 \tag{3.15}$$

The number of pions in each event is determined with KNO (Koba-Nielsen-Olsen) scaling. The forward-backward asymmetry of pion multiplicity in the hadronic center of mass system is included with the results from BEBC experiment [112]:

$$\frac{n_\pi^F}{n_\pi^B} = \frac{0.35 + 0.41 \ln W^2}{0.5 + 0.09 \ln W^2} \tag{3.16}$$

In the region of W>2.0 GeV/c^2, the kinematics of the hadronic system are calculated by PHYTIA/JETSET [113], which treats π, K, η, and so on.

Cross section of charged current ν_μ and $\bar{\nu_\mu}$ DIS interactions are shown in figure 3.12.

3.2.5 Coherent Pion Production

Coherent pion production is a neutrino interaction with an oxygen nucleus in which one pion is produced and the pion is of the same charge as the incoming weak current. As only a very small amount of momentum is transferred to the oxygen nucleus, the angular distribution of the outgoing leptons and pions are peaked at the forward direction. The modified Rein and Sehgal model [114] is adopted to simulate the interactions.

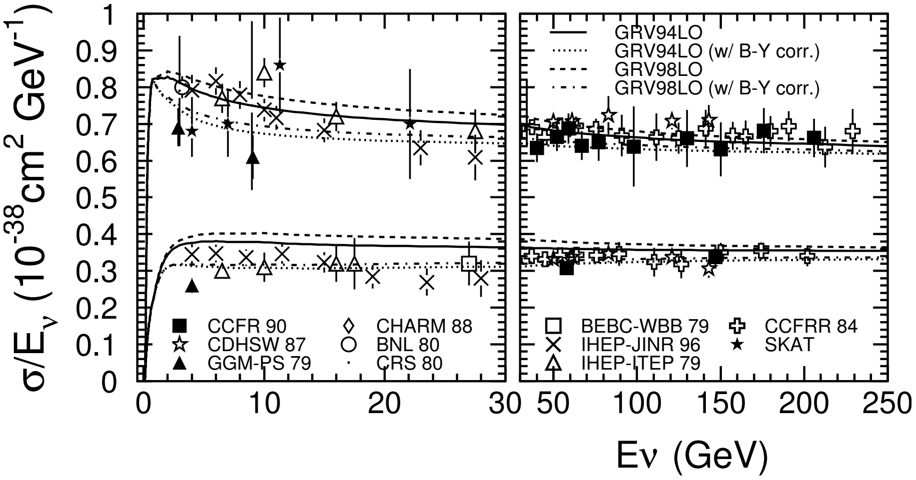

Figure 3.12: Cross section for DIS charged current ν_μ (upper lines and points) and $\bar{\nu_\mu}$ (lower lines and points) interactions. GRV98 is used with Bodek-Yang correction in NEUT, as shown by the dashed lines. The points represent experimental data. [136]

The measurement results by the K2K-SciBar detector set the upper limit of the CC coherent pion production cross section [115]. The upper limit is significantly lower than that predicted by the Rein and Sehgal model. Therefore, the modified Rein and Sehgal model [116] which takes into account the non-vanishing lepton masses in CC interactions is used in NEUT. For ν_μ, the cross section is suppressed by about 25% at 1.3 GeV due to the interference of the axial vector and pseudoscalar (pion-exchange) amplitudes by this modification.

3.2.6 Nuclear Effects

The secondary interactions of mesons and baryons which are produced in the neutrino interactions with nucleons inside the ^{16}O nuclei are also simulated in NEUT. All of the mesons produced within ^{16}O nuclei are tracked from their production points to either their exiting points or their absorption point inside the nuclei. This is simulated for π, K and η by using a cascade model.

As the cross section of pion production for neutrino is large for $E_\nu >$ 1 GeV and the pion-nucleon interaction cross section is also large in this energy region, pion interactions are important. NEUT considers several pion interactions in ^{16}O nuclei: inelastic scattering, charge exchange and absorption.

The probabilities for interactions within a nucleus depends on the nuclear density distribution, so the initial pion production point inside the nucleus where neutrino-nucleus interactions occur, is determined by the Wood-Saxon density distribution [117]. The probabilities for various interactions are calculated at each step of the pion for low and high energy regions respectively.

In NEUT, the calculation of interaction probabilities for pion momenta $p_\pi \leq 500$ MeV/c comes from the model of Salcedo et al. [118]. A tuning with absorption and QE interaction probabilities was done by using $\pi^+ - ^{12}C$ data [119]. As Ashery re-measured the charge exchange cross section and obtained a larger value than before [120], an important correction was made to the Ashery absorption and charge exchange data: the charge exchange data is scaled up and the absorption data is scaled down accordingly. Only absorption probability and QE probability are modified, and a good agreement in charge exchange and reactive channels is also obtained.

As for $p_\pi >$ 500 MeV/c, the energy becomes high enough such that nucleons begin to appear as free particles within the nucleus, $\pi^\pm$ on free proton scattering cross section data are used as inputs to the calculation of interaction probabilities. Tuning was carried out by using $\pi^\pm - ^{12}C$ data. The discrepancy in the absorption channel above $p_\pi =$ 500 MeV/c is fixed by the change in kinematics: more backward scattering which reduces pion momenta to the region where there is a larger absorption probability. Charge exchange and inelastic scattering data above $p_\pi =$ 500 MeV/c are also used to scale the QE probability and charge exchange probability.

Figure 3.13 shows the cross section of $\pi^+ - ^{12}C$ scattering as a function of π^+ momentum before and after tuning.

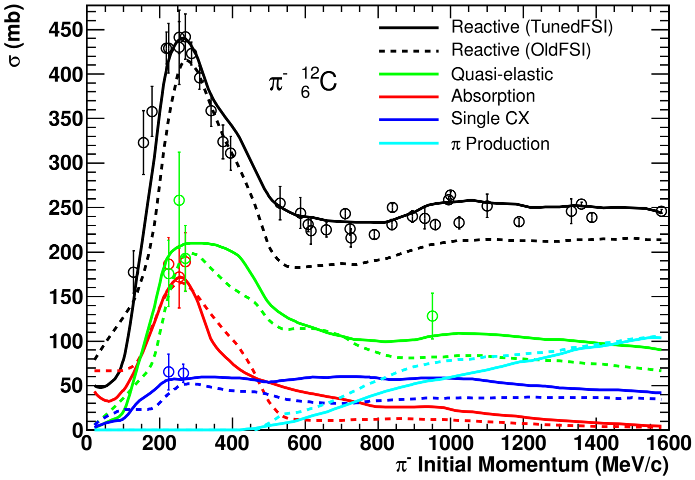

Figure 3.13: Cross section of $\pi^+ - ^{12}C$ scattering as a function of π^+ momentum. Solid lines are NEUT calculation before tuning, dashed lines are NEUT calculation after tuning. Points with error bars are experimental data. [119]

As for kaon interactions, the elastic scattering and charge exchange interaction are considered with the results from the cross sections measured by $K^\pm - N$ scattering experiments [121] [122] [123]. For η interactions, the absorption ($\eta N \rightarrow N^* \rightarrow \pi(\pi)N$) is considered [124].

Nucleon re-scattering inside the oxygen nucleus is also considered with cascade model and the measurements by Bertini et al. [125] in NEUT. Pion production caused by the decay of produced deltas is also taken into account as the isobar production model by Lindenbaum et al. [126].

3.3 Detector Simulation

Produced particles in neutrino interactions are incorporated in a detector simulation code which simulates (1) tracks of the particles, (2) generation and propagation of Cherenkov photons in water, (3) PMT response and readout electronics.

3.3.1 Particle Tracking

The detector simulation was developed based on GEANT3 [127]. Table 3.1 lists the processes which are considered in the simulation program. Hadronic interactions in water are simulated with CALOR package [128], which reproduce pion interactions well including low energy region (about 1 GeV/c). For further lower energy region ($p_\pi \leq 500$ MeV/c), the NEUT cascade model is used.

γ	(e^+, e^-) pair production Compton scattering Photoelectric effect
$e^\pm$	Multiple scattering Ionization and δ-rays production Bremsstrahlung Annihilation of positron Generation of Cherenkov radiation
$\mu^\pm$	Decay in flight Multiple scattering Ionization and δ-rays production Bremsstrahlung Direct (e^+, e^-) pair production Nuclear interaction Generation of Cherenkov radiation
Hadrons	Decay in flight Multiple scattering Ionization and δ-rays production Hadronic interactions Generation of Cherenkov radiation

Table 3.1: List of processes considered in the simulator.

3.3.2 Cherenkov Photon Tracking in Water

Dispersion of the refractive index is taken in account in the simulation. Group velocity

$$v_g = \frac{c}{n(\lambda) - \lambda \frac{\partial n(\lambda)}{\partial \lambda}} \tag{3.17}$$

where c is the speed of light in vacuum, λ is light wavelength, is used as the light velocity in water. The generated Cherenkov light is simulated to be scattered and absorbed in water.

3.3.3 Response of PMT

Charge and timing response of PMTs in considered in the simulation. Detected charge value of each hit PMT is simulated by random numbers distributed as the measured photon distribution in Figure 2.6. The timing distribution depends on the charge. The relation between timing and charge is measured using laster calibration (see next chapter). The timing of each PMT is a random variable distribution as Gaussian with one sigma.

Chapter 4

Calibration

4.1 Detector Calibration

Calibrations of the detector charge and timing information are performed in order to understand and keep high quality of the detector performance. Water transparency is also monitored continuously for the SK detector.

4.1.1 Absolute Gain Calibration

Absolute gain calibration is necessary in order to convert the charge detected by a PMT in pico Coulomb (pC) into the number of photoelectrons (p.e.s). The absolute gain is determined by using the charge distribution of single photoelectron signals.

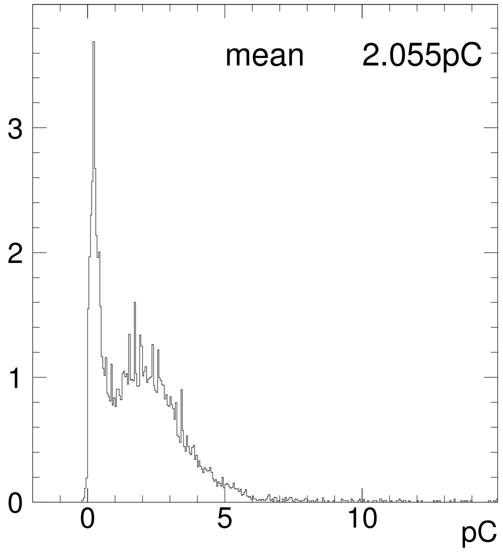

Figure 4.1: The charge distribution of a typical PMT.

The absolute gain was measured by using a gamma-emitting nickel source which gives about 100 photons per gamma emission. The source was placed near the center of the SK tank with coordinates (x = 35.3 cm, y = -70.7 cm, z = 0 cm) with the origin defined as the center of the tank. The nickel source consists of a neutron source put inside nickel material. The nickel source releases gamma rays of energy about 9 MeV which is produced when neutrons are released by spontaneous fission of ^{252}Cf and captured on nickel. The charge distribution of a typical PMT is shown in figure 4.1. The sharp peak near zero is caused by electrons emitted from the photocathode but missing the first dynode, and the peak around 2 pC corresponds to single photoelectrons. The mean value of the 1 p.e. charge distribution is used as a constant to convert PMT charge from pico Coulomb to the number of p.e.s. The constant used for SK-I, SK-II, SK-III and SK-IV are 2.044 pC/p.e., 2.297 pC/p.e., 2.243 pC/p.e. and 2.658 pC/p.e. respectively.

4.1.2 Relative Gain Calibration

The high voltage of each PMT is set to work at approximately uniform gain for all the PMTs in the detector. The uniformity of the gain of all PMTs in the detector is important in terms of determination of momentum without systematic differences.

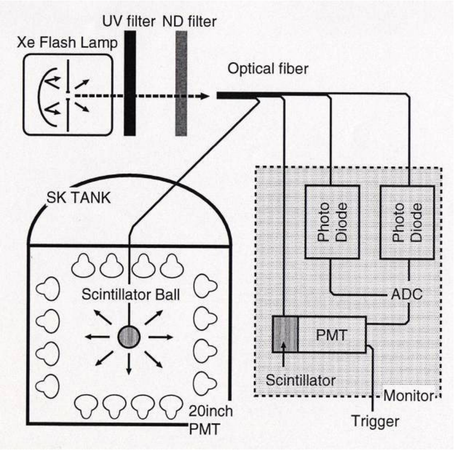

Figure 4.2: Schematic view of the relative gain measurement system.

Figure 4.2 shows the schematic view of the relative gain calibration system. Light from the Xe lamp is passed through an ultraviolet filter and neutral density filter and is injected into a scintillation ball in order to produce uniform diffused light. The other outputs from the Xe lamp are used to monitor the intensity of the Xe light and to make a calibration trigger.

The high voltage of the PMTs are adjusted so that they give the same gains. The relative gain G_i of the i-th PMT is given by:

$$G_i = \frac{Q_i}{Q_0 f(\theta)} \times l_i^2 \times \exp\frac{l_i}{L} \tag{4.1}$$

Q_i is the charge detected by the i-th PMT, l_i is the distance from the light source to the PMT, $f(\theta)$ is the PMT acceptance as a function of the photon incidence angle θ, L is the attenuation length of water and Q_0 is the normalization factor. This measurement is performed with the diffuser ball at several different positions.

The relative gain spread for SK-I is about 7% . From SK-II, the relative gain calibration is improved by using standard PMTs whose gains are adjusted within a few per cents spread relative to one another in advance. The position dependence of the light from the Xe lamp can be reduced by standard PMTs. The relative gain uncertainty was adjusted to 2 % for SK-II, SK-III and SK-IV.

4.1.3 Relative Timing Calibration

The timing of all PMTs must be calibrated so that the event vertices and directions can be reconstructed accurately. The timing response of the PMTs depends on length of cable between each PMT, the process time of electronics and "time walk" (which means different light intensity makes different triggered timing). "Time walk" exists because PMTs with larger charge hits exceed TDC discriminator threshold earlier than those with less charge even if both get photons at the same timing. Hence the timing calibration is to make a correction table for the time walk and the overall process time for each PMT in the detector.

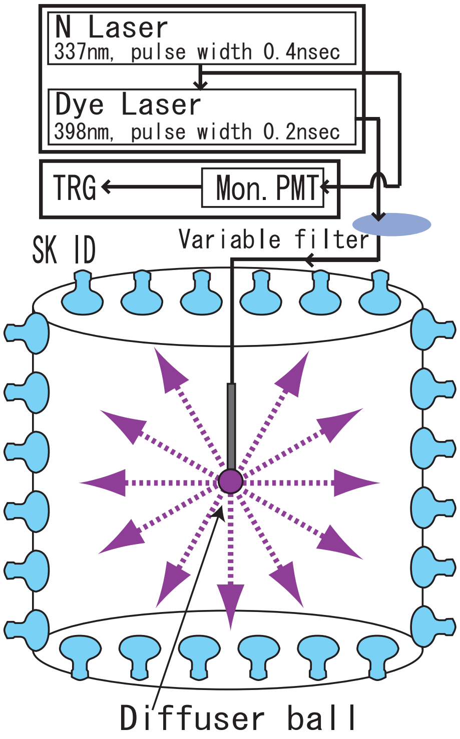

Figure 4.3: Schematic view of the timing measurement system using a laser.

Figure 4.3 shows the schematic view of the timing calibration system. The nitrogen laser pulse is divided into two, one goes to a trigger PMT which makes an external trigger for timing calibration event, the other goes to dye laser module to produce a dye laser pulse. The dye laser pulse which has a wavelength of 398 nm and pulse width 0.2 nsec goes through variable filter which is used to adjust the laser intensity. The dye laser pulse travels through a 70 m optical fiber and then its diffused light is emitted from a diffuser ball. The PMT timing response is measured with various light intensity from 1 p.e. to 250 p.e. by using an adjustable attenuation filter. The result is shown as a scatter plot of timing and charged (TQ-map) in figure 4.4. Each dot represents one measurement. The TQ-map is made for all ID PMTs and is used to correct the timing information.

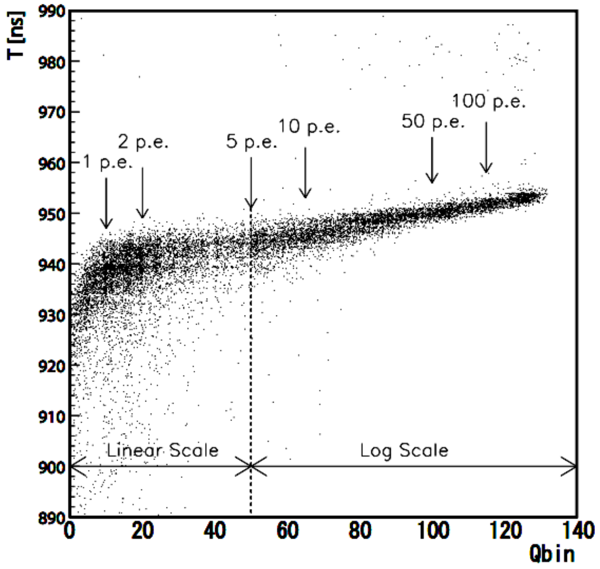

Figure 4.4: TQ-map, a measured two-dimensional plot of timing against charge distribution. Horizontal axis represents charge of each hit and vertical axis represents hit timing.

4.1.4 Water Scattering Measurement with a Laser

Water transparency is important to determine the number of photons arriving PMTs through water in the detector. Water transparency is affected by the combined effect of absorption and scattering of the light. Water attenuation length in water can be described as L = $(\alpha_{abs} + \alpha_{scat.sym} + \alpha_{scat.asym})^{-1}$, where α_{abs}, $\alpha_{scat.sym}$ and $\alpha_{scat.asym}$ are absorption, symmetric scattering and asymmetric scattering coefficients respectively. These coefficients are measured with a N_2 laser and dye laser system which can be tuned to different wavelengths. During SK-III, the wavelengths are 337 nm, 365 nm (371 nm in SK-II), 400 nm and 420 nm. Each laser fires every 1 sec during normal data taking (which is faster than 6 sec of SK-I). In SK-I, there is only one injector, but since SK-II, seven more injectors were installed and there are eight injectors in total now, their positions are shown in figure 4.5.

In SK-IV, the nitrogen/dye laser is replaced with laser diode (LD), as nitrogen laser is unstable and intensity gradually decreases, while LD can be used permanently and the intensity is stable. The nitrogen/dye laser was replaced with LD with wavelengths of 375 nm, 405 nm

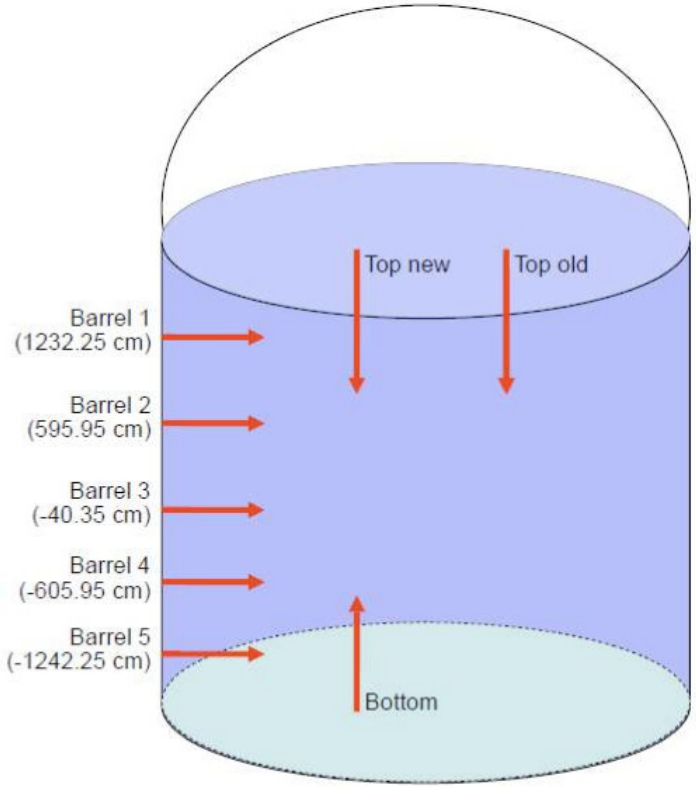

Figure 4.5: Positions of the eight laser light injects in the SK tank. "Top old" refers to the original SK-I light injector which is still being used at the moment.

and 445 nm.

Figure 4.6 shows a typical top laser light injector event. A cluster of hits at the bottom of the tank is due to the unscattered photons from the laser. Other hits at the barrel or top of the tank is due to the dark current or photons scattered in water or reflection by PMTs and black sheet. The number of scattered hits are related to water quality and proportional to light intensity. Figure 4.7 shows the PMT hit timing distributions in each region of the detector for both data and Monte Carlo. The first peaks are characterized by absorption and scattering coefficients while the second peaks are due to the photons reflected by PMTs or black sheets.

In SK-IV, monthly fitting of parameters is carried out. The water coefficient averages and errors on the mean are collected for 3-5 wavelengths as shown in figure 4.8. The coefficients are obtained by fitting shown in figure 4.9.

4.1.5 Water Transparency Measurement with Cosmic Ray Muons

Water transparency is also measured by Cherenkov light from cosmic ray muons passing through the detector. Cosmic ray muons are used as a calibration source because the energy deposit of an energetic muon is almost constant (about 2 MeV/cm). Only vertical downward

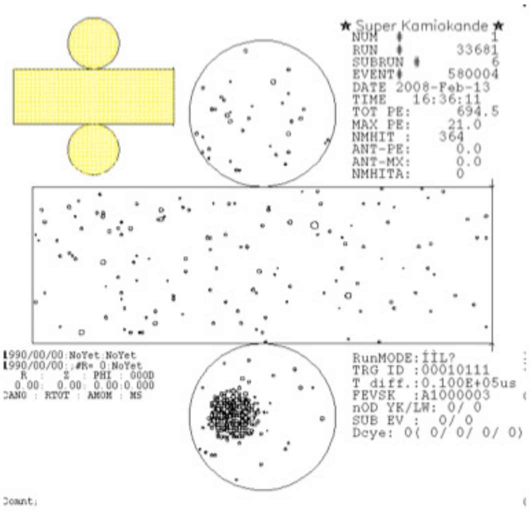

Figure 4.6: Typical laser light injector event.

muons are selected for this measurement. The muon track is reconstructed by connecting the entrance and exit points in the ID. Assuming the light detected by each PMT is not scattered, the detected charge is expressed by:

$$Q = Q_0 \times \frac{f(\theta)}{l} \times \exp - \frac{l}{L} \tag{4.2}$$

where Q_0 is a constant, $f(\theta)$ is the PMT acceptance, l is the photon path length and L is the attenuation length. Figure 4.10 shows the schematic view of the measurement. Figure 4.11 shows $\log(Q \times l/f(\theta))$ as a function of photon pathlengths. The attenuation length is estimated to be 95 m for this data set.

As cosmic ray muons are measured during normal data taking, continuous check of water transparency is possible with this method. Figure 4.12 shows the time variation of the attenuation length of water in the entire period from SK-I to SK-IV (till 20 June 2012).

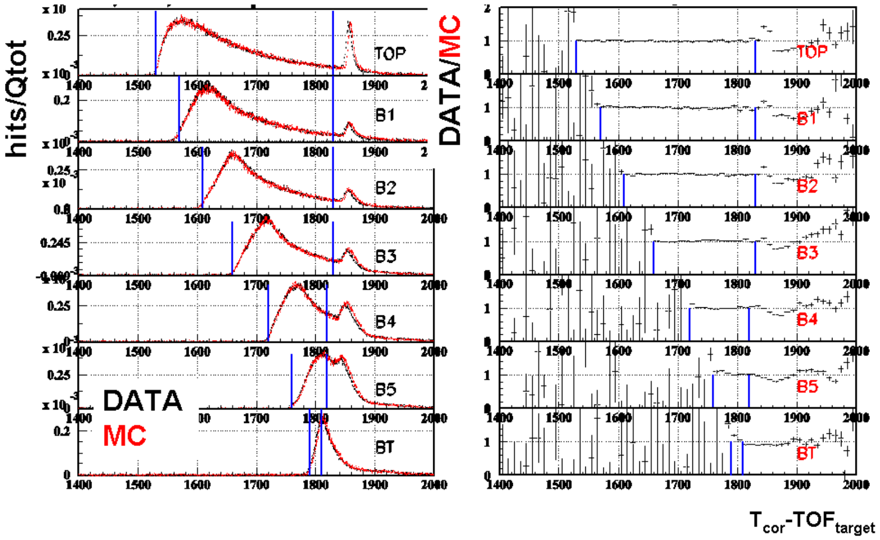

Figure 4.7: PMT hit time distribution in different detector regions for data and Monte Carlo (after tuning by scattering and absorption parameters).

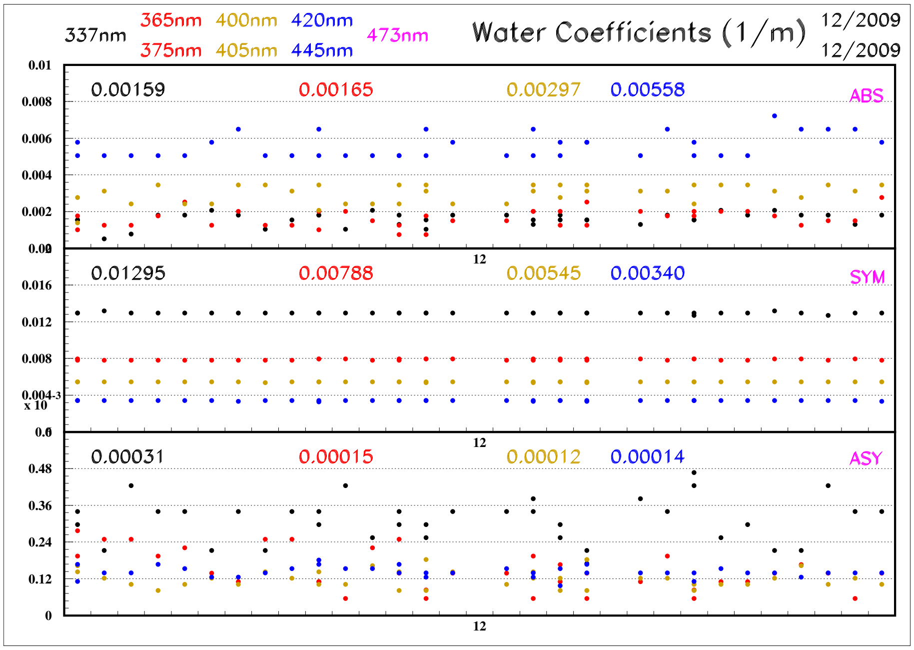

Figure 4.8: Water coefficients for December 2009. The top plot shows absorption, the middle plot shows symmetric scattering and the bottom plot shows asymmetric scattering. From these data, the average and error on the mean are calculated. The averages for 337 nm, 375 nm, 405 nm and 445 nm are shown by the numbers on the plots respectively.

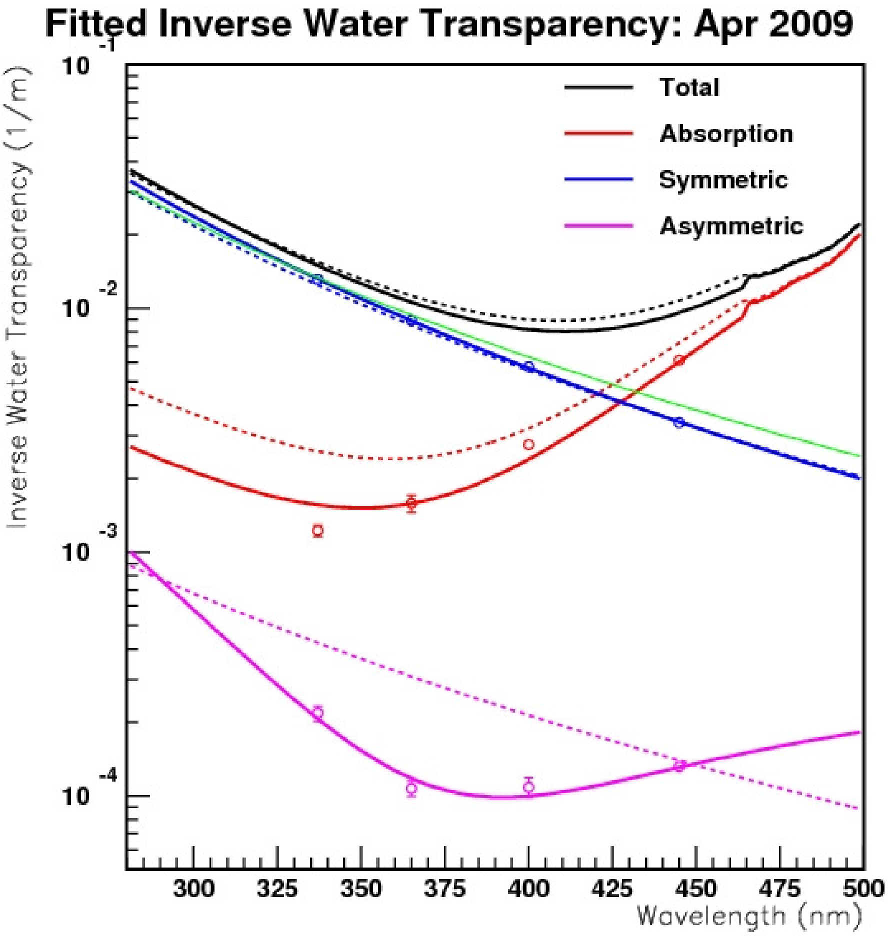

Figure 4.9: A example of fitting. Fitted water coefficient functions for Apr 2009. The solid lines show the fitting in SK4 and the dashed lines show the SK3 functions. Points are coefficient averages and error bars are the error on the mean.

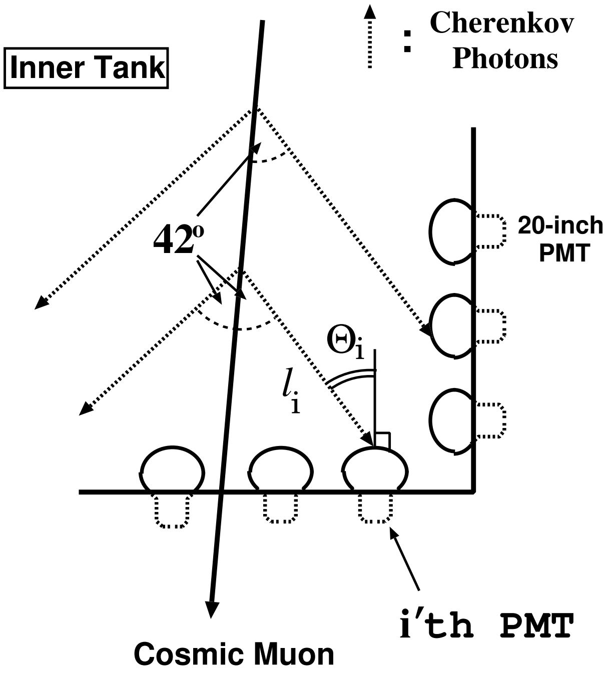

Figure 4.10: Schematic view of the attenuation length measurement with vertically penetrating cosmic ray muons. Arrows from the muon track (solid line) show the trajectories of Cherenkov photons. l_i is the flight length of the Cherenkov photons detected by the i-th PMT.

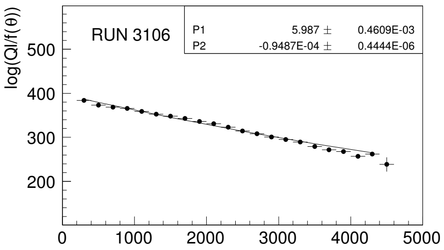

Figure 4.11: Effective observed charge for through-going muons as a function of photon path-lengths (l), where Q is the detected charge and $f(\theta)$ is the PMT acceptance.

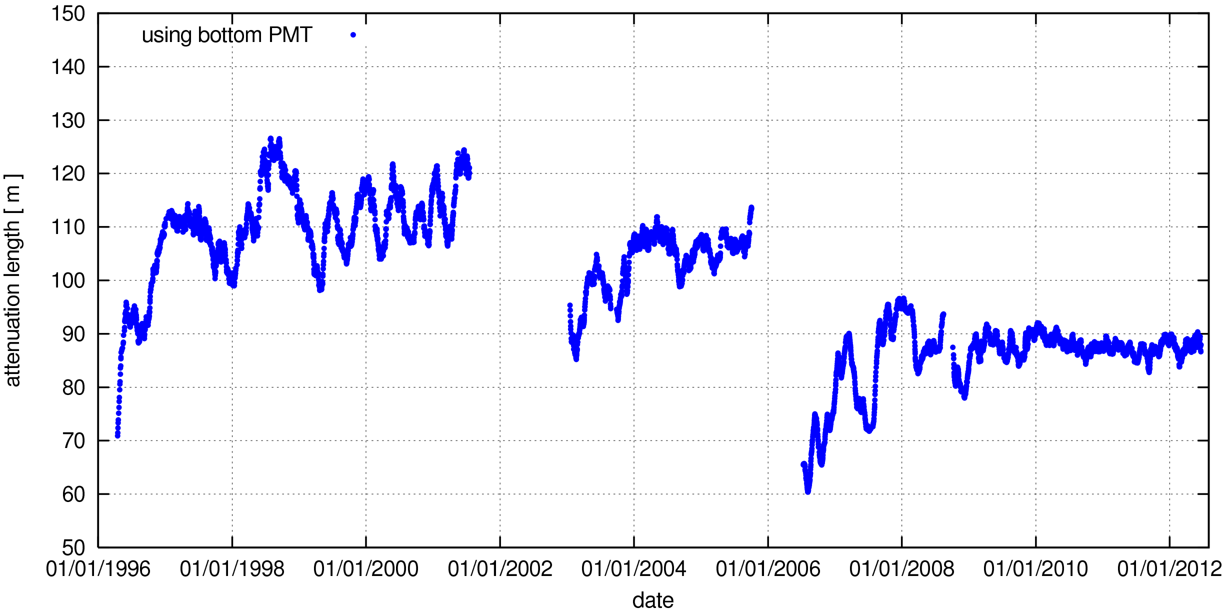

Figure 4.12: Time variation of water attenuation lengths for SK-I, SK-II, SK-III and SK-IV.

4.2 Energy Calibration

Momentum of a particle is determined based on the charge information of PMTs. The accuracy of energy scale is important for atmospheric neutrino analysis. Four independent calibration sources are used for the energy scale calibration in momentum range from a few tens of MeV/c to about 10 GeV/c:

- Track range of high energy stopping muons ($1 \sim 10$ GeV/c)
- Cherenkov angle of low energy stopping muons ($200 \sim 500$ MeV/c)
- Invariant mass of π^0 produced by neutrino interactions (~ 130 MeV/c)
- Momentum of decay electron (~ 50 MeV/c)

The accuracy of the absolute energy scale is checked by comparing data and Monte Carlo simulation for all of the above calibration source. Time variation check of energy scale, detector uniformity of energy scale and uncertainty on energy scale are also estimated.

4.2.1 High Energy Stopping Muons

Momentum of high energy muons can be determined by the track lengths which are approximately proportional to the momentum. The stopping cosmic ray muon track lengths can be estimated by the distance between the entering position at the detector and the vertex position of the subsequent decay electron. Resolutions for stopping muon entering position and decay electron vertexes are better than 50 cm. Selection criteria for stopping muons are listed in the following:

1. Entering position is on the top wall of the detector
2. Direction of the stopping muon is downward ($\cos\theta > 0.94$)
3. One decay electron event is detected
4. Reconstructed range of the muon track is $7 < L < 30$ m.

Criteria (1) and (2) require down-going muon event entering the detector from the top of the detector. Momentum loss per cm is about 2.3 MeV/c. Data and MC agree within 0.7%, 1.1%, 2.0% and 2.2% for SK-I, SK-II, SK-III and SK-IV respectively.

4.2.2 Low Energy Stopping Muons

For low energy stopping muons (< 400 MeV/c), momentum can be estimated by Cherenkov angle which depends on momentum as shown below. The Cherenkov angle of charged particles can be expressed as following:

$$\cos\theta_C = \frac{1}{n\beta} = \frac{1}{n}\sqrt{1 + \frac{m^2}{p^2}} \tag{4.3}$$

where θ_C, n, β, m and p are Cherenkov angle, refraction index of water, v/c, mass and momentum respectively.

Selection criteria for low energy stopping muons are:

1. Entering point is at the top wall of the detector
2. Direction of the stopping muon is downward ($\cos\theta > 0.9$)
3. One decay electron event is detected
4. Total number of p.e.s in ID is less than 1500 p.e.s (750 p.e.s for SK-II)

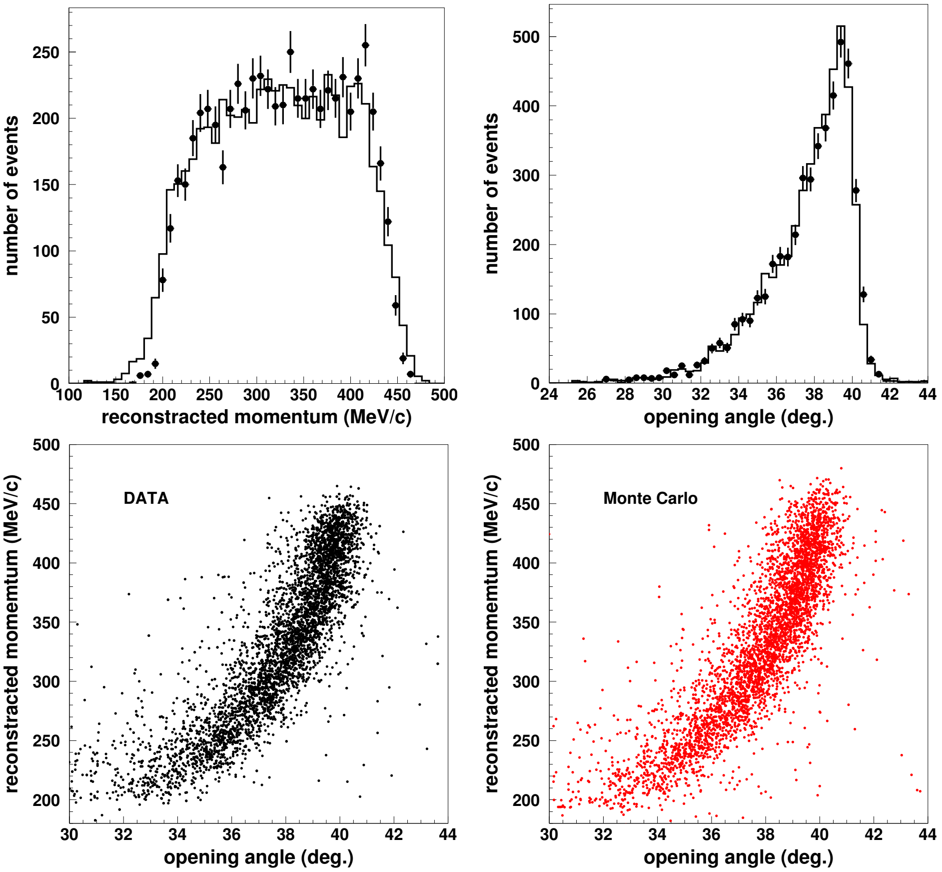

Figure 4.13: Upper left panel shows the reconstructed momentum distribution $P_{p.e.}$ for data (circles with error bars) and MC (solid line). Upper right panel shows the reconstructed opening angle distribution, also for data and MC. Lower two panels show the correlation between reconstructed Cherenkov opening anlge θ_C and the reconstructed momentum $P_{p.e.}$ for data (left) and MC (right). All distributions are made from SK-II.

Criterion (4) selects low momentum stopping muons with momentum < 380 MeV/c. In figure 4.13, the upper left panel shows the reconstructed momentum distribution, upper right panel shows the reconstructed opening angle θ_C distribution. In the lower two panels, the scatter plots of reconstructed momentum and the opening angle θ_C is shown for both data and MC. The momentum and opening angle correlation can be seen in these two scatter plots. Figure 4.14 shows the averaged $P_{p.e.}/P_\theta$ (where P_θ is the momentum estimated with θ_C) and the ratio of MC to data as a function of $P(\theta)$. They agree within 0.7%, 1.3%, 2.1% and 2.1% for SK-I, SK-II, SK-III and SK-IV respectively.

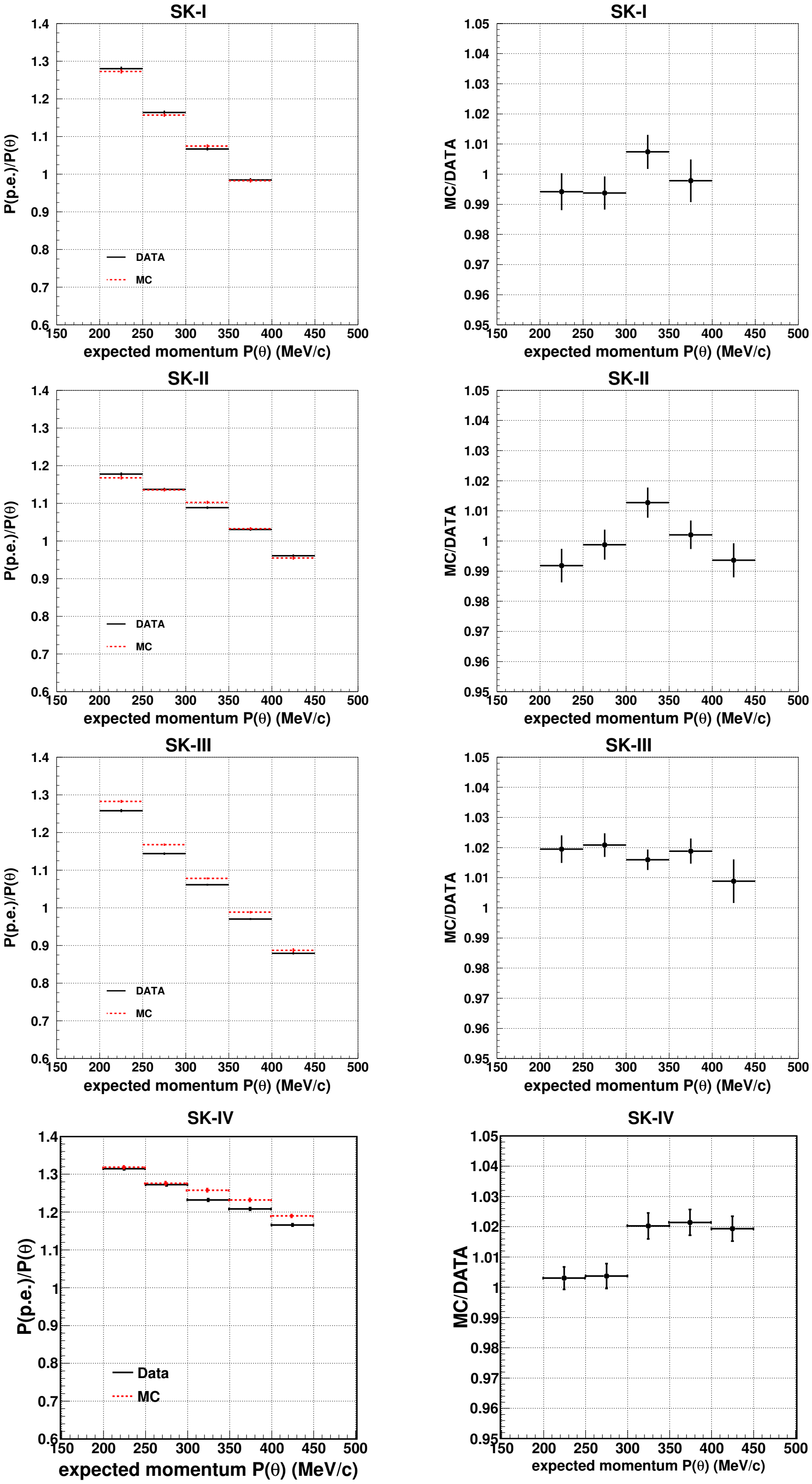

Figure 4.14: Left panels show the averaged ratio of momentum derived from charge to that derived from the opening angle ($P_{p.e.}$ / P_θ) as a function of reconstructed momentum P(θ) for data (solid line) and MC (dashed line). Right panels show the ratio of MC events to data in the corresponding left panel.

4.2.3 Neutrino Induced π^0 Events

π^0 events are produced by interactions of atmospheric neutrinos in the detector. As a π^0 decays into two γ rays immediately, the invariant mass of π^0 can be calculated with the reconstructed momentum of the two γ rays ($P_{\gamma 1}$and $P_{\gamma 2}$):

$$M_{\pi^0} = \sqrt{2P_{\gamma 1}P_{\gamma 2}(1-\cos\theta)} \tag{4.4}$$

where θ is the opening angle between the two γ rays. Neutral current π^0 events are selected from atmospheric neutrino event sample by the following criteria:

1. Two Cherenkov rings are recognized and both are identified as electron-like
2. Electron from muon decay is not detected
3. Vertex position is reconstructed within the fiducial volume ($>$ 2 m away from the ID wall)

Criterion (2) rejects contamination by $\pi^+\pi^0$ or $\mu^\pm\pi^0$ events. Figure 4.15 shows the invariant mass distribution of π^0 events compared with the prediction by MC. The peak positions are fitted by Gaussian distribution. The peak positions of data and MC agree within 0.7%, 1.3%, 0.3% and 1.7% for SK-I, SK-II, SK-III and SK-IV respectively.

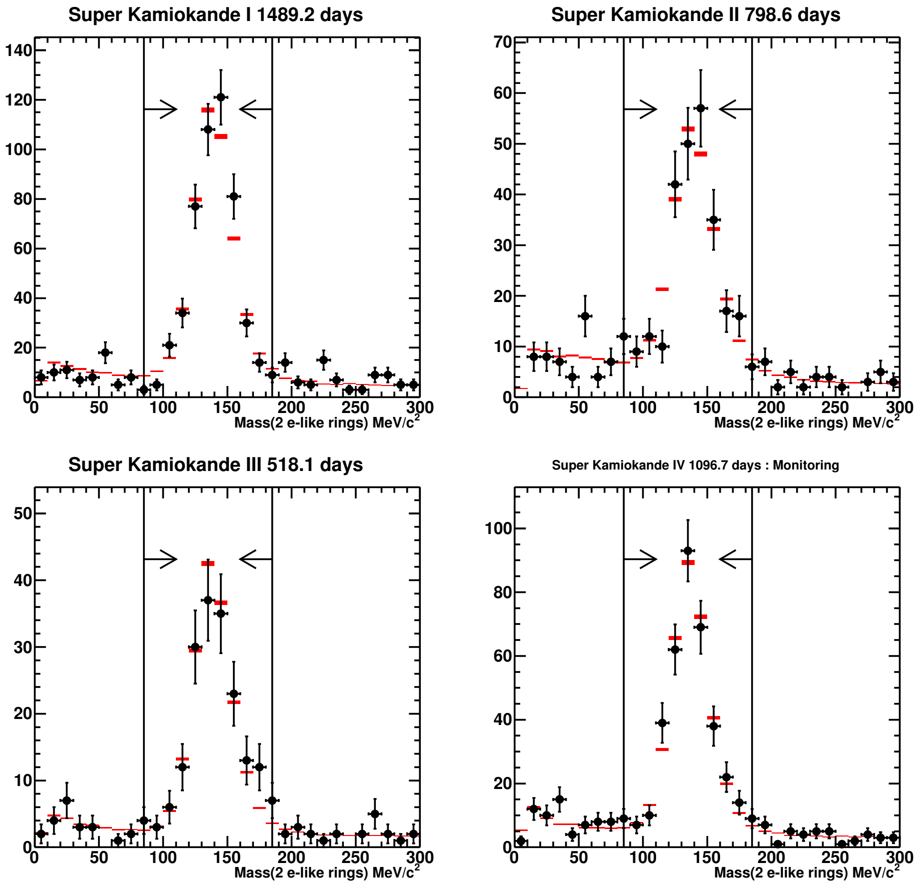

Figure 4.15: Invariant mass distribution of neutrino induced π^0 events of observed data (dot) and MC (boxes). MC are normalized to the livetime of the observed data.

4.2.4 Decay Electrons

Large number of electron events are produced in the detector from the decay of stopping cosmic ray muons. Decay electrons' energy spectrum is well understood and the spectrum spreads around 50 MeV. Selection criteria for decay electrons is listed in the following:

1. Time interval from a stopping muon is 2.0 sec to 8.0 sec
2. Number of PMT hits in a 50 nsec window is > 60 (30 for SK-II)
3. Goodness of vertex fit is greater than 0.5
4. Vertex position is reconstructed within the fiducial volume (> 2 m away from the ID wall)

Criterion (1) is for efficient timing for decay electron tagging. Criterion (2) rejects $\sim$6 MeV γ rays from μ^- capture on nucleons. In simulation, μ^+/μ^- ratio of 1.37 [132] and the effect of μ^- capture by oxygen nuclei are considered. The vertex fitter developed for low energy neutrino observations (such as solar and supernova neutrinos) is used [133]. Figure 4.16 shows the overlaid momentum spectra for decay electrons for data and MC. The mean values of data spectrum agree with MC within 0.6%, 1.6%, 0.8% and 1.6% for SK-I, SK-II, SK-III and SK-IV respectively.

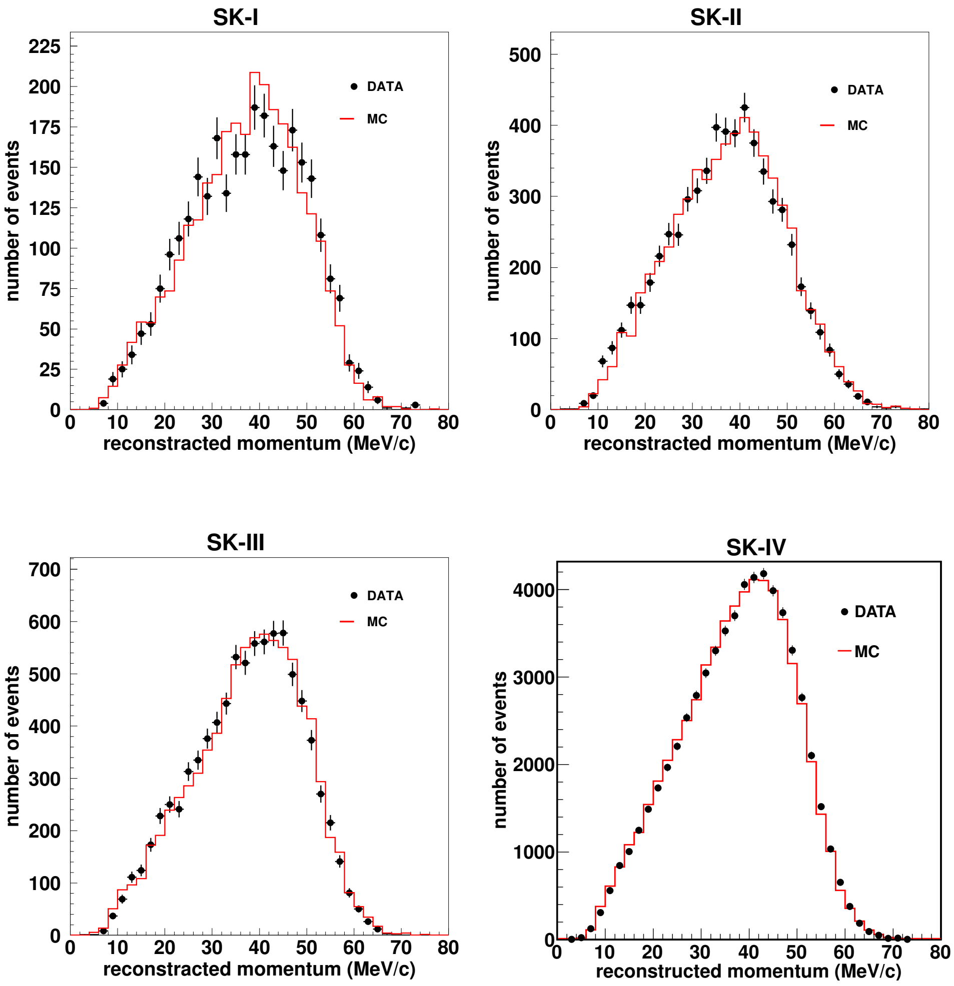

Figure 4.16: Momentum distribution of decay electrons of data (dot) and MC (solid line) for each SK period. MC events are normalized by number of observed data.

4.2.5 Summary of the Energy Scale Calibration

The absolute energy scale is checked by various methods for different momentum ranges (from a few tens of MeV/c to about 10 GeV/c). Figure 4.17 summarizes the absolute energy calibrations.The uncertainty of absolute energy scale is estimated to be less than 0.88%, 0.55%, 1.79% and 2.19% for SK-I, SK-II, SK-III and SK-IV respectively.

4.2.6 Time Variation of Energy Scale

Stability of the energy scale is confirmed with stopping muons and decay electrons. During the reconstruction process, particle momentum is corrected with water transparency. Figure 4.18 shows the time variation of the mean value of momentum/range for stopping muons and the mean value of momentum for decay electrons. As water quality is worse and not stable in SK-III, the stability of energy scale is slightly worse than other SK periods. The fluctuation of absolute energy scale is estimated to be less than 0.74%, 1.60%, 2.08% and 0.39% for SK-I, SK-II, SK-III and SK-IV respectively. SK-IV has smallest time variation among all other SK periods. The main reasons are the treatment of scattered light calculation as a function of time in momentum reconstruction is improved and the measurement of PMT gain correction factor as a function of time in momentum reconstruction is improved.

By adding the energy scale uncertainties discussed in the previous section to the time variation uncertainties in quadrature, the final energy scale uncertainties for SK-I, SK-II, SK-III and SK-IV are estimated to be 1.1%, 1.7%, 2.7% and 2.3% respectively.

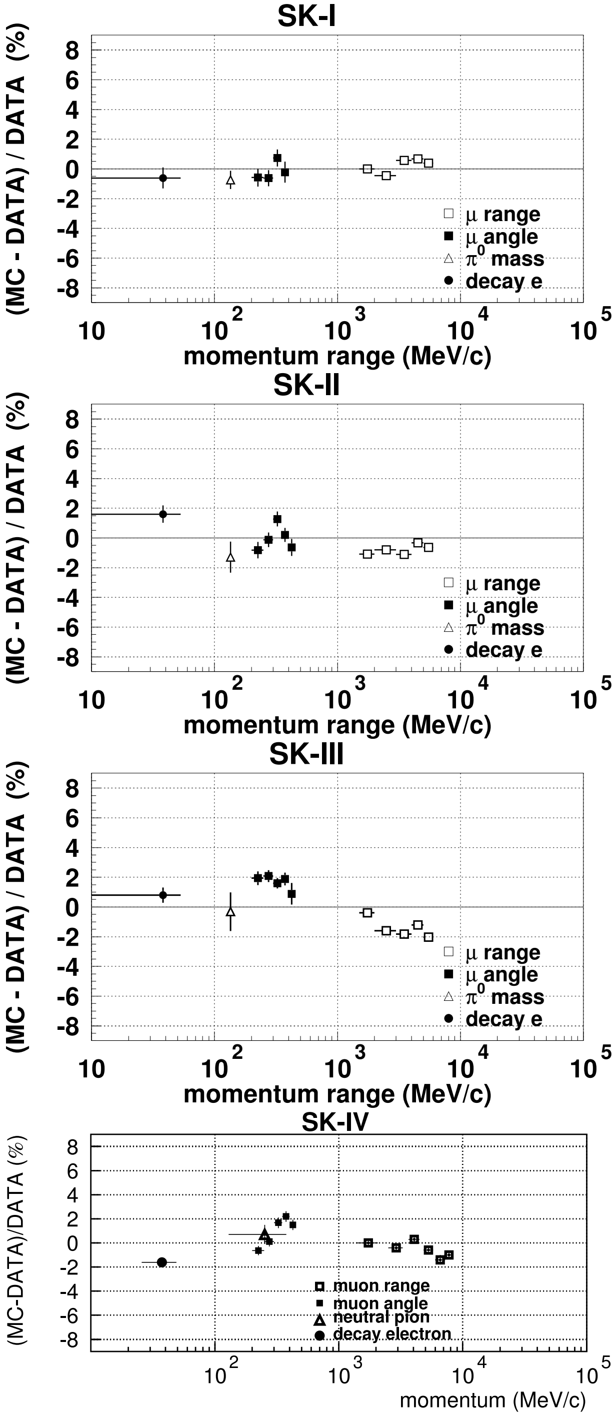

Figure 4.17: Summary of absolute energy scale calibration for each SK period. Horizontal axis shows the momentum range and vertical axis shows the deviation of data from MC predictions.

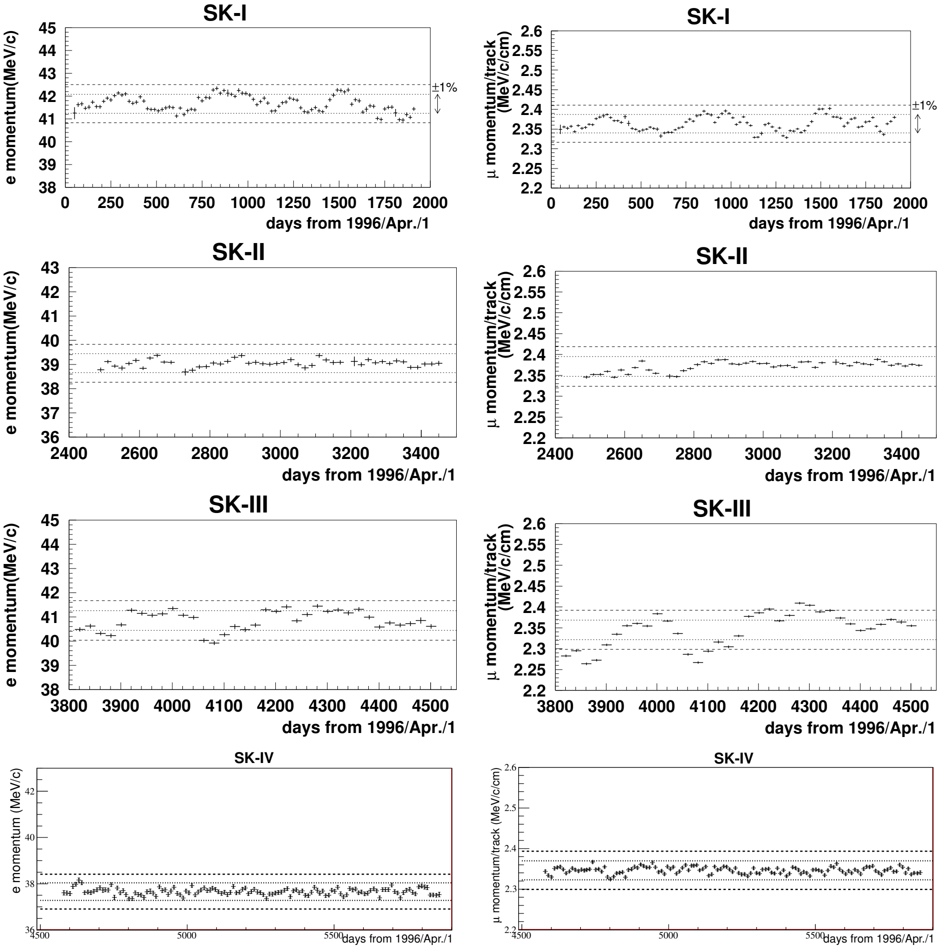

Figure 4.18: Time variation of the reconstructed momentum of decay electrons (left) and the averaged momentum/range of stopping muons (right) as a function of elapsed days from 1 April 1996 for each SK period. Dotted (dashed) lines show ±1% (±2%) from mean value in each SK period.

4.2.7 Detector Uniformity of Energy Scale

Uniformity of the detector is measured with decay electrons from cosmic ray muons. Decay electron vertexes distribute uniformly in the fiducial volume and the momentum distribution is almost uniform, making them a good calibration source to check the detector uniformity. In order to take into account the muon polarization, only electrons whose direction is perpendicular to the parent muon direction is used. This condition is $-0.25 < \cos\Theta_{e\leftrightarrow\mu} < 0.25$, where $\cos\Theta_{e\leftrightarrow\mu}$ is the opening angle between the decay electron and the muon directions. Figure 4.19 shows the ratio of averaged momentum of decay electrons between MC and data. These figures show that the detector gains are uniform within ±0.6%, ±0.6%, ±1.3% and ±1.3% for SK-I, SK-II, SK-III and SK-IV respectively.

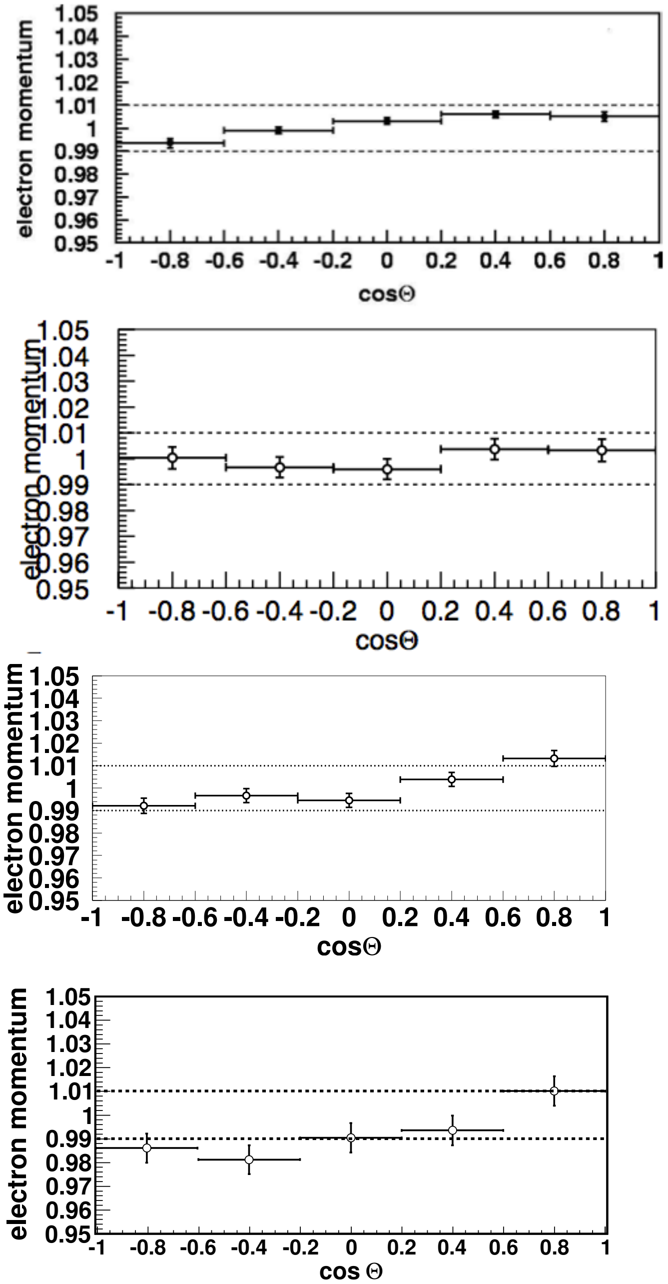

Figure 4.19: Uniformity of the detector gain as a function of zenith angle for each SK period. From top to bottom: SK-I, SK-II, SK-III and SK-IV. Y-axis is the ratio of MC to data of the averaged momentum of decay-electrons.

Chapter 5

Data Selection

About 10^6 high energy and low energy trigger events are collected per day in the SK detector. Most events are background events such as cosmic rays and gamma rays from radioactivity. An efficient data selection is essential to select neutrino events from such a large amount of data.

Atmospheric neutrino events observed in SK are categorized to 3 types:

- Fully contained (FC)
- Partially contained (PC)
- Upward-going muon (UPMU)

For FC and PC event types, the neutrino interacts in the fiducial volume of the detector (at least 2 m away from the ID wall). If all the energy of the generated (charged) particles is deposited inside the ID, the event is classified as FC. If high energy muon exits the ID and deposits its energy in the OD, the event is classified as PC.

UPMU events are high energy muons produced by neutrino interactions with the rock surrounding the detector. As these events cannot be distinguished from cosmic rays which travel in downward direction, only muons traveling in the upward direction through the detector are selected. UPMU events are divided into two types: for events which come to rest in the detector, they are categorized as upward stopping muons, and those which traverse through the entire detector volume, they are categorized as upward through-going muons.

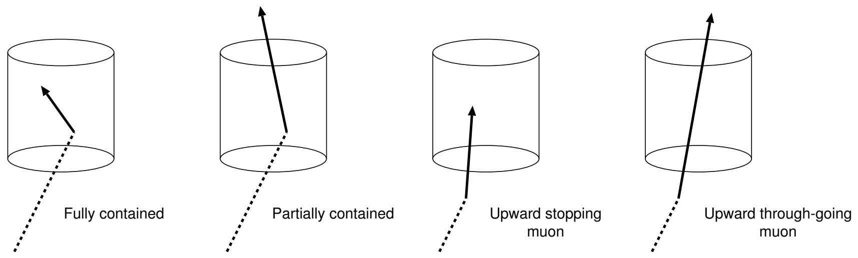

Figure 5.1: Schematic view of observed atmospheric neutrino in SK.

Figure 5.1 shows the schematic view of the above three event types. The neutrino mean energies are ~1 GeV for FC, ~10 GeV for PC and stopping UPMU, ~100 GeV through-going UPMU, as shown in Figure 5.2.

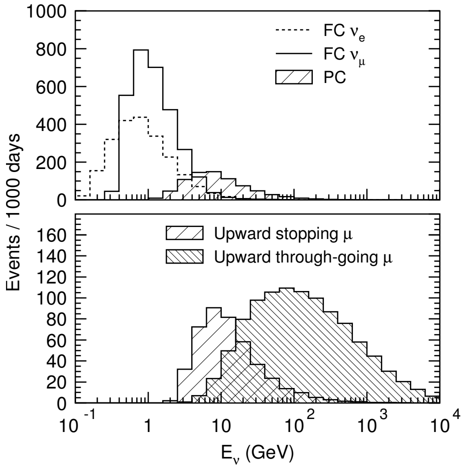

Figure 5.2: Expected neutrino spectra of different event categories.

The event selection process consists of reduction and reconstruction processes.

Reduction is to select neutrino events by removing background events in the collected data. There are several background observed in SK:

- Cosmic ray through-going muons which pass through the detector
- Cosmic ray stopping muons which enter and stop inside the detector
- Cosmic ray corner clipping muons which pass through the corner of the detector
- Flasher event which is caused by PMT emitting light through internal discharge
- Low energy events such as gamma ray from radioactivities

The above background events can be removed during the reduction processes.

5.1 Reduction for Fully Contained Events

FC events are distinguished from PC events by using the number of OD hit PMTs in the highest charge cluster. The data reduction process consists of five steps for FC.

As the number of ID PMTs in SK-II period was only about half of that in other SK periods, the SK-II selection criteria related to the number of hits and observed charge of ID PMTs is different from that in other SK periods.

5.1.1 First Reduction

An event passes the first reduction if it fulfils the following criteria:

1. $PE_{total} > 200$ p.e.s (100 p.e.s for SK-II)
   where PE_{total} is the number of total p.e.s observed by the ID PMTs

2. $NHITA_{800} \leq 50$ or OD trigger is off
   where $NHITA_{800}$ is the number of hit OD PMTs in a fixed 800 nsec time window from 500 nsec to 1300 nsec before and after the trigger timing.

Criterion (1) rejects low energy background events due to radioactivities. 200 p.e.s (100 p.e.s for SK-II) corresponds to 22 MeV/c of electron momentum. As events which have visible energy below 30 MeV are not used in the analysis, this cut can be applied without loss of neutrino events. Criterion (2) removes cosmic ray muon events.

FC 1st reduction reduces the number of events from 10^6 events/day to ~3000 events/day.

5.1.2 Second Reduction

Selection criteria for the second reduction are:

1. $NHITA_{800} \leq 25$ (30 for SK-IV) or $PE_{total} > 100{,}000$ p.e.s (50,000 p.e.s for SK-II) or OD trigger is off

2. $PE_{max}/PE_{300} < 0.5$
   where PE_{max} is the maximum number of p.e.s observed by an ID PMT. PE_{300} is the maximum number of total p.e.s observed by ID PMTs in a sliding 300 nsec time window.

Note that the cut criteria for $NHITA_{800}$ is changed in SK-IV, as the electronics was changed to QBEE and the high voltage gain has changed. The cut criteria is tuned so that it agrees with SK-III.

Criterion (1) rejects cosmic ray muons by a tighter threshold than the first reduction. Figure 5.3 shows the $NHITA_{800}$ distributions for data, FC Monte Carlo simulation events whose vertices are 2 m away from the ID wall, and the FC final sample events.

Criterion (2) rejects low energy events and electrical noise events, which have one larger hit signal from one single PMT. Figure 5.4 shows the PE_{max}/PE_{300} distributions.

Event rate becomes ~200 events/day after the FC 2nd reduction.

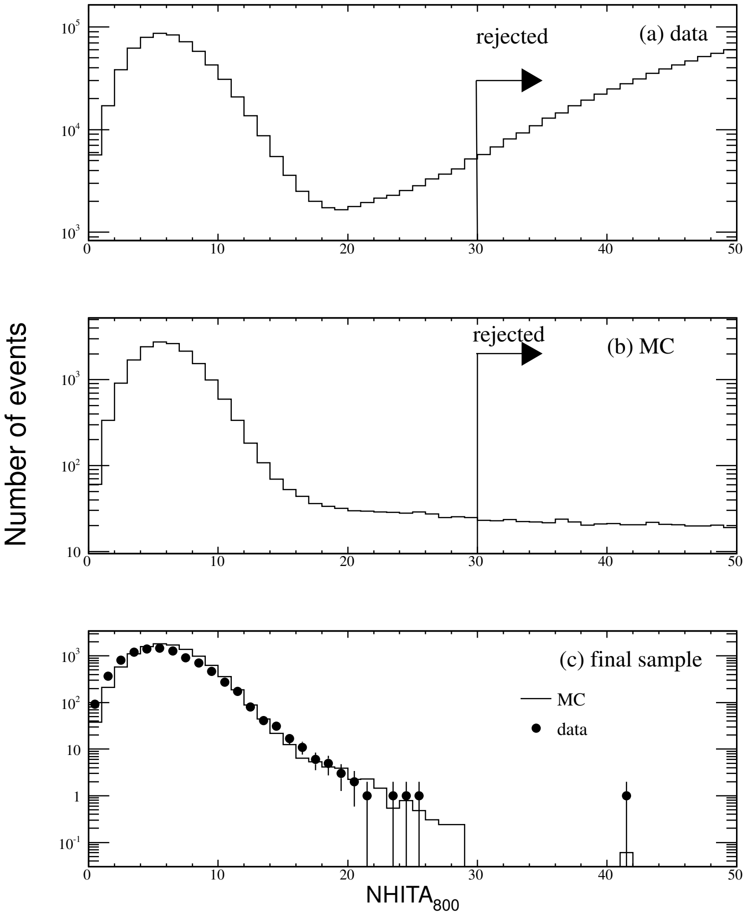

Figure 5.3: FC 2nd reduction criterion (1). NHITA$_{800}$ distributions for SK-IV. (a) shows the observed data after the FC 1st reduction. (b) shows FC Monte Carlo events after FC 1st reduction. (c) shows the final samples for both data and Monte Carlo events, where the number of Monte Carlo events is normalized to that of the data. The arrow at NHITA$_{800}$ = 30 is the cut in the FC 2nd reduction for SK-IV. In Figure (c), there are some events remaining at region NHITA$_{800}$ > 30, they are events with either PE$_{total}$ > 100,000 p.e.s or OD trigger off or both.

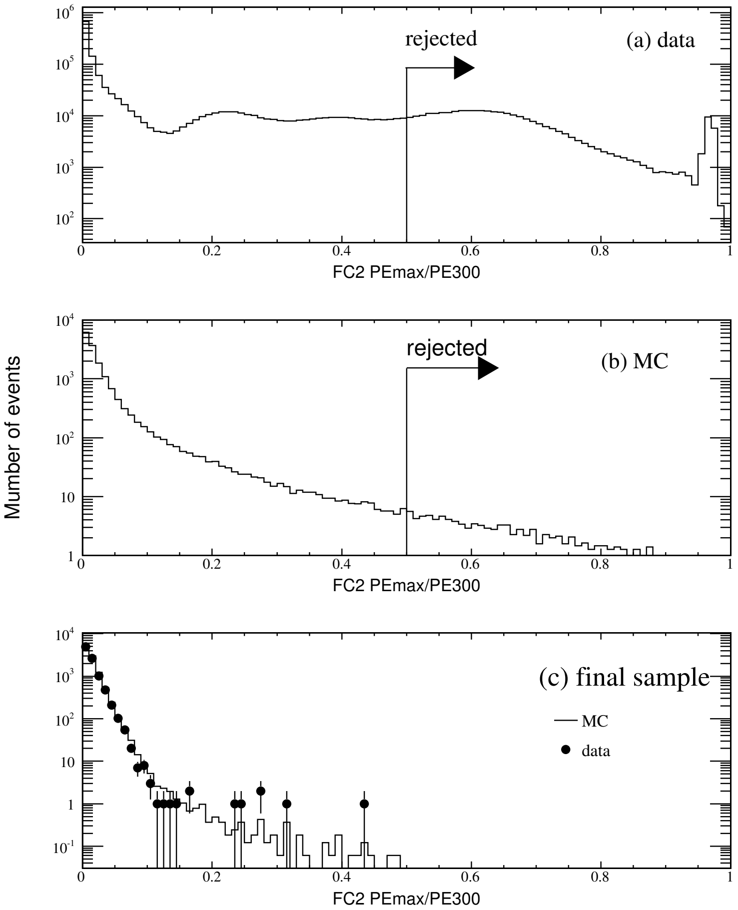

Figure 5.4: FC 2nd reduction criterion (2). $\mathrm{PE}_{max}/\mathrm{PE}_{300}$ distributions for SK-IV. (a) shows the data after the FC 1st reduction. (b) shows FC Monte Carlo events after the FC 1st reduction. (c) shows the final samples for the data and Monte Carlo events, where the number of Monte Carlo events is normalized to that of the data. Selection criteria is shown by arrows in the plots.

5.1.3 Third Reduction

Remaining background events, which consists of mostly noise events and cosmic ray muons which have a small number of OD hits, are rejected by the following cuts.

Through-going Muon Cut

Through-going muons are very energetic and deposit a lot of charge in the ID. In order to eliminate these events, a through-going muon fitter is applied when there are more than 1000 PMTs detecting more than 230 photoelectrons (p.e.s) (for each of them). This fitter finds the through-going muon entering point at the ID by using the earliest hit PMT with some neighbouring hit PMTs. The exiting point at which the through-going muon goes out of the ID is defined as the centre of the saturated ID PMTs. The goodness of through-going muon fit is defined as:

$$goodness = \frac{1}{\sum_i \frac{1}{\sigma_i^2}} \times \sum_i \frac{1}{\sigma_i^2} \exp - \frac{(t_i - T_i)^2}{2(1.5 \times \sigma_i)^2} \tag{5.1}$$

where t_i and σ_i are the observed hit time of the i-th PMT and its resolution, T_i is the hit time estimated from the muon entering time and its track.

The cut criteria is:

1. goodness of through-going muon fit > 0.75

2. NHITA$_{in} \geq 10$ or NHITA$_{out} \geq 10$
where NHITA$_{in}$ (NHITA$_{out}$) is the number of OD hit PMTs located within 8 m from the entrance (exit) point in a fixed 800 nsec time window.

Events that satisfy the above criteria are rejected. Figure 5.5 shows the scatter plots of NHITA$_{in}$ and NHITA$_{out}$ satisfying criterion (1) for data and Monte Carlo after the 2nd reduction and the final samples.

Stopping Muon Cut

For the rejection of stopping muons, a stopping muon fitter is applied to find the entrance point with similar way as the through-going muon fit. The goodness is defined by equation (5.1).

Events fulfilling the following criterion are rejected as stopping muons:

1. NHITA$_{in} \geq 10$ if goodness of stopping muon fit ≥ 0
   where NHITA$_{in}$ is the number of OD hit PMTs located within 8 m from the entrance point in a fixed 800 nsec time window.

   or NHITA$_{in} \geq 5$ if goodness of stopping muon fit > 0.5 (additional criterion for SK-I)

The direction of muon is reconstructed so that the total number of p.e.s inside the cone within half opening angle 42° is maximized. Figure 5.6 shows NHITA$_{in}$ distributions for the data and Monte Carlo after the 2nd reduction and their final samples.

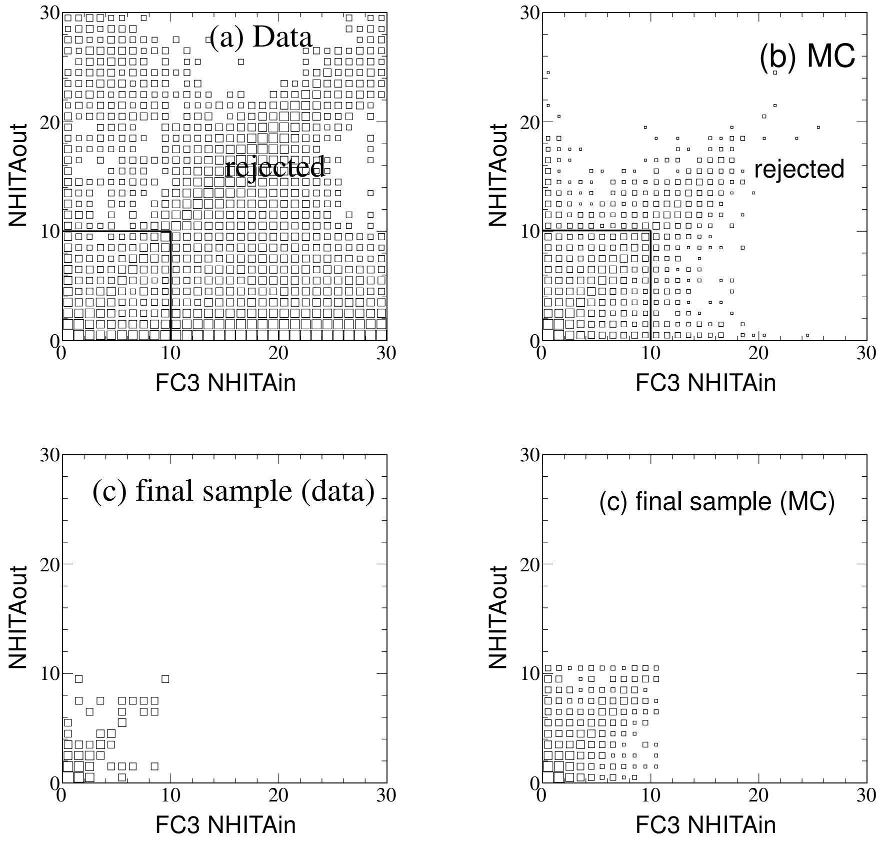

Figure 5.5: FC 3rd reduction criterion (1) for through-going muons cut. Scatter plot of the number of hit OD PMTs within 8 m of the entering point NHITA$_{in}$ (x-axis) and the exiting point NHITA$_{out}$ (y-axis) for SK-IV. (a) shows the data after the FC 2nd reduction. (b) shows FC Monte Carlo events after the FC 2nd reduction. (c) shows the final samples for data (bottom left) and Monte Carlo (bottom right) events. Selection criteria are indicted by solid lines.

Cable Hole Muons

On top of the SK detector tank, there are twelve cable holes for the signal and high voltage supply cables to pass through. There is no OD PMT installed at the positions of these holes as shown in Figure 5.7. When cosmic ray muons enter through these holes, they enter the ID region without hitting the OD PMTs, and these events may be misidentified as contained neutrino events because there is no OD signal.

In order to avoid such mis-identification, veto counters (2 m × 2.5 m plastic scintillation counters) were installed in April, 1997 for four out of the twelve cable holes. A schematic view of the cable hole and the veto counter is shown in figure 5.8. The rejection criteria with the veto counters are:

1. One veto counter hit

2. $L_{veto} < 4$ m
   where L_{veto} is the distance from the cable hole to the reconstructed vertex.

Beside the above veto counter cut, a new cut is introduced in SK-IV reduction. For cable holes which do not have veto counters, the following cut is added:

1. Goodness of stopping muon fit ≥ 0.4
2. $PE_{total} > 4000$
   where PE_{total} is the total number of p.e.s observed by the ID PMTs
3. travel in downward direction ($\cos\theta <$ -0.6)
4. $L_{veto} < 2.5$ m
   where L_{veto} is the distance from the cable hole to the reconstructed vertex.

The inefficiency (of wrongly rejecting neutrino events) is less than 0.01%.

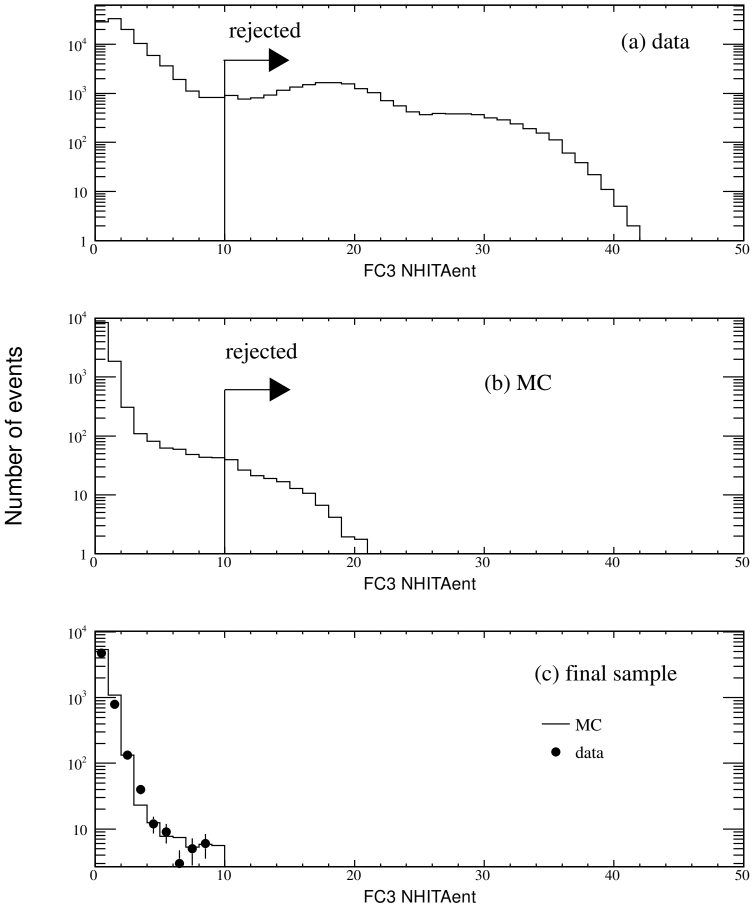

Figure 5.6: FC 3rd reduction criterion for stopping muon cut. Number of hit OD PMTs near the entrance points of muons (NHITA_{in}) for SK-IV. (a) shows the data after the FC 2nd reduction. (b) shows FC Monte Carlo events after the FC 2nd reduction. (c) shows final samples for both data and Monte Carlo. The selection criteria are shown by arrows.

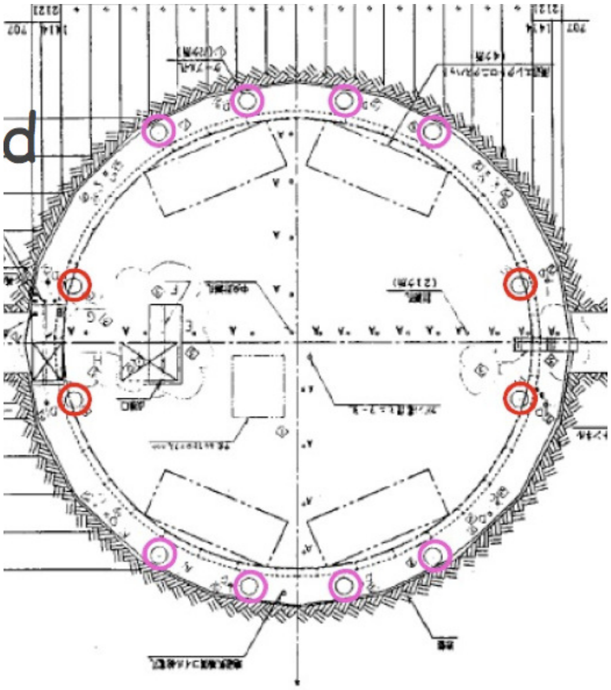

Figure 5.7: Positions of the twelve cable holes. The 4 red circles indicate cable holes installed with veto counters.

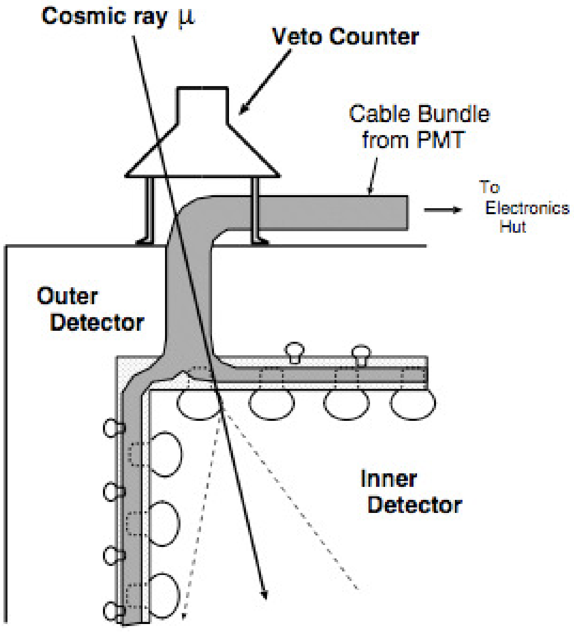

Figure 5.8: Schematic view of a cable hole muon and a veto counter.

Flasher Event Cut

Flasher events usually have a broader hit timing distribution when compared with that of neutrino events. The following cut criteria is applied by using this feature:
For SK-I:

$\text{NMIN}_{100} \geq 15$
or $\text{NMIN}_{100} \geq 10$ if the number of hit ID PMTs ≤ 800

For SK-II to SK-IV:

$\text{NMIN}_{100} \geq 20$
where NMIN_{100} is the minimum number of hit ID PMTs in a sliding 100 nsec time window from +300 nsec to +800 nsec after the trigger.

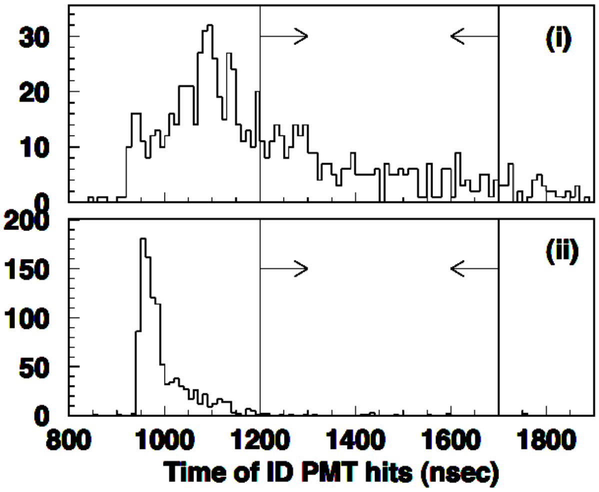

Figure 5.9: FC 3rd reduction criterion for flasher event cut. The timing distributions of (i) a typical flasher event and (ii) a typical FC neutrino event. The arrows show the time window for counting NMIN_{100}.

Figure 5.9 shows the timing distributions of (i) a typical flasher event and (ii) a typical FC neutrino event. Figure 5.10 shows NMIN_{100} distributions for data and FC Monte Carlo after the 2nd reduction and their final samples.

Accidental Coincidence Events Cut

Accidental coincidence occurs when a low every event form a trigger and a cosmic ray muon events follows in the same trigger gate. These events are not rejected in the former reduction steps because there is no OD activities on the trigger timing and there is a large number of total p.e.s in the ID caused by muons. Accidental coincidence event are removed by the following cuts:

1. $\mathrm{NHITA}_{off} \geq 20$
   where NHITA_{off} is the number of hit OD PMTs in a fixed 500 nsec off-timing window from +400 nsec to +900 nsec after the trigger timing.

2. $\mathrm{PE}_{off} > 5000$ p.e.s (2500 p.e.s for SK-II)
   where PE_{off} is the number of p.e.s observed by ID PMTs in a fixed 500 nsec off-timing window from +400 nsec to +900 nsec.

Low Energy Events Cut

This is the rejection of the remaining low energy events such as the decay of radioisotopes and electrical noise. Events satisfying the following criteria are removed:

1. $\mathrm{NHIT}_{50} < 50$ (25 for SK-II)
   where NHIT_{50} is the number of hit ID PMTs in a sliding 50 nsec time window.
   NHIT_{50} is counted after subtracting the time of flight (TOF) of each observed photon assuming all photons are generated at the same point. The vertex is defined as the position at which the timing residual distribution peaks. $\mathrm{NHIT}_{50} = 50$ corresponds to visible energy of 9 MeV, and this cut is low enough to keep efficiency for contained neutrino events which is $\mathrm{E}_{vis} > 30$ MeV.

After the FC third reduction, the event rate is ∼45 events/day.

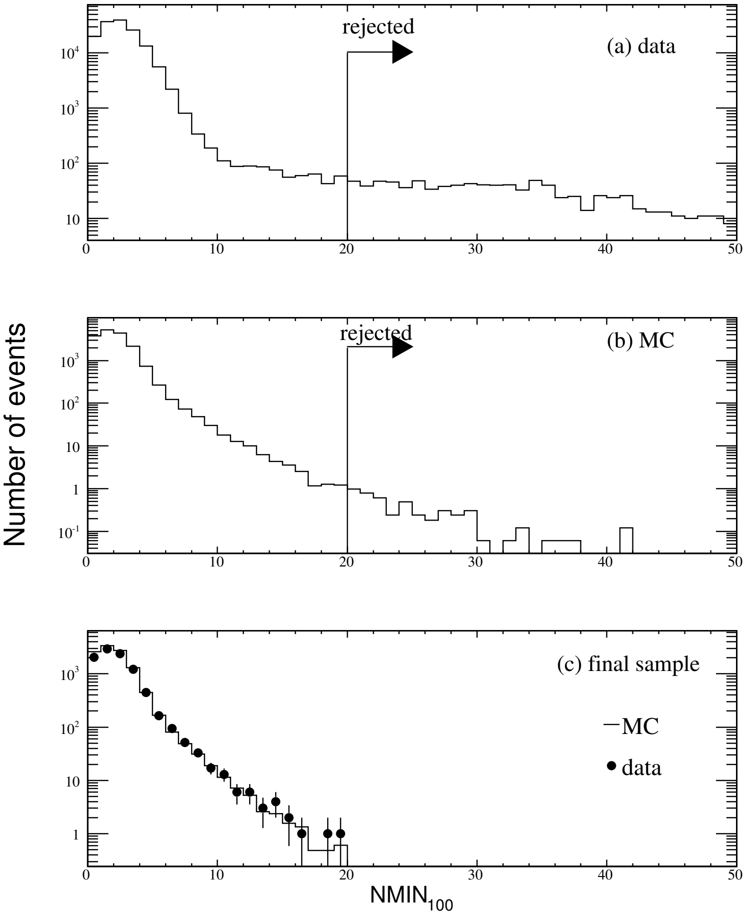

Figure 5.10: FC 3rd reduction criterion for flasher event cut. NMIN_{100} distributions for SK-IV. (a) shows the data after the FC 2nd reduction. (b) shows FC Monte Carlo events after the FC 2nd reduction. (c) shows the final samples for data and the Monte Carlo events, in which the number of Monte Carlo events is normalized to that of the data. Selection criteria are shown by arrows.

5.1.4 Fourth Reduction

In the FC fourth reduction, a pattern matching algorithm is used to remove the remaining flasher events. Flasher events usually repeat with similar hit patterns in the detector, which are not likely to be caused by neutrinos.

Algorithm of pattern matching:

1. Divide the ID wall into 1450 patches for 2m × 2m squares.
2. Computer the correlation factor by comparing the total charge in each patch of two events (A and B). The correlation is defined as follows:

   $$r = \frac{1}{N}\sum_i \frac{(Q_i^A - \langle Q^A\rangle) \times (Q_i^B - \langle Q^B\rangle)}{\sigma_A \times \sigma_B} \tag{5.2}$$

   where N is the number of patches , $\langle Q^{A(B)}\rangle$ and $\sigma_{A(B)}$ are the average charge and its standard deviation for event A and event B respectively.
3. Calculate the distance (DIST_{max}) between the PMTs which have maximum pulse heights in the two events respectively.
4. If $\mathrm{DIST}_{max} < 75$ cm, an offset value is added to r by $r = r + 0.15$.
5. If r exceeds the threshold (r_{th})m events A and B are determined to be matched events, where r_{th} is defined as:

   $$r{>}r_{th} = 0.168 \times \log_{10}((PE_{tot}^A + PE_{tot}^B)/2.) + 0.130 \tag{5.3}$$

   where PE_{tot} is the total number of p.e.s observed in the ID.
6. Repeat the above calculation over 10,000 events around the target event and count the number of matched events.
7. Remove events with large correlation factor r with several events.

The event rate after FC fourth reduction is ∼18 events/day.

5.1.5 Fifth Reduction

The final rejection cut is applied by several criteria specialized for each background source.

Invisible Muon Cut

If a cosmic ray muon has momentum less than the Cherenkov threshold and there is subsequent decay electron observed, the event may be misidentified as a neutrino event. This kind of events is characterized by a low energy signal from a decay electron in the ID and a signal in the OD before the trigger timing. Events fulfilling the following cut are rejected as invisible muons:

1. PE_{tot} <1000 p.e.s (500 p.e.s for SK-II)
   where PE_{tot} is the total number of p.e.s observed in the ID.

2. $\mathrm{NHITAC}_{early} + \mathrm{NHITAC}_{500} \geq 10$ if $\mathrm{DIST}_{clust} < 500$ cm
   $\mathrm{NHITAC}_{early} > 9$ otherwise
   where NHITAC_{early} is the maximum number of hit PMTs in the OD hit cluster in a sliding 200 nsec time window from -8800 nsec to -100 nsec,
   NHITAC_{500} is the number of hit PMTs in the OD hit cluster in a fixed 500 nsec time window from -100 nsec to $+400$ nsec,
   DIST_{clust} is the distance between two OD hit clusters which are used for NHITAC_{early} and NHITAC_{500}

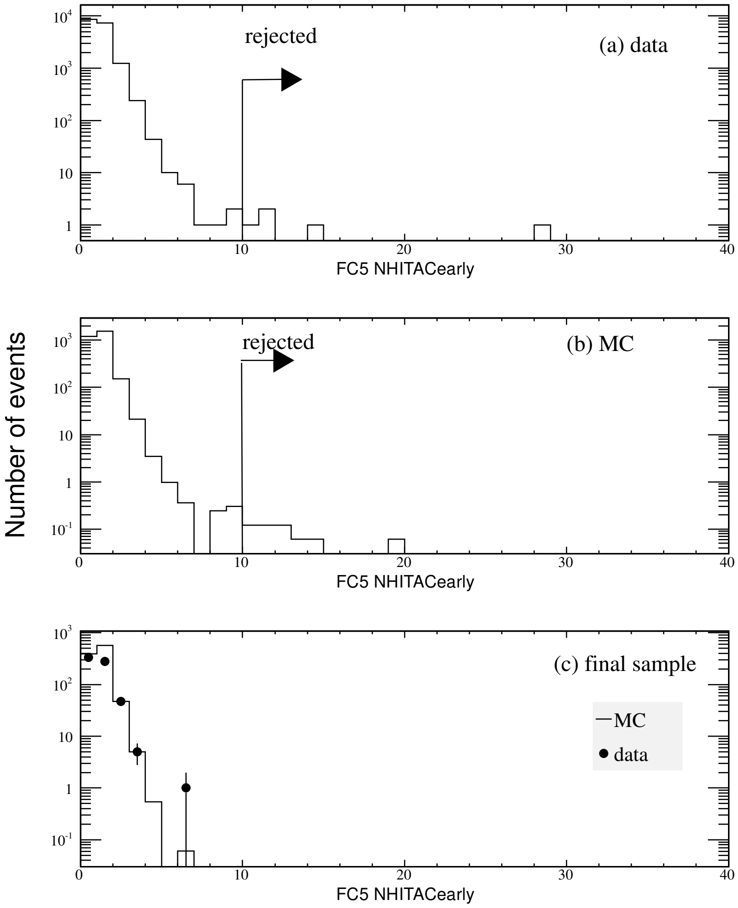

Figure 5.11: FC 5th reduction invisible muon cut. NHITAC_{early} distribution satisfying the criteria $\mathrm{PE}_{tot} < 1000$ p.e.s and $\mathrm{DIST}_{clust} > 500$ cm for SK-IV. (a) shows the data after FC 4th reduction. (b) shows the FC Monte Carlo events after FC 4th reduction. (c) shows the final samples for data and Monte Carlo events whose number is normalized to that of the data. The Selection criteria is shown by the arrows.

Figure 5.11 shows the NHITAC$_{early}$ distribution, satisfying criterion (1) and DIST$_{clust}$ $>$ 500 cm, for the data and Monte Carlo after the FC 4th reduction and the final samples.

Coincidence Muon Cut

The remaining accident coincidence muon events which are not rejected in the third reduction accident coincidence events cut are removed by the following cuts:

1. PE$_{500}$ $<$ 300 p.e.s (150 p.e.s for SK-II)
   where PE$_{500}$ is the total number of p.e.s observed in the ID in a fixed 500 nsec time window from -100 nsec to $+400$ nsec.

2. PE$_{late}$ $\geq$ 20 p.e.s
   where PE$_{late}$ is the maximum number of hit OD PMTs in a 200 nsec sliding time window from $+400$ nsec to $+1600$ nsec.

Figure 5.12 shows the PE$_{late}$ distribution satisfying criterion (2) for data and Monte Carlo after the 4th reduction and their final samples.

Long-tail Flasher Cut

This flasher cut is stricter than the one in FC 3rd reduction.
Events satisfying the following criteria are removed as flasher events:

1. NMIN$_{100}$ $\geq$ 6 if goodness of Point-fit $<$ 0.4
   where NMIN$_{100}$ is the minimum number of hit ID PMTs in a sliding 100 nsec time window from $+300$ nsec to $+800$ nsec.

   From SK-II onwards, additional cuts are added:

2. NMIN$_{100}$ $\leq$ 5 if the goodness of Point-fit $<$ 0.3
   (Point-fit would be explained in Section 5.4.1)

After FC fifth reduction, FC event rate becomes $\sim$16 events/day.

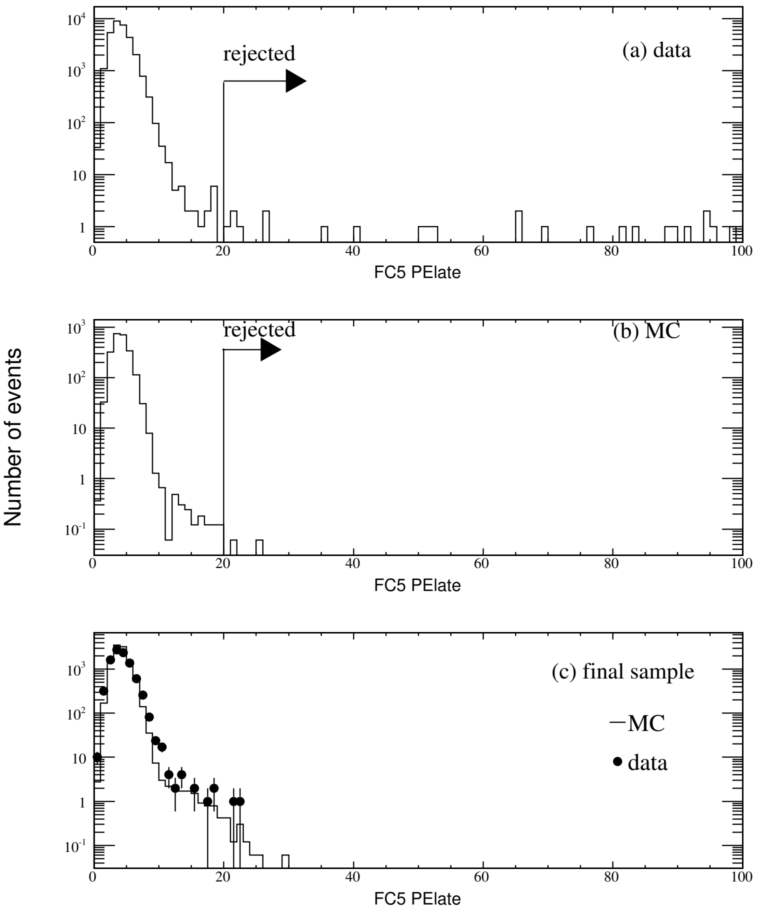

Figure 5.12: FC 5th reduction coincidence muon cut. PE_{late} distributions for SK-IV. (a) shows the data after the FC 4th reduction. (b) shows the Monte Carlo events after the FC 4th reduction. (c) shows the final sample for both data and the Monte Carlo events whose number of events is normalized to that of the data. The selection criteria is shown by the arrows. In (c), there are some events with PElate > 20, as they are events with $\mathrm{PE}_{500} > 300$ p.e.s and hence are not removed by criteria (1).

5.1.6 FC Reduction Summary

Finally FC neutrino events are selected by:

1. Vertex of neutrino interaction is inside the fiducial volume (2 m away from the ID wall).
2. Number of hit PMTs in the highest charge OD cluster (NHITAC) is less than 16 (10 for SK-I).
3. Visible energy (E_{vis}) > 30 MeV.

Figure 5.13 shows the NHITAC distributions for FC and PC final sample for SK-I to SK-IV periods. Detection efficiencies in each reduction step are estimated by atmospheric neutrino MC as shown in table 5.1. The number of events in the final sample and the event rate are also summarized in table 5.1. Event rates are consistent with one another for all SK periods.

Uncertainty of FC reduction efficiency is estimated by comparing the distributions of each cut variable of data and Monte Carlo. Uncertainties for SK-I, SK-II, SK-III and SK-IV are estimated to be 0.2%, 0.2%, 0.8% and 0.3% respectively.

FC	SK-I	SK-II	SK-III	SK-IV
reduction step	selection efficiency (%)			
1st	100.0	99.97	100.0	100.0
2nd	100.0	99.92	99.98	99.99
3rd	99.93	99.78	99.81	99.82
4th	99.29	99.38	99.30	99.00
5th	99.26	99.30	99.24	98.95
5th (FV)	99.25	99.95	99.62	99.19
	number of events			
Monte Carlo	14375.7	7772.7	5085.8	10669.5
Data	12299	6610	4355	8929
Data/MC	0.86 ±0.01	0.85±0.01	0.86±0.02	0.84±0.01
event rate/day	8.26±0.07	8.28±0.10	8.41±0.13	8.14±0.09

Table 5.1: Selection efficiencies and number of events for FC sample are summarized for each SK period. Selection efficiencies are for events whose real vertex is in the fiducial volume for reduction steps 1 to 5, while the selection efficiency for 5th (FV) is for events whose fitted vertex is in the fiducial volume, and number of OD hits < 16 (10 for SK-I) and visible energy > 30 MeV. Number of events for MC are normalized without oscillation to real data livetime, 1489.2, 798.6, 518.1 and 1097.0 days for SK-I, SK-II, SK-III and SK-IV respectively.

The background events contamination in the final FC samples are mainly cosmic ray muons and flasher events. Flasher events is a background source for e-like sample, while cosmic ray muons is a background source for μ-like sample. These background events are largely rejected by the fiducial volume cut (reconstructed vertex position > 2 m from the ID wall). Background events are checked by eye-scan with a visual event display. Flasher events is a background source for e-like sample and cosmic ray muons is a background source for μ-like sample, contaminations by background for each sample are summarized in table 5.2.

	SK-I		SK-II		SK-III		SK-IV	
BG	cosmic ray	flasher	cosmic ray	flasher	cosmic ray	flasher	cosmic ray	flasher
sub-GeV	0.2%	0.1%	0.2%	0.4%	0.3%	0.1%	0.1%	0.1%
multi-GeV	0.3%	0.5%	0.2%	0.2%	0.3%	0.2%	0.1%	0.1%

Table 5.2: Estimated contamination by each background source. Sub-GeV means events with $E_{vis} < 1.3$ GeV and Multi-GeV means events with $E_{vis} > 1.3$ GeV.

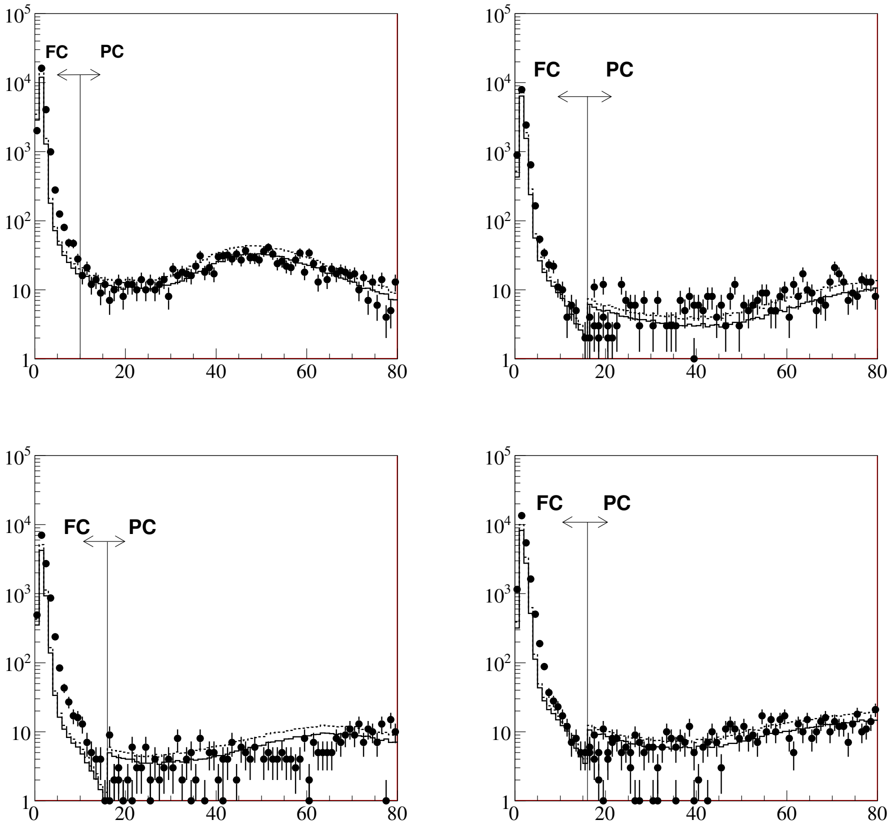

Figure 5.13: NHITAC distributions for FC and PC final examples for SK-I (top left), SK-II (top right), SK-III (bottom left) and SK-IV (bottom right). Points show the observed data and error bars, solid lines show the Monte Carlo events assuming no oscillation (dashed lines) and $\nu_\nu \leftrightarrow \nu_\tau$ 2-flavor oscillation with ($\sin^2 2\theta$, Δm^2) = (1.00, 2.5 × 10^{-3} eV^2) (solid lines).

5.2 Reduction for Partially Contained Events

PC events have OD activities which FC events do not have, hence PC reduction process is different from that of the FC. As OD segmentation was installed in SK-III period, the reduction process is substantially modified to adjust for SK-III onwards. There are 5 steps for PC reduction.

5.2.1 First Reduction

For SK-I and SK-II, the 1st reduction rejects the through-going cosmic ray muons and low energy eventss. Events satisfying the following criteria is selected:
For SK-I:

1. $\mathrm{PE}_{tot} \geq 1000$ p.e.s
   where PE_{tot} is the number of p.e.s observed in the ID.
2. TWIDA $\leq$ 260 nsec
   where TWIDA is the width of the hit timing distribution in the OD PMTs.
3. NCLSTA ≤ 1
   where NCLSTA is the number of the hit clusters in the OD.

For SK-II:

1. $\mathrm{PE}_{tot} \geq 500$ p.e.s
2. TWIDA $\leq$ 170 nec.

In criterion (1), $\mathrm{PE}_{tot} \geq 1000$ p.e.s (500 p.e.s for SK-II) corresponds to 310 MeV/c for muons. As exiting particles in PC samples (mostly muons) must have at least 2 m track length in the ID which corresponds to momentum loss of 500 MeV/c for muons, this criterion rejects events which do not have 2 m track length in the ID. Criterion (2) rejects through-going muons which have broad hit timing distribution and two hit clusters around the entrance and exit point in the OD. As the reflected photons in the OD increased and the quantum efficiency of OD PMTs was increased in SK-II, TWIDA cut criterion is tuned for SK-II.

For SK-III onwards, reduction of through-going muons is more efficient with the OD segmentation. Events satisfying the following criteria would be selected:
For SK-III onwards:

1. $\mathrm{PE}_{tot} \geq 1000$ p.e.s
2. $\mathrm{NHITA}_{top} < 10$ or $\mathrm{NHITA}_{bottom} < 10$
   where NHITA_{top} (NHITA_{bottom}) is the number of OD hits at the top (bottom) part of OD
3. $\mathrm{NHITA}_{endcap} < 25$ or $\mathrm{NHITA}_{side} < 70$
   where NHITA_{endcap} (NHITA_{side}) is the number of OD hits in the top and bottom (side) region of the OD.

4. $\mathrm{ODR}_{mean} < 2100$ cm if OD hits < 20 in 500 nsec time window
   where ODR_{mean} is the average distance between all hit pairs which is defined as follows:

$$ODR_{mean} = \frac{1}{N_{pair}} \sum_{i=1}^{N-1} \mid \vec{x_i} - \vec{x_j} \mid . \tag{5.4}$$

Criterion (2) rejects through-going muons which pass through both top and bottom parts of the detector. Figure 5.14 upper plots show the scatter plots of NHITA_{top} and NHITA_{bottom} of observed data (upper left) and PC Monte Carlo (upper right) events, while bottom plots show the distributions for each of the variables for the final sample.

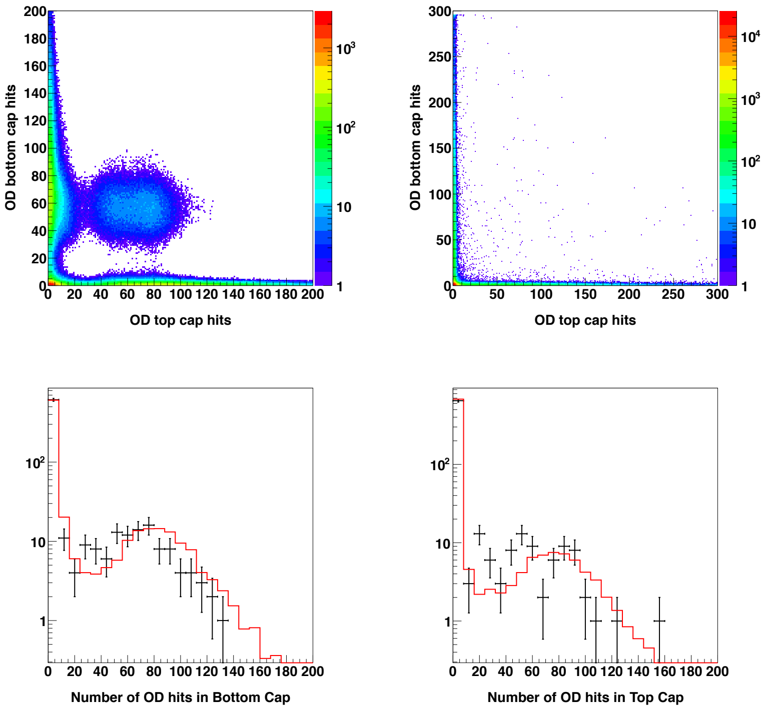

Figure 5.14: PC 1st reduction criterion (2). Top left and right plots are the scatter plots of NHITA_{top} (x-axis) and NHITA_{bottom} (y-axis). Top left figure shows the raw data, and top right figure shows the PC Monte Carlo events with vertex in the fiducial volume. Bottom left and right plots show 1-dimentional plot of NHITA_{top} and NHITA_{bottom} distributions respectively for the final sample for both data (black dots) and Monte Carlo (red lines). All plots are for SK-IV.

Criterion (3) rejects corner clipping muons. Figure 5.15 shows the scatter plots of NHITA_{endcap} and NHITA_{side}.

In criterion (4), ODR_{mean} value for through-going muons is expected to be larger than that of PC events. Figure 5.16 shows the scatter plots of ODR_{mean} and the number of OD hits for both data and Monte Carlo.

PC 1st reduction reduces number of events to $\sim 2 \times 10^4$ events/day.

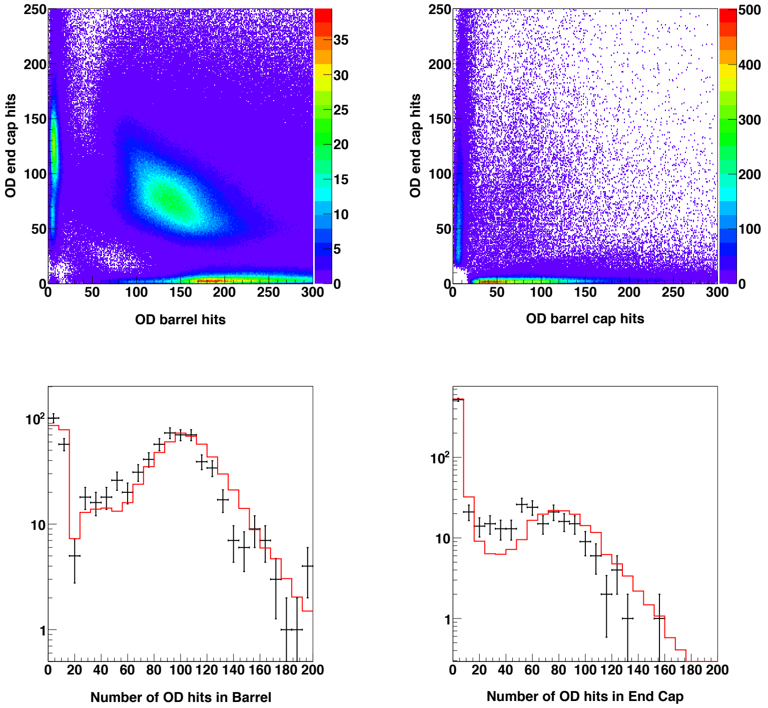

Figure 5.15: PC 1st reduction criterion (3). The upper plots are the scatter plots of NHITA$_{endcap}$ and NHITA$_{barrel}$. The upper left plot shows the raw data and the upper right plot shows the PC Monte Carlo events with vertex in the fiducial volume. Bottom left and right plots show 1-dimentional plot of NHITA$_{endcap}$ and NHITA$_{barrel}$ for final samples for both data and Monte Carlo respectively. All the plots are for SK-IV.

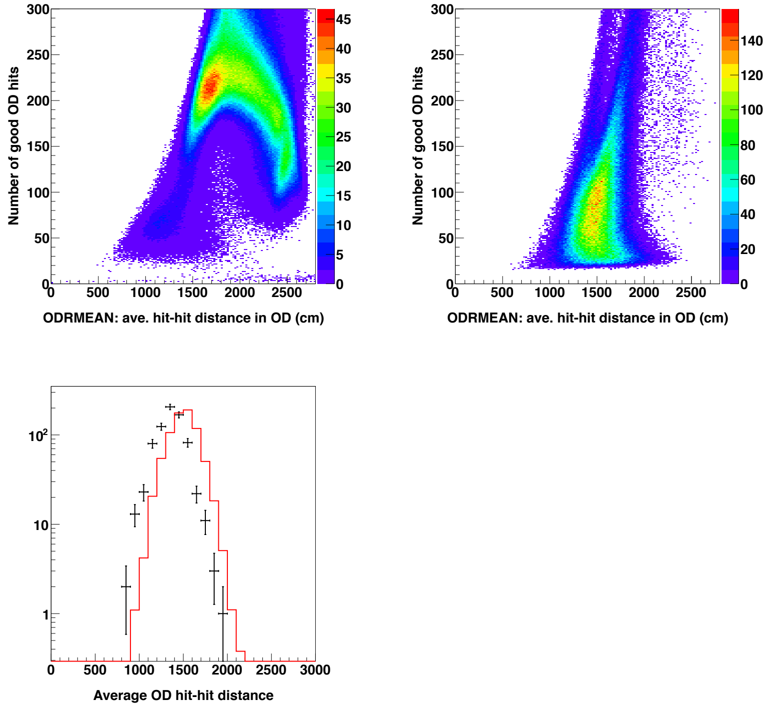

Figure 5.16: PC 1st reduction criterion (4). Top plots are the scatter plots of number of good OD hits and ODR$_{mean}$. Top left plot shows the raw data and top right plot shows the PC Monte Carlo events with vertex in the fiducial volume. The bottom plot shows the 1-dimentional plots of ODR$_{mean}$ of both data (black dots) and Monte Carlo (red line). All the plots are for SK-IV.

5.2.2 Second Reduction

In PC 2nd reduction, a clustering algorithm of OD hits is used to reject through-going muons and stopping muons. OD (ID) walls are divided into 11 × 11 (21 × 21) patches and the charge observed in each patch is counted. Clusters are formed by looking for charge gradient to neighbouring patches. The algorithm is illustrated in Figure 5.17.

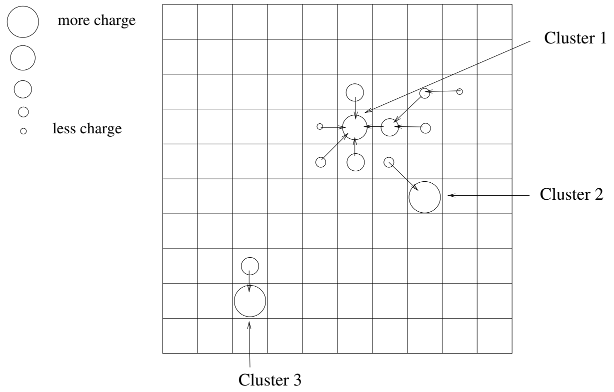

Figure 5.17: Schematic view of the algorithm to find hit clusters in PC 2nd reduction. Charged observed in each patch are represented by circles, whose sizes are proportional to the number of p.e.s. Arrows represent the vector charge gradient, pointing to the highest charge among the neighbouring patches.

Events satisfying the following criteria are selected:

For both SK-I and SK-II:

1. NCLSTA2 ≤ 1
   where NCLSTA2 is the number of OD hit clusters with more than 6 hit PMTs.

For SK-I:

2. NCLSTA2(2) ≤ 1
   where NCLSTA2(2) is the number of the 2nd OD hit clusters with more than 6 hit PMTs.

3. NHITAC$_{min} < 7$
   where NHITAC$_{min}$ is the minimum number of hit PMTs among top (or bottom) and side regions in the OD hit cluster.

4. PE$_{200} > 1000$ p.e.s if NCLSTA2 $= 1$
   where PE$_{200}$ is the number of observed p.e.s within 200 cm from the highest charge PMT in the ID hit cluster closest to the OD hit cluster.

For SK-II:

2. NCLSTA2(2) ≤ 1
   where NCLSTA2(2) is the number of the 2nd OD hit clusters with more than 10 hit PMTs.

3. NHITA$_{endcap}$ $<$ 20 or NHITA$_{endcap}$ $<$ MAX(NHITA$_{side}$)
   where MAX(NHITA$_{side}$) is defined as follows:
   MAX(NHITA$_{side}$) = exp(5.8 - 0.023 × NHITA$_{side}$) if NHITA$_{side}$ $<$ 75
   MAX(NHITA$_{side}$) = exp(4.675 - 0.008 × NHITA$_{side}$) if NHITA$_{side}$ $\geq$ 75
   where NHITA$_{endcap}$ is the number of OD hit PMTs in the top and bottom region of the OD
   and NHITA$_{side}$ is the number of hit OD PMTs in the side region of the OD.

4. NHITAC2 $<$ 12 + 0.085 × PE$_{200}$
   where NHITAC2 is the number of OD hit PMTs in the 2nd cluster.

Criteria (3) rejects corner clipping muons, which leave hit PMTs in both top (or bottom) and side region of the detector.

Criteria (4) rejects stopping muons by using ID hit cluster located behind the OD hit cluster.

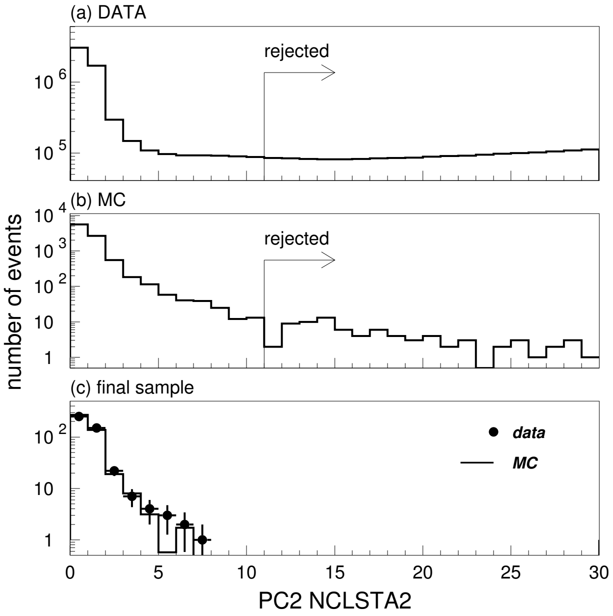

Figure 5.18: PC 2nd reduction criterion (2) for SK-III. Distributions of number of OD hit PMTs in the 2nd OD hit cluster. (a) shows the data after PC 1st reduction. (b) shows PC Monte Carlo after PC 1st reduction. (c) shows the final sample for both data and Monte Carlo. The selection criteria is shown by arrows.

For SK-III onwards, as 1st reduction with the OD segmentation is very efficient, the 2nd reduction only consists of criteria (2) and (3) of SK-II. Figure 5.18 shows the number of OD hit PMTs in the 2nd OD hit cluster for both data and Monte Carlo after PC 1st reduction and their final samples. Criterion (3) is a more strict cut than the criterion (3) in PC 1st reduction. Figure5.19 shows the scatter plots of NHITA$_{endcap}$ and NHITA$_{side}$ for both data and PC Monte Carlo after PC 1st reduction and their final samples.

Event rate after PC 2nd reducction is ∼8000 events/day.

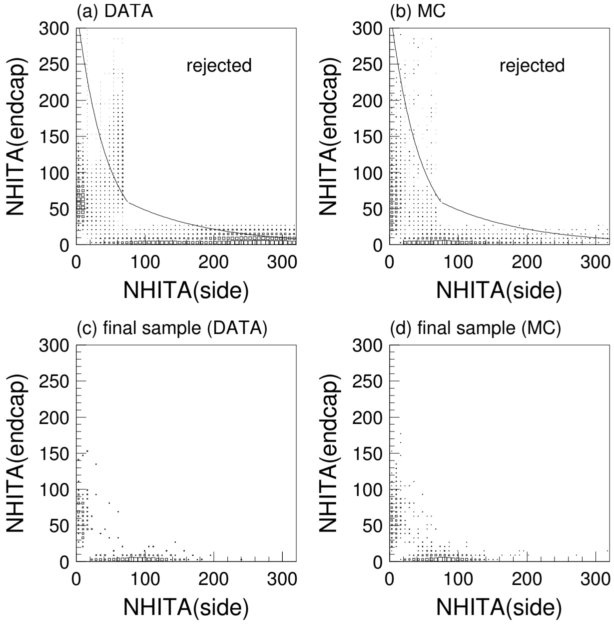

Figure 5.19: PC 2nd reduction criterion (3) for SK-III. Scatter plots of NHITA_{endcap} and NHITA_{side}. (a) shows the data after PC 1st reduction, (b) shows PC Monte Carlo after the 1st reduction. (c) and (d) shows the final samples for data and Monte Carlo respectively. The cut criteria are shown by solid lines.

5.2.3 Third Reduction

PC 3rd reduction rejects flasher events in the same way as that in the FC 3rd reduction, in which the broad timing distribution of flasher events is used for the cut. Events which satisfy the following criteria are rejected as flasher events:

1. $\mathrm{NMIN}_{100} > 14$
   $or_{100} > 9$ if number of hit ID PMTs < 800
   where NMIN_{100} is the minimum number of hit ID PMTs in a sliding 100 nsec time window from +300 nsec to +800 nsec.

PC 3rd reduction also rejects stopping muons by using the number of hit OD PMTs near entrance point. In order to find the entrance point, vertex and direction are fitted by Point-fit. The entrance position is estimated by backward extrapolation from the reconstructed vertex. Events satisfying the following criteria are rejected as stopping muons for SK-I and SK-II:

2. $\mathrm{NHITA}_{in} > 10$
   where NHITA_{in} is the number of hit OD PMTs located within 8 m from the entrance point in a fixed 500 nsec time window.

For SK-III onwards, this cut is removed at this stage and this cut variable is used in the 5th reduction.

Event rate after PC 3rd reduction is ∼100 events/day.

5.2.4 Fourth Reduction

For SK-I and SK-II

PC 4th reduction rejects cosmic ray muons which have relatively less OD activities. Two types of event reconstruction tools are used here: Point-fit and through-going muon fit. Through-going muon fit defines the entrance point as the position of the earliest hit cluster in the ID. For PC events, the entrance point cannot not determined correctly by through-going muon fit because they are generated inside the ID, the goodness tends to be worse when compared with through-going muon events. On the other hand, Point-fit can determine the vertex position and the direction reasonably well for both PC and cosmic ray muons. Events fulfilling the following criteria are selected:

1. $\overrightarrow{d}_{pfit} \bullet \overrightarrow{d}_{PMT} >$ -0.8
   where $\overrightarrow{d}_{pfit}$ is the reconstructed direction by Point-fit, $\overrightarrow{d}_{PMT}$ is the reconstructed vertex to the earliest saturated PMT.
   and

2. DCORN > 150 cm
   where DCORN is the distance from the reconstructed vertex by Point-fit to the nearest fringe of the ID.

3. TLMU > 30 m if goodness of through-going muon fit > 0.85
   where TLMU is the track length of muons from the entrance point to the exit point estimated with through-going muon fit.

Criterion (1) rejects the cosmic ray stopping muons which have entrance points in the opposite direction to the reconstructed direction by Point-fit. Criterion (2) rejects corner clipping muons. Criterion (3) rejects through-going muons which have long track lengths.

For SK-III onwards

Event reconstruction tool is used, which classifies each event as stopping muons, through-going muons, multiple muons or corner clipping muons. 97%s background events are categorized as stopping or through-giong muons, 96% PC events are categorized as other muon types. 5 selections based on the results of the fitter are:

1. $\text{angle}_{muon} < 90^\circ$
   where angle_{muon} is the angle between the fitted direction and the vector between the Point-fit vertex and the center of the highest charge OD cluster.

2. $\text{dotprod}_{muon} >$ -0.8
   where dotprod_{muon} the angle between the fitted direction and the vector between the Point-fit vertex and the earliest saturated ID PMT.

3. $\text{length}_{muon} < 1750$ cm
   where length_{muon} is the length of the fitted muon track. Cosmic ray muons tend to have longer track lengths.

4. $\text{goodness}_{muon} < 0.52$
   where goodness_{muon} is the goodness from muon fitter.

5. $\text{corner}_{muon} \geq 300$ cm
   where corner_{muon} is the distance between fitted entrance point and the corner of the track.

If an event is classified as a through-going muon, it has to pass 4 of the above 5 criteria in order to be selected. If an event is classified as a stopping muon, it has to pass 4 of the above 5 criteria including dotprod_{muon} pass in order to be selected, then it has to pass the criteria $\text{goodness}_{muon} < 0.5$ or $\text{ehit}_{muon} <$ where ehit_{muon} is the number of OD hits located within 8 m from the fitted entrance point in a fixed 500 nsec time window. For a event classified as other types, it only has to pass 2 of the above 5 criteria in order to be selected.

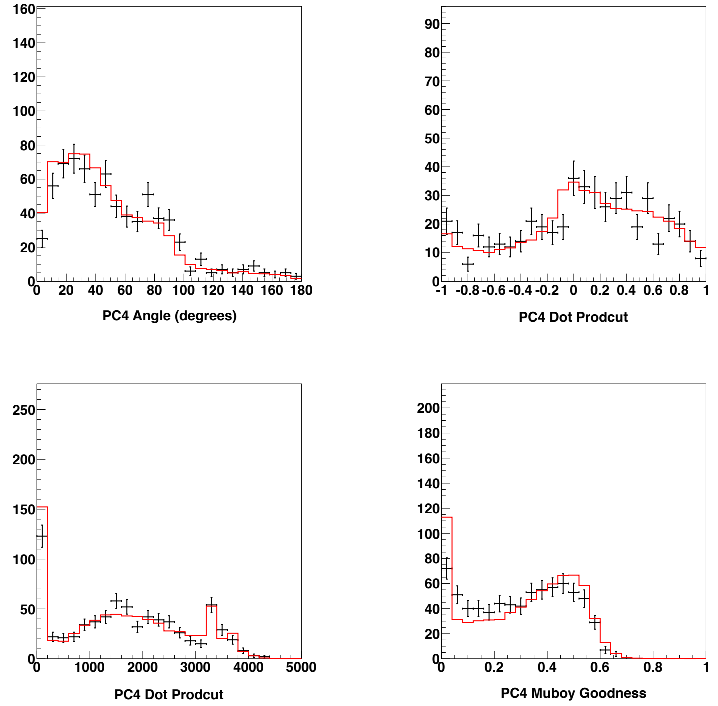

Figure 5.20: PC 4th reduction for SK-IV, criteria (1) to (4) for the final samples. Distributions for criteria (1) to (4) for data (black dots) and Monte Carlo (red lines) for the final sample.

Figure 5.20 shows the distributions for criteria (1) to (4) for both data and MC events for the final sample.

5.2.5 Fifth Reduction

Fifth reduction is done by some elaborate criteria specialized for each remaining background source.

For SK-I and SK-II

Low Energy Event Cut

Events satisfying the following criteria are removed as low energy background events:

1. $\mathrm{PE}_{tot} < 3000$ p.e.s (1500 p.e.s for SK-II)
   where PE_{tot} is the total number of p.e.s observed in the ID

Through-going Muon Cut A

Remaining through-going muons are removed by looking for the existence of two OD hit clusters and the existence of hit OD PMTs near the entrance and exit points. It uses the OD hit cluster information obtained by the algorithm used in PC 2nd reduction. Events satisfying the following criteria are removed as through-going muons:

1. $\mathrm{DIST}_{clust} > 20$ m
   where DIST_{clust} is the distance between the highest charge OD hit cluster and the 2nd highest charge one.

2. $\mathrm{PEAC}_{2nd} \geq 10$ p.e.s
   where PEAC_{2nd} is the number of p.e.s detected in the 2nd highest charge OD hit cluster.

3. $\mathrm{NCLSTA5} \geq 2$
   where NCLSTA5 is the number of OD hit clusters which contain more than 9 hit PMTs.

Criterion (3) uses the same algorithm as that in PC 2nd reduction (only the parameters used are different). The OD wall is divided into 6 × 6 (instead of 11 × 11) in PC 5th reduction to avoid boundary effects of patches.

Event passing through the above two cuts are reconstructed, then the final background rejections are performed as described in the following after the reconstruction.

Through-going Muon Cut B

Some cosmic ray muons enter the detector from the edge on the top part of the detector then exist from the edge of the bottom of the detector. These through-going muons tend to pass through the previous reduction cuts as the light collection efficiency is not good around the edge of the OD and the event reconstruction is relatively not so accurate for these events. In order to reject these events, the number of hit OD PMTs and observed p.e.s in 8 m radius spheres centered at the top and bottom edges are studied. Events satisfying the following criteria are rejected as through-going muons:

1. $\mathrm{NHITA}_{top} \geq 7$ and $\mathrm{NHITA}_{bottom} \geq 7$
   where NHITA_{top} (NHITA_{bottom}) is the maximum number of hit OD PMTs in a 8 m radius sphere centered at the top (bottom) edge.

2. $\mathrm{PEA}_{top} \geq 10$ p.e.s and $\mathrm{PEA}_{bottom} \geq 10$ p.e.s
   where PEA_{top} (PEA_{bottom}) is the number of p.e.s in OD detected in the same sphere as defined for NHITA_{top} (NHITA_{bottom})

3. $0.75 < \mathrm{TDIFFA} \times c/40\ \mathrm{m} < 1.5$
   TDIFFA is the time interval between the averaged hit timing in the to and bottom spheres.

Through-going Muon Cut C

Remaining through-going muons are removed by the number of hit OD PMTs near the entrance and exit points. Their vertex positions and ring directions are reconstructed by a precise fit (MS-fit) which use Cherenkov ring patter. The entrance and exit points on the detector wall are estimated by extrapolation. Cut criteria are listed as follows:

1. $\mathrm{NHITA}_{in} \geq 5$ and $\mathrm{NHITA}_{out} \geq 5$
   where NHITA_{in} (NHITA_{out}) is the number of OD PMTs within 8 m from the entrance (exit) points.

2. $0.75 < \mathrm{TDIFFA} \times c/\mathrm{TRACK} < 1.5$
   where TRACK is the distance between entrance and exit points estimated with vertex position and ring direction reconstructed by MS-fit.

Stopping Muon Cut A

Entrance positions of stopping muons are estimated by reconstructing the vertex position and direction by using MS-fit and extrapolation. The cut is made with counting the number of hit OD PMTs near the entrance point. Events satisfying the following criteria are rejected as stopping muons:

1. $\mathrm{NHITA}_{in} \geq 10$
   where NHITA_{in} is the number of OD hit PMTs within 8 m from the reconstructed entrance.

Stopping Muon Cut B

Opening angles between the OD hit cluster and the ring estimated by two different fitters (TDC-fit and MS-fit) are compared. For stopping muon events, the opening angles are relatively larger than PC events. Events satisfying the following criteria are rejected as stopping muons:

1. $\Theta_{TDC-fit} > 90^\circ$ or $\Theta_{MS-fit} > 90^\circ$
   where $\Theta_{TDC-fit}$ (Θ_{MS-fit}) is the opening angle between the direction to the OD hit cluster and the ring direction reconstructed by TDC-fit (MS-fit).

Stopping Muon Cut C

The charge inside a 42° cone in the ID is used. Vertex and direction are reconstructed by stopping muon fit which defines the entrance point as the position of the earliest hit cluster in the ID. The entrance position cannot be reconstructed correctly for PC events as the vertexes are not on the wall. Events satisfying the following criteria are rejected as stopping muons:

1. goodness of stopping muon fit > 0
2. $\mathrm{PE}_{cone}/\mathrm{PE}_{tot} \geq 0.6$
   where PE_{cone} is the number of p.e.s observed by ID PMTs located inside a 42° cone, and PE_{tot} is the total number of p.e.s observed in ID.
3. $\mathrm{NHITA}_{in} > 6$
   where NHITA_{in} is the number of hit OD PMTs within 8 m from the entrance point.

Cable Hole Muon Cut

Veto scintillation counters are placed over four cable holes (out of twelve) on top of the detector. Events satisfying the following criteria are rejected as cable hole muons:

1. One veto counter hit.
2. $\overrightarrow{d}_{ring} \bullet \overrightarrow{d}_{veto-vertex} >$ -0.8
   where $\overrightarrow{d}_{ring}$ is the reconstructed ring direction by TDC-fit, $\overrightarrow{d}_{vertex-veto}$ is the direction from the hit veto counter to the reconstructed vertex.

Corner Clipping Muon Cut A

Corner clipping muon events have a small hit cluster in the ID, and the vertexes are sometimes mis-reconstructed in the ID. Therefore, the tracklength from vertex to exit point reconstructed by MS-fit is large, while the tracklength estimated with visible energy by using the energy loss of muons ~2 MeV/cm is small. The cut criteria for rejecting corner clipping muons is:

1. E_{vis} /2 (MeV/cm) $<$ TRACK-1500 if TRACK $>$ 15 m
   where E_{vis} /2 is the estimated tracklength by visible energy and TRACK is the tracklength from vertex to the exit point estimated with vertex point and direction by MS-fit.

SK-III onwards

There are two types of cuts: Hard cuts and Soft cuts. PC events are required to pass all Hard cuts, and it is allowed to fail Soft cuts once.

Hard cuts include:

1. Through-going muon cut A
2. Through-going muon cut B
3. Stopping muon cut B
4. Cable hole muon cut
5. Corner clippping muon cut B
   where criteria (1), (2), (3) and (4) are described in the above reductions for SK-I and SK-II.

Corner Clipping Muon Cut B

This cut rejects corner clipping muons:

1. DCORN > 150 cm
   where DCORN is the distance from the vertex reconstructed by Point-fit to the nearest fringe of ID.

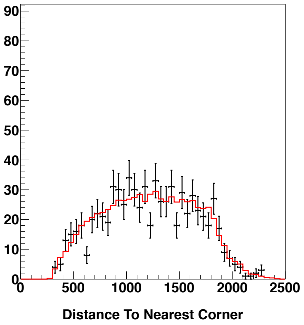

Figure 5.21: PC 5th reduction Corner clipping muon cut B for SK-IV. The plot shows the distribution of the distance from the vertex reconstructed by Point-fit to the nearest fringe of ID, for the final sample for both data (black dots) and Monte Carlo (red line) events.

Figure 5.21 shows the DCORN distributions for both data and PC Monte Carlo and their final samples.

Soft cuts include:

1. Through-going muon cut C
2. Through-going muon cut D
3. Stopping muon cut A
4. Stopping muon cut C
5. Stopping muon cut D
6. Stopping muon cut E
7. Corner clipping muon cut A
8. Decay electron cut
   where criteria (1), (3), (4) and (7) are described in the above reductions for SK-I and SK-II.

Through-going Muon Cut D

Remaining through-going muons are rejected by using the number of hit OD PMTs in the 1st and 2nd highest charge clusters. The cut criterion is:

1. NCLSTA5(1) ≥ 10 and NCLSTA5(2) ≥ 17
   where NCLSTA5(1) (NCLSTA5(2)) is the number of hit OD PMTs in the 1st (2nd) highest charge cluster.

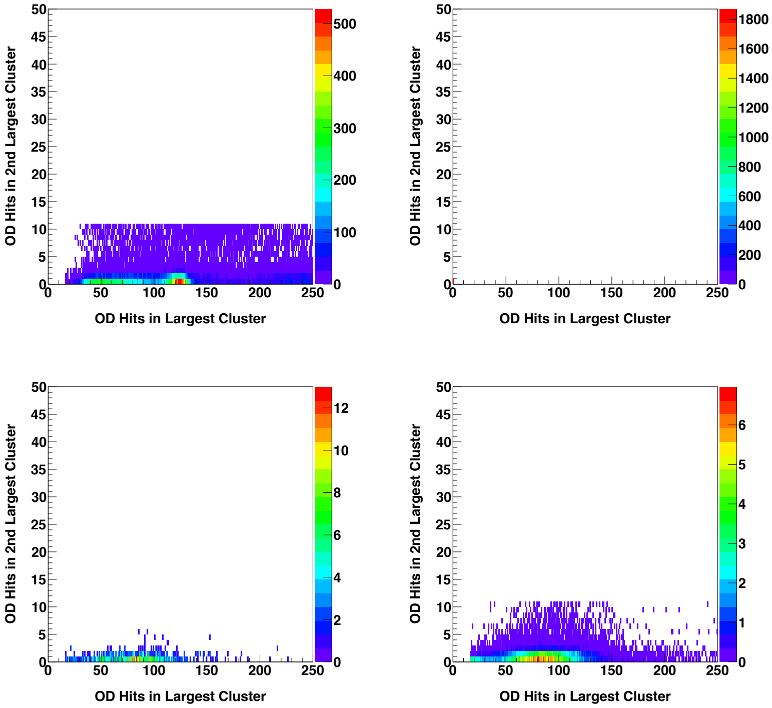

Figure 5.22: PC 5th reduction Through-going muon cut D for SK-IV. Upper left plot shows the data after PC 4th reduction while the upper right plot shows the PC Monte Carlo. The bottom left and right plots show the final samples for data and Monte Carlo respectively.

Figure 5.22 shows scatter plots of NCLSTA5(1) and NCLSTA5(2) for data and PC Monte Carlo and their final samples.

Stopping Muon Cut D

Stopping muons are rejected by using the number of OD hits within 8 m of the reconstructed entry point (NHITA$_{in}$) which is the same as that for SK-I and SK-II in PC 3rd reduction criterion (2), in which the reconstructed entry point is based on Point-fit. If the entry points reconstructed by Point-fit and MS-fit agree, this stopping muon rejection is applied:

1. $\mathrm{NHITA}_{in} > 6$ if $\mid \overrightarrow{P}_{point} - \overrightarrow{P}_{MS} \mid < 1500$ cm
   where NHITA_{in} is the number of hit OD PMTs within 8 m from the entrance point. P_{point} ($\overrightarrow{P}_{MS}$) is the vertex position reconstructed by Point-fit (MS-fit).

Stopping Muon Cut E

The same criterion in PC 4th reduction for SK-III criterion (1) is applied, as the former cut was looser for events which are classified as stopping or through-going muons.

1. $\mathrm{angle}_{muon} < 90°$
   where angle_{muon} is the angle between the fitted direction and the vector between the Point-fit vertex and the center of the highest charge OD cluster.

Decay electron Cut

High energy neutrinos mostly interact with nucleons in water through DIS interactions. They produce hadrons including charged pions. The pions decay into muons which in turn decay into electrons. These decay-electrons are tagged by Decay Electron Search.

For high cosmic ray muon decays in the detector, there is no decay electron as cosmic ray muons decay in flight.

Therefore events having high energy ($\mathrm{E}_{vis} > 25$ GeV) but having no decay electron are rejected as cosmic ray muons.

5.2.6 PC Reduction Summary

Finally, PC neutrino events are selected by the following criteria:

1. Vertex of neutrino interactions is inside the fiducial volume (2 m from the wall of detector).

2. Number of hit PMTs in the highest charge OD cluster (NHITAC) is larger than 15 (9 for SK-I).

3. Visible energy (E_{vis}) $>$ 350 MeV
   (Total observed charge in ID $>$ 3000 p.e.s (1500 p.e.s for SK-II)

Detection efficiency in each reduction step is estimated by MC events as shown in table 5.3. Detection efficiency in final events are estimated to be 81%, 74.8%, 88.8% and 86.3% for SK-I, SK-II, SK-III and SK-IV respectively.

Background events in final PC sample are mainly due to cosmic ray muons. These background events are checked by eye-scan. Most background events are rejected by the fiducial volume cut, so only few background events contaminate the PC final sample. Contamination due to background events is estimated by extrapolating the distribution of background events outside the fiducial volume. Figure 5.23 shows the number of background events outside the fiducial volume for SK-II. Background events inside the fiducial volume may lead to contamination as shown by the fitted exponential curve in Figure 5.23. Table 5.4 summarizes the estimated contamination due to cosmic ray background for each SK period.

PC	SK-I	SK-II	SK-III	SK-IV
reduction step	selection efficiency (%)			
1st	98.98	98.58	99.09	99.63
2nd	96.74	93.43	98.52	98.73
3rd	95.69	92.32	98.51	98.68
4th	89.86	84.60	97.87	97.42
5th	88.66	82.63	96.61	96.15
5th (FV)	80.98	74.80	88.80	86.30
	number of events			
Monte Carlo	913.8	448.6	356.0	744.9
Data	902	427	344	735
Data/MC	0.99±0.05	0.95±0.06	0.97±0.07	0.97±0.05
event rate/day	0.66±0.02	0.65±0.04	0.62±0.03	0.66±0.02

Table 5.3: Selection efficiencies and number of events for PC sample are summarized for each SK period. Selection efficiencies are for events whose real vertex is in the fiducial volume (after 5th (FV) step, fitted vertex instead of real vertex is considered) and number of OD hits > 15 (9 for SK-I) and total observed charge > 3000 p.e.s. Number of events for MC are normalized to real data livetime, 1489.2, 798.6, 518.1 and 1097.0 days for SK-I, SK-II, SK-III and SK-IV respectively, 2-flavor oscillation with $(\sin^2 2\theta, \Delta m^2) = (1.00, 2.5 \times 10^{-3}\ \text{eV}^2)$ is assumed.

	SK-I	SK-II	SK-III	SK-IV
cosmic ray BG	0.2%	0.7%	1.8%	0.6%

Table 5.4: Estimated contamination by cosmic ray muons for PC.

5.2.7 PC OD Stop/Through Separation

OD stopping events have better neutrino energy resolution than through-going events, therefore PC sample is further separated into OD stopping and OD through-going, by considering the energy deposited into the OD region. OD stopping events stop in the OD, while OD through-going events travel through the OD into the rocks surrounding the detector. OD stopping events have less charge in the OD compared to OD through-going events as they have shorter pathlengths through OD. Selection criteria for OD stopping events are listed as follows:

1. Maximum number of p.e.s observed in OD in a sliding 500 nsec time window from -400 nsec to $+600$ nsec (PE_{anti}) is less than $\text{PE}_{exp}/1.5$.
   where PE_{exp} is the expected number of p.e.s in the OD from the tracklength in the OD, PE_{anti} is the observed charge for that event.
2. The most energetic ring or the second energy ring is identified to be μ-like.

The ratio $\text{PE}_{anti}/\text{PE}_{exp}$ is position dependent as the PMT charge response changes along the height of the detector tank.

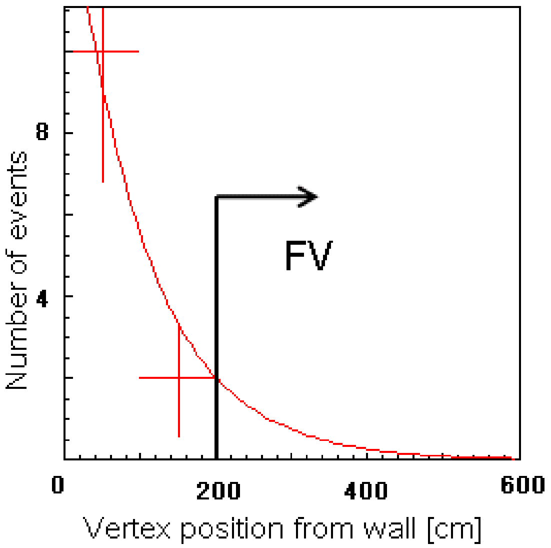

Figure 5.23: Number of background events outside fiducial volume as a function of distance between reconstructed vertex and the ID wall for SK-III. The solid line shows the fitted exponential curve.

Figure 5.24 shows the PE_{anti} / PE_{exp} distributions for data and PC MC events.

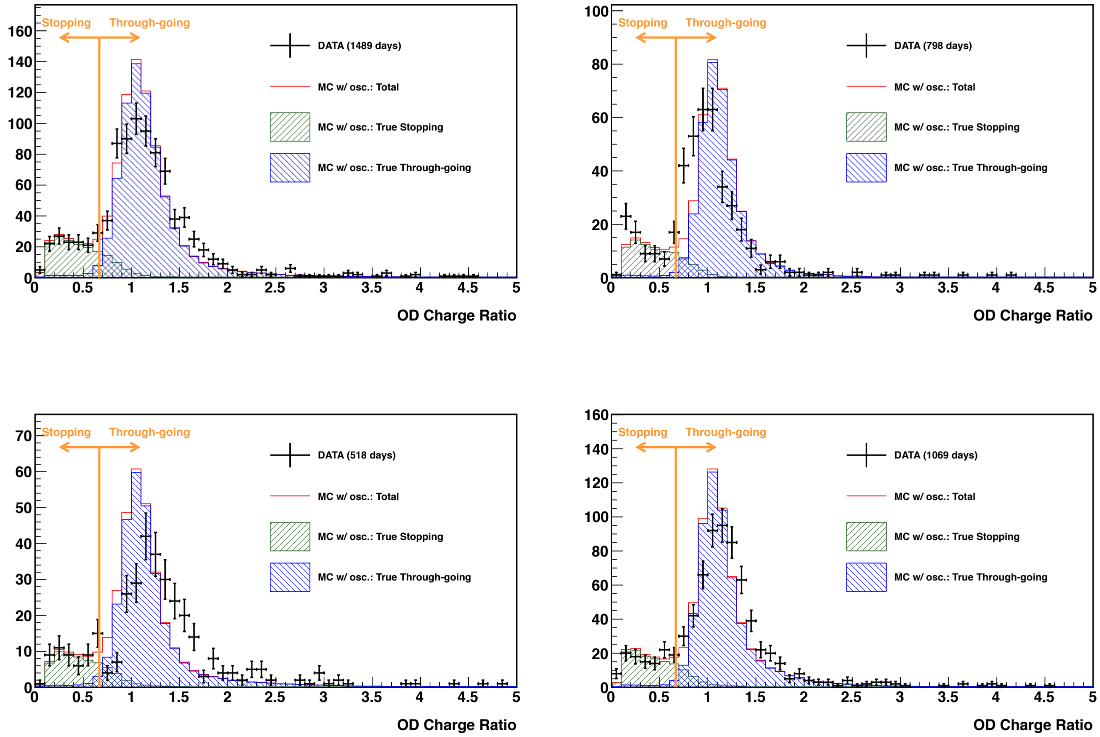

Figure 5.24: Distribution of PE_{anti} / PE_{exp} for PC stop / through separation for SK-I (top left), SK-II (top right), SK-III (bottom left) and SK-IV (bottom right). The points represent the data with error bar. The shaded regions represent MC of true stopping and true through-going events without oscillation and normalized to data livetime. The selection criteria is shown by the arrow.

5.3 Reduction for Upward-going Muon Events

The reduction for upward-going muon (UPMU) events are described in this section.

5.3.1 Charge cut

Low energy and extremely high energy events are rejected in the 1st reduction:

1. $\mathrm{PE}_{tot} > 6000$ p.e.s (3000 p.e.s for SK-II)
2. $\mathrm{PE}_{tot} < 1{,}750{,}000$ p.e.s (800,000 p.e.s for SK-II)
   where PE_{tot} is the total number of p.e.s observed in the ID.

PE_{tot} corresponds to muon momentum of 1 GeV/c and tracklength of 3.5 m (requirement for final sample is tracklength > 7 m). At very high ID charge $\sim$1,750,000 p.e.s, the ID electronics is saturated and muon fitter does not work.

5.3.2 Zenith Angle Cut

In order to reject the the downward-going muon cosmic-ray muons, seven different fitters specialized to fit stopping muons, through-going muons and muons with Bremsstrahlung are used. Algorithm of the zenith angle cut is listed as follows:

1. Apply a muon fitter
2. If the event is classified as upward and goodness of fit is above the threshold, the event is saved.
3. If the event is classified as downward and goodness of fit is above the threshold, the event is rejected.
4. If the event is classifed as horizontal with goodness of fit above the threshold, or if goodness of fit is below the threshold, the judgement is suspended.
5. Go to (1) and apply the next muon fitter.

This algorithm continues until the event has passed through all the fitters or has been classified. If no fitter gives a goodness above the threshold, the event is rejected. If at least one fitter classifies the event as horizontal, the event is saved. Detailed description about the seven muon fitters and definition of goodness can be found in [134].

All events from the output of the upward-going muon reduction are passed through the precise fitter. The fitter results are used to select upward-going events by the criterion of zenith angle $\cos\Theta < 0$.

5.3.3 Scanning

In order to eliminate the remaining misfitted background events, the selected events are scanned using a visual display. Upward-going muon events are selected one by one. All events are checked by two scanners so that no neutrino events is missed. Efficiency of scanning is estimated to be almost 100%. About half of the events remaining after all the automated reduction steps are rejected by this final scan.

5.3.4 UPMU Reduction Summary

The final selection criteria for UPMU stopping events are:

1. Fitter classification is stopping event
2. Fitted momentum $\geq$ 1.6 GeV/c (which correspond to tracklength = 7 m)
3. Number of hit OD PMTs within 8 m from the exit point (NHITEX) $<$ 10 (16 for SK-II)

Selection criteria for UPMU through-going events are:

1. Fitter classification is through-going event
2. Distance from the ID entrance point to the ID exit point $\geq$ 7 m
3. Number of hit OD PMTs within 8 m from the exit point (NHITEX) $\geq$ 10 (16 for SK-II)

Figure 5.25 shows the distribution of NHITEX. Detection efficiency for the final events is estimated to be 98.0% (99.4%) for SK-I stopping muons (through-going muons), 97.0% (98.1%) for SK-II stopping muons (through-going muons), 98.2% (99.4%) for SK-III stopping muons (through-going muons) and 98.0% (99.4%) for SK-IV stopping muons (through-going muons). Number of events in the final sample are summarized in 5.5. The final sample is made by subtracting the expected number of background events.

Note that the disagreement between data and Monte Carlo for SK-III in figure 5.25 is due to the problem in the OD tuning. However, as the cut for stopping muons and through-going muons is far away from the disagreement, the disagreement does not affect the efficiency of separation of UPMU stopping and through-going events.

	SK-I		SK-II		SK-III		SK-IV	
	stop	thru	stop	thru	stop	thru	stop	thru
final sample (MC)	729.6	1892.4	364.6	926.2	286.0	725.1	474.0	1257.6
final sample (data)	462	1866	223	871	210	735	306	1345
BG subtracted	429	1835.6	210	833.4	193	722.9	284	1330.9
BG subtracted/MC	0.59 ±0.04	0.97 ±0.03	0.58 ±0.10	0.90 ±0.04	0.67 ±0.06	1.00 ±0.05	0.60 ±0.04	1.06 ±0.04
event rate (per day)	0.26 ±0.01	1.12 ±0.03	0.25 ±0.02	1.01 ±0.03	0.30 ±0.02	1.14 ±0.04	0.26 ±0.02	1.21 ±0.03

Table 5.5: Number of events of UPMU summarized for each SK period. Number of MC (without oscillation) events and event rate are calculated by normalization of data livetime, 1645.9, 827.7, 635.6, 1096.7 days for SK-I, SK-II, SK-III and SK-IV respectively.

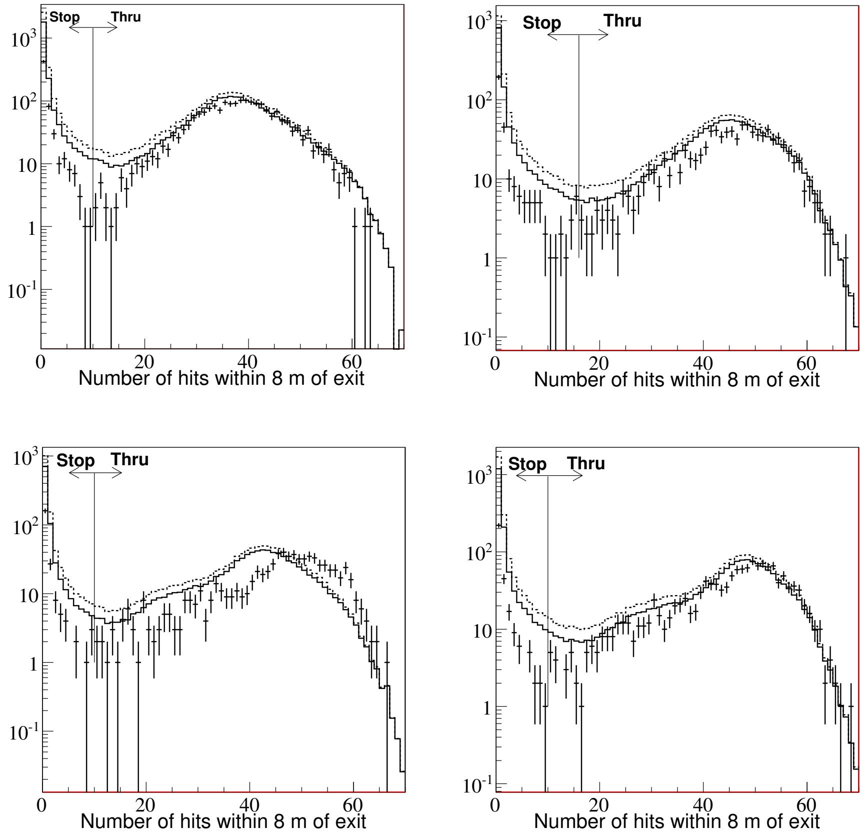

Figure 5.25: Distribution of NHITEX for UPMU stop/through separation for SK-I (top left), SK-II (top right), SK-III (bottom left) and SK-IV (bottom right). Points shows the observed data, dashed line show MC assuming no oscillation and solid line shows MC with $\nu_\mu \leftrightarrow \nu_\tau$ 2-flavor oscillation with $(\sin^2 2\theta, \Delta m^2) = (1.00, 2.5 \times 10^{-3}\ \mathrm{eV}^2)$. Selection criteria are shown by arrows.

5.3.5 Background Estimation for Upward-going Muon

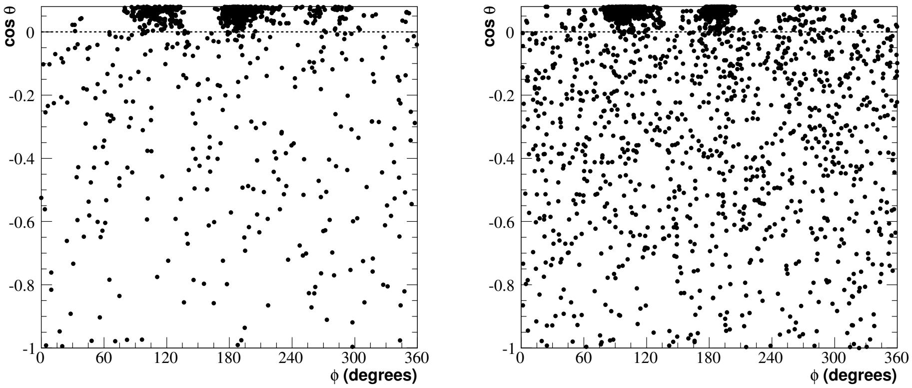

Figure 5.26: Scatter plots of zenith versus azimuth directions for stopping muons (left) and through-going muons (right) for SK-IV.

Background events are mostly cosmic-ray muons, which are reconstructed as upward-going due to multiple Coulumb scattering of the muons or slight mis-reconstruction of near horizontal going muons. Hence they are mostly distributed in the horizontal bin (-0.1 $<$ cosθ $<$ 0). Contamination by the background is estimated by extrapolating the distribution of downward events in 0$<$ cosθ. Figure 5.26 shows the zenith versus azimuth directions for upward going muon samples. Clusters of cosmic ray downward muons are seen in the regions zenith angle cos$\Theta > 0$ (downward) and azimuthal angle around $\phi = 120°$, $180°$ and $270°$. These clusters are caused by thin rock over the detector. When contamination of background is estimated, the UPMU samples are divided into two azimuth angle regions. Figure 5.27 shows the azimuthal angle distributions for upward going muon samples, in which region (2) represents the region with thinner mountain (which is defined as $60° < \phi < 310°$), while region (1) represents the region with thicker mountain.

Figure 5.28 shows the zenith angle distributions for upward-going muon samples, in which region (1) and (2) are normalized by the coverage of azimuthal angle. The zenith angle distribution is almost flat for upward going events (cos$\Theta < 0$), but the number of events in region (2) exponentially increase with cosine of zenith angle for downward-going events (cos$\Theta > 0$). Contamination by cosmic ray muons in the upward-going direction are estimated by extrapolating from the downward direction in region (2) with (exponential + constant) function. In figure **??**, there are best-fitted curves which is defined as $f(\cos\theta) = p0 + \exp p1 + p2(\cos\theta)$. $p0$ is fixed to the value determined by the average of region (1) events. Contaminations of background events are estimated by $N_{bg} = \int_{\cos\theta_x}^{0}(\exp p1 + p2(\cos\theta))$. The uncertainties on the estimated numbers of background events are evaluated by the maximum change on the number of background events when fit parameters ($p0$, $p1$ and $p2$) are shifted to increase or decrease the background events within the parameters' allowed regions. They are summarized in table 5.6.

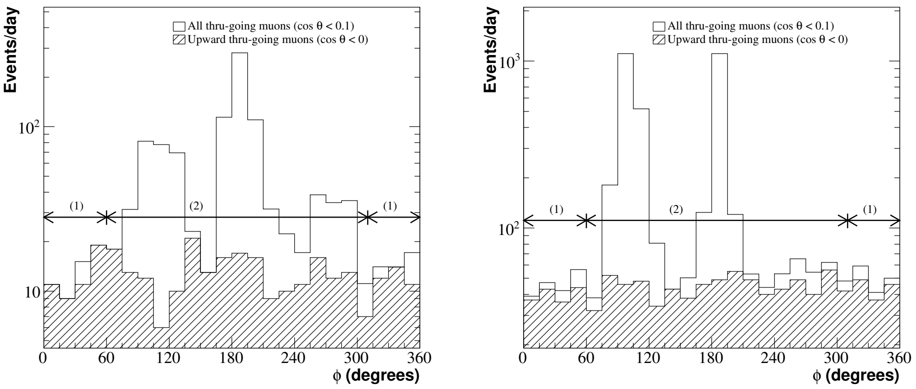

Figure 5.27: Azimuthal angle distributions for stopping muon (left) and through-going muons (right) for SK-IV. Region (1) has thicker-mountain, while region (2) has thinner-mounter. White histograms show the events of downward-going muons, while the black histograms show the upward-going muons.

	SK-I	SK-II	SK-III	SK-IV
stop μ	16%	21%	20%	17%
thru μ (non-shower)	11%	15$	19%	14%
thru μ (shower)	18%	14%	24%	20%

Table 5.6: Uncertainties of background events which is the contamination by horizontal muons to the UPMU sample in the zenith angle -0.1 < cosθ < 0.

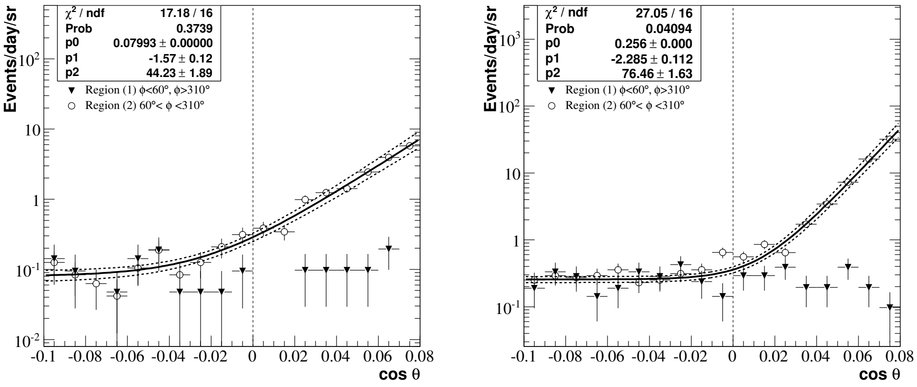

Figure 5.28: Zenith angle distributions for stopping muon (left) and through-going muon (right) for SK-IV in both regions (1) and (2). Solid curves are fitted functions to estimate the background contamination. Zenith angle bins are divided equally to 18 bins between -0.1 $< \cos\theta <$ 0.08.

5.3.6 Upward Through-going Showering Muon

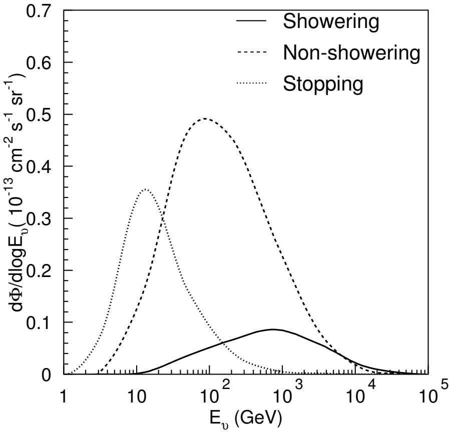

Figure 5.29: Energy spectrum of primary neutrino for upward stopping (dotted line), non-showering (dashed line) and showering (solid line) muon events.

Upward through-going muons are further separated into showering muon sample and non-showering muon sample. This is because some upward through-going muon events are accompanied with electromagnetic shower. Showering muons are observed as high energy muons which lose energy through radiative processes such as Bremstrahlung radiation, e^+ e^- pair production and photo-nuclear interactions. The energy of the parent neutrino is approximately 1 TeV. Figure 5.29 shows energy spectrum of primary neutrino for the UPMU samples.

Selection of showering muons uses χ^2 test based on the observed charge and the expected charge of non-showering muons [134]. Difference between corrected observed charge and expected charge of non-showering muon is defined as $\Delta(Q)$. Criteria of showering muon selection are:

1. Difference between the corrected charge and the expected charge for non-showering muon ($\Delta(Q) = <Q> - q_l$) > 0.5 when χ^2 variable for showering selection ≥ 50.
2. $\Delta(Q) >$ 4.5 - 0.08 χ^2 when $\chi^2 < 50$.

Figure 5.30 shows scatter plot of $\Delta(Q)$ and χ^2,and $\Delta(Q)$ distributions for data and MC events which are classified as through-going muons.

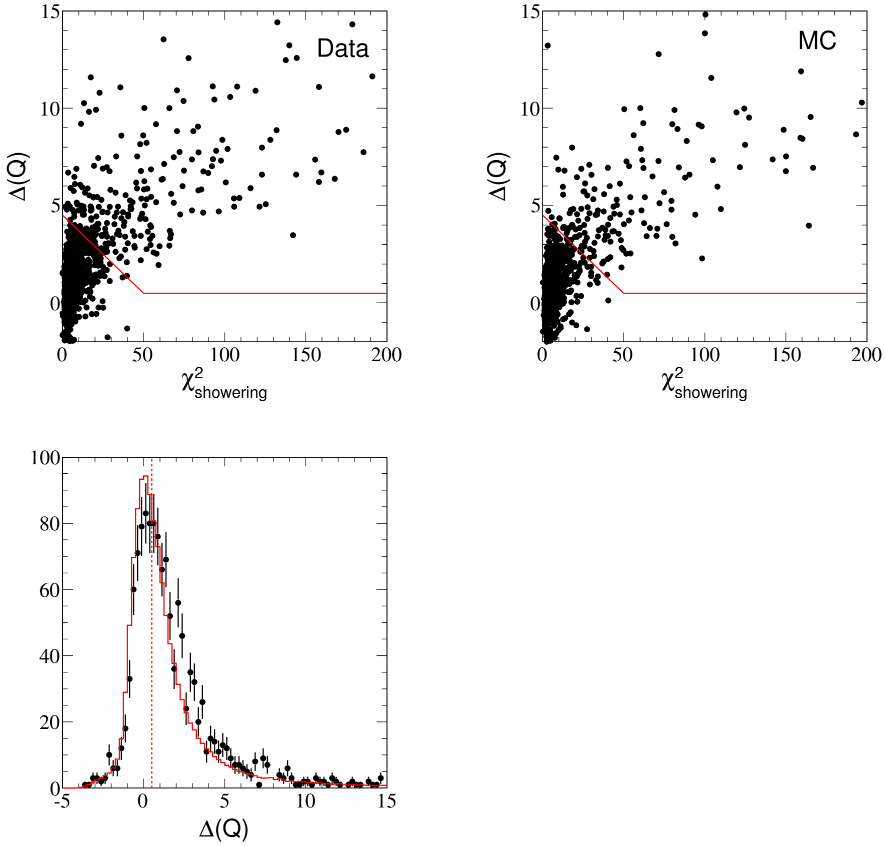

Figure 5.30: Distributions for UPMU showering separation for SK-IV. Scatter plot of $\Delta(Q)$ against χ^2 of UPMU through-going events are shown for data (top left) and MC (top right) (normalized to data lifetime). $\Delta(Q)$ distribution is shown in the bottom panel for data (points) and MC (red solid line). The cut is shown by red dashed line.

5.4 Event Reconstruction

Selected neutrino events are reconstructed to determine their neutrino flavor type, directions, momentum etc. For FC and PC, the reconstruction process consists of the following steps:

1. Vertex fitting
   Vertex position is defined as the point at which the timing residual distribution of hit PMTs has the sharpest peak. The direction and the outer edge of the dominant ring is determined.

2. Ring counting
   Other possible rings are searched for by using the vertex position and the direction of the dominant ring. Ring candidates are tested whether they are true rings or not with a likelihood, then the number of rings is determined.

3. Particle identification
   Each ring is classified as two types: showering type ($e^{\pm}$, γ) as e-like and non-showering type ($\mu^{\pm}$, $\pi^{\pm}$) as μ-like, based on a likelihood using Cherenkov ring pattern and Cherenkov opening angle.

4. Precise vertex fitting (MS-fit) (only for single-ring events)
   Vertex position is determined more accurately by using Cherenkov ring pattering assuming the obtained particle type.

5. Momentum determination
   Momentum of each ring is determined by the detected charge inside a Cherenkov cone. Conversion from the charge to momentum is based on a Monte Carlo simulation and detector calibration.

6. Decay electron search
   Decay electrons produced by primary events are searched.

7. Ring number correction (only for FC multi-ring events)
   Rings which are fitted mistakenly are discarded by using precise reconstructed information.

8. π^0 fitting
   Candidate π^0 events are searched for among the events which are recognized as single-ring e-like by the above reconstruction processes.

UPMU events are also reconstructed by using some of the above processes. PC and UPMU events are basically treated as single-ring μ-like events, information such as PID and number of rings are not used in the analysis for PC and UPMU.

Reconstruction methods are described briefly in the following, detailed explanation of reconstruction can be found in [135]. Distribution and numbers of Monte Carlo events in the following sections are assumed to have undergone 2-flavor oscillation with ($\sin^2\theta$, Δm^2) = (1.00, 2.5×10^{-3} eV^2).

5.4.1 Vertex Fitting

Vertex position is reconstructed by using the timing information of hit PMTs in three steps.

In the first step, a simple fit called Point-fit is applied. Vertex is estimated assuming that all photons are emitted at the same time from a point source. After subtracting the time of flight from a tested vertex, a distribution of residual PMT hit time is constructed for that tested vertex. The vertex is estimated as the point where the timing residual distribution is peaked.

In the second step, the direction and the outer edge of the dominant ring is determined. A pair of direction and opening angle is tested by the parameter defined as:

$$Q(\theta_{edge}) = \frac{\int_0^{\theta_{edge}} PE(\theta)d\theta}{\sin\theta_{edge}} \times (\frac{dPE(\theta)}{d\theta}|_{\theta=\theta_{edge}})^2 \times exp(-\frac{(\theta_{edge}-\theta_{exp})^2}{2\sigma_\theta^2}) \tag{5.5}$$

where θ_{exp} and σ_θ are the Cherenkov opening angle expected from the charge within the Cherenkov cone and its resolution respectively.
$PE(\theta)$ is the angular distribution of the observed charge as a function of opening angle θ.
The observed charge is corrected for the effect from water transparency and PMT acceptance.
The direction and the ring edge which maximize $Q(\theta_{edge})$ are taken as the results of fit by Point-fit.

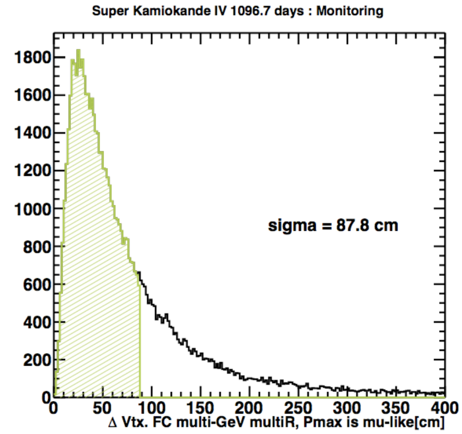

Figure 5.31: Distance between the reconstructed vertex and the true vertex for FC MC Multi-GeV multi-ring μ-like sample for SK-IV. Colored region shows 68% of all events.

In the final step, the vertex position is determined more precisely with TDC-fit. Unlike Point-fit, photons are assumed to be generated along the track of the particle. Then the time residual for PMTs inside the Cherenkov ring is calculated with this effect also considered. For photons outside the ring, the time residual is also computed assuming all photons originated from the vertex. The goodness-of-fit is determined including the effect of scattered photons. The vertex is determined to be the position which maximize the goodness parameter. The vertex position is used for multi-ring events. Figure 5.31 shows the estimated vertex position resolutions for SK-IV multi-GeV multi-ring μ-like sample.

5.4.2 Ring Counting

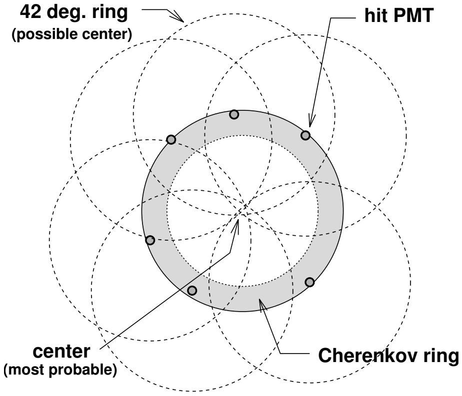

Figure 5.32: The basic idea to find ring candidates. By drawing rings around the hit PMTs with Cherenkov opening angle of 42° from the vertex, center of the actual Cherenkov ring can be identified.

After the initial Cherenkov ring and the vertex is determined, other ring candidates are searched for by a Hough transform method [137], which is a technique to extract a particular shape from an image. Figure 5.32 illustrates the method to find other possible rings, in which a spherical coordinate centred on the vertex position is considered. The shaded circle in the figure represents the Cherenkov ring image projected to a plane perpendicular to the ring direction. Hit PMTs are picked up and virtual circles (dashed lines) centred at the position of the hit PMTs are drawn with 42° half angle. The direction of the Cherenkov ring is identified as the intersection point of these dashed line circles. The second ring candidate is searched by choosing possible ring directions based on this method. Likelihood technique is used to determine if the candidate ring is consistent with a ring. If the second ring is determined to exist, the same procedure is repeated to find other possible rings up to 5 rings.

Figure 5.33 and figure 5.34 show the ring counting likelihood distributions between single-ring and multi-ring for both Data and MC. The cut threshold is at 0 to separate single-ring and multi-ring events. The difference between data and MC is taken as a source of systematic uncertainty in event selection.

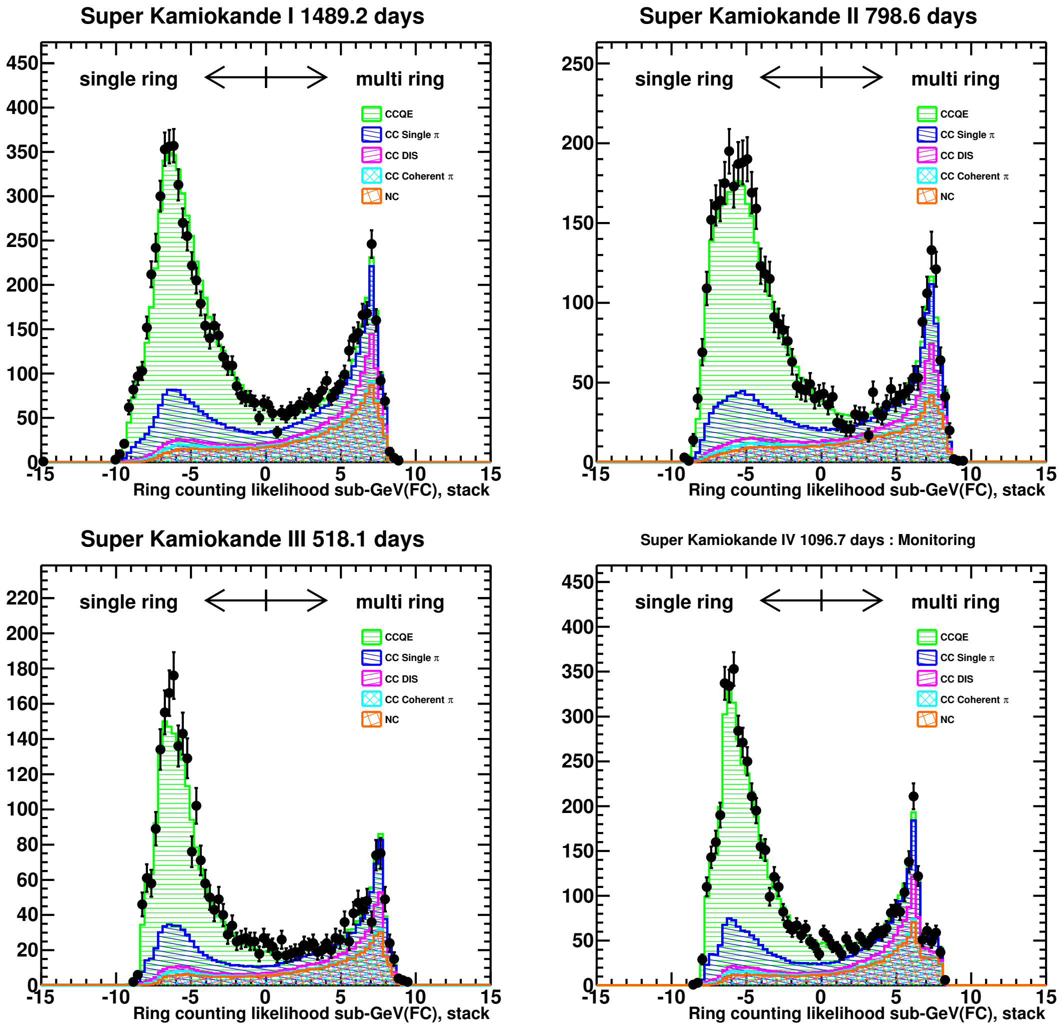

Figure 5.33: Ring counting likelihood distribution for SK-I, SK-II, SKIII and SK-IV sub-GeV samples. Dots are data and solid lines are MC events.

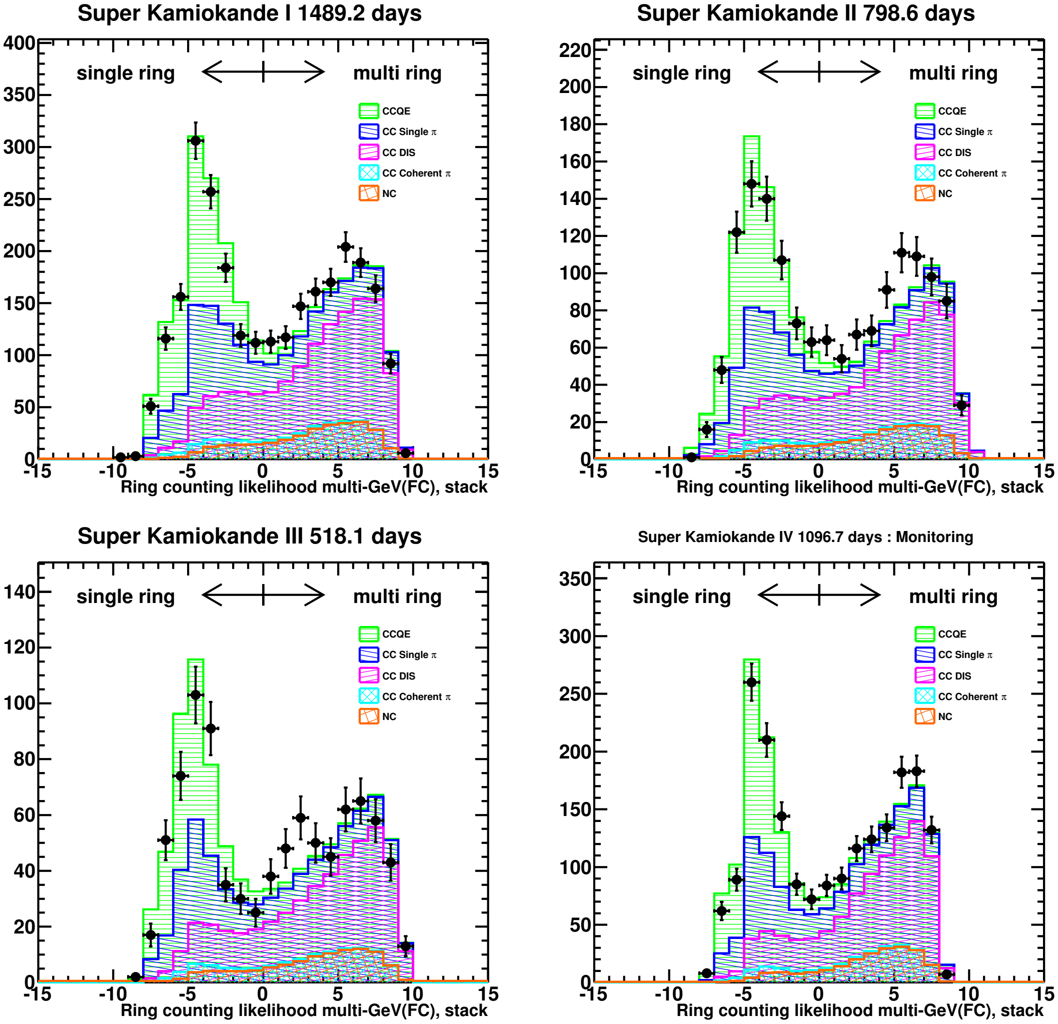

Figure 5.34: Ring counting likelihood distribution for SK-I, SK-II, SKIII and SK-IV multi-GeV samples. Dots are data and solid lines are MC events.

5.4.3 Particle Identification

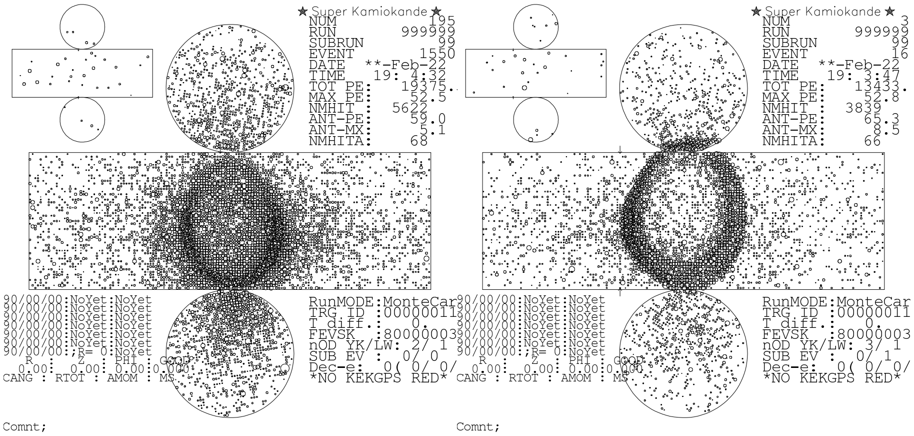

Figure 5.35: Event display of single-ring electron (left) and single-ring muon (right) neutrino MC event.

The detected Cherekov rings are identified as e-like or μ-like by Particle Identification (PID). Figure 5.35 shows the event display for single-ring electron (left) and muon (right) neutrino MC events. An electron (and a gamma ray) produces diffused ring patterns as electrons produce electromagnetic shower and low energy electrons undergo multiple scattering. Muon (and a charged pion) produces ring with sharp edge. Moreover, Cherenkov rings from muons or charged pions have smaller Cherenkov angles if they are not highly relativistic ($\beta = v/c < 1$) These differences are taken into account when events are classified into two types by PID algorithm.

Figure 5.36, figure 5.37 (single-ring) figure 5.38 and figure 5.39 (multi-ring) show the PID likelihood for FC samples. Separation of particle type in multi-ring events is not as good as that for single-ring events because Cherenkov photons from multiple rings overlap. The difference between data and MC is taken as a source of systematic uncertainty in event selection.

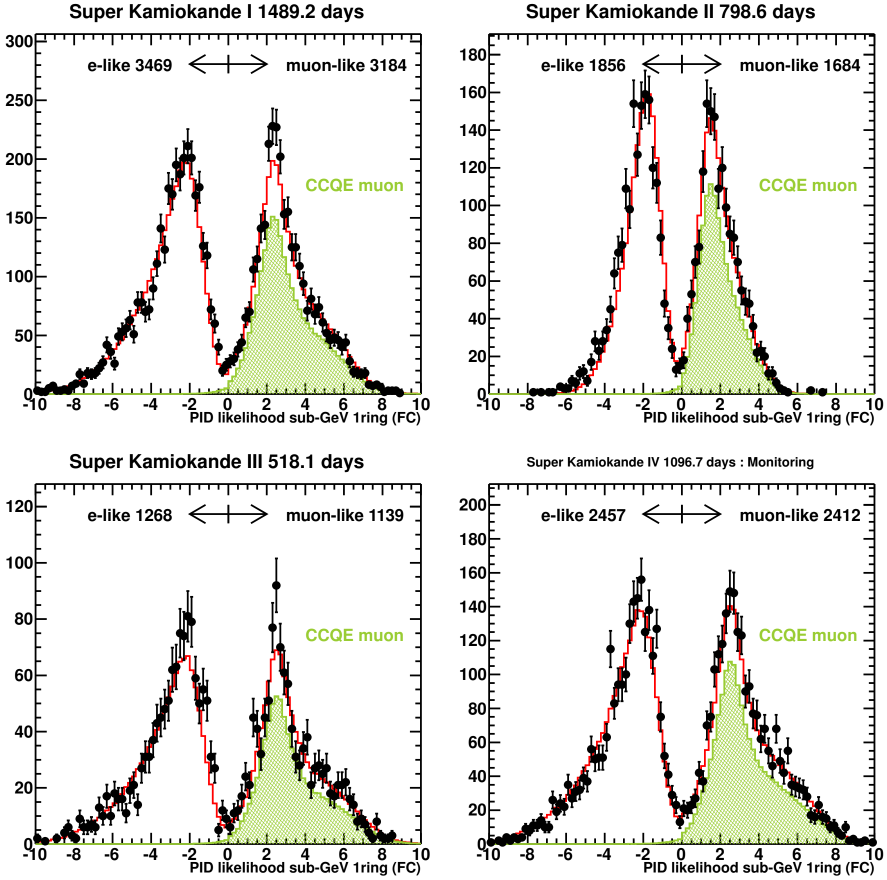

Figure 5.36: PID likelihood distribution for FC sub-GeV 1-ring samples for SK-I, SK-II, SK-III and SK-IV. Points represent the data, red lines represent Monte Carlo, the shaded green regions represent the MC CCQE ν_μ events.

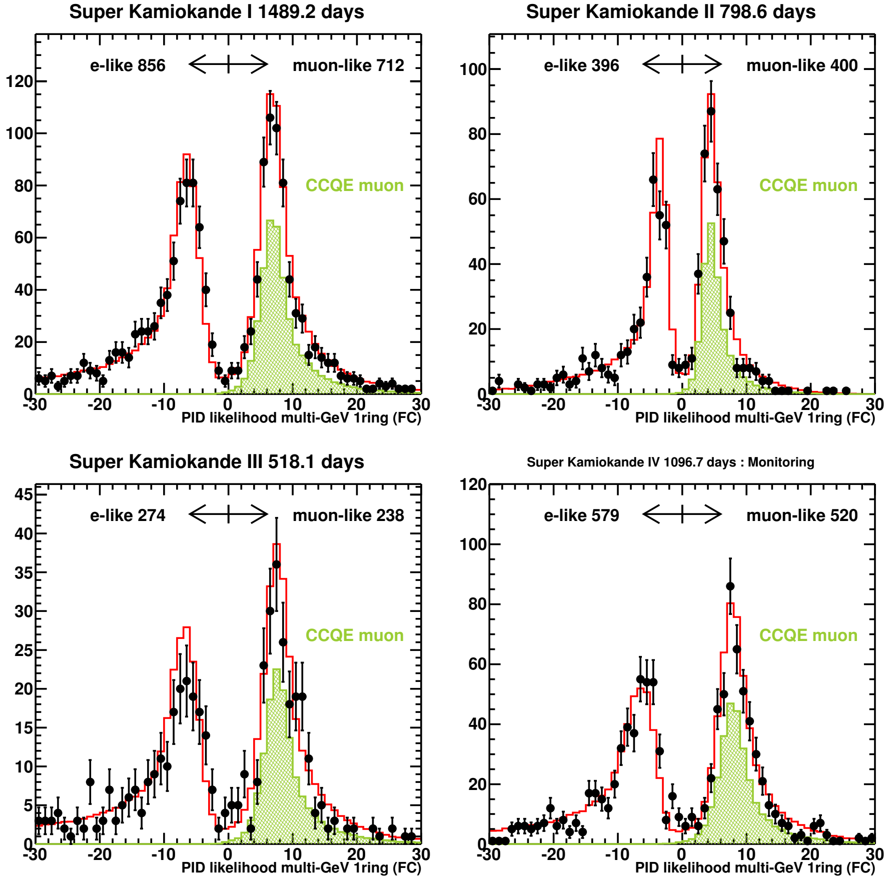

Figure 5.37: PID likelihood distribution for FC multi-GeV 1-ring samples for SK-I, SK-II, SK-III and SK-IV. Points represent the data, red lines represent Monte Carlo, the shaded green regions represent the MC CCQE ν_μ events.

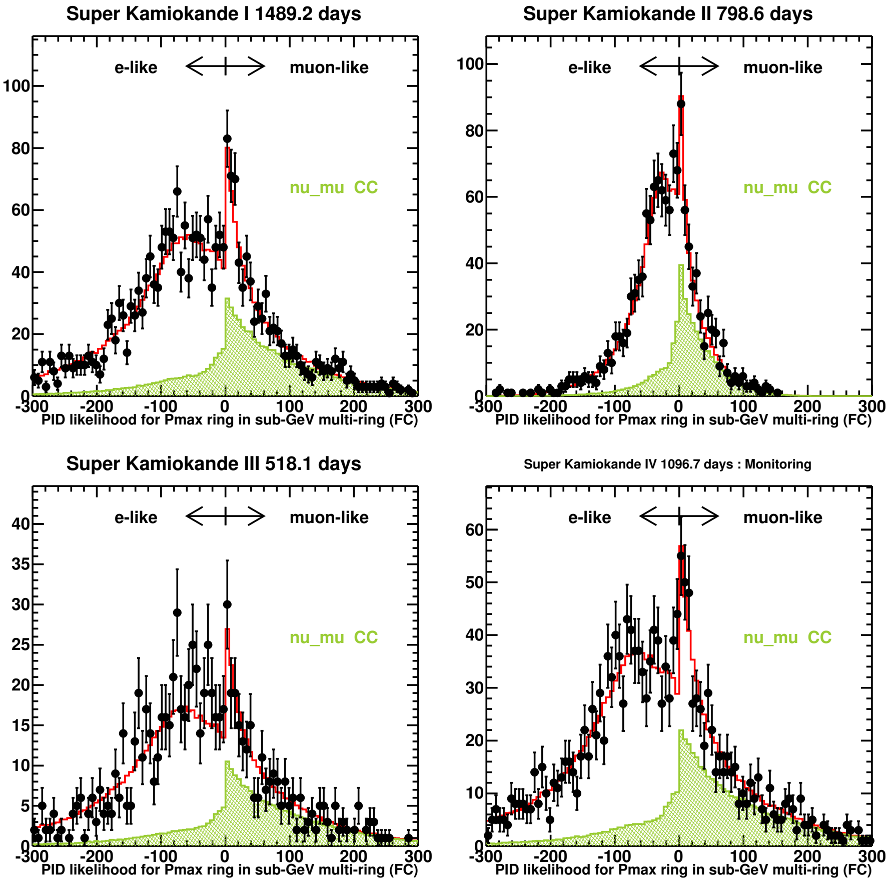

Figure 5.38: PID likelihood distribution for FC sub-GeV multi-ring samples for SK-I, SK-II, SK-III and SK-IV. Points represent the data, red lines represent Monte Carlo, the shaded green regions represent the MC CCQE ν_μ events.

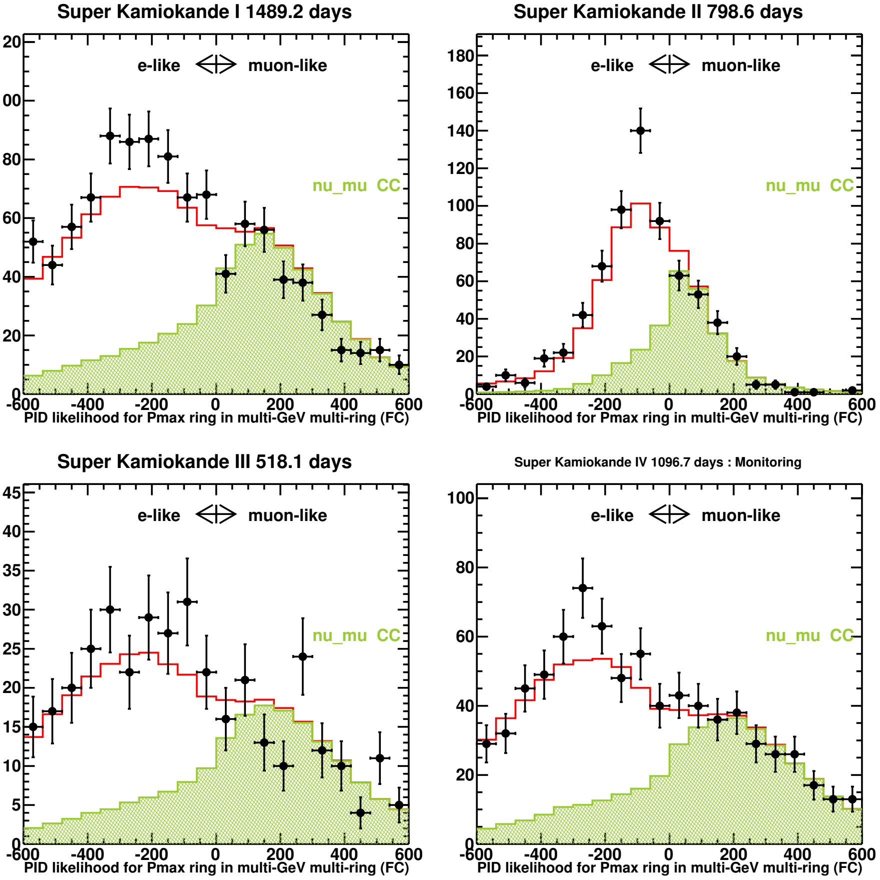

Figure 5.39: PID likelihood distribution for FC multi-GeV multi-ring samples for SK-I, SK-II, SK-III and SK-IV. Points represent the data, red lines represent Monte Carlo, the shaded green regions represent the MC CCQE ν_μ events.

5.4.4 Precise Vertex Fitting

Since Point-fit only uses timing information, FC/PC single-ring events are re-fitted to optimize their vertex position and direction by using expected light pattern as e-like or μ-like events. This precise vertex fitter is called MS-fit. UPMU events are also fitted by MS-fit assuming that the particle is a single-ring muon and the vertex is at the ID surface.

MS-fit adjusts the vertex position parallel to the particle direction obtained by Point-fit with timing information. The process is iterated until the changes in the vertex position and the particle direction is less than 5 cm and 0.5 degrees.

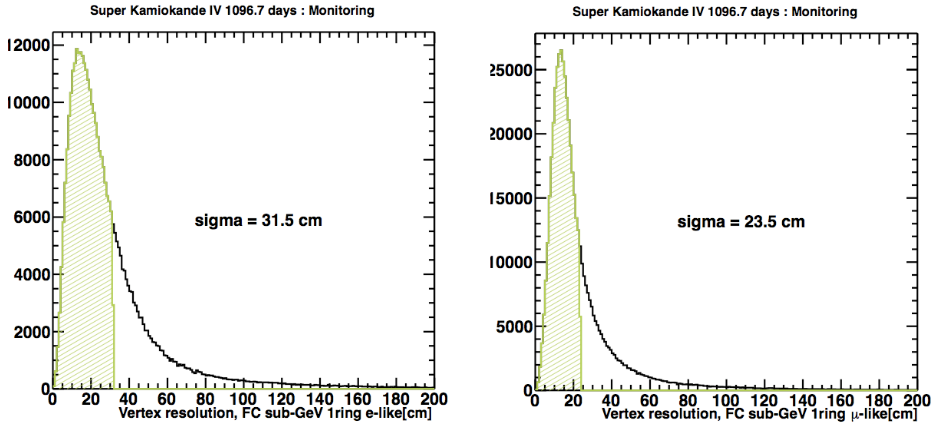

Figure 5.40: Distance between the true vertex and the reconstructed vertex of FC MC sample for SK-IV. Left: Sub-GeV 1-ring elike. Right: Sub-GeV 1-ring μ-like.

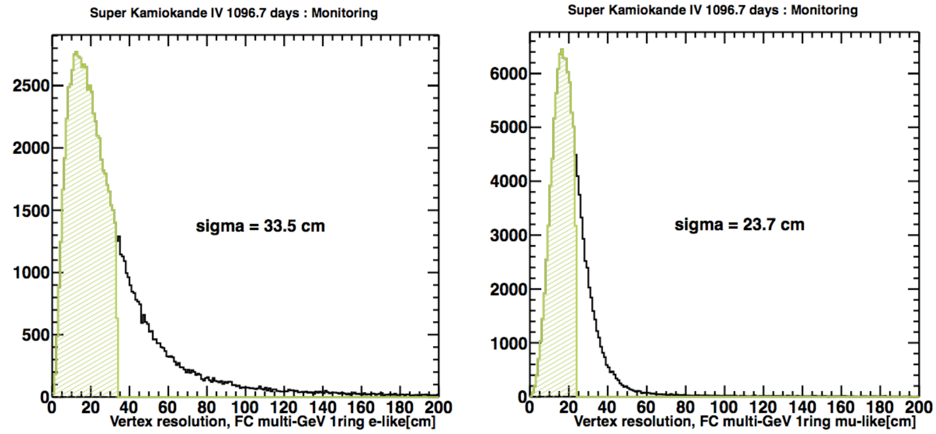

Figure 5.41: Distance between the true vertex and the reconstructed vertex of FC MC sample for SK-IV. Left: Multi-GeV 1-ring elike. Right: Multi-GeV 1-ring μ-like.

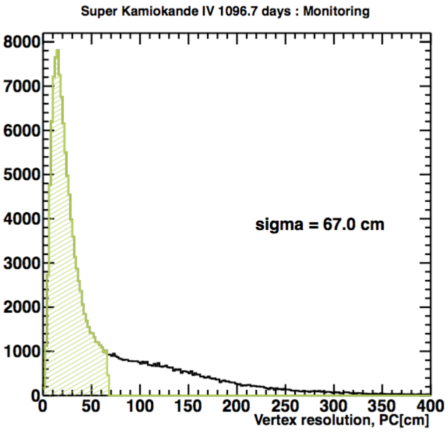

Figure 5.42: Distance between the true vertex and the reconstructed vertex of PC MC sample for SK-IV.

Performance of MS-fit for single-ring events is represented by the resolution which is estimated by using MC. Figure 5.40, figure 5.41 and figure 5.42 show the distance between the true vertex and the reconstructed vertex for single-ring samples. Figure 5.43 and figure 5.44 show the angular difference between true direction and the reconstructed direction.

Table 5.7 and table 5.8 summarize the estimated resolutions for different samples in each SK period.

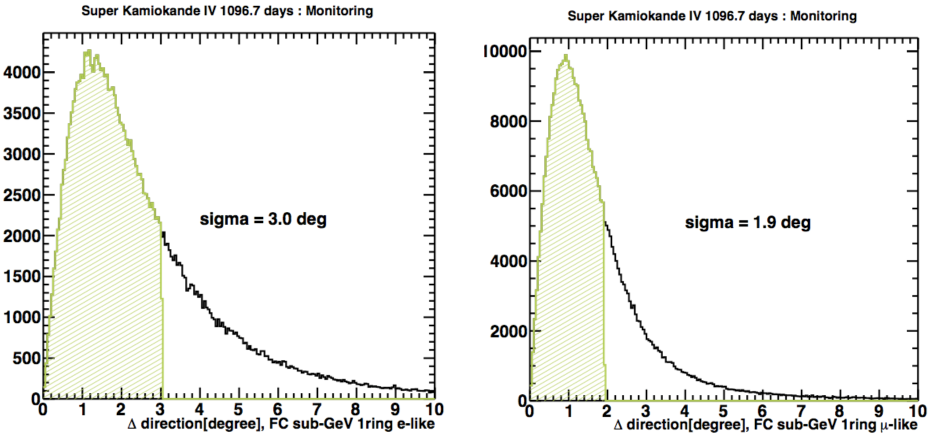

Figure 5.43: Angular difference between true direction and reconstructed direction of FC MC samples for SK-IV. Left: Sub-GeV 1-ring e-like. Right: Sub-GeV 1-ring μ-like.

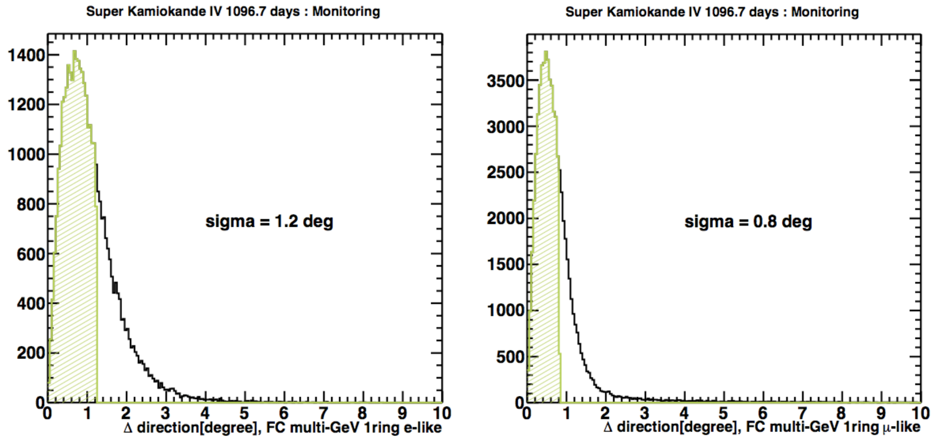

Figure 5.44: Angular difference between true direction and reconstructed direction of FC MC samples for SK-IV. Left: Mult-GeV 1-ring e-like. Right: Multi-GeV 1-ring μ-like.

Vertex resolution (cm)				
	SK-I	SK-II	SK-III	SK-IV
FC sub-GeV				
single-ring				
e-like	31.2	35.6	31.1	31.5
μ-like	23.8	30.3	23.9	23.5
FC multi-GeV				
single-ring				
e-like	33.5	34.3	33.4	33.5
μ-like	24.8	26.9	25.1	23.7
multi-ring				
μ-like	67.4	111.8	73.8	87.8
PC	53.6	62.8	52.6	67

Table 5.7: Vertex resolutions for each SK period.

Angular resolution (degree)				
	SK-I	SK-II	SK-III	SK-IV
FC sub-GeV				
single-ring				
e-like	3.1	3.2	3.0	3.0
μ-like	1.9	2.1	1.9	1.9
FC multi-GeV				
single-ring				
e-like	1.2	1.3	1.2	1.2
μ-like	0.8	1.0	0.8	0.8
PC	1.0	1.2	0.9	0.9

Table 5.8: angular resolutions for each SK period.

5.4.5 Momentum Reconstruction

Momentum for each particle is estimated by the observed p.e.s inside a Cherenkov cone with half opening angle of 70° (in order to include all the hits). In order to determine the momentum for individual rings, the observed p.e.s in hit PMTs are separated into contribution from each ring. Separation of the observed p.e.s is carried out based on the expected p.e. distribution from each ring as a function of the opening angle θ, assuming uniformity in azimuthal angle ϕ. The observed p.e.s in the i-th PMT from the n-th ring is estimated as:

$$q_{i,n}^{obs} = q_i^{obs} \times \frac{q_{i,n}^{exp}}{\sum_{n'} q_{i,n'}^{exp}} \tag{5.6}$$

where $q_{i,n}^{obs}$ is the fractional p.e.s from the n-th ring in the i-th PMT,
q_i^{obs} is the observed p.e.s in the i-PMT
$q_{i,n}^{exp}$ is the expected p.e.s.

To calculate the total number of p.e.s inside the 70° cone, the number of p.e.s in eac PMT is corrected considering the light attenuation and scattering in water, light reflection correction and the acceptance of PMTs as:

$$RTOT_n = \frac{G_{MC}}{G_{data}}[\alpha \times \sum_{\theta_{i,n}<70^\circ and -50nsec<t_i<250nsec} (q_i^{obs} \times exp(\frac{r_i}{L}) \times \frac{cos\Theta_i}{f(\Theta_i)}) - \sum_{\theta_{i,n}<70^\circ} S_i - \sum_{\theta_{i,n}<70^\circ} R_i] \tag{5.7}$$

where
α = normalization factor
G_{data}, G_{MC} = relative PMT gain parameters for data and MC
$\theta_{i,n}$ = opening angle between the n-th ring direction and the i-th PMT direction
t_i = photon time-of-flight subtracted hit timing of i-th PMT
L = light attenuation length in water
r_i = distance from the vertex position to i-th PMT
$f(\Theta_i)$ = correction function for the PMT acceptance as a function of photon incidence angle Θ_i
S_i = expected p.e.s for i-th PMT from scattered photons
R_i = correction for the reflected photons from black sheets in the detector

The summation is restricted to the time window -50 nsec to +250 nsec around the peak of the photon time-of-flight subtracted hit timing distribution to reject the effect from muon decay electrons. Attenuation length in water L is measured continuously by using cosmic ray through-going muons. The absolute energy scale is calibrated by using the four independent calibration sources as described in Chapter 4.

5.4.6 Decay Electron Search

Electrons may be produced from the decay of muons which stopped in the detector. π^+ produced by a neutrino interaction may decay into $\mu^\pm$ which in turn decays into e^+. Therefore, for example, if a muon decay is observed for a single-ring e-like event, the event is likely to be a CC-non QE ν_e event that produces π^+ along with an electron. Hence the information from decay-electrons is useful to determine the type of neutrino interactions. Decay-electrons are observed in a later independent time window (900 nsec) from that of the primary event or in the same time window of the primary event. If the decay occurs around 900 nsec, the electron event may be observed separately in the primary trigger or subsequent event trigger.

Detection efficiency of decay electron is 80% for μ^+ and 63% for μ^-, as approximately 20% of μ^- is captured by ^{16}O nuclei [138] for SK-I, SK-II and SK-III. As the detection efficiency of decay electrons is improved in SK-IV, the tagging efficiency is 96% for decay electrons from μ^+ and 83% for decay electrons from μ^-.

Note that detection efficiency of decay electron also includes low energy de-excitation gammas from μ^- captures. There is a cut from SK-I to SK-III to remove low energy events (in which most of them are de-excitation gammas from μ^- captures), and this cut is removed for SK-IV in order to improve the decay electron efficiency. This explains why the ratio of detection efficiencies of decay electrons from μ^+ to that from μ^- is larger for SK-IV when compared to SK-I to SK-III.

5.4.7 π^0 Reconstruction

π^0 reconstruction is applied to only single-ring e-like samples. In FC sub-GeV single-ring e-like event sample, the contamination by NC events is estimated to be about 9%. These NC events are mostly from NC single π^0 production. π^0 immediately decays into two gamma rays which produce two e-like Cherenkov rings. In case one of these two gammas is not detected due to too low energy or overlapping rings, the event can be misidentified to be single-ring e-like. In order to find these π^0 events, π^0 fitter reconstructs the second gamma ray on the assumption of existence of two Cherenkov rings by comparing the observed photoelectron distribution with the expected photoelectron distribution of two gamma rays. Then likelihood technique is used to determine the best-fit configuration of two gamma rays.

Chapter 6

Neutrino Oscillation Analysis

6.1 Overview

Atmospheric neutrino oscillation is studied with the information of detected neutrino momenta and directions. Observed data is compared with MC expectation by using a χ^2 method. In this chapter, data samples for this analysis and expected effects from the full oscillation on these samples are explained. Analysis method, systematic errors and results will be presented in this chapter.

6.2 Data Set

All data samples including FC, PC and UPMU are used for this analysis.

In order to separate CCQE, CC non-QE and NC events from 1-ring sample, FC sub-GeV 1-ring samples are further separated to sub-samples by considering number of muon decay-electrons.

In order to obtain higher purity of charged current e-like events in Multi-GeV multi-ring e-like sample, the sample is processed with likelihood method to reject NC events and μ-like events.

Multi-GeV e-like samples are further divided into ν_e and anti-ν_e-like samples, so as to improve the sensitivity to mass hierarchy.

These additional selection methods are described in the following sections.

6.2.1 Selection for Sub-GeV sample

FC sub-GeV single-ring e-like sample contains background events which are mainly NC π^0 events producing two gamma rays. In case one out of the two gamma rays is missed by the event reconstruction, the NC π^0 event would be identified as a single-ring e-like event, as the electromagnetic shower from gamma gives similar light pattern to that of an electron. In order to reduce this kind of background, a specialized π^0 fitter is used. This fitter reconstructs the second gamma-ray based on the first fitted ring. It predicts the light pattern resulting from two gamma rays propagating through the tank with the vertex of the fitted ring and the best fitted direction.

Figure 6.1 shows the invariant mass distributions from the π^0 fitter for CCQE (black solid lines) and NC (red dashed line) in FC sub-GeV single-ring e-like sample MC in five energy

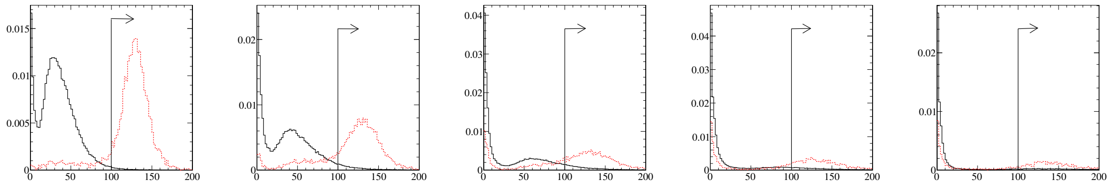

Figure 6.1: Distribution of invariant mass from the π^0 fitter for CCQE (black solid line) and NC (red dashed line) in SK-IV FC sub-GeV single-ring e-like MC events, in five energy regions (from left to right): (1) $P_e < 250$ MeV/c, (2) 250 MeV/c $\leq P_e < 400$ MeV/c, (3) 400 MeV/c $\leq P_e < 630$ MeV/c, (4) 630 MeV/c $\leq$ P $<$ 1000 MeV/c, (5) 1000 MeV/c $< P_e$. The arrows show the events which are taken to be π^0-like.

regions. NC events tend to form a peak near the π^0 mass while CCQE events do not. For events with electron momentum below 250 MeV/c, a cut at 100 MeV/c^2 of π^0 mass is used to create a π^0 sample. This cut is not efficient for events at higher electron momentum, so a likelihood selection is done by using three variables: fraction of the reconstructed momentum of the second ring, π^0 invariant mass and the difference of two likelihood variables which results from a π^0-fit and electron fit. Distribution of these three variables are shown in Figure 6.2 for each energy region starting from 250 MeV/c. The π^0-like selection likelihood functions are defined as:

$$L_{\pi^0} = \sum_{i=1}^{3} log(\Gamma_i^S(x_i)) - log(\Gamma_i^B(x_i)) \tag{6.1}$$

where $\Gamma_i^S(x_i)$ and $\Gamma_i^B(x_i)$ are CCQE (NC) events' probability distribution function (PDF) for the i^{th} variable with observable x.

After separating the π^0-like sample, the remaining e-like events are divided into two categories: 0-decay with no decay electrons and 1-decay with one or more decay electrons. As ν_e CCQE events are not expected to produce decay electrons, there is a high fraction of CCQE interactions in the 0-decay sample.

As for FC sub-GeV single-ring μ-like sample, there are three categories according to the number of decay electrons reconstructed: 0-decay, 1-decay and 2-decay (2 or more decay electrons). As these events produce one muon, so they are expected to have one decay electron. The fraction of CCQE events is high in 1-decay μ-like sample.

Table 6.1 shows the interaction mode compositions for FC sub-GeV samples.

		FC sub-GeV single-ring e-like 0-decay	 1-decay	 π^0-like	FC sub-GeV single-ring e-like
MC events		1932.9	196.1	95.9	2224.9
CC $\nu_e + \overline{\nu}_e$	Q.E.	81.5%	3.7%	13.0%	72.2%
	single meson	12.5%	56.0%	6.0%	16.2%
	multi π	0.9%	10.4%	1.0%	1.0%
	coherent π	1.0%	8.4%	0.4%	1.6%
CC $\nu_\mu + \overline{\nu}_\mu$		0.2%	12.1%	1.3%	1.3%
NC		3.9%	9.3%	78.2%	7.6%

		FC sub-GeV single-ring μ-like 0-decay	 1-decay	 2-decay	FC sub-GeV single-ring μ-like
MC events		365.8	1651.9	130.2	2147.9
CC $\nu_\mu + \overline{\nu}_\mu$	Q.E.	63%	79.6%	5.4%	72.3%
	single meson	11.7%	15.1%	69.3%	17.8%
	multi π	0.9%	1.3%	14.8%	2.0%
	coherent π	0.4%	1.1%	7.5%	1.4%
CC $\nu_e + \overline{\nu}_e$		5.4%	0.1%	0.05%	1.0%
NC		18.5%	2.8%	3.0%	5.5%

Table 6.1: Number of FC sub-GeV events and their compositions of neutrino interaction modes for SK-IV MC scaled to the SK-IV livetime 1097 days with 2-flavor oscillation with ($\sin^2 2\theta$, Δ_m) = (1.0, 2.5×10^{-3} eV^2). The upper (lower) table shows e-like (μ-like) samples. The right column shows the composition before separation into sub-samples. After the separation, the CCQE purity has increased.

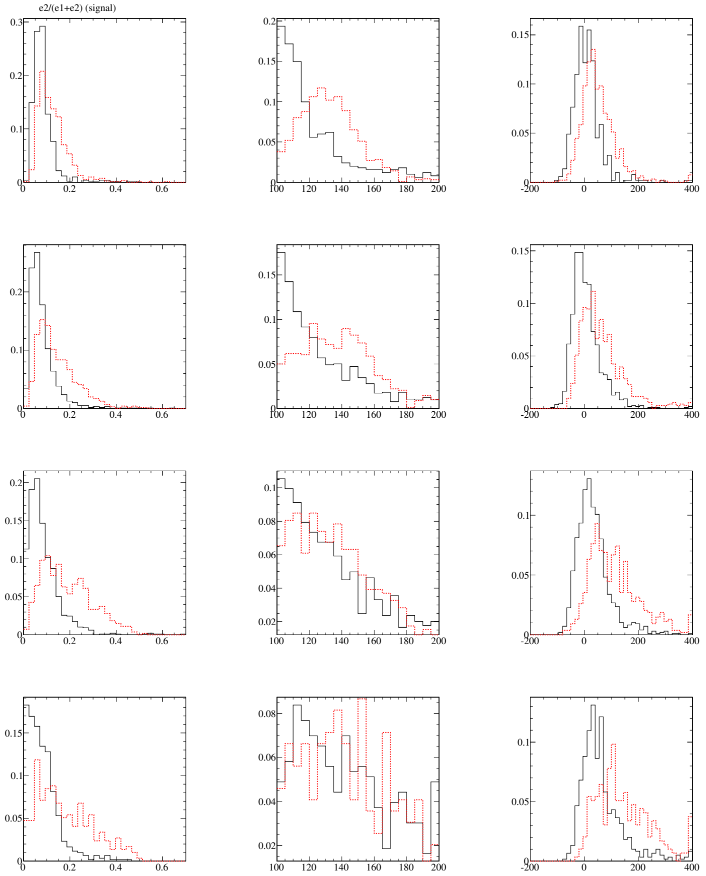

Figure 6.2: Distributions used in the π^0 selection for CCQE (black solid line) and NC (red dashed line) in SK-IV FC sub-GeV single-ring e-like MC events, in four energy regions (from top to bottom): (1) 250 MeV/c $\leq P_e <$ 400 MeV/c, (2) 400 MeV/c $\leq P_e <$ 630 MeV/c, (3) 630 MeV/c $\leq$ P $<$ 1000 MeV/c, (4) 1000 MeV/c $< P_e$. In order to select π^0-like and e-like events more efficiently, an additional likelihood selection is applied for events with momentum above 250 MeV/c. The distributions of the three likelihood variables used are shown: energy fraction carried by the second fitted ring (left column), the π^0 mass (middle column) and Δ-likelihood (right column). All distributions are normalized to the histogram area.

6.2.2 Selection for Multi-GeV Multi-Ring E-like Sample

In order to make CC $\nu_e + \overline{\nu}_e$-enriched Multi-GeV Mult-ring e-like (MME) sample, a selection is applied based on likelihood method. Four variables are used in this likelihood:

1. PID likelihood
2. momentum fraction of the most energetic ring
3. number of decay electrons
4. the distance between the neutrino vertex and any muon decay electrons.

Distributions of these variables are shown in Figure 6.3 for each energy region. Likelihood function is defined as:

$$L_{MME} = \sum_{i=1}^{4} log(\Gamma_i^S(x_i)) - log(\Gamma_i^B(x_i)) \tag{6.2}$$

where $\Gamma_i^S x_i(\Gamma_i^B x_i)$ represents the CCν_e and the background (CCν_μ and NC) events' PDF for the i^{th} variable with observable x_i.

This MME likelihood selection increases CCν_e purity and decrease background events (CC ν_μ events and NC events) significantly. Table 6.2 shows the interaction mode compositions for the cases without and with the MME likelihood.

Interaction mode composition	Without L_{MME}	With L_{MME}
CC $\nu_e + \overline{\nu}_e$	53.8%	75.5%
CC $\nu_\mu + \overline{\nu}_\mu$	21.5%	7.2%
NC	24.7%	17.3%
Total number of events	654.3	341.2

Table 6.2: Composition of interaction modes in case of with and without MME likelihood for SK-IV MC scaled to 1097 days. Two-flavor oscillations ($\sin^2 2\theta$, Δ_m) = (1.0, 2.5×10^{-3} eV^2) is assumed.

Due to the improved electronics in SK-IV, decay-electron tagging efficiency is improved and the charge dynamic range becomes wider in SK-IV, hence purity of CC$\nu_e + \overline{\nu}_e$ becomes higher in multi-GeV multi-ring e-like samples, as shown in Table 6.2 and 6.3 for SK-IV and SK-III respectively.

Interaction mode composition	Without L_{MME}	With L_{MME}
CC $\nu_e + \overline{\nu}_e$	53.0 %	74.1%
CC $\nu_\mu + \overline{\nu}_\mu$	22.0%	8.9%
NC	25.0%	17.1%
Total number of events	298.9	154.3

Table 6.3: Composition of interaction modes in case of with and without MME likelihood for SK-III MC scaled to 518.1 days. Two-flavor oscillations ($\sin^2 2\theta$, Δ_m) = (1.0, 2.5×10^{-3} eV^2) is assumed.

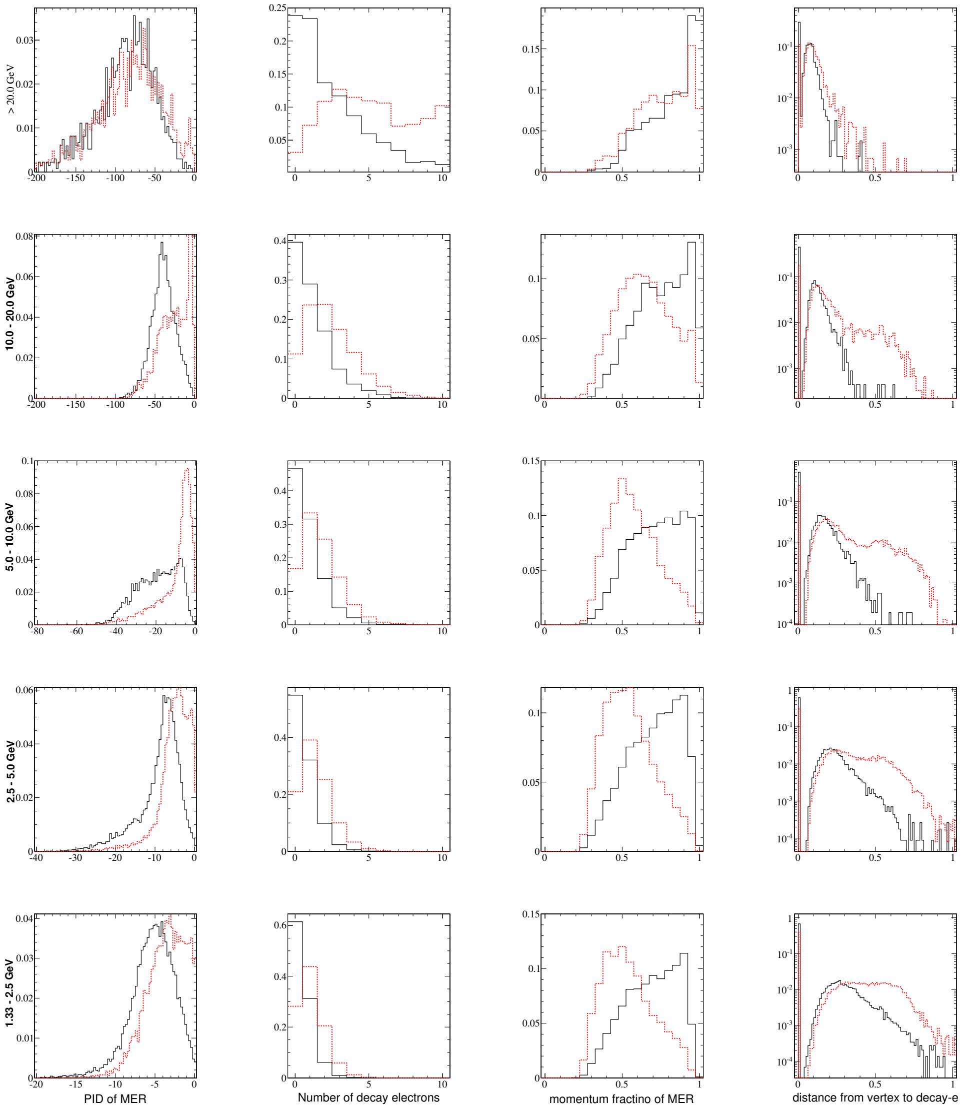

Figure 6.3: Distributions of the variables used in the multi-GeV multi-ring e-like (MME) likelihood for SK-IV. From left to write: PID of the most energetic ring, number of decay electrons, momentum fraction of the most energetic ring, distance between the vertex and the decay electron. From bottom to top, each plot represents an energy bins: (1) 1.33 - 2.5 GeV, (2) 2.5 - 5.0 GeV, (3) 5.0 - 10.0 GeV, (4) 10 - 20 GeV, (5) > 20 GeV. Energy bins correspond to the energy of the most energetic ring. Black solid line represents CC$\nu_e + \overline{\nu}_e$ and red dashed line represents CC$\nu_\mu + \overline{\nu}_\mu$ and NC. All distributions are normalized to the histogram area.

6.2.3 Separation of CCν_e and CC$\overline{\nu}_e$ events in Multi-GeV E-like samples

As the enhancement of electron neutrinos due to matter effect (as shown in figure 1.4) occurs for neutrinos in normal hierarchy and anti-neutrinos in inverted hierarchy, the sensitivity to mass hierarchy can be improved by further dividing multi-GeV e-like samples into ν_e and $\overline{\nu}_e$-like samples.

Multi-GeV Single-Ring E-like Sample

Due to the improved electronics in SK-IV, the charge dynamic range becomes wider in SK-IV, which helps to improve the PID, hence the purity of CC$\nu_e + \overline{\nu}_e$ becomes slightly higher in SK-IV when compared to previous SK periods, as shown in Table 6.4.

Interaction mode composition	SK-III	With SK-IV
CC $\nu_e + \overline{\nu}_e$	87.2%	88.1%
CC $\nu_\mu + \overline{\nu}_\mu$	3.4%	3.1%
NC	9.4%	8.8%
Total number of events	286.5	568.7

Table 6.4: Composition of interaction modes for multi-GeV single-ring e-like samples for SK-III and SK-IV respectively. Purity of CC$\nu_e + \overline{\nu}_e$ is higher for SK-IV due to the improvement in electronics in the SK-IV period.

In order to improve the sensitivity to mass hierarchy, this multi-GeV single-ring e-like sample is further divided into ν_e-like and $\overline{\nu}_e$-like samples by considering the difference in interactions of ν_e and $\overline{\nu}_e$ in water:

For CC ν_e:
$\nu_e + n \rightarrow e^- + N' +$ pions (Total charge for the N' and pion system is +1)
$\nu_e + p \rightarrow e^- + N' +$ pions (Total charge for the N' and pion system is +2)
where the pion further decays into

$$\begin{aligned} \pi^+ \rightarrow \quad & \mu^+ \quad +\nu + \mu \\ & \hookrightarrow \; e^+ + \nu_e + \overline{\nu}_\mu \end{aligned}$$

producing decay electrons.

For CC$\overline{\nu}_e$:
$\bar{\nu}_e + p \rightarrow e^+ + N' +$ pions (Total charge for the N' and pion system is 0)
$\bar{\nu}_e + n \rightarrow e^+ + N' +$ pions (Total charge for the N' and pion system is -1)
where π^- is more likely to be absorbed by water nuclei and hence no decay electrons are emitted. Therefore, by considering the number of decay electrons, multi-GeV single-ring e-like sample is further separated as follows:

$$\text{Number of decay electrons} > 0 \rightarrow \nu_e\text{-like}$$
$$\text{Number of decay electrons} = 0 \rightarrow \overline{\nu}_e\text{-like}$$

Figure 6.4 shows the number of decay electrons distribution for multi-GeV single-ring e-like sample in SK-IV. The arrows represent the cut described above. Table 6.5 shows the compositions of interaction modes in the separated multi-GeV single-ring ν_e-like sample and $\overline{\nu}_e$-like sample. The separation increases the composition of CCν_e in ν_e-like sample by 5.2% and that of CC$\overline{\nu}_e$ in $\overline{\nu}_e$-like sample by 6.1%.

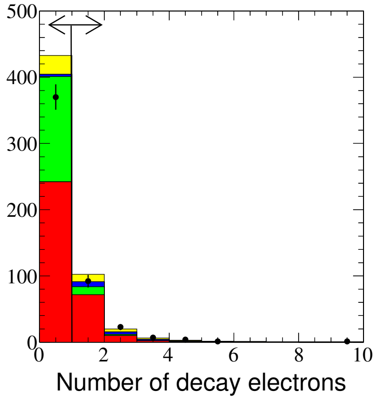

Figure 6.4: Distribution of number of decay electrons in both data and MC for SK-IV multi-GeV single-ring e-like sample. From bottom to top regions: CCν_e (red), CC$\overline{\nu}_e$ (green), CC$\nu_\mu + \overline{\nu}_\mu$ (blue) and NC (yellow). Data is represented by black dots. MC is normalized to data livetime 1097 days. Two-flavor oscillations ($\sin^2 2\theta$, Δ_m) = (1.0, 2.5×10^{-3} eV^2) is assumed. Events on left hand side of the arrow is taken as $\overline{\nu}_e$-like sample and those on the right hand side of the arrow is taken as ν_e-like sample.

Interaction mode	Without separation	ν_e-like	$\overline{\nu}_e$-like
CC ν_e	57.6%	62.8%	55.9%
CC $\overline{\nu}_e$	30.6%	10.8%	36.7%
CC$\nu_\mu + \overline{\nu}_\mu$	3.2%	10.6%	0.8%
NC	8.8%	15.7%	6.6%
Total	568.7	135.9	432.8

Table 6.5: Interaction mode composition of multi-GeV single-ring ν_e-like and $\overline{\nu}_e$-like samples for SK-IV. MC is normalized to data livetime 1097 days. Two-flavor oscillations ($\sin^2 2\theta$, Δ_m) = (1.0, 2.5×10^{-3} eV^2) is assumed. The separation increases the composition of CCν_e in ν_e-like sample by 5.2% and that of CC$\overline{\nu}_e$ in $\overline{\nu}_e$-like sample by 6.1%.

Multi-GeV Multi-Ring E-like Sample

Multi-GeV multi-ring e-like (MME) sample, after passing through the MME likelihood described in subsection 6.2.2, the sample is passed through another likelihood to separate into

ν_e-like and $\bar{\nu}_e$-like samples. Unlike the multi-GeV single-ring e-like sample which is separated into ν_e-like and $\bar{\nu}_e$-like samples with a simple cut depending on number of decay electrons, a likelihood method is used, the MME sample is passed through another likelihood for the separation of ν_e-like and $\bar{\nu}_e$-like events.

Figure 6.5 shows the interaction of an incoming ν_e with initial energy E with water nuclei and the outgoing electron carries energy E'. Feynman y of the interaction is defined as:

$$y = \frac{E' - E}{E} \tag{6.3}$$

As Feynman y distribution is larger for CCν_e than for CC$\overline{\nu}_e$, the outgoing electrons from CCν_e interaction with water nuclei tend to have smaller energy. This implies:

- CCν_e has smaller momentum fraction for the most energetic ring than CC$\overline{\nu}_e$
- CCν_e has more number of rings than CC$\overline{\nu}_e$
- CCν_e has larger transverse momentum than CC$\overline{\nu}_e$
- CCν_e has more decay electrons than CC$\overline{\nu}_e$

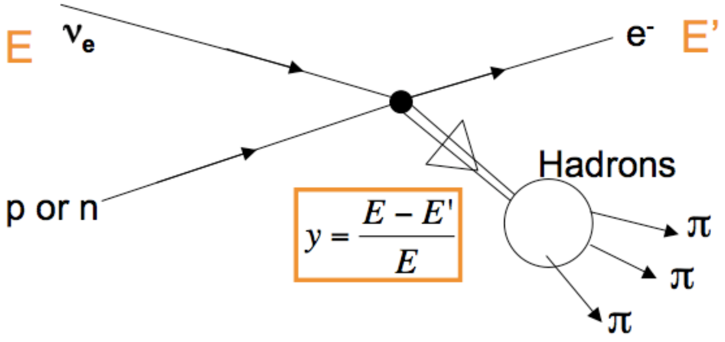

Figure 6.5: Diagram showing the interaction of ν_e with the nuclei in water, and the Feynman y = (E'-E)/E where E is the initial energy of the incoming ν_e and E' is the energy of the outgoing electron.

By using the above properties, a likelihood is newly made for the separation into ν_e-like and $\bar{\nu}_e$-like samples. In the ν_e and $\bar{\nu}_e$ separation, the following parameters are used.

1. number of decay electrons
2. number of rings
3. transverse momentum

Figure 6.6 shows the distributions of the variables used in the ν_e and $\overline{\nu}_e$ separation likelihood for SK-IV in each energy region. Likelihood functions are defined as:

$$L_{\nu_e/\overline{\nu}_e} = \sum_{i=1}^{3} log(\Gamma_i^S(x_i)) - log(\Gamma_i^B(x_i)) \tag{6.4}$$

where $\Gamma_i^S(x_i)$ $(\Gamma_i^B(x_i)) representsCC\nu_e$ (CC$\overline{\nu}_e$) events' PDF for the i^{th} variable with observable x_i.

Figure 6.7 shows the likelihood distribution for SK-IV MC events, in which the separation is made at $L_{\nu_e/\overline{\nu}_e} = 0$. Table 6.6 shows the compositions of interaction modes in the separated multi-GeV multi-ring ν_e-like sample and $\overline{\nu}_e$-like sample. The separation increases the composition of CCν_e in ν_e-like sample by 3.3% and that of CC$\overline{\nu}_e$ in $\overline{\nu}_e$-like sample by 1.5%.

Interaction mode	Without separation	ν_e-like	$\overline{\nu}_e$-like
CC ν_e	56.1%	59.4%	53.1%
CC $\overline{\nu}_e$	19.5%	17.9%	21.0%
CC$\nu_\mu + \overline{\nu}_\mu$	7.2%	8.3%	6.1%
NC	17.3%	14.4%	19.8%
Total	341	161.9	168.1

Table 6.6: Interaction mode composition of multi-GeV multi-ring ν_e-like and $\overline{\nu}_e$-like samples for SK-IV. MC is normalized to data livetime 1097 days. Two-flavor oscillations ($\sin^2 2\theta$, Δ_m) = (1.0, 2.5×10^{-3} eV^2) is assumed. The separation increases the composition of CCν_e in ν_e-like sample by 3.3% and that of CC$\overline{\nu}_e$ in $\overline{\nu}_e$-like sample by 1.5%.

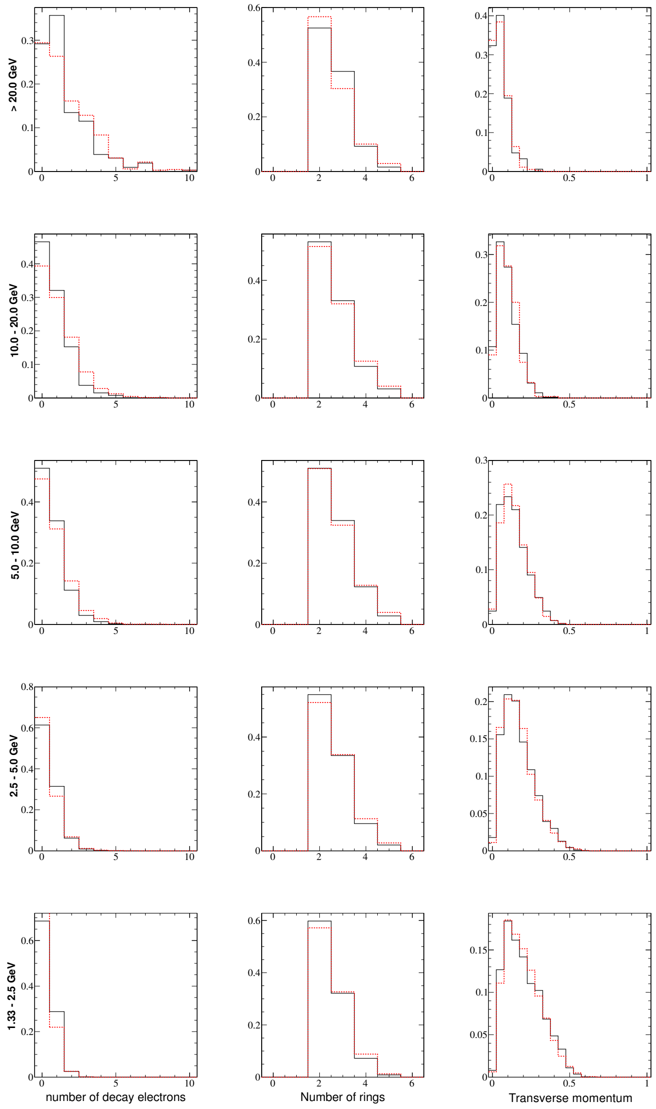

Figure 6.6: Distributions of the variables used in the MME ν_e and $\overline{\nu}_e$ separation likelihood for SK-IV. From left to right: number of decay electrons, number of rings, momentum fraction of the most energetic ring. From bottom to top, there are five energy bins: (1) 1.33 - 2.5 GeV, (2) 2.5 - 5.0 GeV, (3) 5.0 - 10.0 GeV, (4) 10 - 20 GeV, (5) $>$ 20 GeV. Energy bins correspond to the energy of the most energetic ring. Black solid line represents CCν_e and red dashed line represents CC$\overline{\nu}_e$. All distributions are normalized to the historgram area. Area of the histograms are normalized to their corresponding areas.

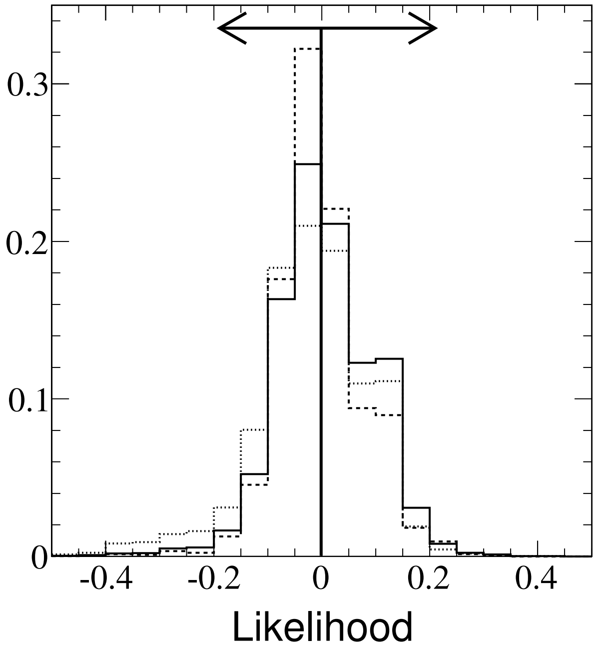

Figure 6.7: Distribution of the ν_e and $\overline{\nu}_e$ separation likelihood for SK-IV 500 years MC. Solid line represents CC ν_e, dashed line represents CC$\overline{\nu}_e$ and dotted line represents NC events. The arrow shows the cut which is made at 0. For events having $L_{\nu_e/\overline{\nu}_e} > 0$, they are taken as ν_e-like events, and for events having $L_{\nu_e/\overline{\nu}_e} < 0$, they are taken as $\overline{\nu}_e$-like events.

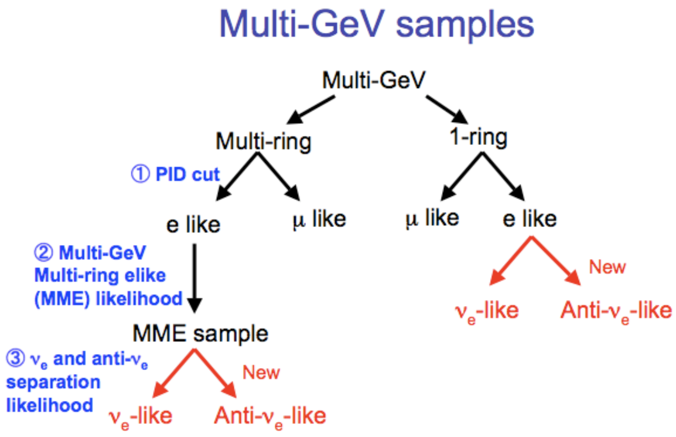

Figure 6.8: Summary of selection steps for the Multi-GeV e-like samples.

Summary for Multi-GeV E-like Samples Selection

Figure 6.8 shows the schematic diagram which summarizes the steps for selection of Multi-GeV e-like samples.

6.2.4 Data Set For the Oscillation Analysis

In summary, data sets for the analysis are listed as follows:

1. FC sub-GeV single-ring e-like 0-decay electron sample
   single-ring identified as e-like
   $p_e > 100$ MeV/c
   $E_{vis} < 1.33$ GeV
   without any decay electrons

2. FC sub-GeV single-ring e-like 1-decay electron sample
   single-ring identified as e-like
   $p_e > 100$ MeV/c
   $E_{vis} < 1.33$ GeV
   with one decay electron

3. π^0-like sample
   single-ring identified as e-like
   $p_e > 100$ MeV/c
   $E_{vis} < 1.33$ GeV
   fitted as π^0-like by π^0-fitter and π^0 likelihood

4. FC sub-GeV single-ring μ-like 0-decay electron sample
   single-ring identified as μ-like

$p_\mu > 200$ MeV/c
$E_{vis} < 1.33$ GeV
without any decay electrons

5. FC sub-GeV single-ring μ-like 1-decay electron sample
   single-ring identified as μ-like
   $p_\mu > 200$ MeV/c
   $E_{vis} < 1.33$ GeV
   with one decay electron

6. FC sub-GeV single-ring μ-like 2-decay electron sample
   single-ring identified as μ-like
   $p_\mu > 200$ MeV/c
   $E_{vis} < 1.33$ GeV
   with two or more decay electrons

7. FC sub-GeV 2-ring π^0-like sample
   Two rings are recognized and both of them are identified as e-like
   No decay electrons

8. FC multi-GeV single-ring ν_e-like sample
   single ring identified as e-like
   $E_{vis} > 1.33$ GeV
   Number of decay electrons > 0

9. FC multi-GeV single-ring $\overline{\nu}_e$-like sample
   single ring identified as e-like
   $E_{vis} > 1.33$ GeV
   Number of decay electrons $= 0$

10. FC multi-GeV single-ring μ-like sample
    single ring idenfied as μ-like
    $E_{vis} > 1.33$ GeV

11. FC multi-GeV multi-ring ν_e-like sample
    Most energetic ring identified as e-like
    $E_{vis} > 1.33$ GeV
    Events that passed through the MME likelihood cut
    Events that have ν_e and $\overline{\nu}_e$ separation likelihood > 0

12. FC multi-GeV multi-ring $\overline{\nu}_e$-like sample
    Most energetic ring identified as e-like
    $E_{vis} > 1.33$ GeV
    Events that passed through the MME likelihood cut
    Events that have ν_e and $\overline{\nu}_e$ separation likelihood < 0

13. FC multi-GeV multi-ring μ-like sample
    Most energetic ring identified as μ-like
    Momentum $p_\mu > 600$ MeV/c
    $E_{vis} > 600$ MeV

14. PC OD stopping sample
    Maximum number of p.e.s observed in OD in a sliding 500 nsec time window from -400 nsec to $+600$ nsec (PE_{anti}) is less than $\mathrm{PE}_{exp}/1.5$.
    The most energetic ring or the second one is identified as μ-like.

15. PC OD through-going sample
    Remaining of the PC events after the OD stopping events are selected in the above step.

16. Upward stopping muon sample
    Classified as stopping event by fitter
    Number of hit OD PMTs within 8 m from the exit point (NHITEX) < 10 for SK-I, SK-III and SK-IV (16 for SK-II)
    Fitted momentum ≥ 1.6 GeV/c

17. Upward muon through-going showering sample
    Classified as through-going event by fitter
    Number of hit OD PMTs within 8 m from the exit point (NHITEX) ≥ 10 for SK-I, SK-III and SK-IV (16 for SK-II)
    Distance from the entrance point to the exit point ≥ 7 m.
    Difference between average corrected charge and the expected charge for non-showering muon ($\Delta(Q) = <Q> - q_l$) > 0.5 when χ^2 valuable for showering selection ≥ 50
    $\Delta(Q) > 4.5 - 0.08\chi^2$ when $\chi^2 < 50$.

18. Upward muon through-going non-showering sample
    Classified as through-going event by fitter
    Number of hit OD PMTs within 8 m from the exit point (NHITEX) ≥ 10 for SK-I, SK-III and SK-IV (16 for SK-II)
    Distance from the entrance point to the exit point ≥ 7 m.
    Remaining of the UPMU events after the showering event selection.

In this analysis, FC, PC and UPMU data during:

- SK-I, with livetime of 1489.2 days for FC and PC, 1645.9 days for UPMU
- SK-II, with livetime of 798.6 days for FC and PC, 827.7 days for UPMU
- SK-III, with livetime of 518.1 days for FC and PC, 635.6 days for UPMU
- SK-IV with livetime of 1097 days for FC and PC, 1096.7 days for UPMU

The livetime is determined by the requirement of good detector condition. As the reconstruction of long pathlength muon for UPMU is less affected by detector condition, the livetime is in general longer than that for FC and PC. The amount of simulated MC atmospheric neutrino events are equivalent to SK exposure of 500 years for FC and PC, 200 years for UPMU for each SK run period. Table 6.7 summarizes the number of events in each categorized event sample for both data and MC in each SK period.

	SK-I		SK-II		SK-III		SK-IV	
	Data	MC	Data	MC	Data	MC	Data	MC
FC sub-GeV								
single-ring								
e-like								
0-decay	2992	2705.4	1573	1445.4	1092	945.3	2098	1934.9
1-decay	301	248.1	172	138.9	118	85.3	243	198.4
π^0-like	176	160.0	111	96.3	58	53.8	116	96.2
μ-like								
0-decay	1025	893.7	561	501.9	336	311.8	405	366.3
1-decay	2012	1883.0	1037	1006.7	742	664.1	1833	1654.1
2-decay	147	130.4	86	71.3	61	46.6	174	132.2
2-ring π^0-like	524	492.8	266	259.8	182	172.2	380	355.9
FC multi-GeV								
single-ring								
ν_e-like	191	152.8	79	78.4	68	54.9	156	135.9
$\overline{\nu}_e$-like	665	656.2	317	349.5	206	231.6	423	432.8
μ-like	712	775.3	400	415.7	238	266.4	420	554.8
multi-ring								
ν_e-like	216	224.7	143	121.9	65	81.8	175	161.9
$\overline{\nu}_e$-like	227	219.7	134	121.1	80	72.4	212	179.1
μ-like	603	640.1	337	337.0	228	231.4	479	499.0
PC								
OD stopping	143	141.4	77	71.3	54	52.0	109	115.0
OD through-going	759	772.4	350	377.3	290	304.0	626	629.9
UPMU								
stopping	435.9	388.3	241.2	210.1	193.7	210	286.7	248.7
non-showering	1564.4	1306.3	725.3	687.7	612.9	486.3	1047.6	847.6
showering	271.6	285.1	108.1	106.9	110	123.2	282.9	f 209.2

Table 6.7: Summary of number of events for both data and MC in each SK run period. Number of MC events is normalized by data livetime, assuming 2-flavor mixing at $(\Delta m^2_{23}, \sin^2\theta_{23}) = (2.1 \times 10^{-3}, 0.5)$.

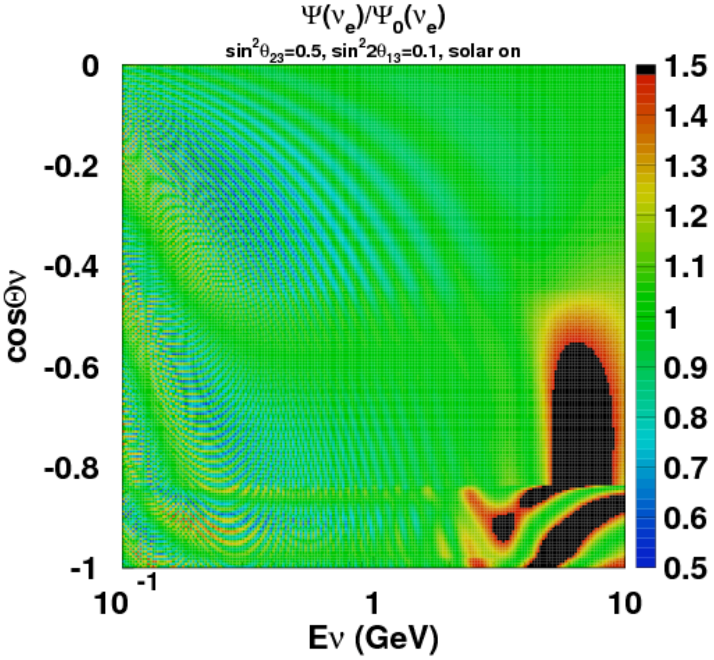

Figure 6.9: Flux ratio of electron neutrino for oscillations with parameters (Δm^2_{12}, Δm^2_{32}, $\sin^2\theta_{12}$, $\sin^2\theta_{23}$, $\sin^2\theta_{13}$, δ_{CP}) = (7.6×10^{-5}, 2.4×10^{-3}, 0.31, 0.5, 0.025, 220°). The flux ratio is the comparison between flux with and without oscillation.

6.3 Oscillation Effect

As discussed in Section 1.3, electron neutrino oscillation is observable by sub-dominant oscillation. Figure 6.9 shows the expected flux ratio at the detector for electron neutrino as a function of zenith angle (y-axis) and energy (x-axis). The expected events are calculated with both disappearance and appearance oscillation probabilities. Figure 6.9 shows flux ratio for electron neutrino at (Δm^2_{12}, Δm^2_{32}, $\sin^2\theta_{12}$, $\sin^2\theta_{23}$, $\sin^2\theta_{13}$, δ_{CP}) = (7.7×10^{-5}, 2.4×10^{-3}, 0.31, 0.5, 0.025, 220°). For electron neutrino, the oscillation effect due to θ_{13} is dominant from a few GeV to 10 GeV.

In multi-GeV region, resonance enhancement of $\nu_\mu \to \nu_e$ ($\overline{\nu}_\mu \to \overline{\nu}_e$) oscillation due to non-zero θ_{13} is expected for normal hierarchy (inverted hierarchy) in the upward direction, while there is no enhancement for inverted hierarchy (normal hierarchy). Therefore, by separation the multi-GeV e-like samples into ν_e-like and $\overline{\nu}_e$-like samples (as described in section 6.2.3), the enhancement is expected to be seen in ν_e-like samples in case of normal hierarchy, while the enhancement is expected to be seen in $\overline{\nu}_e$-like samples in case of normal hierarchy. Hence by tagging the increase in number of upward events in these samples, mass hierarchy can be probed. Figure 6.10 shows the zenith angle distribution of ratio of number of events with oscillation (at (Δm^{12}, Δm^2_{32}, $\sin^2\theta_{12}$, $\sin^2\theta_{13}$, δ_{CP}) = (7.6×10^{-5} eV^2, 2.4×10^{-3} eV^2, 0.31, 0.025, 40°)) to that without oscillation. The enhancement can be seen in the upward direction (-1 $< \cos\theta <$ 0), and a sizable difference can be seen between the normal hierarchy (dashed line) and the inverted hierarchy (solid line). Moreover, as the absolute cross section and $d\sigma/dy$ (where y is Feynman y = $(E_\nu - E_{lepton})/E_\nu$) are different between neutrinos and anti-neutrinos, upward electron neutrino appearance observed in the detector is larger in normal hierarchy case than that in the inverted hierarchy case as shown by the dashed lines (normal hierarchy) being above the solid line (inverted hierarchy) in Figure 6.10.

CP phase also change the sub-dominant effects. Figure 6.11 shows the zenith angle distributions of ratio of number of events with to that without oscillations at three different CP phase values. The plots show that the enhancement is dependent on the value of δ_{CP}. Hence by studying the excess in upward direction in sub-GeV e-like 0-decaye and multi-GeV elike samples, δ_{CP} may also be probed.

In this analysis, an algebraical computation for neutrino oscillation analysis described in [139] is used. Earth density is mesaured by seismic velocity observation. Density described in [140] is used.

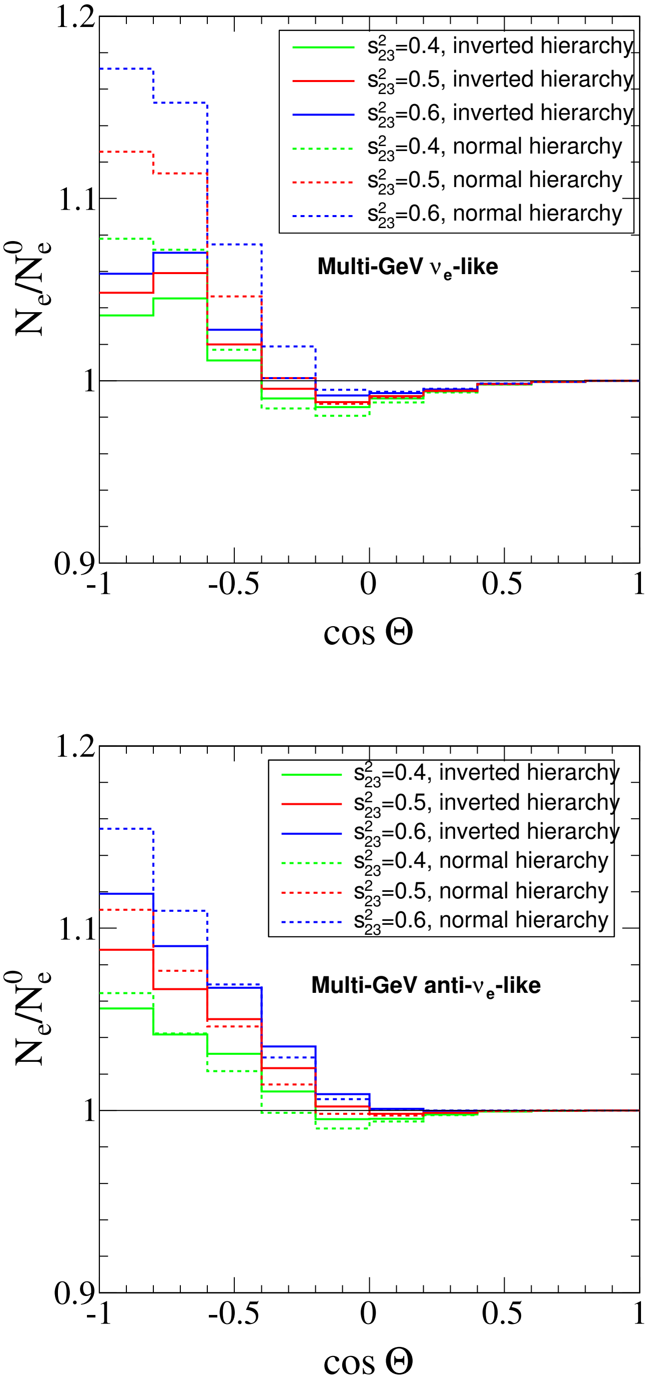

Figure 6.10: Zenith angle distribution for multi-GeV single-ring + multi-ring ν_e-like (top) and multi-GeV single-ring + multi-ring $\overline{\nu}_e$-like (bottom) samples in SK-IV. The y-axis shows the number of events with oscillations divided by the number of events without oscillations. Oscillation paramters are (Δm^2_{12}, Δm^2_{32}, $\sin^2\theta_{12}$, $\sin^2\theta_{13}$, δ_{CP}) = (7.6×10^{-5} eV^2, 2.4× 10^{-3} eV^2, 0.31, 0.025, 40°). Oscillations at different values of $\sin^2\theta_{23} = 0.4$ (green), 0.5 (red), 0.6 (blue) for normal hierarchy (dashed line) and inverted hierarchy (solid line) are shown.

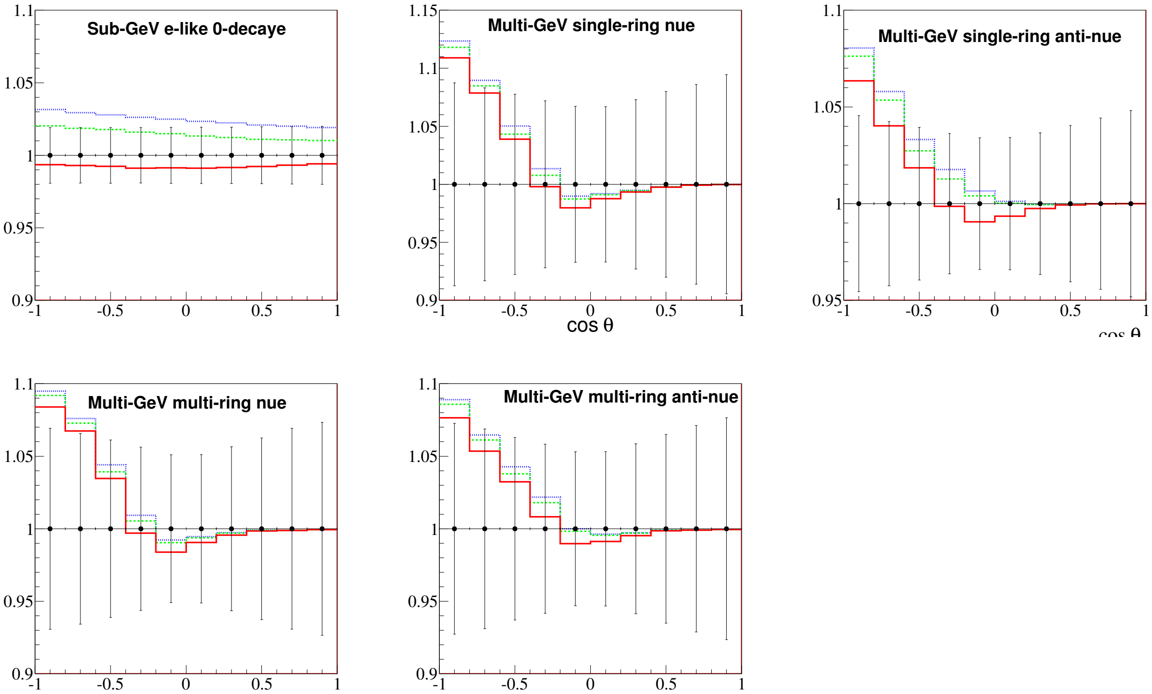

Figure 6.11: Zenith angle distributions of the ratio of number of events with oscillation to that without oscillation, assuming oscillation parameters $(\Delta m^2_{12},\ \Delta m^2_{32},\ \sin^2\theta_{12},\ \sin^2\theta_{23}, sin^2\theta_{13}) = (7.7 \times 10^{-5},\ 2.66 \times 10^{-3},\ 0.30,\ 0.425,\ 0.025)$ in normal hierarchy case for SK-IV. Cases with $\delta_{CP} = 80^\circ$ (blue dotted line), 220° (red solid line) and 300° (green dashed line) are shown. The error bars represent the size of the error with SK-I + SK-II + SK-III + SK-IV data livetime.

6.4 Analysis Method

In order to examine the neutrino oscillation parameters, data are compared with MC expectation by using a pull χ^2 method based on Poisson probability distribution.

6.4.1 Definition of χ^2

Assume that there are n bins for data, the likelihood can be defined as [136]:

$$L(N^{exp}, N^{obs}) = \prod_{i=1}^{n} \frac{e^{-N_i^{exp}} N_i^{exp N_i^{obs}}}{N_i^{obs}!} \tag{6.5}$$

where
N_i^{obs} is the number of observed events in the i-th bin

N_i^{exp} is the expected number of events (MC) in the i-th bin.

χ^2 is given by the log likelihood ratio:

$$\chi^2 \equiv -2\ln\frac{L(N^{exp}, N^{obs})}{L(N^{obs}, N^{obs})} = 2\sum_{i=1}^{n}(N_i^{exp} - N_i^{obs} + N_i^{obs}\ln\frac{N_i^{obs}}{N_i^{exp}} \tag{6.6}$$

The effect of systematic uncertainties are included into the bin with "pull approach" [151]. The number of expected events in a bin is allowed to vary according to the systematic uncertainties, so N_i^{exp} is replaced as:

$$N_i^{exp} \rightarrow N_i^{exp}(1 + \sum_j^m f_j^i \epsilon_j) \tag{6.7}$$

where
ϵ_j is a variation of j-th systematic uncertainty.
f_j^i is the fractional change of the event rate in the i-th bin due to the j-th systematic uncertainty.
m is the total number of systematic uncertainties.

For each uncertainty, $_j$ is determined during the fitting to χ^2 and the quantity $\epsilon_j/\sigma_j^{sys}$ follow Gaussian distribution, where σ_j^{sys} is the 1σ value of the j-th systematic uncertainty. In order to constrain the range of σ_j, an additional term

$$\sum_j^m(\frac{\epsilon_j}{\sigma_j^{sys}})^2 \tag{6.8}$$

is added to equation 6.6.

Therefore, χ^2 is defined as:

$$\chi^2 \equiv 2\sum_i[(N_i^{exp}(1 + \sum_j f_j^i\epsilon_j) - N_i^{obs}) + N_i^{obs}ln(\frac{N_i^{obs}}{N_i^{exp}(1 + \sum_j f_j^i\epsilon_j)})] + \sum_j(\frac{\epsilon_j}{\sigma_j^{sys}})^2 \tag{6.9}$$

Explanation about the systematic errors would be presented in the next section.

At the minimum χ^2 location for each combination of oscillation parameters, each of the parameter ϵ_j is estimated according to $\partial\chi^2/\partial\epsilon_j = 0$. Hence the minimization of χ^2 in equation 6.9 is equivalent to solving the following equation for every ϵ_j [141]:

$$\sum_{j=1}\left(\frac{1}{(\sigma_j^{sys})^2}\delta_{jk} + \sum_{i=1} N_j^{obs} f_j^i f_k^i\right)\epsilon_j = \sum_{i=1}\left((1 + (\sum_{j=1} f_j^i \epsilon_j)^2 - ...)N_i^{obs} - N_i^{exp}\right) f_k^i \tag{6.10}$$

In order to ensure a proper function in equation 6.9, the binning is defined such that there are at least 5 expected MC events for each bin after scaling to data livetime. The binning is defined by zenith angle and momentum information as shown in figure 6.12. All sub-GeV samples are divided into 5 momentum bins. Sub-GeV e-like 0-decay, μ-like 0-decay and 1-decay samples are divided into 10 zenith angle bins. All multi-GeV samples (FC, PC and UPMU) are all divided into 10 zenith angle bins. The total number of bins is 480 for each SK-I, SK-II, SK-III and SK-IV period.

SK-I, SK-II, SK-III and SK-IV bins are merged after evaluating the systematic error parameters by equation 6.10:

$$\begin{aligned} N_i^{obs} &\rightarrow \sum_i N_{i,SKn}^{obs} \\ N_i^{exp}(1 + \sum_j f_j^i \epsilon_j) &\rightarrow \sum_n N_{i,SKn}^{exp}(1 + \sum_j f_j^i \epsilon_j) \end{aligned}$$

Systematic error coefficients for each SK period are computed and their effects specific to each SK period are properly taken into account.

6.5 Systematic Uncertainties

Details of systematic error terms and best fit results of the error parameter ϵ_j is described in this section.

151 systematic error parameters are used in this analysis, among which 19 are errors related to neutrino flux model, 20 are related to neutrino interactions, 17 x 4 = 68 are related to event reduction and 11 x 4 = 44 are related to event reconstruction and selection.

The best fit systematic uncertainty parameters ϵ_j for the fit in normal hierarchy case are summarized with the estimated 1σ value (σ_j^{sys}) for each systematic error term from tables 6.8 to 6.14.

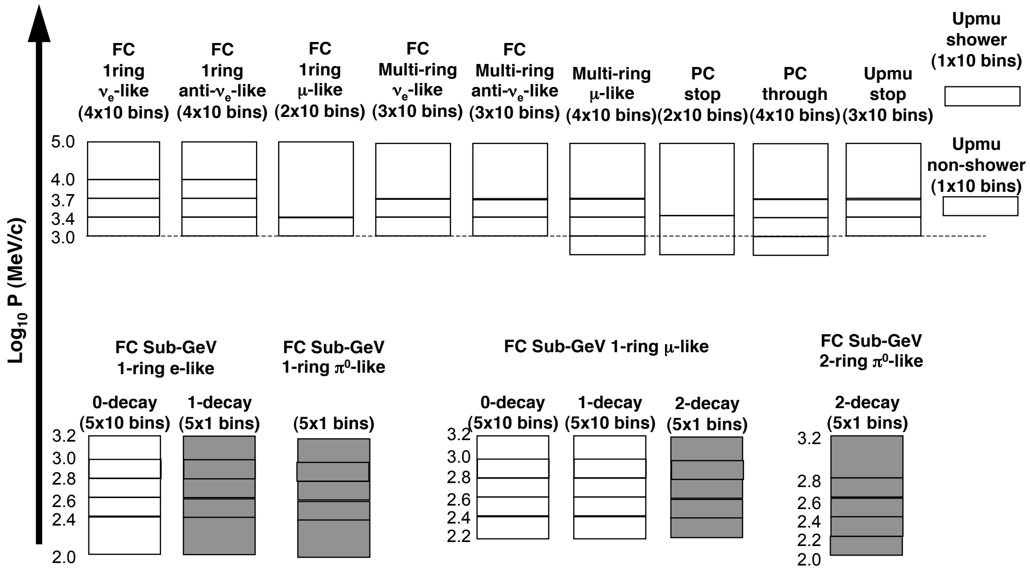

Figure 6.12: Definition of the binning used in the neutrino oscillation analysis. FC: 370 bins, PC: 60 bins, UPMU: 50 bins. White boxes indicate that momentum bin is divided into 10 zenith angle bins between -1 $< \cos\theta <$ 1 for FC and PC, -1 $< \cos\theta <$ 0 for UPMU. Shaded boxes indicate the momentum bin is not further divided into zenith angle bins. FC single-ring e-like 1-decay, π^0-like, μ-like 2-decay samples and 2-ring π^0 sample are not divided into zenith angle bins.

Systematic error related to neutrino flux		Fit value (%)	σ(%)
Flux normalization	$E_\nu < 1$ GeV	32.50	25[a]
	$E_\nu > 1$ GeV	18.33	15[b]
$(\nu_\mu + \overline{\nu_\mu})/(\nu_e + \overline{\nu_e})$			
	$E_\nu < 1$ GeV	-0.43	2
	$1 < E_\nu < 10$ GeV	-1.46	3
	$E_\nu > 10$ GeV	0.83	5[c]
$\overline{\nu_e}/\nu_e$			
	$E_\nu < 1$ GeV	3.0	5
	$1 < E_\nu < 10$ GeV	1.62	5
	$E_\nu > 10$ GeV	-0.36	8[d]
$\overline{\nu_\mu}/\nu_\mu$			
	$E_\nu < 1$ GeV	0.06	2
	$1 < E_\nu < 10$ GeV	0.64	6
	$E_\nu > 10$ GeV	-0.08	15[e]
K/π ratio in flux calculation		-10.41	10[f]
Neutrino path length		0.15	10
Sample-by-sample normalization	FC Multi-GeV	-6.92	5
	PC + UPMU stop	-6.68	5
Matter effect		-0.17	1.0[g]
Solar Activity	SK-I	2.23	20
	SK-II	19.28	50
	SK-III	3.50	20
	SK-IV	-0.42	10

---

[a] Uncertainty linearly decreases with log E_ν from 25% (0.1 GeV) to 7% (1 GeV).

[b] Uncertainty is 7% upto 10 GeV, linearly increases with log E_ν from 7% (10 GeV) to 12% (100 GeV) and then from 12% (100 GeV) to 20% (1 TeV).

[c] Uncertainty linearly increases with log E_ν from 5%(30 GeV) to 30%(1 TeV).

[d] Uncertainty linearly increases with log E_ν from 8%(100 GeV) to 20%(1 TeV).

[e] Uncertainty linearly increases with log E_ν from 6% (50 GeV) to 40% (1 TeV).

[f] Uncertainty increases linearly from 5% to 20% between 100 GeV and 1 TeV.

[g] Difference of electron density in the core region from heavy element case is set to 1.0.

Table 6.8: Systematic errors related to neutrino flux calculation. They (except for solar activities) are common in all SK periods. The second column shows the best fit value of the systematic error parameter ϵ_i and the third column shows the estimated 1σ error size.

Systematic error in neutrino interaction	Fit value(%)	σ(%)
CCQE cross section	11.1	1.0[a]
CCQE $\overline{\nu}_i/\nu_i$ (i = e, μ) ratio	14.54	1.0[a]
CCQE ν_μ/ ν_e ratio	2.26	1.0[a]
M_A in CCQE and single meson production	-0.35	10
Single meson production cross section	-2.80	20
Single π production, $\pi^0/\pi^\pm$ ratio	-42.39	40
Single π production, $\overline{\nu_i}/\nu_i$ (i=e,μ) ratio	-4.22	1.0[b]
DIS cross section (E_ν < 10 GeV)	-4.47	1.0[c]
DIS cross section	5.11	5
Q^2 spectrum in DIS (W < 1.3 GeV/c^2)	3.33	1.0[d]
Q^2 spectrum in DIS (W > 1.3 GeV/c^2)	0.00	1.0[d]
Coherent π production	-30.6	100
NC/CC ratio	14.3	20
Nuclear effect in ^{1}6O nucleus	-2.32	1.0[e]
ν_τ contamination	-5.5	30
NC in FC μ-like (hadron simulation)	2.0	10
Decay electron taggig (π^+ interaction)[f]	-4.79	10

---

[a] Difference from the Nieves model is set to 1.0.

[b] Difference from the Hernandez model is set to 1.0.

[c] Difference from CKMT parametrization is set to 1.0.

[d] Difference from original GRV98 model is set to 1.0.

[e] Uncertainty depends on the difference between NEUT model and external data.

[f] They are assumed to be identical and fully correlated for each SK period

Table 6.9: Systematic errors related to neutrino interactions. They are common between all SK periods. The second column shows the best fit value of the systematic error parameter ϵ_i and the third column shows the estimated 1σ error size.

		SK-I		SK-II		SK-III		SK-IV	
Systematic error in event reduction		fit	σ	fit	σ	fit	σ	fit	σ
FC/PC separation		-0.06	0.6	0.06	0.5	-0.09	0.9	0.00	0.38
FC reduction		0.008	0.2	0.007	0.2	-0.03	0.8	0.006	0.3
PC reduction		-0.55	2.4	-2.46	4.8	-0.02	0.5	-0.11	1.0
Non-ν BG (e-like)	Sub-GeV e-like	0.03	0.5	0.004	0.2	-0.004	0.1	-0.003	0.1
	Multi-GeV e-like	0.018	0.1	0.01	0.1	0.008	0.4	-0.007	0.1
Non-ν BG (μ-like)	Sub-GeV μ-like	0.018	0.1	0.01	0.10	0.002	0.1	-0.007	0.1
	Multi-GeV μ-like	0.018	0.1	0.01	0.10	0.004	0.2	-0.056	0.8
	PC	0.036	0.2	0.07	0.7	0.036	1.8	-0.03	0.49
PC-stop/through separation	Top	31.6	46.1	-7.0	19.37	-19.22	86.6	2.48	40.44
	Barrel	-1.17	7.01	-3.90	9.44	-6.61	28.7	-0.95	8.54
	Bottom	-27.7	22.7	2.41	12.9	-0.47	12.1	-1.02	6.8
Fiducial volume		0.37	2	-0.04	2	-0.57	2	-0.18	2
UPMU reduction	stopping	-0.091	0.7	-0.028	0.7	0.084	0.7	0.065	0.5
	Through-going	-0.065	0.5	-0.02	0.5	0.06	0.5	0.039	0.3
UPMU stop/through separation		0.006	0.4	0.002	0.6	0.03	0.4	-0.06	0.6
UPMU through-going showering separation		3.0	3.4	0.14	4.4	1.88	2.4	0.59	3.0
Energy cut for UPMU stop		-0.03	-0.9	-0.03	-1.3	0.75	2.0	-0.03	1.7
Pathlength cut for upward through-going μ		-0.44	-1.5	-0.33	-2.3	-0.21	-2.8	1.0	-1.5
BG subtraction for UPMU		5.83	20	-8.84	21	8.79	20	9,17	20

Table 6.10: Systematic errors related to event reduction for each SK period. "Fit" column shows the best fit value of the systematic error parameter ϵ_i and "σ" column shows the estimated 1σ error size.

(SK-I) Systematic error in event reconstruction and selection			Fit value(%)	σ(%)
Ring separation	$<$ 400 MeV	e-like	1.51	2.3
		μ-like	0.46	0.7
	$>$ 400 MeV	e-like	0.26	0.4
		μ-like	0.46	0.7
	Multi-GeV	e-like	2.42	3.7
		μ-like	1.12	1.7
	Multi-ring sub-GeV	μ-like	-2.95	-4.5
	Multi-ring multi-GeV	e-like	-2.03	-3.1
	Multi-ring multi-GeV	μ-like	-2.69	-4.1
PID (single-ring)	sub-GeV	e-like	-0.01	0.1
		μ-like	0.01	-0.1
	Multi-GeV	e-like	0.02	-0.2
		μ-like	-0.02	0.2
PID (multi-ring)	sub-GeV	μ-like	0.49	-3.9
	Multi-GeV	e-like	-0.21	1.7
		μ-like	0.37	-2.9
Energy calibration			-0.55	1.1
Up/down asymmetry energy calibration			0.13	0.6
Multi-GeV single-ring e-like non CCν_e BG			1.97	13.2
Multi-GeV multi-ring elike non CCν_e BG			2.55	12.1
Multi-GeV multi-ring ν_e and $\overline{\nu}_e$ separation (likelihood)			-4.17	7.16
Sub-GeV 2-ring π^0			-0.24	2.0
Decay-e tagging (μ-decay)			-3.43	10

Table 6.11: Systematic errors related to event reconstruction and selection for SK-I. The second column shows the best fit value of the systematic error parameter ϵ_i and the third column shows the estimated 1σ error size.

(SK-II) Systematic error in event reconstruction and selection			Fit value(%)	σ(%)
Ring separation	$<$ 400 MeV	e-like	-1.2	1.3
		μ-like	-2.12	2.3
	$>$ 400 MeV	e-like	-1.57	1.7
		μ-like	-0.65	0.7
	Multi-GeV	e-like	-2.4	2.6
		μ-like	-1.57	1.7
	Multi-ring sub-GeV	μ-like	7.57	-8.2
	Multi-ring multi-GeV	e-like	1.75	-1.9
		μ-like	0.74	-0.8
PID (single-ring)	Sub-GeV	e-like	0.075	0.5
		μ-like	-0.06	-0.4
	Multi-GeV	e-like	0.015	0.1
		μ-like	-0.015	-0.1
PID (multi-ring)	Sub-GeV	μ-like	0.80	2.2
	Multi-GeV	e-ilke	0.65	1.8
		μ-like	-1.2	-3.4
Energy calibration			-0.42	1.7
Up/down asymmetry energy calibration			-0.08	0.6
Multi-GeV single-ring e-like non CCν_e BG			-7.26	38.1
Multi-GeV multi-ring elike non CCν_e BG			-0.74	11.1
Multi-GeV multi-ring ν_e and $\overline{\nu}_e$ separation (likelihood)			0.55	7.91
Sub-GeV 2-ring π^0			-0.71	2.0
Decay-e tagging (μ-decay)			-1.18	10

Table 6.12: Systematic errors related to event reconstruction and selection for SK-II. The second column shows the best fit value of the systematic error parameter ϵ_i and the third column shows the estimated 1σ error size.

(SK-III) Systematic error in event reconstruction and selection			Fit value(%)	σ(%)
Ring separation	< 400	e-like	0.54	1.8
		μ-like	0.9	3.0
	> 400	e-like	0.39	1.3
		μ-like	0.18	0.6
	Multi-GeV	e-like	0.39	1.3
		μ-like	0.3	1.0
	Multi-ring sub-GeV	μ-like	0.78	-2.6
	Multi-ring multi-GeV	e-like	-0.33	-1.1
		μ-like	-0.63	-2.1
PID (single-ring)	Sub-GeV	e-like	0.03	0.3
		μ-like	-0.04	-0.4
	Multi-GeV	e-like	0.06	0.5
		μ-like	-0.06	-0.5
PID (multi-ring)	Sub-GeV	μ-like	-0.13	3.1
	Multi-GeV	e-like	-0.10	2.5
		μ-like	-0.18	4.5
Energy calibration			-0.34	2.7
Up/down asymmetry energy calibration			0.18	1.3
Multi-GeV single-ring e-like non CCν_e BG			1.65	26.7
Multi-GeV multi-ring elike non CCν_e BG			-0.22	11.4
Multi-GeV multi-ring ν_e and $\overline{\nu}_e$ separation (likelihood)			-6.86	7.68
Sub-GeV 2-ring π^0			-0.14	1.0
Decay-e tagging (μ-decay)			2.25	10

Table 6.13: Systematic errors related to event reconstruction and selection for SK-III. The second column shows the best fit value of the systematic error parameter ϵ_i and the third column shows the estimated 1σ error size.

(SK-IV) Systematic error in event reconstruction and selection			Fit value(%)	σ(%)
Ring separation	$<$ 400 MeV	e-like	-1.0	-1.6
		μ-like	-1.89	-3.0
	$>$ 400 MeV	e-like	0.63	1.0
		μ-like	0.38	0.6
	Multi-GeV	e-like	0.63	1.0
		μ-like	-0.76	-1.2
	Multi-ring sub-GeV	μ-like	-1.45	-2.3
	Multi-ring multi-GeV	e-like	-0.57	-0.9
		μ-like	1.51	2.4
PID (single-ring)	Sub-GeV	e-like	-0.09	0.4
		μ-like	0.09	-0.4
	Multi-GeV	e-like	-0.09	0.4
		μ-like	0.09	-0.4
PID (multi-ring)	Sub-GeV	μ-like	0.83	2.2
	Multi-GeV	e-like	1.29	3.4
		μ-like	2.57	6.8
Energy calibration			-0.23	2.3
Up/down asymmetry energy calibration			0.02	0.3
Multi-GeV single-ring e-like non CCν_e BG			-0.23	17.6
Multi-GeV multi-ring elike non CCν_e BG			-2.25	11.6
Multi-GeV multi-ring ν_e and $\overline{\nu}_e$ separation (likelihood)			-4.24	6.82
Sub-GeV 2-ring π^0			0.75	1.8
Decay-e tagging (μ-decay)			4.98	10

Table 6.14: Systematic errors related to event reconstruction and selection for SK-IV. The second column shows the best fit value of the systematic error parameter ϵ_i and the third column shows the estimated 1σ error size.

6.5.1 Systematic Errors in Neutrino flux

Absolute Normalization

Uncertainty in the absolute atmospheric neutrino flux is calculated by Honda et al. [78], taking into account the atmospheric muon data (δ_π pion production in the hadronic interaction model), Kaon production (δ_K), hadronic interaction cross section (δ_σ) and the atmospheric density profile (δ_{air}) as shown in the upper plot of Figure 6.13.

The sum of dominant uncertainties which are δ_π and δ_σ is shown in the lower plot of Figure 6.13. It is taken as the absolute normalization uncertainty. The systematic error is divided into two terms for two energy regions: $E_\nu < 1$ GeV and $E_\nu > 1$ GeV.

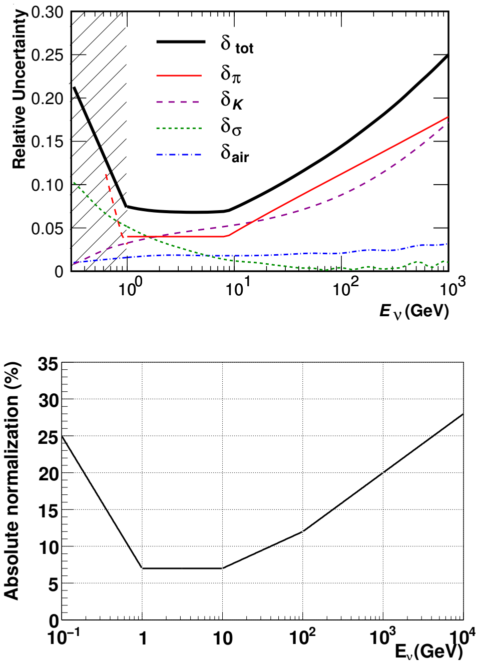

Figure 6.13: Contribution of each error source for atmospheric neutrino flux [78] is shown in the upper plot. Absolute normalization uncertainty due to only δ_π (atmospheric muon data (pion producion)) and δ_σ (hadronic interaction mode) as a function of neutrino energy is shown in the lower plot, which is considered to be the absolute normalization error. The kaon production and air density uncertainties are separately taken into account in the systematic errors.

Flavor Ratio

Systematic uncertainty in the flavor ratio $(\nu_\mu+\overline{\nu}_\mu)/(\nu_e+\overline{\nu}_e)$ of the atmospheric neutrino flux is estimated by comparing the Honda flux [78] with FLUKA [57] and Bartol [58] flux models. Figure 6.14 shows the flavor ratio normalized by Honda flux model. Uncertainty estimated is 2% for $E_\nu < 1$ GeV, 3% for $1 < E_\nu < 10$ GeV, and 5% for $10 < E_\nu < 30$ GeV. Above 30 GeV, the uncertainty increases as a function of logE_ν from 5% to 30% up to 1 TeV. As the error sources in each energy region are different, the uncertainty is divided into three terms according to the energy ranges: $E_\nu < 1$ GeV, $1 < E_\nu < 10$ GeV , $10 < E_\nu$.

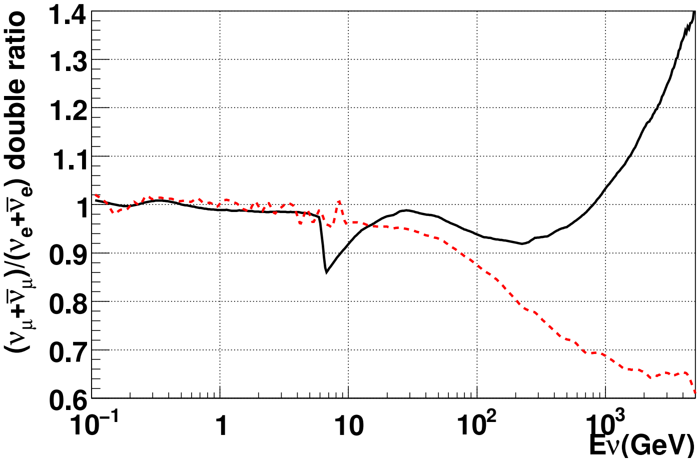

Figure 6.14: Flavor ratio $(\nu_\mu+\overline{\nu}_\mu)/(\nu_e+\overline{\nu}_e)$ of the atmospheric neutrino flux. Vertical axis stands for the double ratio, FLUKA flux/Honda flux is represented by solid lien, Bartol flux/Honda flux is represented by dashed line. The kink at 8 GeV in FLUKA flux due to technical treatment is corrected in the application.

Anti-Neutrino / Neutrino Ratio

The systematic uncertainty in anti-neutrino to neutrino ratio comes from π^+ / π^- and K^+/K^- ratio in hadronic interaction of the flux calculation. The uncertainty is estimated by comparing Honda flux with FLUKA and Bartol flux models [78] [57] [58]. Figure 6.15 shows anti-neutrino to neutrino ratio normalized by Honda flux for ν_e and ν_μ.

For $\overline{\nu}_e$ / ν_e , the estimated uncertainty is 5% in $E_\nu < 1$ GeV, 5% for $1 < E_\nu < 10$ GeV, 8% for $10 < E_\nu < 100$ GeV, for above 100 GeV, the error increases with logE_ν upto 30% (1 TeV).

For $\overline{\nu}_\mu$ / ν_μ, the estimated uncertainty is 2% for $E_\nu < 1$ GeV, 6% for 1 <$E_\nu < 10$ GeV, 6% for $10 < E_\nu < 50$ GeV. For energy above 50 GeV, the error increases with log E_ν upto 60 % (1 TeV).

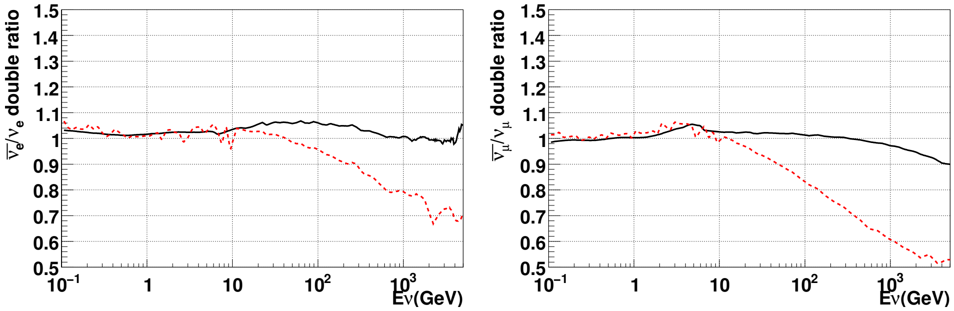

Figure 6.15: Anti-neutrino / neutrino double ratio for $\overline{\nu}_e/\nu_e$ (left) and $\overline{\nu}_\mu/\nu_\mu$ (right). Solid (dashed) line indicates the double ratio with FLUKA (Bartol) flux.

Up/Down Ratio

Neutrino flux has up/down asymmetry due to the geomagnetic field, but the uncertainty in the low energy neutrino flux does not affect the zenith angle distribution, as the up/down asymmetry in low energy region is largely smeared by the poor angular correlation in neutrino interactions. The systematic uncertainties of up/down ratio are estimated by comparison of the zenith angle distributions with the three flux models [78] [57] [58] for each neutrino event sample, as shown in table 6.15.

Horizontal/Vertical Ratio

The systematic uncertainty of horizontal/vertical ratio is caused mainly by the difference the 3-dimentional calculation method in each flux calculation model [78] [57] [58] below neutrino energy of 3 GeV. For neutrino energy above 3 GeV, the uncertainty is caused by the difference in the predicted K/π ratio in hadronic interactions in the atmosphere. The systematic uncertainties are estimated by comparing the zenith angle distributions using the three flux models for each neutrino sample, as summarized in table 6.16.

		fit value (%)	1σ (%)
$<$ 400 MeV	e-like 0-decay	-0.02	0.1
	μ-like 0-decay	-0.2	1.1
	μ-like 1-decay	-0.07	0.3
$>$ 400 MeV	e-like 0-decay	-0.2	0.8
	μ-like 0-decay	-0.4	1.7
	μ-like 1-decay	-0.1	0.5
Multi-GeV	e-like	-0.2	0.7
	μ-like	-0.04	0.2
Multi-ring sub-GeV	μ-like	-0.04	0.2
Multi-ring multi-GeV	e-like	-0.07	0.3
	μ-like	-0.04	0.2
PC		-0.04	0.2

Table 6.15: Estimated uncertainties of up/down ratio (1σ values) for different event samples. They are common for SK-I, SK-II, SK-III and SK-IV periods.

		fit value (%)	1σ (%)
$<$ 400 MeV	e-like 0-decay	0.02	0.1
	μ-like 0-decay	0.07	0.3
	μ-like 1-decay	0.02	0.1
$>$ 400 MeV	e-like 0-decay	0.3	1.4
	μ-like 0-decay	0.3	1.4
	μ-like 1-decay	0.4	1.9
Multi-GeV	e-like	0.7	3.2
	μ-like	0.5	2.3
Multi-ring sub-GeV	μ-like	0.3	1.3
Multi-ring multi-GeV	e-like	0.5	2.8
	μ-like	0.3	1.5
PC		0.4	1.7

Table 6.16: Estimated uncertainties of horizontal/vertical ratio (1σ values) for different event samples. They are common for SK-I, SK-II, SK-III and SK-IV periods.

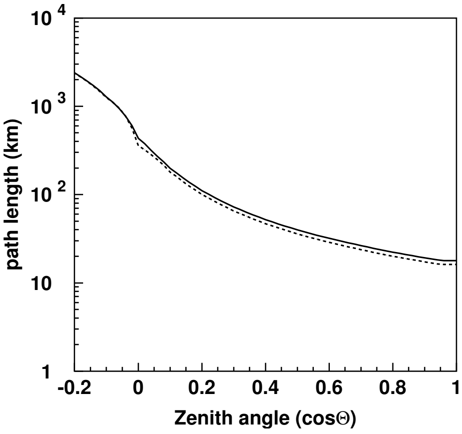

Figure 6.16: Neutrino flight length as a function of zenith angle. Solid curve represents the flight length used in our analysis and dashed curve represents that for the compressed density structure of atmosphere by 10%.

K/π Ratio

Source of atmospheric neutrino is mainly π^+ and π^- in the neutrino energy range below 10 GeV. K's contribute to neutrino production above a few tens of GeV. The uncertainty of K/π production ratio in cosmic ray interactions in atmosphere is taken as the systematic error. According to the SPY experiment [142], the measurement of the K/π ratio is obtained with an accuracy of 3%, where K and π momentum ranges from 7 GeV/c to 135 GeV/c. By using the SPY experiment results and the correspondence between handron momentum and neutrino energy, the uncertainty of K/π ratio is estimated to be 5% below $E_\nu = 100$ GeV and 20% above $E_\nu = 1$ TeV. The uncertainty increases linearly from 5% to 20% between 100 GeV and 1 TeV.

Neutrino Path Length

As atmospheric neutrino flight length is used in the calculation of neutrino oscillation probabilities, the uncertainty in neutrino production height has to be taken into account, especially for downward going and horizontal going neutrinos. The uncertainty of neutrino production height is related to the structure of atmosphere. The systematic uncertainty is estimated by using the flux calculation and by changing the density structure of atmosphere by 10%. This 10% number is given by comparison between US-standard '76 and MSISE90 [143]. Figure 6.16 shows the comparison of flight path lengths in two different density structures. The difference of the comparison of neutrino flux due to the change of path length is taken to be the systematic uncertainty.

Solar Activity

Primary cosmic ray flux is affected by the solar activity in an 11 year cycle. ±1 year of uncertainty is assigned to the modulation of solar activity, which corresponds to uncertainty in the solar activity of 20% for SK-I, 50% for SK-II, 20% for SK-III and 10% for SK-IV.

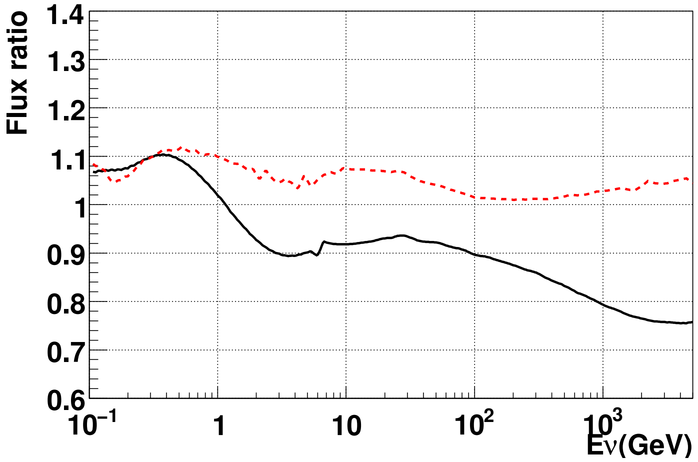

Figure 6.17: Ratio of calculated neutrino flux in which the fluxes and Bartol (solid line) and FLUKA (dashed line) are normalized by Honda flux.

Sample-by-sample Normalization

Energy dependence of the absolute normalization is different for each flux model, and the difference cannot be represented by a simple function, as shown in figure 6.17. 5% is assigned as the relative normalization uncertainty for FC multi-GeV, PC and UPMU-stop samples.

Matter Effect

Electron density in the Earth affects the calculation of neutrino oscillation probabilities. Matter density is well measured by [140], but electron density depends on the chemical composition of the Earth. As the core region is expected to consist of mostly heavy elements (iron), the electron density is less than that of the light elements by about 6.8%. The difference of number of oscillated neutrino events from reduced electron density is taken as the uncertainty of the matter effect.

6.5.2 Systematic Errors in Neutrino Interactions

CCQE Cross Section

Cross section of CCQE for bound nucleon is calculated based on the Smith and Monitz Fermi-gas model. The difference from Nieves et al. model [91] is set to be the 1σ uncertainty for CCQE cross section.

The uncertainties in CCQE cross section ($\overline{\nu}/\nu$) ratio and flavor ratio ($\nu_\mu + \overline{\nu}_\mu$)/ ($\nu_e$+$\overline{\nu}_e$) are also set by the difference from the Nieves model.

Figure 6.18 shows the calculated CCQE cross section ratio of Nieves model to Smith and Monitz model, as a function of neutrino energy for total cross section, flavor ratio and $\overline{\nu}/\nu$.

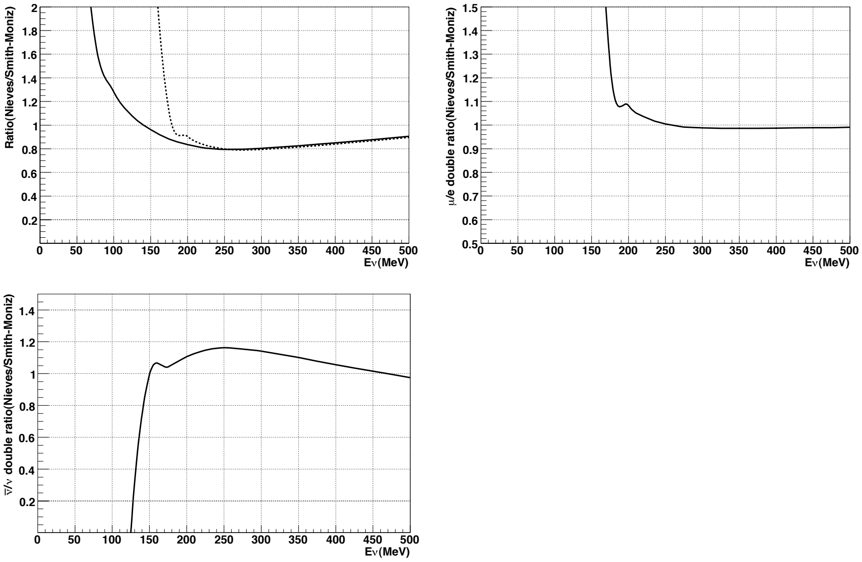

Figure 6.18: Top left: ratio of CCQE cross section, Nieves model normalized by the Smith and Monitz model, for $\nu_e + \overline{\nu}_e$ (solid line) and $\nu_\mu + \overline{\nu}_\mu$ (dashed line). Top right: $(\nu_\mu + \overline{\nu}_\mu)/(\nu_e + \overline{\nu}_e)$ ratio. Bottom: $(\overline{\nu}/\nu)$ ratio.

M_A in CCQE and Single Meson Production

For M_A in CCQE and single meson production, the difference of Q^2 spectrum between M_A = 1.2 and M_A = 1.1 is set to be the systematic uncertainty in order to take into account the 10% uncertainty of M_A parameter.

Single Meson Production Cross Section

Uncertainty in the cross section of single meson production is estimated to be 20% by investigating the difference between the expectation and experimental data of $\nu_\mu p \rightarrow \mu^- p \pi^+$ observation. $\nu_\mu n \rightarrow \mu^- p \pi^0$ interaction is less understood as there are only few experiment results. Hence the additional uncertainty is estimated by comparison with the Hernandez model [144]. The cross section ratio of $\nu_\mu n \rightarrow \mu^- p \pi^0$ is shown the dashed line in the left panel of figure 6.19. It is considered that π^0 production interaction has 40% uncertainty relative to the $\pi^\pm$ emitting interactions.

Uncertainty in the single meson production cross section of $\overline{\nu}/\nu$ ratio is also estimated by using the difference from the Hernandez model. Right panel of figure 6.19 shows the $\overline{\nu}/\nu$ ratio of CC cross section nomalized by Rein and Sehgal model.

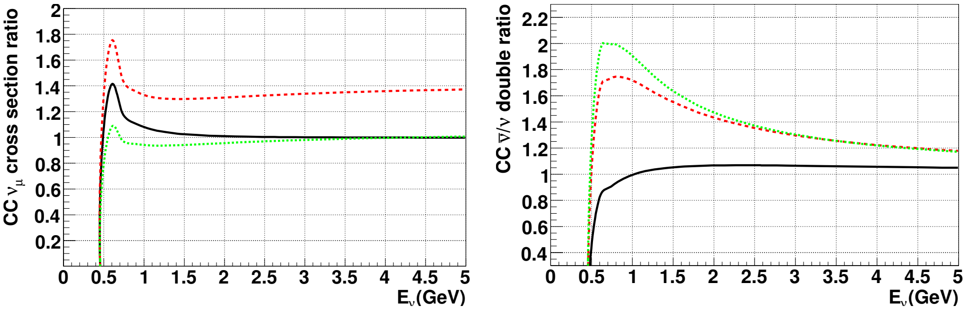

Figure 6.19: Predicted cross section (left) and the $\overline{\nu}/\nu$ ratio (right) of the Hernandez model normalized by that of the Rein and Sehgal model for $\nu_\mu p \to \mu^- p \pi^+$ (solid line), $\nu_\mu n \to \mu^- p \pi^0$ (dashed line) and $\nu_\mu n \to \mu^- p \pi^+$ (dotted line).

Deep Inelastic Scattering Cross section

Calculation of cross section for DIS agrees with experimental measurement within 5% for energies above 10 GeV, but the uncertainty is larger in lower energy region (< 10 GeV), the additional error is estimated by the difference from CKMT model [48].

Q^2 Spectrum in Deep Inelastic Scattering

The uncertainty of Q^2 spectrum is taken into account by comparing with the original GRV98 model. This uncertainty is separated into 2 terms for $W < 1.3$ GeV/c^2 and $W > 1.3$ GeV/c^2.

Coherent Pion Production Cross Section

This uncertainty is obtained as 50% by the difference between the Rein and Sehgal model and experimental measurement for NC and CC ν_e interactions. As CC ν_μ coherent pion has no experimental measurement, the uncertainty is taken to be 100%.

NC/CC ratio

This uncertainty is estimated to be 20%.

Nuclear Effect in ^{16}O Nucleus

The cross section of pion final state interactions inside nuclei are compared between simulation by NEUT and external experimental data [145]. The cross sections of these final state interactions in the simulation are varied with weighing method so that the difference with the experimental data is 1σ as shown in figure 6.20. Then difference between the minimum weight and maximum weight on each simulated event is used to compute the uncertainty on the nuclear effect in ^{16}O nucleus.

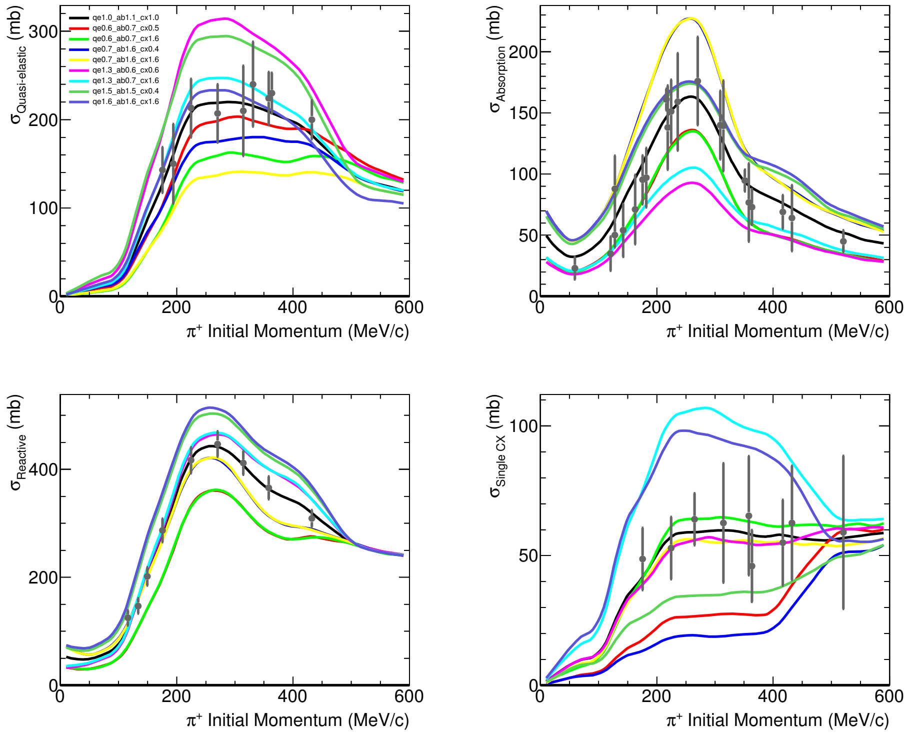

Figure 6.20: π^+ scattering on carbon target in: quasi-elastic channel (top left), absorption channel (top right), total reaction channel (bottom left) and single charge exchange channel (bottom right).

6.5.3 Systematic Errors in Event Selection and Reconstruction

FC/PC separation

FC and PC events are separated by number of OD hit PMT clusters (NHITAC). The systematic uncertainty is estimated to be 0.6% for SK-I, 0.5% for SK-II, 0.9% for SK-III and 0.38% for SK-IV by using the difference between the observed data and the MC NHITAC distribution (Figure 5.13).

FC Reduction Related

The uncertainty in FC reduction efficiency is estimated to be 0.2%, for SK-I, 0.2% for SK-II, 0.8% for SK-III and 0.3% for SK-IV by comparing the distributions of each cut variable for observed data and MC. Contamination of the background is estimated in Chapter 5.

PC Reduction Related

The uncertainty in PC reduction efficiency is estimated to be 2.5% for SK-I, 4.8% for SK-II , 0.5% for SK-III and 1.0% for SK-IV by comparing the distributions of each cut variables for observed data and MC. The contamination of background is estimated in Chapter 5.

PC Stop/Through Separation

PC OD stopping and through-going events are separated by using the energy deposit in the OD region (PE_{anti} / PE_{exp}). The systematic uncertainty is estimated by the difference between the observed data and MC PE_{anti} / PE_{exp} distributions. The estimation is separately down for OD bottom, barrel and top, as the OD calibration has difference depending on the OD position.

UPMU Reduction Related

The uncertainty in UPMU reduction effiiciency is estimated by comparing the distributions of each cut variables for the observed data and MC. For stopping muons, the estimated uncertainty are 0.7% for SK-I, 0.7% for SK-II, 0.7% for SK-III and 0.5% for SK-IV. For through-going muons, the estimated uncertainty are 0.5% for SK-I, 0.5% for SK-II, 0.5% for SK-III and 0.3% for SK-IV. These uncertainties for stopping and through-going muons are assumed to be correlated.

The stopping and through-going muons are separated by using the number of hit OD PMTs within 8 m from the projected exit point (NHITEX). The separation uncertainty are estimated to be 0.4% for SK-I, 0.6% for SK-II, 0.4% for SK-III and 0.6% for SK-IV, by using the difference between observed data and MC NHITEX distributions (Figure 5.25).

UPMU Non-Showering/Showering Separation

UPMU non-showering and showering events are separated by using the difference between the average corrected charge and expected charge for non-showering events ($\Delta(Q)$). The systematic uncertainty is estimated by comparing the $\Delta(Q)$ distribution (figure 5.29) for data and MC. The estimated uncertainty are 3.4% for SK-I, 4.4% for SK-II , 2.4% for SK-III and 3.0% for SK-IV.

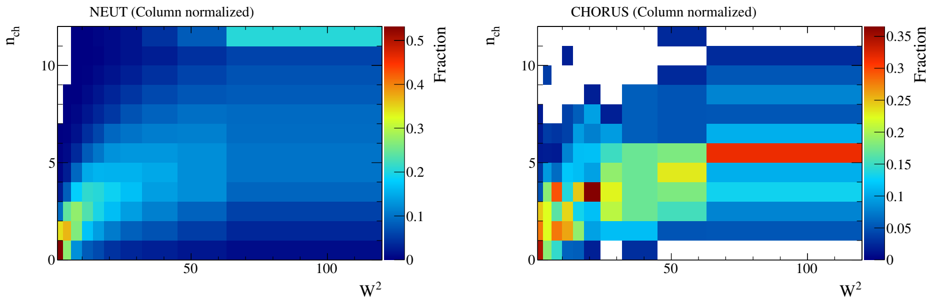

Figure 6.21: Pion multiplicity plotted as a function of W^2 for NEUT simulation (left) and for the data from the CHORUS experiment (right).

Ring Separation

Ring separation is done based on the ring-counting algorithm. The uncertainties are estimated by the difference of likelihood distribution between observed data and MC for each sample.

Particle Identification

Uncertainty in particle identification are estimated by the difference of PID likelihood distribution between observed data and MC for each sample.

Energy Calibration

Energy scale uncertainties are estimated in Chapter 4. The systematic uncertainty for absolute energy scale is estimated to be 1.1% for SK-I, 1.7% for SK-II , 2.7% for SK-III and 2.3% for SK-IV.

Multi-GeV Multi-Ring ν_e and $\overline{\nu}_e$ Separation

Multi-GeV multi-ring ν_e and $\overline{\nu}_e$ separation likelihood depends on number of decay electrons, number of rings, etc, which depend on the number of pions which in turn depends on the cross section of the final state interactions of pions and pion multiplicity.

In order to take into account the effect of pion final state interaction cross sections, the MC is compared with external experimental data, then the MC events are weighed so that the pion final state interaction cross sections are 1σ from the experimental data [145].

As for pion multiplicity, the NEUT model MC is compared with the experimental data from the CHORUS experiment [146]. The left and the right plots in figure 6.21 are compared and each bin is weighed with the ratio of CHORUS/NEUT.

Each MC event is weighed with both final state interaction cross section weight and pion multiplicity weight respectively, then the difference in purities of CCν_e events in the weighed MC likelihood and the original likelihood are taken as the systematic uncertainty.

The estimated systematic uncertainties are 7.16% for SK-I, 7.91% for SK-II, 7.68% for SK-III and 6.82% for SK-IV.

The non-CCν_e background uncertainty for multi-GeV multi-ring e-like events is also evaluated by the same method.

Single-Ring π^0-Like Sample Selection

The uncertainty in the selection efficiency of FC sub-GeV single-ring π^0-like events are estimated by comparing observed data with MC for the π^0 mass and likelihood distributions. As the likelihood distributions are different for each momentum, the systematic uncertainties are estimated for each momentum region. Part of the uncertainty in the selection efficiency also comes from the absolute energy scale uncertainty. The combined uncertainties from the difference of distribution and shift of energy scale, are summarized in table 6.17.

	SK-I		SK-II		SK-III		SK-IV	
	fit value	$\sigma(\%)$	fit value	$\sigma(\%)$	fit value	$\sigma(\%)$	fit value	$\sigma(\%)$
$100 < P_e < 250$ MeV/c	1.14	11.2	1.91	7.5	1.73	7.7	6.48	10.8
$250 < P_e < 400$ MeV/c	1.17	11.5	2.26	8.9	5.94	26.4	6.96	11.6
$400 < P_e < 630$ MeV/c	2.39	23.4	4.45	17.5	2.81	12.5	6.06	10.1
$630 < P_e < 1000$ MeV/c	1.95	19.1	2.72	10.7	6.01	26.7	9.06	15.1
$1000 < P_e < 1330$ MeV/c	1.33	13.0	2.82	11.1	6.01	26.7	8.7	14.5

Table 6.17: 1σ values for systematic uncertainties of single-ring π^0-like events selection for SK-I, SK-II, SK-III and SK-IV.

Two-Ring π^0 Selection

The uncertainty in selection of two-ring π events comes from ring-counting and PID. The estimated uncertainties are 2.0% for SK-I, 2.0% for SK-II, 1.0% for SK-III and 1.8% for SK-IV.

Decay Electron Tagging

Systematic error in decay electron detection efficiency is estimated to be 1.5% by using cosmic ray muons [147], which is assumed to be identical for each SK period. In addition, π^+ decay probability uncertainty is considered, as π^+ interacts in water depending on its energy, the decay probability are between 3% to 13% depending on the π^+ momentum, hence the decay probability also affects the uncertainty for decay electron tagging by 0.3% to 0.6% for FC sub-GeV single-ring e-like 0-decay sample.

6.6 Sensitivity Study

Sensitivity study was carried out to study the effect of the new binning of multi-GeV ν_e and $\overline{\nu}_e$-like samples.

The sensitivity study was carried out with SK-I, SK-II, SK-III and SK-IV MC corresponding to data livetime, assuming the following set of parameters:

Δm^2_{23}	2.66×10^{-3} eV^2
$\sin^2\theta_{23}$	0.5
δ_{CP}	300°

In case of assumed true normal hierarchy, the $\Delta\chi^2$ between normal and inverted hierarchies is

$$\Delta\chi^2 = \chi^2(IH) - \chi^2(NH) = 1.06 \tag{6.11}$$

Figure 6.22 shows the χ^2 distribution for oscillation parameters $\sin^2\theta_{23}$, Δm^2_{23} and δ_{CP} for both normal and inverted hierarchies for the sensitivity study.

The same study was carried out with assumed true inverted hierarchy, assuming the same oscillation parameters as in Table 6.6.

In case of assumed true inverted hierarchy, the $\Delta\chi^2$ between normal and inverted hierarchies is

$$\Delta\chi^2 = \chi^2(IH) - \chi^2(NH) = 0.90 \tag{6.12}$$

The above sensitivity study on mass hierarchy was repeated for combined binnings of multi-GeV ν_e and $\overline{\nu}_e$-like samples, in which Multi-GeV single-ring ν_e-like and $\bar{\nu}_e$-like samples are combined as Multi-GeV single-ring e-like sample, and Multi-GeV multi-ring ν_e-like and $\bar{\nu}_e$-like samples are combined as Multi-GeV multi-ring e-like sample. The results are listed in Table 6.18. The results shows that the introduction of ν_e-like and $\bar{\nu}_e$-like samples in Multi-GeV e-like events improves the sensitivity to the mass hierarchy.

	Assumed true inverted hierarchy	Assumed true normal hierarchy
Combined $\nu_e/\overline{\nu}_e$ bins	$\Delta\chi^2 = 0.68$	$\Delta\chi^2 = 0.81$
Separated $\nu_e/\overline{\nu}_e$ bins	$\Delta\chi^2 = 0.90$	$\Delta\chi^2 = 1.06$

Table 6.18: $\Delta\chi^2$ ($= \mid \chi^2_{min(NH)} - \chi^2_{min(IH)} \mid$) estimated with and without multi-GeV 1-ring and multi-ring e-like samples separated into ν_e and $\overline{\nu}_e$-like samples.

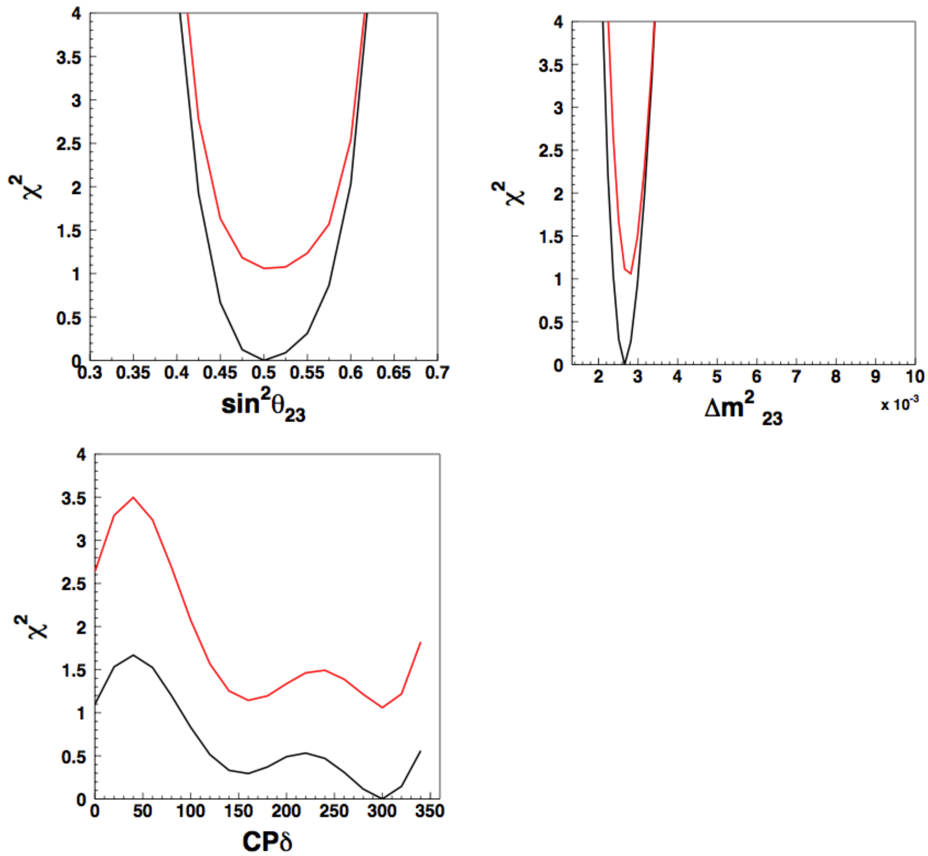

Figure 6.22: The plots show χ^2 distributions for $\sin^2\theta_{23}$ (top left), Δm^2_{23} (top right) and δ_{CP} (bottom) for the sensitivity study carried out with data livetime assuming normal hierarchy and oscillation parameters of ($\sin^2\theta_{12}$, Δm^2_{12}, $\sin^2\theta_{23}$, Δm^2_{32}, $\sin^2\theta_{13}$, δ_{CP}) = (0.304, 7.66 × 10^{-5}, 0.5, 2.66 × 10^{-3}, 0.025, 300°). Black line represents the distribution for normal hierarchy, and red line represents the distribution for inverted hierarchy.

6.7 Results

In this analysis, the zenith angle and momentum distributions of different event samples are fitted with the simulated distributions, considering all oscillation parameters, which includes two mass differences Δm^2_{12}, δm^2_{32}, three mixing angles θ_{12}, θ_{23}, θ_{13}, CP phase δ_{CP} and mass hierarchy cases: normal and inverted mass hierarchies.

χ^2 is calculated in the fitting process by four dimensional oscillation parameter spaces of Δm^2_{32}, θ_{23}, θ_{13} and δ_{CP}. Parameters Δm^2_{12} and $\sin^2\theta_{12}$ are fixed to the values determined by solar neutrino analyses, as they are already well constrained.

The examined oscillation parameter spaces are:

- $(\Delta m^2_{12}, \sin^2\theta_{12}) = (7.65 \times 10^{-5}, 0.304)$ (fixed)
- $\Delta m^2_{32} = 1.33 \times 10^{-3}$ to 10×10^{-3} (36 points)
- $\sin^2\theta_{23} = 0.3$ to 0.7 (17 points)
- $\sin^2\theta_{13} = 0.0$ to 0.2 (65 points) (2 studies: free and fixed)
- $\delta_{CP} = 0°$ to 340° (18 points)

for normal hierarchy and inverted hierarchy.

As the mixing angle θ_{13} is measured and well constrained by reactor experiments [6] [7], two studies: one with θ_{13} free as usual and another one with θ_{13} fixed at the value obtained by the reactor experiments are carried out.

With Free θ_{13}

With free θ_{13}, in the normal hierarchy case, the best-fit is found at $(\Delta m^2_{32}, \sin^2\theta_{23}, \sin^2\theta_{13}, \delta_{CP}) = (2.51 \times 10^{-3}, 0.55, 0.003, 260°)$ with χ^2_{min}/dof = 555.33 / 476. In the inverted hierarchy case, the best-fit is found at $(\Delta m^2_{32}, \sin^2\theta_{23}, \sin^2\theta_{13}, \delta_{CP}) = (2.51 \times 10^{-3}, 0.55, 0.006, 240°)$ with χ^2_{min} /dof = 554.91 / 476. Tables 6.19 and 6.20 summarize the 68% C.L. and 90% C.L. allowed region for $(\Delta_{32}, \sin^2\theta_{23}, \sin^2\theta_{13}, \delta_{CP})$.

	Normal hierarchy	
	68% C.L.	90% C.L.
Δm^2_{32} (eV^2)	$(2.22 < \Delta m^2_{32} < 2.81) \times 10^{-3}$	$(2.06 < \Delta m^2_{32} < 3.04) \times 10^{-3}$
$\sin^2\theta_{23}$	$0.420 < \sin^2\theta_{23} < 0.601$	$0.391 < \sin^2\theta_{23} < 0.619$
$\sin^2\theta_{13}$	$0.00037 < \sin^2\theta_{13} < 0.015$	$\sin^2\theta_{13} < 0.0655$
δ_{CP}	all values allowed	all values allowed

Table 6.19: Results of the allowed region of each neutrino oscillation parameter at 68% and 90% C.L. for normal hierarchy at fixed θ_{13}, where 68% C.L. is defined as $\chi^2 - \chi^2_{min} = 1.0$ and 90% C.L. is defined as $\chi^2 - \chi^2_{min} = 2.7$.

	Inverted hierarchy	
	68% C.L.	90% C.L.
Δm^2_{32} (eV^2)	$(2.32 < \Delta m^2_{32} < 2.79) \times 10^{-3}$	$(2.14 < \Delta m^2_{32} < 3.04) \times 10^{-3}$
$\sin^2\theta_{23}$	$0.430 < \sin^2\theta_{23} < 0.605$	$0.393 < \sin^2\theta_{23} < 0.630$
$\sin^2\theta_{13}$	$0.00067 < \sin^2\theta_{13} < 0.034$	$\sin^2\theta_{13} < 0.0944$
δ_{CP}	all values allowed	all values allowed

Table 6.20: Results of the allowed region of each neutrino oscillation parameter at 68% and 90% C.L. for inverted hierarchy at fixed θ_{13}, where 68% C.L. is defined as $\chi^2 - \chi^2_{min} = 1.0$ and 90% C.L. is defined as $\chi^2 - \chi^2_{min} = 2.7$.

With Fixed θ_{13}

With fixed θ_{13} at $\sin^2\theta_{13} = 0.025$ [6] [7], in the normal hierarchy case, the best-fit is found at (Δ_{23}, $\sin^2\theta_{32}$, δ_{CP}) = (2.66×10^{-3}, 0.425, 300°) with χ^2_{min}/dof = 556.70 / 477. In the inverted hierarchy case, the best-fit is found at (Δ_{32}, $\sin^2\theta_{23}$, $\sin^2\theta_{13}$, δ_{CP}) = (2.66×10^{-3}, 0.575, 260°) with χ^2_{min}/dof = 555.50 / 477. Summary of 68% C.L. and 90% C.L. allowed regions of each oscillation parameter is summarized in Tables 6.21 and 6.22.

Zenith angle distributions of data and MC at best fit (both normal and inverted hierarchies) with SK-I, SK-II, SK-III and SK-IV combined are shown from Figure 6.23 to figure 6.27.

	Normal hierarchy	
	68% C.L.	90% C.L.
Δm^2_{32} (eV^2)	$(2.26\ \Delta m^2_{32} < 2.81) \times 10^{-3}$	$(2.11\ \Delta m^2_{32} < 3.09) \times 10^{-3}$
$\sin^2\theta_{23}$	$0.398 < \sin^2\theta_{23} < 0.511$	$0.380 < \sin^2\theta_{23} < 0.628$
δ_{CP}	$180° < \delta_{CP} < 340°$	all values allowed

Table 6.21: Results of the allowed region of each neutrino oscillation parameter at 68% C.L. and 90% C.L. for normal hierarchy at fixed θ_{13}, where 68% C.L. is defined as $\chi^2 - \chi^2_{min} = 1.0$ and 90% C.L. is defined as $\chi^2 - \chi^2_{min} = 2.7$.

	Inverted hierarchy	
	68% C.L.	90% C.L.
Δm^2_{32} (eV^2)	$(2.43\ \Delta m^2_{32} < 2.83) \times 10^{-3}$	$(2.21 < \Delta m^2_{32} < 3.11) \times 10^{-3}$
$\sin^2\theta_{23}$	$0.416 < \sin^2\theta_{23} < 0.612$	$0.388 < \sin^2\theta_{23} < 0.630$
δ_{CP}	$162° < \delta_{CP} < 330°$	all values allowed

Table 6.22: Results of the allowed region of each neutrino oscillation parameter at 68% C.L. and 90% C.L. for inverted hierarchy at fixed θ_{13}, where 68% C.L. is defined as $\chi^2 - \chi^2_{min} = 1.0$ and 90% C.L. is defined as $\chi^2 - \chi^2_{min} = 2.7$.

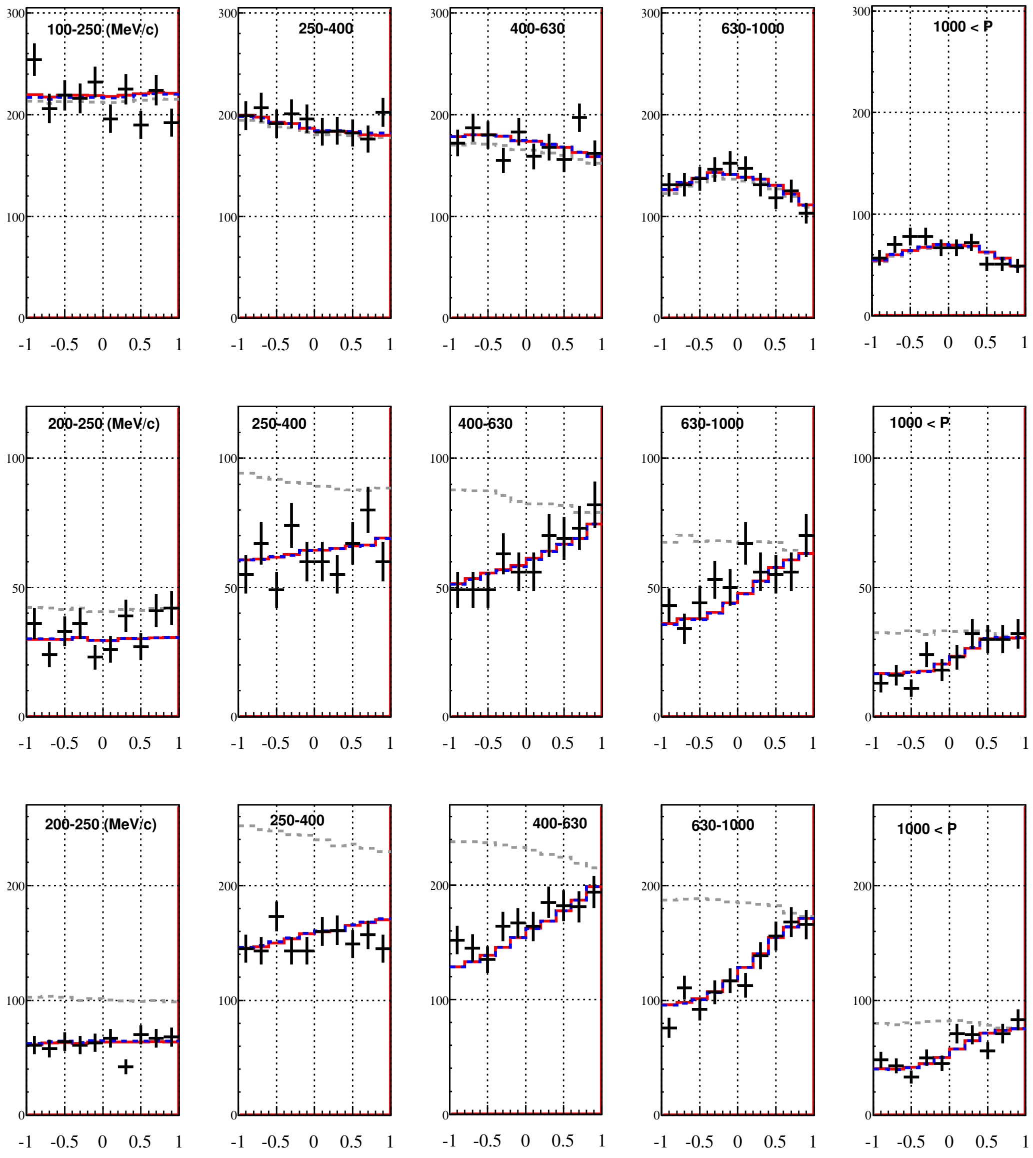

Figure 6.23: SK-I + SK-II + SK-III + SK-IV zenith angle distributions for FC events for data (line with error bar) and MC assuming no oscillation (grey dashed line), best fit results at normal hierarchy (red solid line) and best fit results at inverted hierarchy (blue dashed line). From top to the bottom: Sub-GeV 1-ring e-like 0-decay, Sub-GeV μ-like 0-decay, Sub-GeV μ-like 1-decay

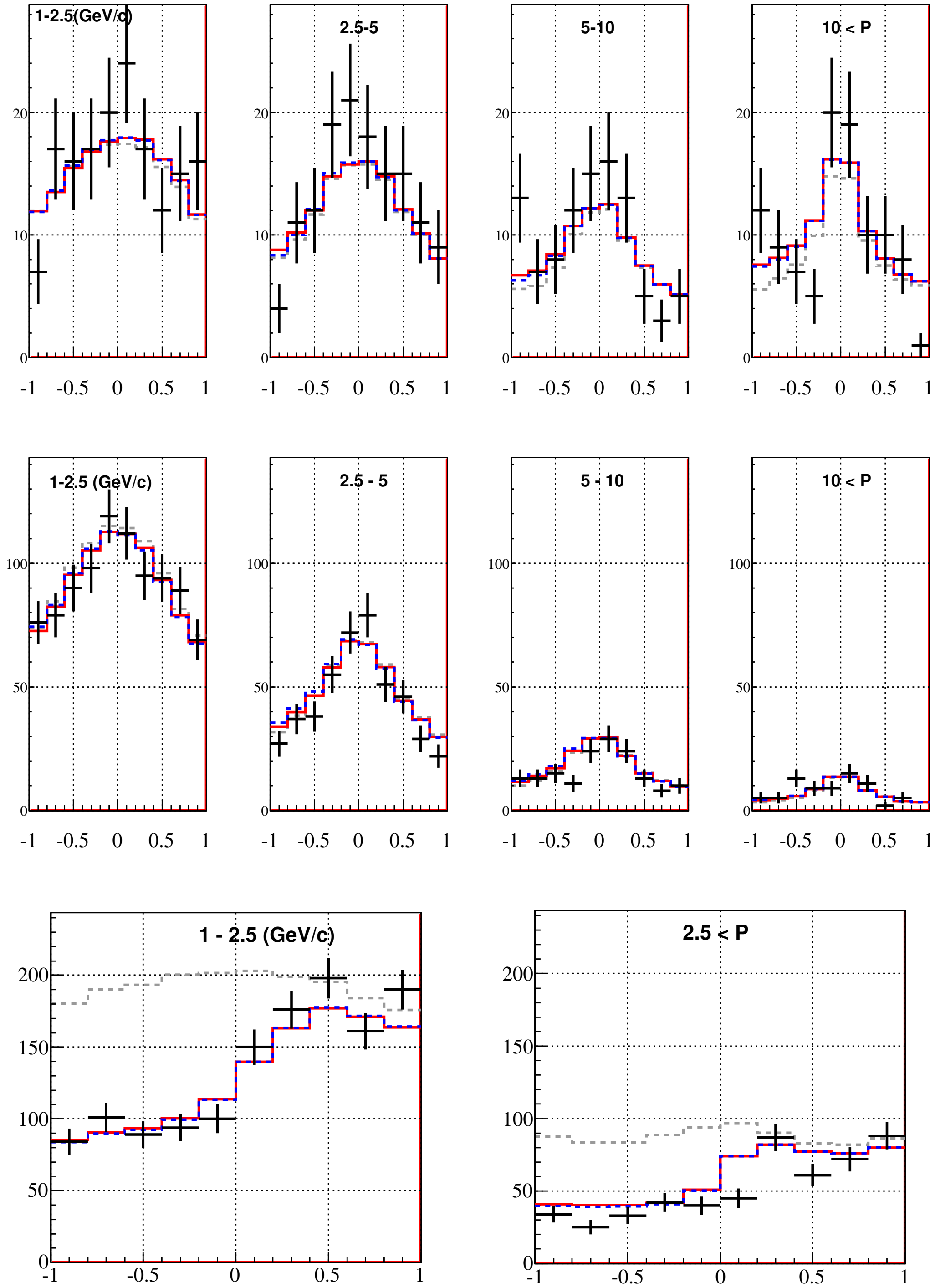

Figure 6.24: SK-I + SK-II + SK-III + SK-IV zenith angle distributions for FC events for data (line with error bar) and MC assuming no oscillation (grey dashed line), best fit results at normal hierarchy (red solid line) and best fit results at inverted hierarchy (blue dashed line). From top to the bottom: Multi-GeV 1-ring ν_e-like, Multi-GeV 1-ring $\overline{\nu}_e$-like, Multi-GeV 1-ring μ-like.

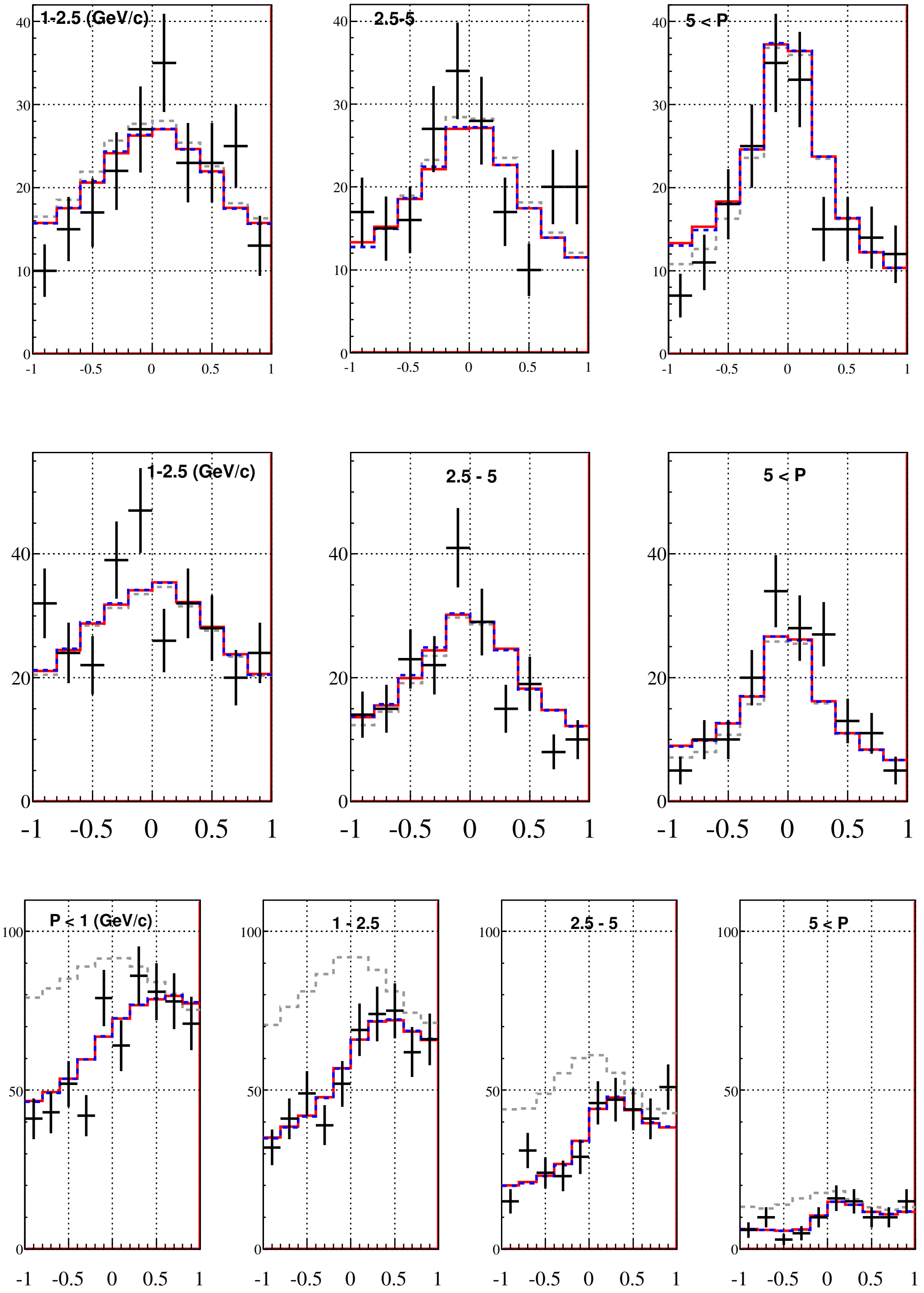

Figure 6.25: SK-I + SK-II + SK-III + SK-IV zenith angle distributions for FC events for data (line with error bar) and MC assuming no oscillation (grey dashed line), best fit results at normal hierarchy (red solid line) and best fit results at inverted hierarchy (blue dashed line). From top to the bottom: Multi-GeV multi-ring ν_e-like, Multi-GeV multi-ring $\overline{\nu}_e$-like, Multi-GeV multi-ring μ-like.

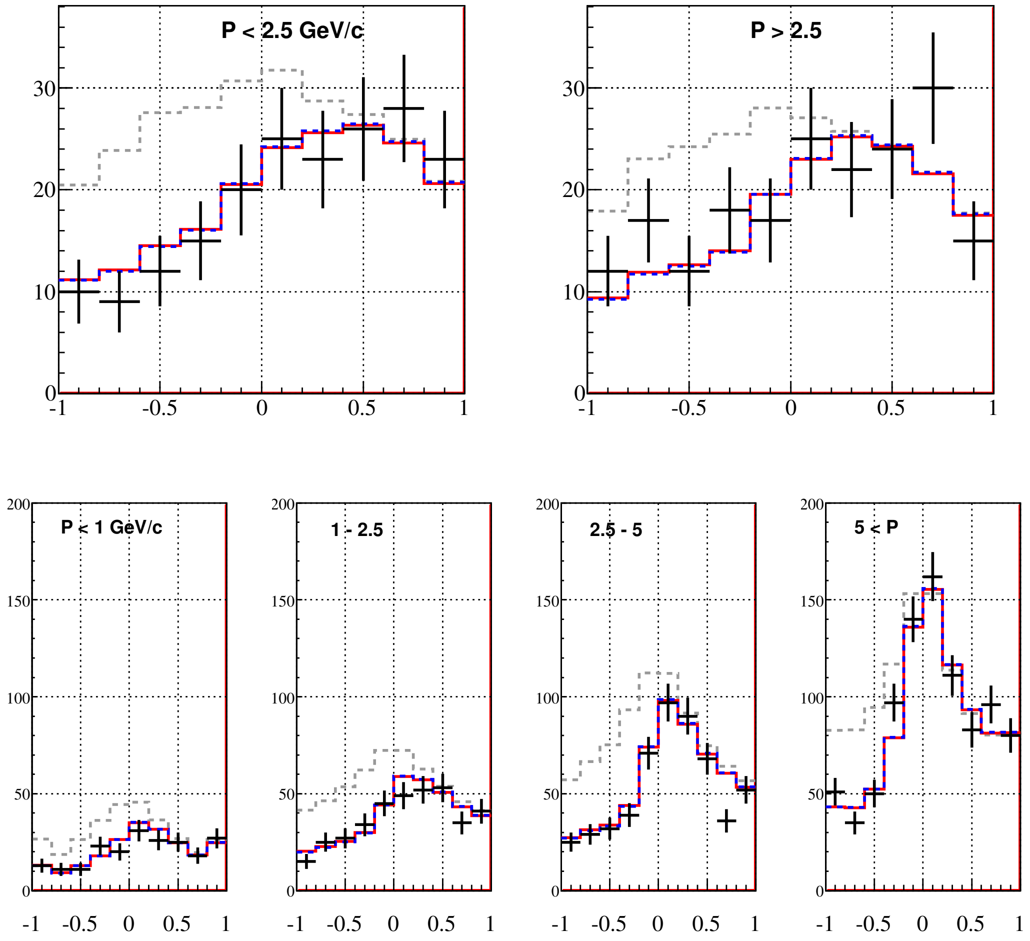

Figure 6.26: SK-I + SK-II + SK-III + SK-IV zenith angle distributions for FC events for data (line with error bar) and MC assuming no oscillation (grey dashed line), best fit results at normal hierarchy (red solid line) and best fit results at inverted hierarchy (blue dashed line). From top to the bottom: PC stop, PC through

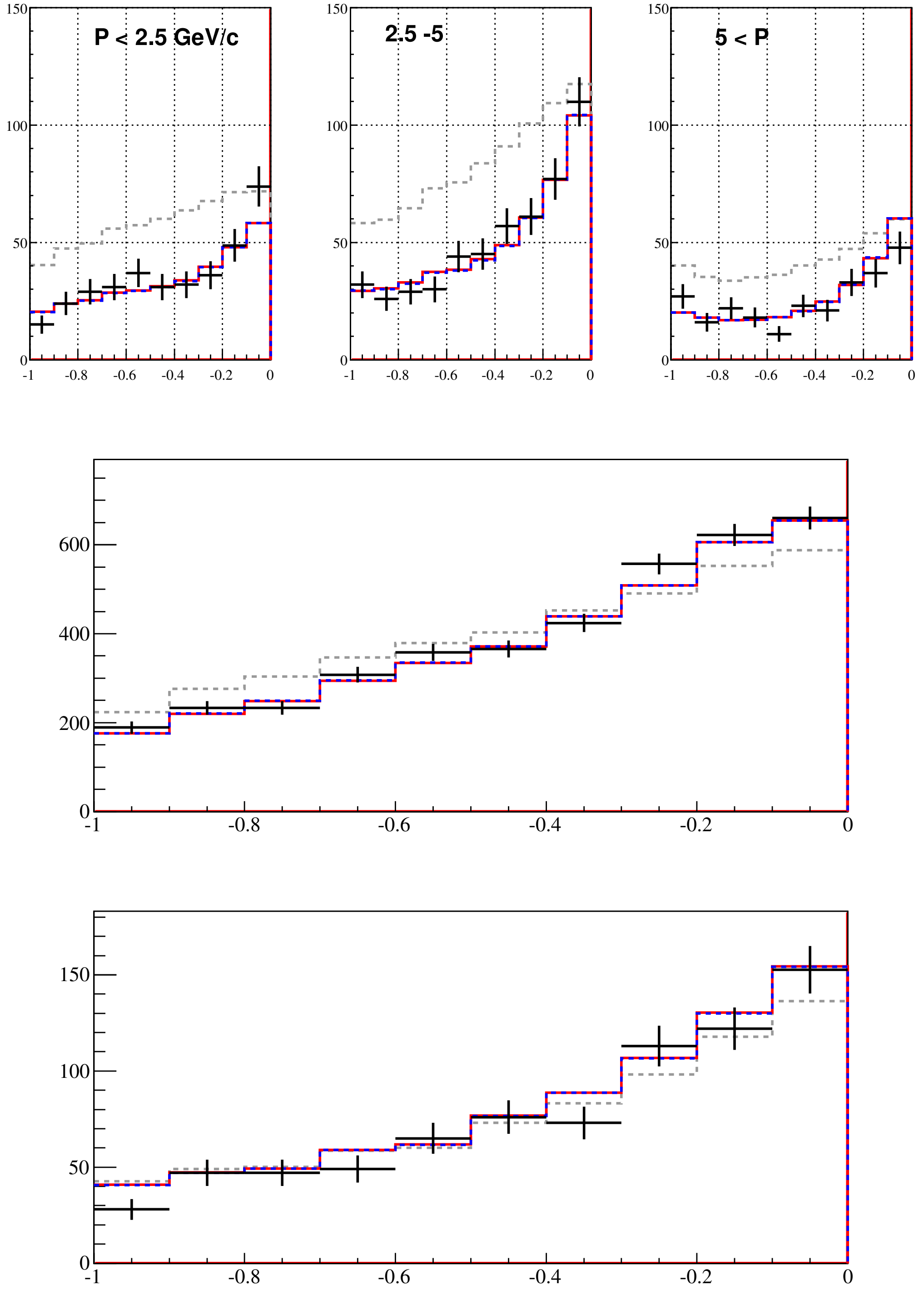

Figure 6.27: SK-I + SK-II + SK-III + SK-IV zenith angle distributions for FC events for data (line with error bar) and MC assuming no oscillation (grey dashed line), best fit results at normal hierarchy (red solid line) and best fit results at inverted hierarchy (blue dashed line). From top to the bottom: UPMU stopping, UPMU non-showering, UPMU showering.

Figures 6.28 and 6.29 show the $\chi^2 - \chi^2_{min}$ distributions as a function of oscillation parameters. When finding the minimum χ^2 against one oscillation parameter, the other parameters are chosen so that χ^2 is minimized. 90% C.L. is at $\chi^2 = \chi^2_{min}$+2.7.

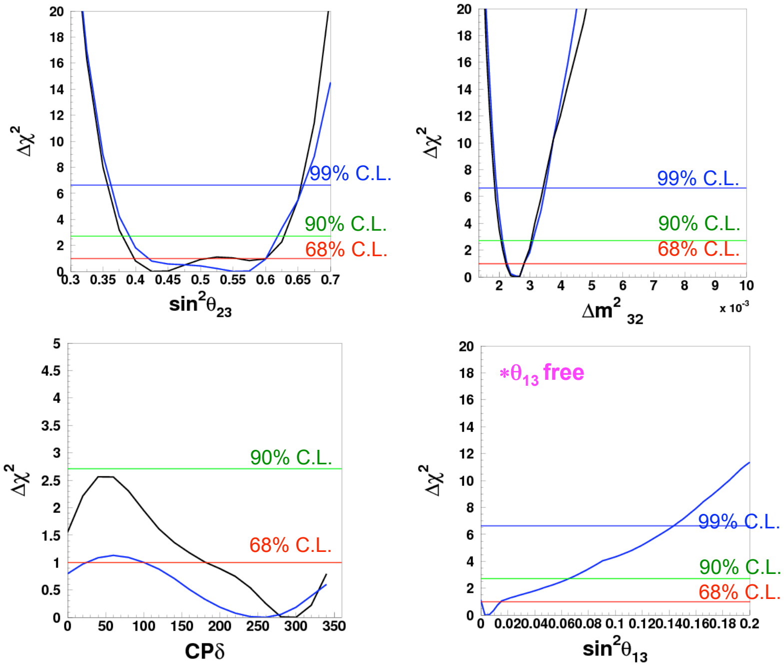

Figure 6.28: $\Delta\chi^2 = \chi^2 - \chi^2_{min}$ distributions as a function of Δm^2_{32}, $\sin^2\theta_{23}$, δ_{CP} and $\sin^2\theta_{13}$ (in case of free θ_{13}) for normal hierarchy case. Black line represents fixed $\sin^2\theta_{13} = 0.025$ and blue line represents free θ_{13}.

Figures 6.30 and 6.31 show the allowed regions drawn in two dimensions at 68%, 90% and 99% C.L..

$\Delta\chi^2_{min}$ ($= \Delta\chi^2_{min(NH)} - \Delta\chi^2_{min(IH)}$) is found to be 556.7 (normal hierarchy) - 555.50 (inverted hierarchy) = 1.2, with inverted hierarchy slightly preferred. However, the significance is still too low to draw a conclusion on mass hierarchy. Figure 6.33 shows the distribution of χ^2 as a function of δ_{CP} for both normal and inverted hierarchies.

As for δ_{CP}, with θ_{13} fixed, the best fit values are 300° and 260°, and $180^\circ < \delta_{CP} < 340^\circ$ and $162^\circ < \delta_{CP} < 330^\circ$ at 68% C.L., for normal and inverted hierarchies respectively. However, the χ^2 is still low to draw a conclusion on the value of δ_{CP}. More statistics is needed to improve the sensitivity on δ_{CP}.

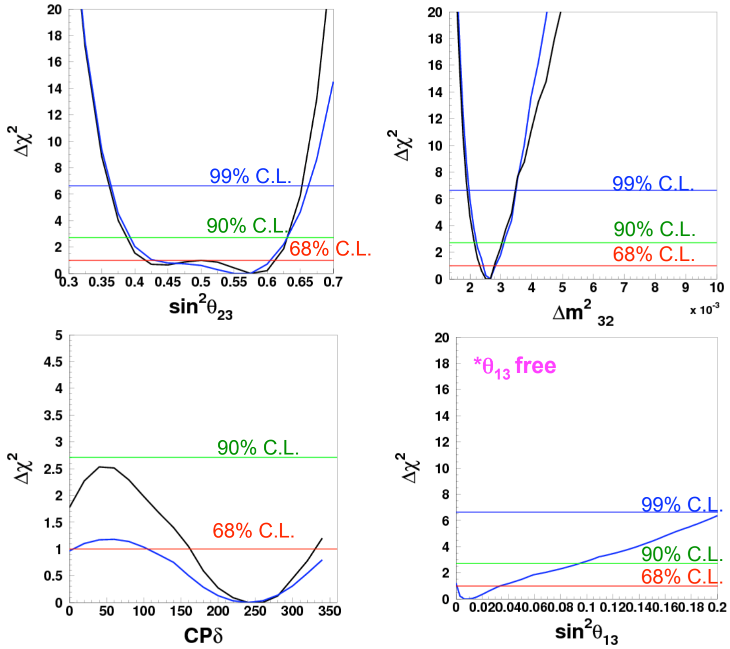

Figure 6.29: $\Delta\chi^2 = \chi^2 - \chi^2_{min}$ distributions as a function of Δm^2_{32}, $\sin^2\theta_{23}$, δ_{CP} and $\sin^2\theta_{13}$ (in case of free θ_{13}) for inverted hierarchy case. Black line represents fixed $\sin^2\theta_{13} = 0.025$ and blue line represents free θ_{13}.

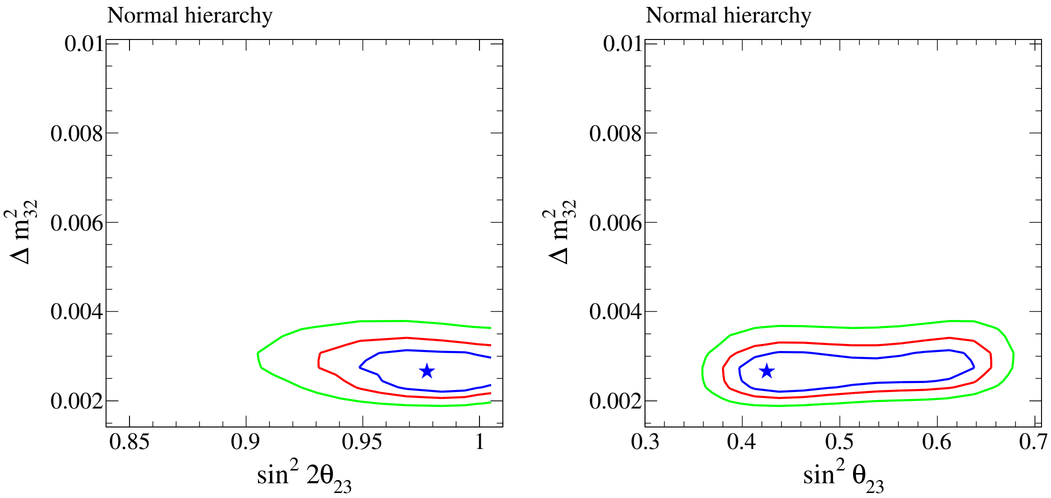

Figure 6.30: Contours of Δm^2_{32} and $\sin^2 2\theta_{23}$ (left) and Δm^2_{32} and $\sin^2\theta_{23}$ (right) for the normal mass hierarchy, at fixed θ_{13}. The three lines indicate allowed regions at 68% C.L. 90% C.L. and 99% C.L. respectively, defined as $\Delta\chi^2$ = 2.3, 4.6 and 9.2 respectively. The star shows the best fit point.

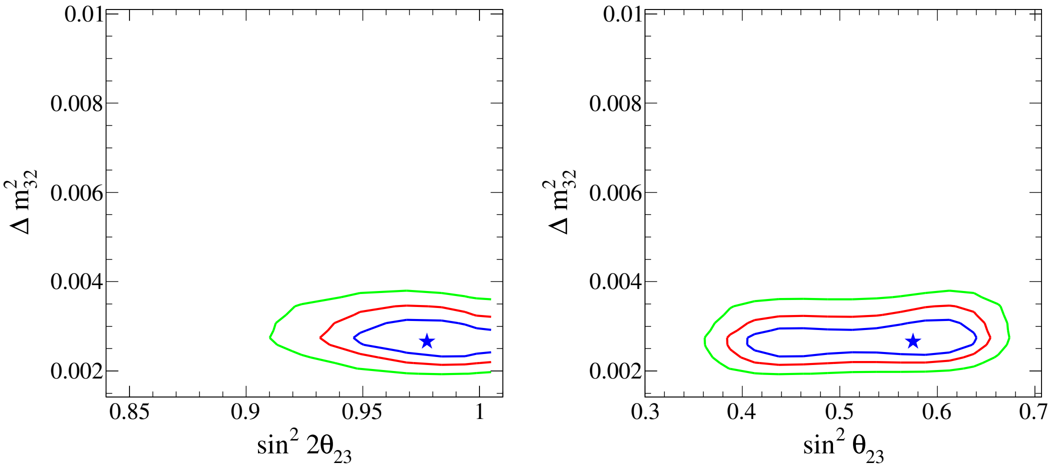

Figure 6.31: Contours of Δm^2_{32} and $\sin^2 2\theta_{23}$ (left) and Δm^2_{32} and $\sin^2\theta_{23}$ (right) for the inverted mass hierarchy, at fixed θ_{13}. The three lines indicate allowed regions at 68% C.L. 90% C.L. and 99% C.L. respectively, defined as $\Delta\chi^2$ = 2.3, 4.6 and 9.2 respectively. The star shows the best fit point.

6.8 Discussion

6.8.1 Event Samples Contributing to the Sensitivity to Mass Hierarchy

This full neutrino oscillation analysis is the first attempt to use ν_e and $\overline{\nu}_e$ enriched samples of the atmospheric neutrino data observed in the Super-Kamiokande to increase the sensitivity of mass hierarchy.

The sensitivity of mass hierarchy was carried out with fixed θ_{13} (at $\sin^2\theta_{13} = 0.025$), by assuming the "true" mass hierarchy as the inverted hierarchy case, oscillation parameters (Δ_{23}, $\sin^2\theta_{32}$, δ_{CP}) are assumed to be at (2.66 10^{-3}, 0.425, 300°) (best fit of normal hierarchy with fixed θ_{13}).

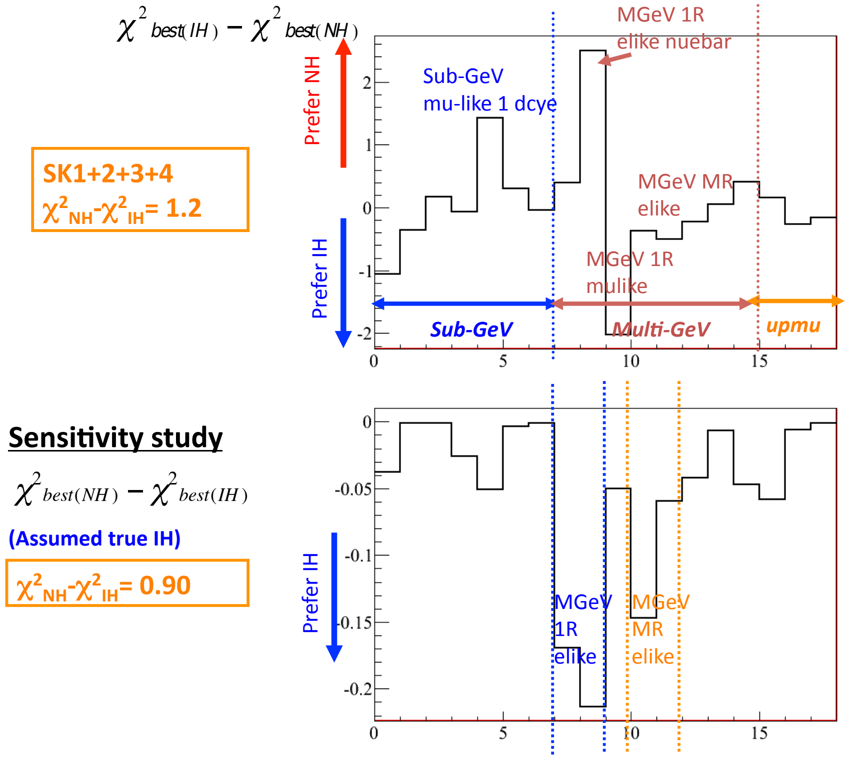

Figure 6.32: The numbers on the x-axis indicate the event sample types (18 types in total, with SK-I + SK-II + SK-III + SK-IV data). The upper panel shows the $\Delta\chi^2$ between normal hierarchy and inverted hierarchy contributed by each event sample of the data at the best fit oscillation parameters. The lower panel shows the $\Delta\chi^2$ between normal hierarchy and inverted hierarchy expected to be contributed by each event sample for MC, assuming the "true" oscillation parameters the same as the best fit parameters.

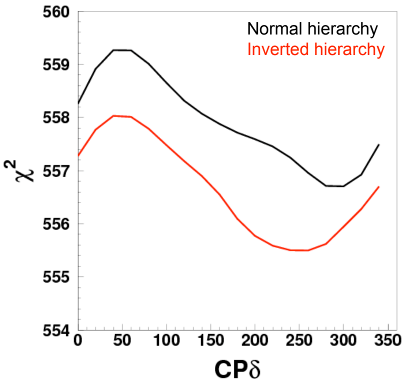

Figure 6.33: Distribution of $\Delta\chi^2$ as a function of δ_{CP} for normal hierarchy (black line) and inverted hierarchy (red line).

$\Delta\chi^2$ is calculated by fitting the assumed inverted hierarchy case with normal hierarchy MC. $\Delta\chi^2 = \chi^2_{min(IH)} - \chi^2_{min(NH)}$ is 1.06 when normal hierarchy is assumed to be true, and 0.90 when inverted is assumed to be true (Table 6.18). Contribution from each event sample in the sensitivity study is shown in the lower panel of Figure 6.32. It can be seen that the event samples which give the largest contributions of $\Delta\chi^2$ are multi-GeV 1-ring ν_e and $\overline{\nu}_e$-like samples and multi-GeV multi-ring ν_e and $\overline{\nu}_e$-like samples.

From the upper panel of Figure 6.32 which shows the $\Delta\chi^2$ distribution for observed data fitted with MC, it can be seen that multi-GeV 1-ring $\overline{\nu}_e$ like sample prefers the normal hierarchy, while multi-GeV 1-ring μ-like sample prefers the inverted hierarchy. As mention in the previous section, with θ_{13} fixed ($\sin^2\theta_{13} = 0.025$), χ^2_{min} for normal hierarchy is 556.70, while χ^2_{min} for inverted hierarchy is 555.50. Hence $\Delta\chi^2$ ($= \Delta\chi^2_{min(NH)} - \Delta\chi^2_{min(IH)}$) $= 1.2$. As χ^2_{min} is smaller for the inverted hierarchy, it is slightly favoured, but the significance is still low to draw a conclusion. The distribution of χ^2 of both normal and inverted hierarchies as a function of δ_{CP} is shown in Figure 6.33, the difference between the χ^2 of normal and inverted hierarchies at different values of δ_{CP} can be seen from the plot. It is expected that with more statistics, and further improved purity of CC ν_e and CC $\overline{\nu}_e$ in e-like samples, the sensitivity to mass hierarchy could be further improved and probed with atmospheric neutrino analysis.

6.8.2 Effect of Systematic Errors

A study was carried out by taking a particular category of systematic errors as ±50% of their original values. The assumed true values of the oscillation parameters are the same as that in Section 6.6.

The best fit oscillation parameters at assumed true normal and inverted hierarchies in the sensitivity study in Section 6.6 are listed in the Table 6.23:

	Best fit for assumed normal hierarchy	Best fit for assumed inverted hierarchy
Δm^2_{32}	2.82×10^{-3} eV^2	2.51×10^{-3} eV^2
$\sin^2\theta_{23}$	0.5	0.475
δ_{CP}	300°	300°
$\Delta\chi^2$	1.06	0.90

Table 6.23: Best fit values at assumed normal and inverted hierarchies in the original sensitivity study carried out in Section 6.6.

ν flux systematic errors

Systematic errors related to ν flux were set to half of their original values.

In the case of assumed inverted hierarchy, $\Delta\chi^2 = \chi^2(\text{NH}) - \chi^2(\text{IH})$ is 0.93, increased by 0.03 when compared with the original sensitivity study, with the best fit point the same as the original sensitivity study best fit point.

In case of assumed normal hierarchy, $\Delta\chi^2 = \chi^2(\text{NH}) - \chi^2(\text{IH})$ is 1.08, which increased by 0.02, with the best fit point same as the original sensitivity study best fit point.

Data was also fitted with systematic errors related to ν flux halved. The best fit points and the χ^2 is listed in Table 6.24 for both normal and inverted hierarchies. Both best fit points shifted when compared with the original fitting. $\Delta\chi^2$ between normal and inverted hierarchies becomes 0.8 (decreased by 0.4 when compared with the original fit), with inverted hierarchy slightly preferred.

	Normal hierarchy	Inverted hierarchy
Δm^2_{32}	2.37×10^{-3} eV^2	$2.51 \times 10^{-3} eV^2$
$\sin^2\theta_{23}$	0.425	0.45
δ_{CP}	260°	260°
$\Delta\chi^2$	569.1 / 477 dof	568.3 / 477 dof

Table 6.24: Best fit values and $\Delta\chi^2$ for normal and inverted hierarchies for data fitted with ν flux related systematic errors halved.

The errors are also increased by 50% and the effect $\Delta\chi^2 = \chi^2(\text{NH}) - \chi^2(\text{IH})$ is studied.

In the case of assumed inverted hierarchy, $\Delta\chi^2 = \chi^2(\text{NH}) - \chi^2(\text{IH})$ is 0.88, decreased by 0.02 when compared with the original sensitivity study, with the best fit point the same as the original sensitivity best fit point.

In case of assumed normal hierarchy, $\Delta\chi^2 = \chi^2(\text{NH}) - \chi^2(\text{IH})$ becomes 1.05, decreased by 0.01 when compared with the original value, with the best fit point the same as the original sensitivity study.

The study with ν flux systematic errors increased by 50% was also done for fitting with data. The best fit point the χ^2 for both normal and inverted hierarchies are listed in Table 6.25. Both best fit points changed when compared with the original fitting. $\Delta\chi^2$ between normal and inverted hierarchies becomes 1.6 (increased by 0.4), with inverted hierarchy slightly preferred.

	Normal hierarchy	Inverted hierarchy
Δm^2_{32}	2.66×10^{-3} eV^2	$2.66 \times 10^{-3} eV^2$
$\sin^2\theta_{23}$	0.425	0.6
δ_{CP}	300°	260°
$\Delta\chi^2$	550.4 / 477 dof	548.8 / 477 dof

Table 6.25: Best fit values and $\Delta\chi^2$ for normal and inverted hierarchies for data fitted with ν flux related systematic errors increased by 50%.

ν interactions systematic errors

Systematic errors related to ν interactions were set to half of their original values.

In the case of assumed inverted hierarchy, $\Delta\chi^2 = \chi^2(\text{NH}) - \chi^2(\text{IH})$ is 0.96, increased by 0.06 when compared with the original sensitivity study, with the best fit point the same as the original sensitivity study best fit point.

In the case of assumed normal hierarchy, $\Delta\chi^2 = \chi^2(\text{NH}) - \chi^2(\text{IH})$ is 1.13, increased by 0.07 when compared with the original sensitivity study, with the best fit point the same as the original sensitivity study best fit point.

Data fitting was also performed with ν interaction systematic errors halved. The best fit points and χ^2 for both normal and inverted hierarchies are listed in Table 6.26. $\Delta\chi^2$ between normal and inverted hierarchies becomes 2.0 (increased by 0.8) with inverted hierarchy slightly preferred. Best fit point for $\sin^2\theta_{23}$ and δ_{CP} for normal hierarchy and δ_{CP} for inverted hierarchy changed when compared with the original data fitting.

	Normal hierarchy	Inverted hierarchy
Δm^2_{32}	2.66×10^{-3} eV^2	$2.66 \times 10^{-3} eV^2$
$\sin^2\theta_{23}$	0.6	0.6
δ_{CP}	260°	240°
$\Delta\chi^2$	569.4 / 477 dof	567.4 / 477 dof

Table 6.26: Best fit values and $\Delta\chi^2$ for normal and inverted hierarchies for data fitted with ν interactions related systematic errors halved.

The ν interactions errors are also increased by 50% to see how $\Delta\chi^2 = \chi^2(\text{NH}) - \chi^2(\text{IH})$ changes.

In the case of assumed inverted hierarchy, $\Delta\chi^2 = \chi^2(\text{NH}) - \chi^2(\text{IH})$ is 0.86, decreased by 0.04 when compared with the original sensitivity study, with the best fit point the same as the original one.

In the case of assumed normal hierarchy, $\Delta\chi^2 = \chi^2(\text{NH}) - \chi^2(\text{IH})$ becomes 1.01, decreased by 0.05 when compared with the original value, with the best fit point also the same as that in the original sensitivity study.

Data fitted was also carried with ν interaction related errors increased by 50%. The best fit points for both normal and inverted hierarchies are listed in Table 6.27. The best fit point for

δ_{CP} for normal hierarchy and $\sin^2\theta_{23}$ for inverted hierarchy changed when compared with the original fitting. $\Delta\chi^2$ between normal and inverted hierarchy becomes 0.3 (decreased by 0.9), with inverted hierarchy very slightly preferred.

	Normal hierarchy	Inverted hierarchy
Δm^2_{32}	2.66×10^{-3} eV^2	$2.66 \times 10^{-3} eV^2$
$\sin^2\theta_{23}$	0.425	0.425
δ_{CP}	280°	280°
$\Delta\chi^2$	549.7 / 477 dof	549.4 / 477 dof

Table 6.27: Best fit values and $\Delta\chi^2$ for normal and inverted hierarchies for data fitted with ν interactions related systematic errors increased by 50%.

Event reconstruction systematic errors

Systematic errors related to event reconstruction were set to half of their original values.

In the case of assumed inverted hierarchy, $\Delta\chi^2 = \chi^2(\text{NH}) - \chi^2(\text{IH})$ is 0.91, increased by 0.01 when compared with the original sensitivity study, with the best fit point the same as the original sensitivity study best fit point.

In the case of assumed normal hierarchy, $\Delta\chi^2 = \chi^2(\text{NH}) - \chi^2(\text{IH})$ is 1.07, increased by 0.01 when compared with the original sensitivity study, with the best fit point the same as the original sensitivity study best fit point.

Data fitting was also performed with event reconstruction related errors halved. The best fit points for both normal and inverted hierarchies are listed in Table 6.28. The best fit points for Δm^2_{32} and δ_{CP} for normal hierarchy and Δm^2_{32}, $\sin^2\theta_{23}$ and δ_{CP} for inverted hierarchy changed when compared with the original fit. $\Delta\chi^2$ between normal and inverted hierarchy becomes 0.9 with inverted hierarchy slightly preferred.

	Normal hierarchy	Inverted hierarchy
Δm^2_{32}	2.37×10^{-3} eV^2	$2.66 \times 10^{-3} eV^2$
$\sin^2\theta_{23}$	0.425	0.575
δ_{CP}	280°	260°
$\Delta\chi^2$	561.0 / 477 dof	560.1 / 477 dof

Table 6.28: Best fit values and $\Delta\chi^2$ for normal and inverted hierarchies for data fitted with event reconstruction related systematic errors halved.

This category of errors are also increased by 50% to see how $\Delta\chi^2 = \chi^2(\text{NH}) - \chi^2(\text{IH})$ changes.

In the case of assumed inverted hierarchy, $\Delta\chi^2 = \chi^2(\text{NH}) - \chi^2(\text{IH})$ is 0.89, decreased by 0.01 when compared with the original sensitivity study, with the best fit point the same as the one in the original sensitivity study.

In the case of assumed normal hierarchy, $\Delta\chi^2 = \chi^2(\text{NH}) - \chi^2(\text{IH})$ becomes 1.06, no change when compared with the original sensitivity study, with the best fit point the same as the original sensitivity study.

Data was also fitted with event reconstruction related systematic errors increased by 50%. The best fit points are listed in Table 6.29. $\Delta\chi^2$ between normal and inverted hierarchies becomes 1.3 (increased by 0.1) with inverted hierarchy slightly preferred, but the best fit points for both normal and inverted hierarchy changed significantly when compared with the original fit.

	Normal hierarchy	Inverted hierarchy
Δm^2_{32}	2.66×10^{-3} eV^2	$2.66 \times 10^{-3} eV^2$
$\sin^2\theta_{23}$	0.45	0.575
δ_{CP}	300°	240°
$\Delta\chi^2$	552.4 / 477 dof	551.1 / 477 dof

Table 6.29: Best fit values and $\Delta\chi^2$ for normal and inverted hierarchies for data fitted with event reconstruction related systematic errors increased by 50%.

In conclusion, the errors related to ν interactions have the largest effect on the sensitivity on mass hierarchy, but the effect is still not very significant. Increasing or decreasing each of the three categories of systematic errors does not have significant effect on the sensitivity of mass hierarchy.

6.8.3 Consistency with Other Experiments

The new results of Δm^2_{32} and $\sin^2\theta_{23}$ is compared with other experiments are shown in Figure 6.34 for free θ_{13} and Figure 6.35 for fixed θ_{13}. The results is shown to be consistent with results from other experiments.

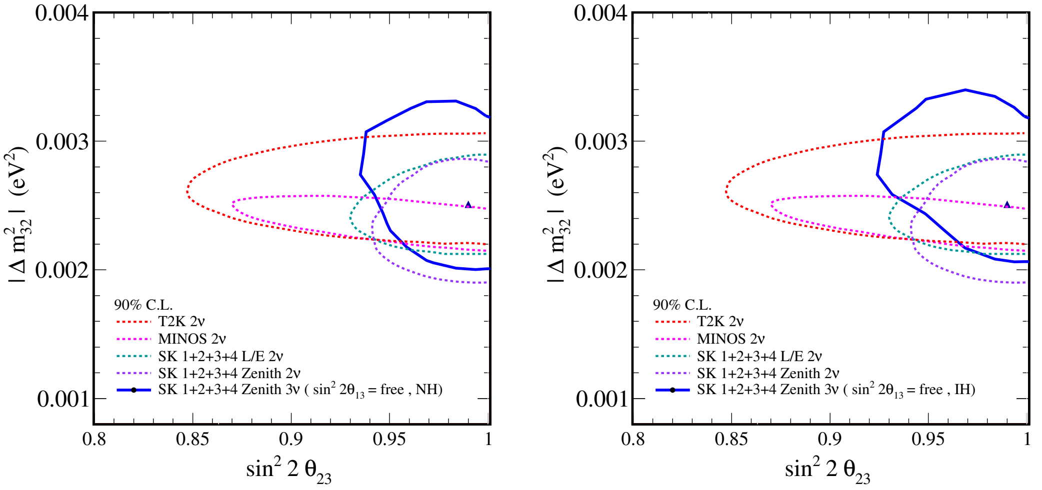

Figure 6.34: Contours of Δm^2_{32} and $\sin^2 2\theta_{23}$ allowed regions for normal hierarchy (left) and inverted hierarchy (right) for free θ_{13}. New results from this study is represented by blue solid line, and the best fit point is represented by the triangle.

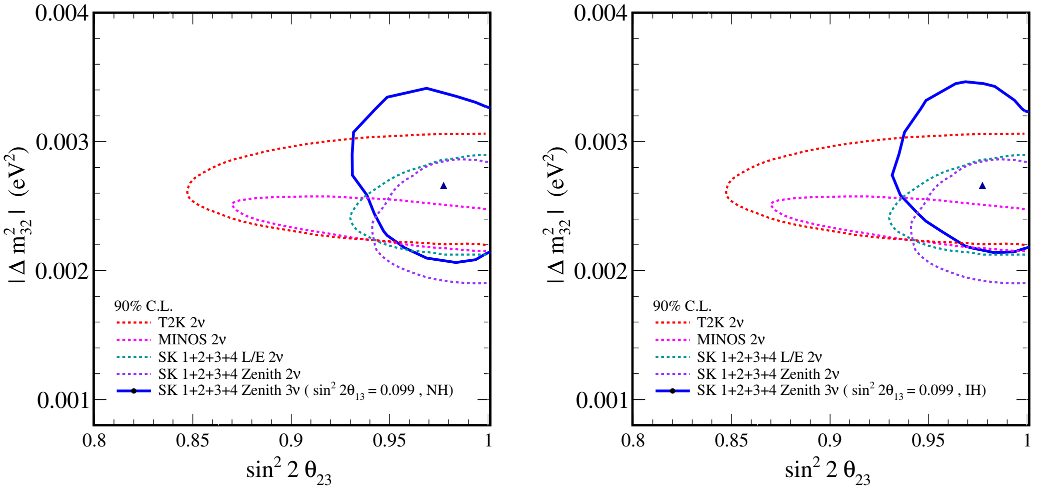

Figure 6.35: Contours of Δm^2_{32} and $\sin^2 2\theta_{23}$ allowed regions for normal hierarchy (left) and inverted hierarchy (right) for fixed θ_{13}. New results from this study is represented by blue solid line, and the best fit point is represented by the triangle.

Chapter 7

Conclusion

Full three flavor oscillation analysis was carried out with Super-Kamiokande atmospheric neutrino data in order to obtain information on the mass hierarchy for the first time. It is the first time to separate multi-GeV e-like samples into ν_e and $\overline{\nu}_e$ enriched samples so as to increase the sensitivity to the mass hierarchy. All data observed in SK-I (1489.2 days exposure for FC and PC, 1645.9 days for UPMU), SK-II (798.6 days exposure for FC and PC, 827.7 days for UPMU), SK-III (518.1 days exposure for FC and PC, 635.6 days for UPMU) and SK-IV (1097 days exposure for FC and PC, 1096.7 days for UPMU) period through Apr. 1996 to Feb 2012 were used.

For both free and fixed θ_{13} cases, the allowed regions of the Δm^2_{32} and $\sin^2\theta_{23}$ are consistent with other experiments (Figures 6.34 and 6.34).

As for the constraint on mass hierarchy, it is probed with ν_e and $\overline{\nu}_e$-like samples. The inverted hierarchy is slightly favoured with $\Delta\chi^2 = 1.2$. The significance is still low to draw a conclusion. However the sensitivity study shows that the newly developed ν_e and $\overline{\nu}_e$ enriched samples improve the sensitivity on the mass hierarchy. This study demonstrated the contribution by the separation of ν_e and $\overline{\nu}_e$ samples.

As $\Delta\chi^2$ between the normal and inverted mass hierarchies is expected to be proportional to the exposure as shown in Figure 7.1, it is expected that the mass hierarchy could be constrained with atmospheric neutrino analysis in the future. Longer exposure time or larger detector size (such as Hyper-Kamiokande experiment [148]) which both give higher statistics would help to constrain the mass hierarchy.

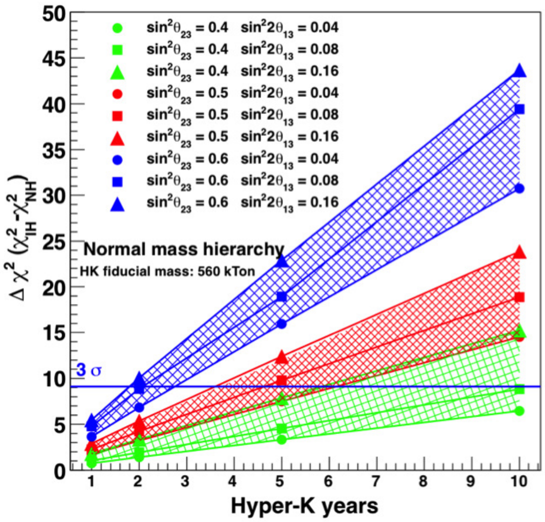

Figure 7.1: Expected sensitivity of mass hierarchy by Hyper Kamiokande (whose fiducial volume is 25 times of Super Kamiokande) as a function of years of exposure.

Bibliography

[1] M. Fukugita, T. Yanagida, Phys. Lett. B. 174, 45 (1986).

[2] J.H. Christenson, J.W. Cronin, V.L. Fitch, R. Turlay, Phys. Rev. Lett. 13, 138 (1964).

[3] R. Davis, Jr., D.S. Harmer, K.C. Hoffman, Phys. Rev. Lett. 20, 1205 (1968).

[4] Y. Fukuda et al., Phys. Rev. Lett. 81, 1562 (1998).

[5] E. Aliu et al., Phys. Rev. Lett. 94 081802 (2005).

[6] The Daya Bay Collaboration, Phys. Rev. Lett. 108, 171803 (2012).

[7] J. K. Ahn et al. (RENO Collaboration), Phys. Rev. Lett. 108. 191802 (2012).

[8] H. Ray, The MiniBooNE Experiment, hep-ex/0701040v1.

[9] Z. Maki, M. Nakagawa, S. Sakata, Prog. Theo. Phys. 28, 870 (1962).

[10] B. Pontecorvo, Sov. Phys. JETP 26, 984 (1968).

[11] A.I. Abazov et al., Phys. Rev. Lett. 67, 3332 (1991); J.N. Abdurashitov et al., JETP 95, 181 (2002).

[12] P. Anselmann et al., Phys. Lett. B 285, 376 (1992); W. Hampel et al., Phys. Lett. B 447, 127 (1999).

[13] K.S. Hirata et al., Phys. Rev. Lett. 63, 16 (1989); K.S. Hirata et al., Phys. Rev. D 44, 2241 (1991), Erratum-ibid. D45, 2170 (1992).

[14] Q.R. Ahmad et al., Phys. Rev. Lett. 87, 071301 (2001); Q.R. Ahmad et al., Phys. Rev. Lett. 89, 011301 (2002); Q.R. Ahmad et al., Phys. Rev. Lett. 92, 181301 (2002).

[15] S. Fukuda et al., Phys. Lett. B 539, 179 (2002).

[16] J.N. Bahcall, M.H. Piinsonneault, Rev. Mod. Phys. 64, 885 (1992).

[17] M.B. Smy et al., Phys. Rev. D 69, 011104 (2004).

[18] J. Hosaka et al., Phys. Rev. D73, 112001 (2006).

[19] S. Abe et al., Phys. Rev. Lett. 100, 221803 (2008).

[20] C. Arpesella et al., Phys. Rev. Lett. 101, 091302 (2008).

[21] K. Abe et al., Phys. Rev. D 83, 052010 (2011).

[22] A. Yamamoto et al., Nuc. Phys. B (Proc. Suppl.) 166 (2007) 6267 (2007).

[23] M. Honda et al., Phys. Rev. D 75, 043006 (2007).

[24] K.S. Hirata et al., Phys. Lett. B 205, 416 (1988).

[25] K.S. Hirata et al., Phys. Lett. B 280, 146 (1992).

[26] D. Casper et al., Phys. Rev. Lett. 66, 2561 (1991).

[27] R. Becker-Szendy et al., Phys. Rev. D 46, 3720 (1992).

[28] M.C. Sanchez et al., Phys. Rev. D 68, 113004 (2003).

[29] MACRO collaboration, Phys. Lett. B 434, 451 (1998).

[30] Y. Fukuda et al., Phys. Rev. Lett. 82, 2644 (1999).

[31] Y. Ashie et al., Phys. Rev. Lett. 93, 101801 (2004).

[32] M.H. Ahn et al., Phys. Rev. D 74, 072003 (2006).

[33] P. Adamson et al., Phys. Rev. Lett. 101, 131802 (2008).

[34] P. Adamson et al., Phys. Rev. Lett. 106, 181801 (2011).

[35] Y. Ashie et al., Phys. Rev. Lett. 93, 101801 (2004).

[36] R. Wendell, In proceedings of 11th international conference on Topics in Astroparticle and Underground Physics (2009).

[37] M. Apollonio, et al. (Chooz collaboration), Eur. Phys. J., C27, 331 (2003).

[38] K. Abe, et al. (T2K collaboration), Phys. Rev. Lett. 107, 041801 (2011).

[39] G.L. Fogli, E. Lisi, A. Marrone, A. Palazzo, A.M. Rotunno,

[40] S.P. Mikheyev and A.Y. Smirnov, Sov. Jour. Nucl. 42, 913 (1985); L. Wolfenstein, Phys. Rev. D 17, 2369 (1978).

[41] C. Giunti, C.W. Kim, M. Monteno, Nucl. Phys. B521, 3 (1998).

[42] O. L. G. Peres and A. Y. Smirnov, Phys. Lett. B 456, 204(1999).

[43] C. Ishihara, Ph.D. Thesis, University of Tokyo (2010).

[44] R. Wendell et al., Phys. Rev. D 81, 092004 (2010).

[45] O.L.G. Peres and A.Y. Smirnov, Nucl. Phys. B 680 479 (2004).

[46] I. Frank and I. Tamm, C.R. Acad. Sci. USSR 14, 109 (1937).

[47] H. Kume et al., Nucl. Inst. and Meth. 205, 443 (1983).

[48] A. Suzuki et al., Nucl. Inst. and Meth. A 329, 299 (1993).

[49] Y. Takeuchi et al., Phys. Lett. 452, 418 (1999).

[50] H. Ikeda et al., Nucl. Inst. and Meth. A 320, 310 (1992).

[51] T. Tanimori et al., IEEE Trans. Nucl. Sci. NS-36, 497 (1989).

[52] J. George, Ph.D. Thesis, University of Washington (1998).

[53] H. Nishino et al., IEEE Trans. Nucl. Sci. 57, 428 (2010).

[54] M. Honda et al., Phys. Rev. D 64, 053001 (2001).

[55] M. Honda et al., Phys. Rev. D 70, 043008 (2004).

[56] T.K. Gaisser, M. Honda, Annu. Rev. Nucl. Part. Sci. 2002. 52: 153-99 (2002).

[57] G. Battistoni at el., Astropart. Phys. 19, 269 (2003).

[58] G. Barr et al., Phys. Rev. D 70, 0423006 (2004).

[59] L.V. Volkava, Sol. J. Nucl. Phys. 31, 784 (1980).

[60] W.R. Webber, R.L. Golden and S.A. Stephens, In Proceedings of the 20th International Cosmic Ray Conference (1987).

[61] E.S. Seo et al., Astrophys. J. 378 763 (1991).

[62] P. Pappini et al., In Proceedings of the 23rd International Cosmic Ray Conference (1993).

[63] M. Boezio et al., Astrophys. J. 518 457 (1999).

[64] W. Menn et al., Astrophys. J. 533 281 (2000).

[65] T. Sanuki et al., Astrophys. J. 545 1135 (2000).

[66] J. Alcarez et al., Phys. Lett. B 490 27 (2000).

[67] M.J. Ryan, J.F. Ormes and V.K. Balasubrahmanyan, Phys. Rev. Lett. 28 985 (1972).

[68] K. Asakamori et al., Astrophys. J. 502 985 (1998).

[69] I.P. Ivanenko et al., In Proceedings of the 23rd International Cosmic Ray Conference (1993).

[70] Y. Kawamura et al., Phys. Rev. D 40 729 (1989).

[71] A.V. Apanasenko et al., Astropart. Phys. 16 13 (2001).

[72] http://ccmc.gsfc.nasa.gov/modelweb/atmos/us_standard.html

[73] http://www.ngdc.noaa.gov/IAGA/vmod/igrf.html

[74] K. Hanssget and J. Ranft, Comput. Phys. 39 37 (1986).

[75] S. Roesler, R. Engel and J. Ranfit, Phys. Rev. D 57 2889 (1998).

[76] M. Motoki et al., Astropart. Phys. 19 113 (2003).

[77] P. Achard et al. (L3 Collaboration), Phys. Lett. B 598 15 (2004).

[78] M. Honda et al., Phys. Rev. D 75, 043005 (2007).

[79] S. Haino et al., (BESS Collaboration), Phys. Lett. B 594, 35 (2004).

[80] K. Abe et al. (BESS), Phys. Lett. B 564, 8 (2003).

[81] T. Sanuki et al., Phys. Lett. B 541, 234 (2002).

[82] O.C. Allkofer et al., Nucl. Phys. B 259, 1 (1985).

[83] S. Matsuno et al., Phys. Rev. D 29, 1 (1984).

[84] Y. Hayato, Nucl. Phys. Proc. Suppl. 112, 171 (2002).

[85] G. Mitsuka, AIP Conf. Proc. 967:208-211 (2007), AIP Conf. Proc. 981:262-264 (2008).

[86] C.H. Llewellyn Smith, Phys. Rep. 3, 261 (1972).

[87] R.A. Smith and E.J. Moniz, Nucl. Phys. B 43, 605 (1972). [Erratum-ibid. B 101, 547 (1975).]

[88] R. Gran, E. J. Jeon et al., Phys. Rev. D 74, 052002 (2006).

[89] A.A. Aguilar-Arevalo et al., Phys. Rev. Lett. 100, 032301 (2008).

[90] F. Sanchez, Talk at Fifth International Workshop on Neutrino-Nucleus Interactions in the Few-GeV Region (NuInt07), http://conferences.fnal.gov/nuint07/

[91] J. Nieves et al., Phys. Rev. C 70, 055503 (2004).

[92] H. Nakamura et al., Nucl. Phys. B (Proc. Suppl.) 112, 197 (2002).

[93] S. Barish et al., Phys. Rev. D 16, 3103 (1977).

[94] S. Bonetti et al., Nuovo Cimento 38, 260 (1977).

[95] M. Pohl et al., Nuovo Cimento 26, 332 (1979); N. Arimenise et al., Nucl. Phys. B 152, 365 (1979).

[96] A.S. Vovenko et al., Yad. Fiz. 30, 1014 (1979).

[97] S. Belikov et al, Z. Phys. 320, 625 (1985).

[98] J. Brunner et al., Z. Phys. C 45, 551 (1990).

[99] K. Ueno, T2K Technical Note 58 v3.1 (2012).

[100] D. Rein and L.M. Sehgal, Ann. of Phys. 133, 1780 (1981).

[101] D. Rein, Z. Phys. C 35, 43 (1987).

[102] T. Kitagaki et al., Phys. Rev. D 34, 2554 (1986).

[103] S.K. Singh, M.J. Vicente-Vacas and E. Oset, Phys. Lett. B 416, 23 (1998).

[104] H. Faissne et al., Phys. Lett. B 125, 230 (1983).

[105] W. Krenz et al., Nucl. Phys. B 135, 45 (1978).

[106] C.H. Albright and C. Jarlskog, Nucl. Phys. B 84, 467 (1975).

[107] M. G*ü*ck, E. Reya and A. Vogt, Eur. Phys. J. C 5, 461 (1998).

[108] A. Bodek and U.K. Yang, hep-ex/0308007

[109] P. Musset and J.P. Vialle, Phys. Rep. C 39, 1 (1978).

[110] J.E. Kim et al., Rev. Mod. Phys. 53, 211 (1981).

[111] S.J. Barish et al., Phys. Rev. D17, 1 (1978).

[112] S. Barlag et al., Z. Phys. C 11, 283 (1982).

[113] T. Sj*ö*strand et al., CERN-TH-7112-93 (1994).

[114] D. Rein and L.M. Sehgal, Nucl. Phys. B 233, 29 (1983).

[115] M. Hasegawa et al., Phys. Rev. Lett. 95, 252301 (2005).

[116] D. Rein and L.M. Sehgal, Phys. Lett. B 657, 207 (2007).

[117] R. Woods and D. Saxon, Phys. Rev. 95, 577 (1954).

[118] L. Salcedo et al., Nucl. Phys. A 484, 557 (1988).

[119] P. de Perio, Y. Hayato, R. Tacik, T2K Technical Note 33 v2.0

[120] D. Ashery et al., Phys. Rev. C 23, 2173 (1981).

[121] B.R. Martin and M.K. Pidcock, Nucl. Phys. B 126, 266 (1977).

[122] B.R. Martin and M.K. Pidcock, Nucl. Phys. B 126, 285 (1977).

[123] J.S. Hyslop et al., Phys. Rev. D 46, 961 (1992).

[124] D.A. Sparrow, Proc. of the Conf. on the intersection between particle and nuclear physics, 1019 (1984).

[125] H.W. Bertini et al., Phys. Rev. C 6, 631 (1972).

[126] S.J. Lindenbaum et al., Phys. Rev. 105, 1874 (1957).

[127] GEANT, CERN Program Library Long Writeup W5013 (1994).

[128] C. Zeinitz and T.A. Gabriel, Nucl. Inst. and Meth. A 349, 106 (1994).

[129] M. Nakahata et al., J. Phys. Soc. Jpn. 55, 3786 (1986).

[130] E. Bracci et al., CERN/HERA 72-1 (1972).

[131] A.S. Carrol et al., Phys. Rev. C 14, 635 (1976).

[132] M. Yamada et al., Phys. Rev. D 44, 617 (1991).

[133] Hirokazu Ishino, PhD Thesis, University of Tokyo (1999).

[134] S. Desai, Ph.D. Thesis Boston University (2004).

[135] Y. Takenaga, Ph.D. Thesis, University of Tokyo (2008).

[136] G. Mitsuka, Ph.D. Thesis, University of Tokyo (2009).

[137] E.R. Davies, Machine Vision: Theory, Algorithms, Practicalities, Academic Press, San Diego (1997).

[138] P. Hanggi et al., Phys. Lett. B 51, 119 (1974).

[139] V. Barger et al., Phys. Rev. D 22, 2718 (1980).

[140] Dziewonski and Anderson, Phys. Earth. Planet. Int. 25, 297-356 (1981).

[141] S. Baker and R.D. Cousins, Nucl. Inst. and Meth. 221, 437 (1984).

[142] G. Ambrosini et al., Phys. Lett. B 420, 225 (1998).

[143] A.E. Hedin, J. Geophys., Res. 96, 1159 (1991).

[144] E. Hernandez et al., Phys. Rev. D 76, 033005 (2007).

[145] P. de Perio, AIP Conf. Proc. 1405, pp. 223-228 (2011).

[146] The CHORUS Collaboration, Eur. Phys. J. C51 775-785 (2007).

[147] Y. Fukuda et al., Phys. Lett. B 433, 9 (1998).

[148] K. Abe et al., hep-ex/1109.3262v1

[149] M. Honda et al., Phys. Rev. D83, 123001 (2011).

[150] K. Niita et al., Radiat. Meas. 41, 1080(2006).

[151] G.L. Fogli et al., Phys. Rev. D 66, 053010 (2002).